Dynamic Response of RC Structural Elements under Impact Loading

Noosha Madjlessi

October 2019

A thesis submitted for the degree of Doctor of Philosophy of the Heriot-Watt University

The School of Energy, Geoscience, Infrastructure and Society (EGIS)

Heriot-Watt University

Edinburgh EH14 4AS

ABSTRACT

The effect of loading rate on the dynamic response of reinforced concrete (RC) beams under impact loading is investigated experimentally, via drop-weight testing, and numerically, through the use of three-dimensional (3D) dynamic nonlinear finite element analysis (NLFEA). During drop-weight testing, the behaviour of each specimen is established through the combined use of conventional instrumentations and a high-speed (HS) camera. The primary objective of the experimental work is to investigate the reasons that trigger the observed shift in specimen behaviour (compared to that established during static testing), once certain thresholds of applied loading rate and intensity are surpassed. The analysis of the test data suggests that the observed shift in specimen behaviour is largely attributed to the nature of the problem at hand (i.e. a wave propagation problem within a highly nonlinear medium) as well as the inertia forces developing along the element span (during the application of the impact load) and the ensuing localised response. The strain-rate sensitivity of the material properties of concrete does not appear to have a significant effect on the behaviour of the specimens tested as high values of strain-rate appear to be associated with the development of cracking along the element span.

The data obtained from the drop-tests conducted on slender and short beams reveal that the response exhibited under impact loading differs significantly from that established during equivalent static testing. This shift in structural response predominantly takes the form of an increase in the maximum sustained load as well as a reduction in the portion (span) of the beam reacting to the imposed action which tends to concentrate around the area of impact. However, measurements obtained from the drop-weight tests, concerning certain important aspects of RC structural response (e.g. maximum sustained load or deflection) often correspond to a specimen physical-state characterised by high concrete disintegration in combination with low residual load-bearing capacity and stiffness. This stage of structural response has little practical significance as it depends heavily on post-failure mechanisms for transferring the applied load to the specimen supports. In view of the above, the available test data cannot provide insight into the mechanisms underlying RC structural response nor can it identify the true ultimate limit state of the specimens when subjected to impact loading.

To achieve further insight into the mechanics underlying RC structural response under impact loading a well-established structural analysis packages (ADINA version 9.3.1) is employed which is capable of carrying out three-dimensional dynamic nonlinear finite element analysis while realistically accounting for the nonlinear behaviour of concrete and steel. The numerical predictions obtained are validated against available data obtained from the drop-weight tests. The validated models are then used to conduct a parametric investigation to study the dynamic response exhibited by RC beams when subjected to different rates and intensities of impact loading. The latter investigation reveals that 'true' load-carrying capacity is often significantly lower than the maximum sustained load recorded experimentally. In fact, the higher the loading rate and intensity characterising the impact load imposed the larger the latter difference becomes.

Based on the available test data and the numerical predictions obtained, a simplified model is proposed aiming to describe the behaviour of the RC beams under impact loading. The model attempts to link the observed shift in structural response to the localised behaviour exhibited by the beams with increasing rates of applied loading. A comparison of the predictions obtained with the relevant test data reveals good agreement.

To my parents for their unconditional love,

support and continuous guidance.

ACKNOWLEDGEMENTS

I am thankful to my supervisor Dr Demitrios Cotsovos, for providing me with guidance, his time and expertise, during my PhD studies. I would like to express my gratitude to The School of Energy, Geoscience, Infrastructure and Society (EGIS) of Heriot-Watt University, for providing a scholarship for my PhD studies.

Special thanks to my sister Niloofar Madjlessi for always encouraging me and believing in me.

Above all, I would like to express my utmost profound gratitude to my parents, Azizollah Majlessi and Fatemeh Saadat Talab for their continuous support and unconditional love, without whom I would never have enjoyed so many opportunities. I would also like to express my gratitude to my father whose success and passion for engineering have always been my inspiration and guidance in my professional life.

ACADEMIC REGISTRY

Research Thesis Submission

Name*:*	**Noosha Madjlessi**		
School/PGI:	**School of Energy, Geoscience, Infrastructure and Society**		
Version: (*i.e. First, Resubmission, Final)*	**Final**	Degree Sought (Award **and** Subject area)	**PhD in Civil Engineering**

Declaration

In accordance with the appropriate regulations, I hereby submit my thesis and I declare that:

1) the thesis embodies the results of my own work and has been composed by myself
2) where appropriate, I have made acknowledgement of the work of others and have made reference to work carried out in collaboration with other persons
3) the thesis is the correct version of the thesis for submission and is the same version as any electronic versions submitted*.
4) my thesis for the award referred to, deposited in the Heriot-Watt University Library, should be made available for loan or photocopying and be available via the Institutional Repository, subject to such conditions as the Librarian may require
5) I understand that as a student of the University I am required to abide by the Regulations of the University and to conform to its discipline.

* *Please note that it is the responsibility of the candidate to ensure that the correct version of the thesis is submitted.*

Signature of Candidate*:*		Date:	

Submission

Submitted By *(name in capitals):*	**Noosha Madjlessi**
Signature of Individual Submitting:	
Date Submitted:	

For Completion in the Student Service Centre (SSC)

Received in the SSC by (name in capitals):			
Method of Submission (Handed in to SSC; posted through internal/external mail):			
E-thesis Submitted ***(mandatory for final theses)***			
Signature:		Date:	

Table of Contents

List of Abbreviations

A_s	Total area of the longitudinal steel reinforcement in the RC beam specimen acting in tension
A_{sw}	Area of each shear link
s	Spacing of shear links
a_v	Shear span
b	Width of beam cross-section
d	Effective depth of beam cross-section
C	Damping constants
ε	Strain
$\dot{\varepsilon}$	Strain rate
δ	Displacement
σ_{ii}	Stress
σ_0	Octahedral normal stress
ϑ	Angle of similarity
s_{ij}	Deviatoric stress
E_s	Young's modulus of steel
f_{cm}	Mean compressive strength of 100mm concrete cubes
$f_{t,sp}$	Mean splitting strength of concrete cylinders with a diameter of 150mm and a height of 300mm
f_y	Yield strength of steel
f_u	Ultimate strength of steel
F_D	Vertical component of load
F_{int}	Internal force
F_I	Inertia force
G	Gap
h	Height of beam cross-section
I_1	First stress invariant
J_2	Second deviatoric stress invariant
J_3	Third deviatoric stress invariation
K	Element stiffness
$\widehat{K}$	Effective stiffness matrix
L	Full length of beam
L_0	Clear span of beam
L_{eff}	Effective length of beam

Λ	Normal contact force
M	Constant mass of a body
M_f	Flexural capacity
μ	Coefficient of friction
P_s	Equivalent static loading
$maxP_s$	Static load-carrying capacity of the specimen
P_d	Dynamic (contact) loading generated during impact
$maxP_d$	Peak value of dynamic loading
$maxd_d$	maximum deflection recorded during drop-weight testing
$\dot{P}$	Loading rate
P_f	Load-carrying capacity
P_D	Load-carrying capacity corresponding to inclined leg
R_d	Dynamic reaction force
P_f	Static flexural capacity
ρ_l	Longitudinal reinforcement ratio$(A_s/b \cdot h)$
ρ_w	Shear reinforcement ratio$(A_{sw}/b \cdot s)$
R(t)	External force
r	Elliptic function
SP	percentage of f_c that represents the amount of additional octahedral shear stress
τ	Shear stress
TP	percentage of f_c that represents the amount of tensile hydrostatic stress
t_0	Time corresponding to initial contact between the beam and the striker
t_I	Time corresponding to peak value of impact force
t_p	Time used to define the rate of impact loading
t_r	Time corresponding to peak value of reaction force
$T_{II,1,0}$	transverse tension developing at location 1 for N=0
$T_{II,1,N}$	transverse tension developing at location 1 for N≠0
F_T	Tangential force
U	Element deformation
U_j	Multiple independent degrees of freedom
U_k	Dependent degree of freedom
$\dot{U}$	Element velocity
$\ddot{U}$	Acceleration
V_c	Design shear resistance
V	Shear force
V_f	Flexural capacity
W	Natural frequency

CHAPTER 1 - INTRODUCTION

1.1 BACKGROUND

Concrete structures can be subjected to the action of loads (generated by industrial activities, high-speed trains, accidents due to collisions or explosions, natural disasters and acts of terrorism) induced at rates and intensities significantly higher than those of the dynamic loads (e.g. seismic and those generated by moving trains) considered by current design codes (Eurocode 2-1992, Eurocode 8-1998 and ACI-318-02). High-rise buildings, tunnels, bridges, slab-track for high-speed railways, off-shore and marine structures, storage and industrial facilities, as well as nuclear power plants, are examples of such structures, the majority of which are fully or partially constructed from reinforced concrete (RC). The application of such loads can often result in catastrophic failures and partial or full collapse of the structures considered with detrimental implications for economy and safety. Therefore, it is essential that such structures achieve an intended level of resilience in order to sustain the action of extreme loads (e.g. impact loads). As a consequence, it is becoming increasingly important for practical structural analysis to accurately account for the effects of such loads on RC structural response in order to allow for the development of efficient design solutions capable of safeguarding an elevated level of resilience.

When investigating the response of RC structural configurations/specimens under impact loading, the dynamic problem at hand must be viewed as a wave-propagation problem within a highly nonlinear medium (Cotsovos and Pavlović 2008[a, b, c],2012). The collision of an object on an RC structural element, results in the generation of stress waves at the area of impact which propagates towards the supports. The latter stress waves can be reflected by the boundary conditions imposed onto the structural elements considered continuously travelling within the structural element causing the development of a complex stress field within the concrete medium (Kotsovos 2014). This field is further accentuated by the formation of cracks thus increasing the complexity of the problem considered herein.

To date a large number of drop-weight test (Hughes & Spiers 1981, Miyamoto et al 1989, Kulkarmi & Shah 1998, Kishi et al 2001, 2002, May & Chen 2006, Zhang et al 2008, Fujiukake et al 2009, Saacti & Vecchio 2009, Abbas et al 2010, Zhao et al 2017, Isaac et al 2017) and numerical studies (via nonlinear finite element analysis- NLFEA) (Miyamoto et al 1989, Thabet & Haldaen 2000, Kishi et al 2001, Abbas et al 2004, Cotsovos et al 2008, Saatci & Vecchio (2009), Kishi et al 2011, Adhikary et al 2012, Cotsovos & Pavlović 2012, Pham and Hao 2017, Guo et al 2017) have been carried out to investigate the response of reinforced concrete (RC) structural elements (mainly beams and slabs) under impact loading. The above studies suggest that the available test data is characterised by considerable scatter (Cotsovos and Pavlovic, 2012) and fails to accurately quantify the effect of a range of parameters on the response of the RC specimens considered. Furthermore, both experimental and numerical methods employed for investigating RC structural response are usually complex and can be often applied only to simple structural configurations (i.e. beams, columns, and slabs). A review of these assessment methods will be discussed in the following sections.

The assessment of RC structures under impact loading in practice is carried out through the use of physical models (such as the Truss Analogy (TA)) describing the mechanics underlying RC structural response under static and seismic load-conditions in combination with Single Degree of Freedom (SDOFs) models adopted – mainly by codes of practice employed mainly by the military (TM5-855-1 1998) – for describing the dynamic response exhibited under impact loading. Such models essentially bypass the complexities associated with drop-weight testing and the application of advanced nonlinear finite element methods employed largely for research purposes. Such methods, however, fail to account for the triaxiality and brittleness characterising concrete material behaviour (Kotsovos & Pavlović 1995, Kotsovos 2014) and ignore the nature of the problem at hand (a wave propagation problem within a highly nonlinear medium).

When subjected to loads characterised by increasing values of loading rate and intensity the available experimental data (Hughes & Spiers 1981, Miyamoto et al 1989) suggest that RC structural response is characterised by higher values of stiffness and strength compared to their counterparts established under equivalent static loading. The causes of the observed shift in specimen behaviour with increasing levels of loading rates and

intensities (in relation to the behaviour established under equivalent static loading) do not appear to be as yet fully understood. It is widely considered (Bischoff and Perry 1991, Ross and Tedesco 1995, Kulkarni and Shah 1998, Saatci and Vecchio 2009, Ožbolt et al. 2014) that the response of RC beams under impact loading is linked with *'strain-rate sensitivity'* of the mechanical properties of concrete and steel; in fact, strain-rate sensitivity underlies current code specifications for the design of mainly military structures (TM5-855-1 1998). Nevertheless, the validity of this concept has been disputed in recent years by demonstrating numerically that it is possible to obtain realistic predictions of RC structural response under impact loading without considering strain-rate sensitivity at the material level (Cotsovos et al 2008, Cotsovos 2010, Cotsovos & Pavlović 2010). However, experimental evidence in support of these numerical findings is currently lacking. Available test data is often restricted to measurements of the contact force (generated in the impact region), the corresponding mid-span deflections and the reaction forces (developing at the supports), as well as observations of the specimen crack-patterns exhibited 'after' the impact load, is applied. However, such data are insufficient for studying in detail the causes underlying structural behaviour under impact loading as information concerning the variation of the deformation and cracking profiles '*throughout'* the loading process is often not captured during testing.

1.2 RESEARCH AIMS AND OBJECTIVES

The work described in the present thesis aims at producing valid experimental and numerical data via drop-weight testing and detailed nonlinear finite element analysis (NLFEA) respectively. The combined (numerical and test) data produced provides insight into the mechanics underlying RC structural response under impact loading improving our understanding of the causes of the observed shift in the behaviour exhibited by RC beams (characterised by different shear spans) when subjected to increasing levels of loading rate and intensity. During testing attention is focused on recording a number of characteristics (e.g. impact and reaction forces, displacement and the strain in particular regions of the specimens) of the exhibited response, the exhibited crack-patterns and deformation profiles throughout the entire loading process, as well as the modes of failure, ultimately exhibited.

The NLFEA package (ADINA, 1986) employed incorporates a concrete material model capable of realistically describing the triaxiality and brittle nature characterising concrete

material behaviour. The subject package is capable of accounting for the nature of the problem at hand: a wave propagation problem within a nonlinear medium. Furthermore, the current study aims to use the data obtained from the above analyses to develop a practical assessment method for RC beams subjected to impact. The latter model is aimed at bypassing the complexities associated with experimental and numerical analyses. Furthermore, it accounts for the localised response exhibited by the RC beams when subjected to high rates of impact loading.

The main objectives of the current work are:

1) To investigate experimentally the response of RC beams, by carrying out a series of drop-weight test. During impact testing, the transverse external load is applied through a steel mass (impactor) which is allowed to fall freely from a specified height (depending on the desired rate of loading) onto the mid-span of the RC beam. The RC beams considered are characterised by different design parameters such as the amount of longitudinal and transverse reinforcement, shear span-to-depth ratio and concrete strength. The setup employed for the drop-weight test made use of available infrastructure at the structure's laboratory at Heriot-Watt University. Attention focused on recording the deformation profile and cracking process (through conventional instrumentations as well as a high-speed camera) of the specimens up to failure. The latter information is essential for accurately determine the internal state of stress developing within the specimens throughout the loading process which is not usually available in the literature. The cracking process and deformation profile are often recorded after (and not throughout) the application of the impact load. As a result, it usually refers to a specimen physical state characterised by high concrete disintegration and low residual strength and stiffness that relies on the post-failure mechanism rather than the concrete itself.

2) To develop numerical (finite element) models capable of realistically representing the RC specimens considered during testing and providing accurate predictions concerning the exhibited response established. The combined use of the numerical predictions will complement the experimental data recorded during drop-weight testing thus providing insight into the mechanics underlying the behaviour of RC beams under impact loading. The available NLFEA packages used in academia and industry, rely on a number of assumptions concerning concrete material behaviour. These include the use of simple uniaxial material laws, the description of post-failure

behaviour as well as empirical amplification factors attributed to strain-rate sensitivity of concrete behaviour. However, such assumptions do not allow the models at hand to accurately account for the brittle nature of concrete and its sensitivity to triaxial stress conditions. This raises questions concerning the validity of the predicted behaviour and the effectiveness of the obtained design solutions. The NLFEDA used in this research (i.e. ADINA) adopts a brittle model to describe the nonlinear behaviour of concrete. This model accounts for triaxiality and brittle nature of concrete.

3) To use the validated numerical models to conduct parametric studies aiming to identify the true ultimate limit state of the RC beams associated with a range of rates and intensities of applied impact loading. The term 'true' ultimate limit state refers to a critical physical state at which the specimen considered has sustained the maximum level of damage that will allow load transfer to be facilitated by mechanisms associated with RC structural behaviour. Beyond this point, the measurements obtained are associated with a specimen physical state characterised by high concrete disintegration and low residual strength and stiffness that relies on the post-failure mechanism rather than the concrete itself. The behaviour of a specimen that is loaded up to the ultimate limit state when unloaded and then reloaded is characterised by stiffness and load-carrying capacity comparable to that of the undamaged specimen. The behaviour of a specimen that is loaded beyond the ultimate limit state when unloaded and then reloaded is characterised by significantly less stiffness and load carting capacity compared to that of the undamaged specimen. The effect of design parameters associated with concrete strength, reinforcement configurations, axial loading and the shear span to depth ratio on certain characteristics of RC structural response such as the cracking process, deformation profile and the load-carrying capacity exhibited by beams under impact loading are investigated. The latter parameters have not been extensively and systematically investigated to date numerically or experimentally.

4) Further develop a simplified (equivalent static) assessment method based on the Compressive Force Path (CFP) method (Kotsovos 2014) which is capable of realistically accounting for the effect of the localised response exhibited by the RC beams on the mechanics underlying the RC structural performance under impact and realistically predict the load-carrying capacity.

1.3 CONTENTS OF THE THESIS

The following thesis consists of seven chapters and two Appendices. Chapter 2 provides an extensive literature review on the available published experimental and numerical studies carried out in order to investigate the behaviour of RC beams under impact loads. Initially, a brief discussion of the key aspects of impact problem is provided. Then the behaviour of concrete at both material (i.e. plain concrete) and structural levels (i.e. RC members) under impact loading is reviewed and discussed. The experimental techniques adopted as well as the measurements obtained concerning certain characteristics of RC structural response are critically reviewed and analysed. The test data available in the literature are then used to study the RC structural response under impact loading in relation to the different assumptions (such as strain-rate sensitivity) adopted by researchers when studying the behaviour of reinforced concrete (RC) members under impact loading. The effect of a range of parameters (such as loading rate and intensity of the impact load imposed, the reinforcement arrangement, the impact velocity, the axial loading and the shear-span-to-depth ratio) on the response of RC beams under impact loading is investigated. Finally, the key points and findings are summarised and gaps within the literature are identified.

Chapters 3 and 4 are dedicated to the experimental programmes of associated with the RC beams slender ($a_v/d>5$) and short ($a_v/d<5$) beams respectively to investigate the effect of shear span-to-depth ratio on the exhibited response when subjected to consecutive impact loads. A detailed description of the test setup and the instrumentation used is provided. Recorded data describing the impact and reaction force-time history, the variation of strain, strain rate and displacement at specific points along the element span with time, the deformation profile and the corresponding crack pattern at different stages of the loading process are presented. Apart from conventional instrumentation (consisting of strain gauges, load-cells LVDTs, etc) photographic evidence recorded using a high-speed camera is also presented, analysed and discussed. The use of this camera is aimed at confirming the measurements obtained from the instrumentation described above and compensating for the occasional loss of data. The photographic evidence was successful in providing a more detailed description of the specimen behaviour in the impact region

by tracking the movement of a number of points marked in the form of a grid on the side surface of the specimen, the pad and the impactor.

The work described in Chapter 5 is concerned with the numerical investigation of RC beams under impact loading through the use of 3D NLFEA. General aspects of the FE model presently adopted such as the nonlinear solution procedure, the material model adopted for describing concrete material behaviour, the modelling of the structural configurations considered, the modelling of cracking and the failure criteria used are discussed. The predictions obtained for the behaviour of the RC structural configurations considered under static and impact loading are presented in the form of load-displacement curves, curves describing the variation of the dynamic increase factor (DIF) with increasing values of loading rate, crack patterns and deformation profiles associated with different stages of the loading process and failure modes. The effects of parameters such as axial loading, shear span-to-depth ratio, on the response of the RC beams considered are discussed.

Chapter 6 provides a description of a simplified equivalent static method for assessing the response of RC beams under high rate loading. The validation of the proposed method is achieved by comparing its predictions to its counterparts established experimentally, via drop-weight testing, and numerically, through the use of nonlinear finite element analysis (NLFEA) for the case of slender and short RC beams. The assessment method is then used to assess the effect of axial loading on the behaviour of RC beams under impact loading. The predictions provided are presented and discussed.

The final conclusions drawn from the work described in the previous chapters are presented and discussed in Chapter 7. These are accompanied by recommendations for future work.

CHAPTER 2 - LITERATURE REVIEW

2.1 INTRODUCTION

The present chapter sets out to review the information available in the literature concerning the behaviour of RC members when subjected to impact loads. Initially, a description of the impact problem is provided followed by a concise discussion on the material behaviour of concrete under increasing loading rates as well as the response exhibited by RC structural elements (i.e. RC beams) when subjected to impact loading. Furthermore, a review of the available methods employed in research and in practice for assessing RC structural response under impact loading is provided with attention being focussed on the benefits and limitations characterising these methods. Finally, the existing gaps in the literature (state of the art) are identified and discussed.

2.2 GENERAL ASPECTS OF IMPACT

The term '*impact*' is presently used to define the process associated with the collision of an object (impactor) onto a structural element. During this process, the forces generated are characterised by short durations as well as high intensities and loading rates. The application of an impact force onto a structural element results in the generation of stress waves that propagate, away from the impact region, towards the supports/boundaries of the specimen considered. In the case of RC members, the generated stress waves result in the development of a complex stress field within the concrete medium which is further extenuated by the cracking process that characterises concrete behaviour (Goldsmith, 1960).

The classic theory of impact (Goldsmith,1960; Norman Jones, 1990) describes the impact process by employing impulse-momentum law for rigid bodies. The subject problem is governed by Newton's laws of motion which describes the relationship between the momentums of a body when subjected to an impulse load (i.e. F_t) for a certain duration of time t; hence,

$$M\,(v_2 - v_1) = \int_{t1}^{t2} F\,dt \qquad \text{Eq. (2.1)}$$

where M is the constant mass of a body (impactor) moving towards the target (structural member); v_1 and v_2 are the values of the velocity of the impactor before and after impact: F is the constant force applied over a certain period of time t, However, this approach considered only the initial and final velocities of the impactor. It cannot consider however the transient stresses, forces, overall and localised deformations exhibited at the point of impact (Goldsmith 1960). Despite these limitations, the latter theory has been found valid for describing the impact of two spheres or the collision of a sphere against a rigid body with reasonably high mass. However, this theory cannot be used for impact problems of beams or thin plates (Rayleigh, 1906).

Early studies of the impact problem were associated with a missile striking a target and the use of a penetrating model (Corbett, Reid et al. 1996) to predict the trajectory of the missile within the mass of the target. The exhibited response of the target after the coming into contact with the impactor can be categorised as:

(i) localised: when most of the impact energy is dissipated in the impact region resulting in localised damage being exhibited

(ii) global: when the whole structural form considered responds to the application of the impact force and

(iii) combined/mixed: when both types of response described earlier are exhibited.

Li, et al. (2005) provided a more extensive survey on the response exhibited by concrete structural forms when subjected to impacts with seven phases as follow;

i. Penetration: A tunnel is created into the target by the projectile/striker
ii. Cone cracking and plugging: A cone-like crack is formed under the projectile that possible leads to the formation of a subsequent punching-shear plug
iii. Spalling: The target material is ejected from the proximal face of the target
iv. Radical cracking: Global cracks are generated at the impact point on either the proximal or distal face of the target or both and penetrate deeply into the target thickness

v. *Scabbing: Fragments of the target material are ejected from the distal face of the target*

vi. *Perforation: The complete passage of the projectile through the target with or without residual velocity occurs*

vii. *Overall structural response and failure: Global bending, shear and membrane responses as well as their induced failures throughout the target*

The above types of behaviour demonstrate that an impact problem associated with the collision of an impactor onto an RC structural form cannot be effectively described as a single step process. Moreover, when studying the response of a simply supported RC beam under impact loading, the exhibited response can be described as a two-step process.

- *Localised response* characterises the behaviour of the beam during and immediately after collision (impact) as the generated stress waves have started propagating away from the impact region causing only a portion of the span on the beam to respond. During this stage, high-stress concentrations develop around the impact region causing the development of localised damage in this region

- *Global response* characterises the exhibited behaviour *after* the stress waves have reached (and are deflected by) the boundaries/supports of the beams. During this stage of the exhibited behaviour, the full span of the beam begins to deform. The duration of this stage depends on how quickly the impact energy is dissipated (e.g. to the damage being sustained along the span of the beam).

2.3 SINGLE DEGREE OF FREEDOM (SDOF) METHOD

Single-degree-of-freedom (SDOF) method is an approach for assessing the behaviour of RC structural elements under impact loading which rely on the available physical models (e.g. strut & tie models) generally adopted for describing the mechanisms underlying RC structural response when approaching the ultimate limit state (ULS). The latter method is adopted by the military design codes (e.g. TM5-855-1,1998). A structural element (e.g. an RC beam or slab) is modelled as an equivalent single lumped-mass spring system, in which the parameters of the governing equation of motion corresponding to the distributed mass are replaced by equivalent values of the simple lumped-mass spring system. Such equivalence is based upon energy approximations that rely on an assumed deflected shape of the RC beam. The latter usually corresponds to the first eigenvector of the structural

response. The latter response is considered to be governed by either elastic or elasto-plastic laws. The above simplified method bypasses the complexities associated with the available experimental and numerical assessment methods but fails to accurately account for the nature of the problem at hand (a wave propagation problem within a highly nonlinear material) and the true mechanisms underlying RC structural response.

The SDOF system, on the other hand, does not consider localised response exhibited by concrete structures under impact loading instead it assumes a global response. Furthermore, the elasto-plastic laws are not able to describe the brittle failure/shear mode of failure as well as the cracking process. It assumes a type of behaviour that is not always compatible with concrete structural behaviour.

A SDOF system (Fig. 2.1) consists of a mass, a damper and a spring (or resistance element). The mass and spring are selected so that the frequency of the SDOF system will equal the natural frequency of the structure.

$$F(t) - R_R - (M_s\, a) = 0 \qquad (1.1)$$

Where $F(t)$ = forcing function (function of time t)

R_R = resistance function

M_s = mass

a = acceleration

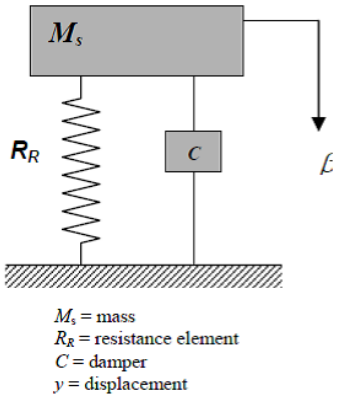

Figure 2-1 Single Degree of Freedom System (SDOFs) (Adhikary et al. 2012).

2.4 CONCRETE MATERIAL BEHAVIOUR

To accurately predict the response of an RC structural element under impact loading, it is important to first understand the material behaviour of concrete and under static and dynamic loading. In the present section, a review of the available experimental and numerical data is provided that describes the behaviour of concrete under static and impact loading.

2.4.1 Static Loading

It is well known that concrete is characterised by a low tensile strength (i.e. 10% of its compressive strength, f_c) and that its behaviour is essentially brittle, resulting in an abrupt loss of load-carrying capacity once peak-load is attained. The application of an external load onto a concrete specimen results in the development of a complex internal stress field within the concrete medium. The complexity of this field is further. extenuated by the development of high concentrations of tensile stresses at the tips of the micro-cracks (Kotsovos and Newman 1981,). Once the local tensile strength of concrete (at the tip of the micro-cracks) is surpassed, the micro-cracks extend in the direction of the maximum principal compressive stress temporarily providing relief to concrete since it reduces the tensile stress concentrations acting at the tips of the micro-cracks. This process repeats itself as the external load increases and at some stage, the micro-cracks interconnect and larger (macro-) cracks begin to form. While the micro-cracking is associated with the nonlinear behaviour of concrete, the larger (macro-) cracks represent localised failure of the material (Kotsovos and Newman 1981). The extension of the latter cracks ultimately leads to the failure of the specimen.

Obtaining an accurate description of concrete material behaviour is not straightforward; due to the two following reasons: (1) the necessity of obtaining triaxial test data and (2) the scatter which characterises the available test data (Kotsovos & Pavlović 1995). The triaxial test data describes the behaviour of concrete under a three-dimensional (3-D) state of stress (Kotsovos and Pavlović, 1995). It should be noted that the concrete strength is often governed by the so-called *'negligible stress'* which acts perpendicular to the direction at which the primary (principle) stresses are applied. Therefore, the effect of secondary components of stress on concrete material behaviour should not be ignored. In view of the above, the triaxial test data form the basis of achieving a realistic concrete material model, regardless of the difficulty in conducting these tests.

The scatter that characterises the available test data describing concrete material behaviour, is affected by a range of parameters associated with: the concrete mix, the shape/size of the specimen and the test methods adopted, the variation of which is a function of the boundary conditions imposed onto the specimen during testing. The boundary restraints are

characterised by i) degree of normal constraint in the direction of applied load and ii) degree of lateral constraint present at the interface between steel platen and specimen which in turn will result in a different observed specimen behaviour For example, the use of rigid steel platen, induce high frictional stresses at the loading device- specimen interface which is due to the incompatibility of the lateral deformation of specimen and the loading device. The latter stresses provide confining pressure through constraining the specimen boundary against lateral displacement, as a result, shear stresses are developed on the interface. The degree of confining pressure provided may have a key effect on specimen behaviour which will be discussed in the following sections, see Fig. 2.2. It should be noted that the rigid steel platen is an extreme example of induced frictional stresses associated with the type of boundary condition; on other hands, such frictional stresses can be significantly reduced through the use of fluid cushions the specimen. The latter allows the specimen to laterally deform more freely (Kotsovos 1983, Van. Mier 1984, Zissopoulos et. al. 2000, Van. Mier et al. 1997). The elimination of the frictional stressed results in the brittle behaviour of concrete following an abrupt loss in load-carrying capacity immediately after the peak load is attained. The effects of the testing techniques on observed specimen behaviour of concrete are described in the following section.

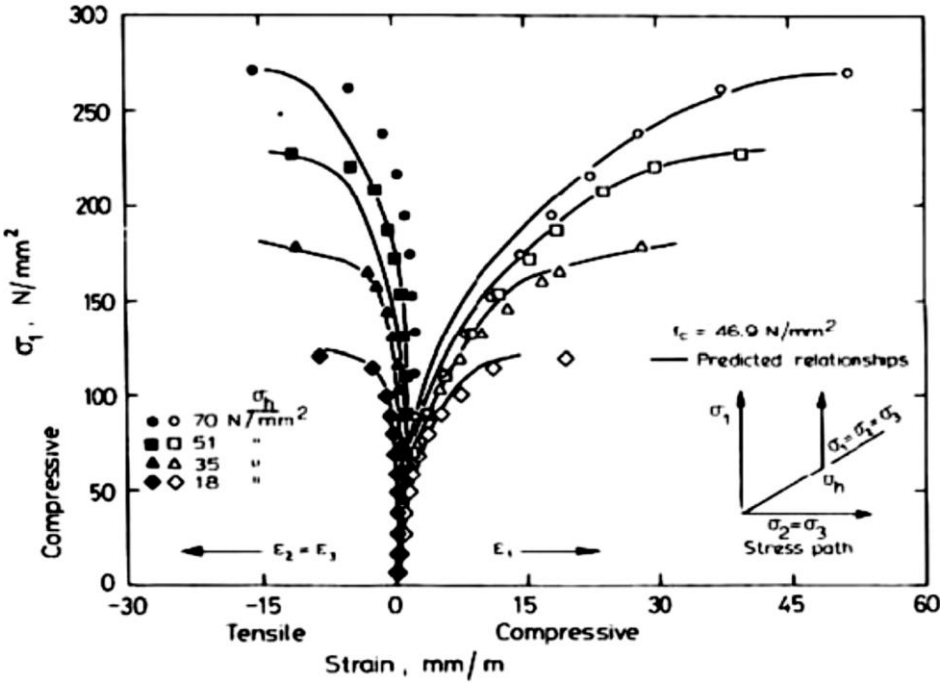

Figure 2-2 Variation of the peak axial compressive stress sustained by the cylinders with increasing confining pressure under triaxial test (Kotsovos and Pavlović 1995).

When conducting uniaxial compression tests, the shear stresses generated at the interface between the loading device and the specimen, (cube or cylinder) result in a confining pressure (Kotsovos and Pavlović 1995, Zissopoulos et al. 2000) being applied to the top and bottom of this specimen. This confining pressure can affect both the peak load attained during testing as well as the behaviour of the specimens after peak-load is attained.

A typical stress-strain curve, describing the behaviour of concrete, is shown in Fig. 2.3. It consists of an ascending (i.e. strain-hardening) and descending (i.e. strain-softening) branch. The behaviour of concrete is elastic up to 30% its compressive strength (f_c), beyond this point concrete exhibit a nonlinear behaviour; where in the vicinity of the peak-ultimate strength damage begins and the descending branch falls down rapidly until the total failure is reached. Fig. 2.3 describes the deformation behaviour of the concrete specimen parallel and normal to the direction of loading, it can be seen that the effects of boundary conditions and hence confinement pressure in the strength of concrete in compression is observed in the descending branch (i.e. post-failure) (Kotsovos and Pavlović 1995, Kotsovos 1983). Such behaviour implies that the presence of small secondary *confining* stresses can have a significant effect on the load-carrying capacity of the specimen and indicates some level of ductility beyond the ultimate (peak) strength. Fig. 2.3 reveals that beyond the ultimate strength of concrete (i.e. post-failure), the transverse (tensile) strain increases at a rate significantly higher than axial (compressive) strain (Barnard, 1964). Such behaviour is described by the ratio of transverse strain to the axial strain, which may vary from 1 to 10 for stress levels beyond peak strength. Similar to any isotropic continuum (which concrete is assumed to be), the value of Poisson's ratio cannot exceed 0.5, beyond which the concrete is no longer a continuum and the concrete will become affected by the internal fracture processes.

Despite the fact that concrete is no longer a continuum when the value of Poisson's ratio exceeds 0.5 (at the vicinity of the ultimate-load), it is still possible to obtain the descending branch, describing the post-failure of concrete. This suggests that frictional stresses come into effect at the late stages of the deformational response and these exist at the interface (of loading-device and specimen) and provide ductility beyond the peak strength which is expressed as descending branch. The above discussion reveals that the descending branch does not describe material behaviour but the interaction between specimen and testing

device due to the development of frictional forces between the specimen and the steel platens used to apply the external load. When effectively eliminating the frictional forces the behaviour of concrete becomes essentially brittle.

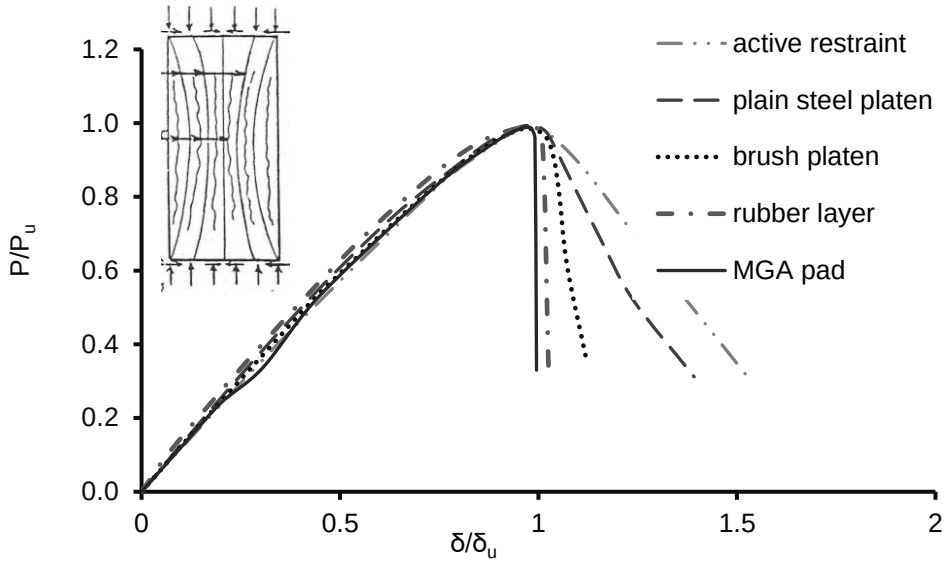

Figure 2-3 Load displacement relationships established from cylinder tests fc= 50 Mpa (Kotsovos, 1983)

Another important aspect of concrete behaviour in compression is that it exhibits an abrupt increase in the rate of lateral expansion as the load approaches the peak level. The latter level corresponds to the minimum volume level marking the beginning of a drastic volume dilation which, as discussed earlier in the absence of any frictional restraint is considered to lead rapidly to failure even under constant loading. Similar trends of behaviour are also observed under triaxial compression states of stress. In the view of the above discussion, the behaviour of concrete under static loading should be considered prior to the impact loading since the interpretation of obtained static test data, affects the studies concerning the behaviour of concrete subjected to impact loading.

2.4.2 Effect of Loading Rate

Although it has been established, both experimentally (Reinhardt et al. 1990,Bischoff and Perry 1995, Ross et al. 1995, Ross et al.1996, , Grote and Park 2001, Brara and Klepaczko 2006, Shaha 2011), and numerically (Cotsovos and Pavlović 2008[a,b,c],Xu, et al.

2012,Ožbolt et al. 2014,), that the behaviour of concrete specimens under high-rate (compressive and tensile) loading differs significantly from that observed during equivalent static loading once certain thresholds of applied loading-rates are surpassed , there has been considerable debate concerning the reasons that trigger this change. The majority of researchers agree that inertia has a significant effect, however (Zielinski 1984, Cotsovos and Pavlović 2008[a,b,c], Takeda et al. 1982[a,b]); disagreement exists regarding the influence of strain-rate sensitivity on the material properties of structural concrete. Many researchers consider that the material properties of concrete are strain-rate dependent (Bischoff and Perry 1991, Ross and Tedesco 1995, Kulkarni and Shah 1998, Saatci and Vecchio 2009, Ožbolt et al. 2014), a view which until recently was widely accepted and incorporated into the framework of existing military codes (i.e. TM5-855-1 19978) for the design and analysis of RC structures under blast and impact. However, an increasing number of researchers (Takeda et al. 1982 [a,b] ,Zielinski 1984, Cotsovos and Pavlović 2008[a,b,c],) have expressed the opposite view, suggesting that concrete material properties are essentially strain-rate independent and that the observed change in specimen behaviour with increasing loading rates is linked to the structural response.

The observed shift in specimen behaviour with increasing loading rates primarily takes the form of an increase in maximum sustained load and stiffness. This change becomes more apparent with increasing loading rates. A summary of available experimental data is presented in Fig. 2.4 (Bischoff and Perry 1991,Ross et al. 1995, Ross et al. 1996, Bischoff and Perry 1995,Gary and Bailly 1998, Grote et al. 2001, Wu et al. 2005, Schuler et al. 2006, Brara and Klepaczko 2006) printed in (Cotsovos and Pavlović 2008[a,c]), expressing the relationship between the dynamic increase factor-DIF (i.e. ratio of dynamic maximum sustained load P_d to the static load carrying capacity P_s) and the rate of axial deformation (strain-rate) $\dot{\varepsilon}$ exhibited by the specimen in compression or tension.Based on the available test data and the use of regression-analysis a number of curves have been proposed to date describing the increase of specimen strength under uniaxial compression and tension with an increasing rate of loading.

While the behaviour of the concrete specimens under high-rate loading differs considerably from those obtained during equivalent static testing, when inspecting the available experimental data it is clear that it characterised by significant scatter which is linked to a

wide range of parameters which vary from test to test (i.e. experimental techniques adopted, the shape, size and moisture content of the specimens, the different types of concrete used, etc.) (Kotsovos and Pavlović 1995). As a result, the available test data cannot provide a quantitative description of the effect of loading rate on the specimen behaviour.

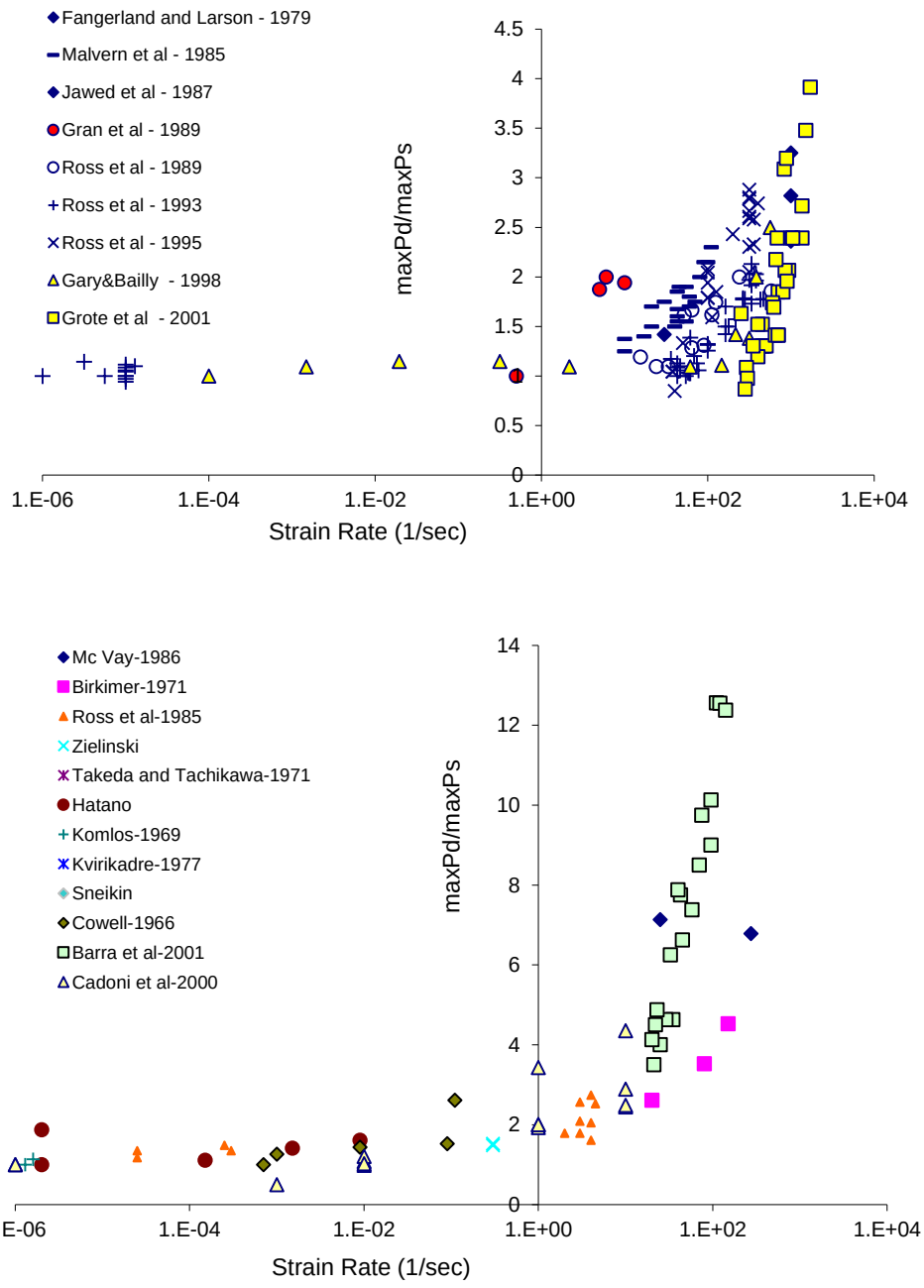

Figure 2-4 Variation of load-carrying capacity with strain rate for concrete in (Top) uniaxial compression ($maxP_d$=load carrying capacity, $maxP_s$=load-carrying capacity under static loading) presented by Cotsovos and Pavlović 2008a and (Bottom) uniaxial Tension presented by Cotsovos and Pavlović 2008[c]

In an attempt to achieve a clear understanding and quantitative description of the structural concrete behaviour under high loading rates and to quantitatively investigate the effect of the certain parameters on the dynamic response of plain concrete specimen NLFEA was employed (Cotsovos and Pavlović 2008 [a,b,c]). Through a comparison of the numerical predictions with the available experimental data (Bischoff and Perry 1991, Ross et al. 1995, Ross et al. 1996, Bischoff and Perry 1995, Gary and Bailly 1998, Grote et al. 2001, Schuler et al. 2006, Wu et al. 2005, Brara and Klepaczko 2006) it was suggested that concrete specimens must be viewed as structures rather than as material units from which average material properties can be established because their behaviour is directly linked to the inertia effect of their mass as well as to their geometry properties and their boundary conditions. More specifically, the problem at hand must be view a wave propagation problem within a highly nonlinear brittle material as the application of the external loads leads to the generation of stress waves which propagate through the concrete medium, away from the load point. The speed of propagation of these waves depends on the material properties of concrete and the level of localised damage (cracking) sustained by the concrete medium, while their intensity level depends on the rate of loading and the magnitude of the applied load.

In the case of low loading rates, the stress waves that develop, travel along the entire length of the specimens and are the deflected at its boundaries resulting in the development of a complex stress field inside the specimen in which it is extremely difficult to predict the locations at which high concentrations of stress and strain will develop. Under high rates of loading the numerical results reveal that the specimen exhibits a localised response as failure occurs prior to the stress waves being able to travel the full length of the specimen. As a result, only, the region of the concrete specimen close to the point of loading deforms whereas the rest remains practically unaffected by the application of the external load see Fig. 2.5. This region is placed under a rigid element used to apply the external load and its height becomes smaller as the rate of loading increases resulting in a similar interaction to that discussed for the case of static loading.

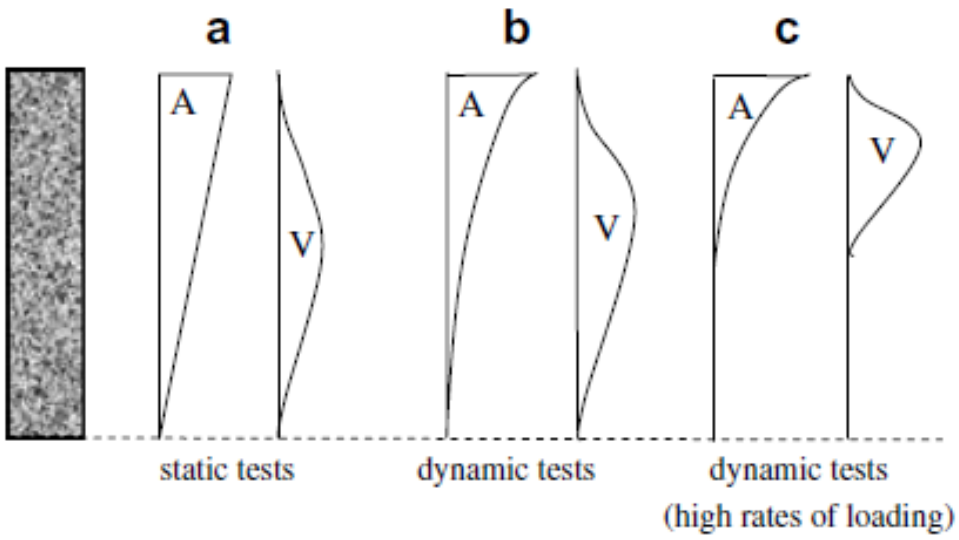

Figure 2-5 Qualitative representation of axial displacement (A) and vertical displacement (V) exhibited prior to failure along the longitudinal axis of the specimen (Cotsovos. & Pavlović, 2008[a,b]).

Furthermore, under high rates of uniaxial compression high rates of axial and lateral deformation are also exhibited which trigger the development of significant inertia forces in these directions. These forces have a confining effect on the concrete prism and tend to restrict the deformations both axially and laterally, thus essentially confining the concrete specimen (inertial confinement) and slowing down the cracking process it undergoes compared to that established under static testing. This confinement effect allows the concrete prisms to exhibit higher load-carrying capacities and maximum values of strain compared to those established under static loading; (Cotsovos. & Pavlović, 2008[a,b]).

Based on the above it becomes evident that plain concrete specimens under dynamic loading cannot be used to describe concrete behaviour (as usually assumed) since, in contrast with static loading, they do not constitute a material unit from which average material properties may be obtained. Therefore, the use of experimental data from dynamic tests in order to develop constitutive models of concrete behaviour under dynamic loading is questionable. When realistically accounting for the brittle nature and triaxiality which is known to characterise concrete material behaviour the experimentally and numerically observed variation in specimen behaviour with increasing loading rates is primarily attributed to parameters associated with structural response (i.e. such as boundary

conditions and loading technique) and not, as widely considered to strain-rate sensitivity of the material properties of concrete.

2.5 RC STRUCTURAL RESPONSE UNDER IMPACT LOADING

Concerning the reasons that trigger the change in the response of RC structural element under impact loading (when compared with their static counterparts), disagreement exists. The latter shift is primarily attributed to strain rate sensitivity and the inertia forces that develop as the element deforms, associated with the change of span element length, referred to as L_{eff}. The latter is the portion of the span that reacts to the applied load. When looking at the impact problem as a wave propagation problem, L_{eff} is the portion within which the impact-induced stress wave travels. Parameters such as amount and arrangement of the reinforcement, the impact velocity, the rate and intensity of impact load generated, the shear and flexural capacity under equivalent static loading, the geometry of the specimen also influence the exhibited response under impact loading. A brief description of the effects of some of the above parameters is presented in this section in the form of a literature review on the established experimental test data on RC beams.

To date a large number of experiments have been conducted to investigate the response of RC beams subjected to impact loadings (Hughes & Spiers 1981, Miyamoto et al 1989, Kulkarmi & Shah 1998, Miyamoto et al 1989, Kishi et al 2001[a,b], 2002, May & Chen (2006), Fujiukake et al 2009, Saacti & Vecchio 2009, Abbas et al 2010, Adhikary et al 2015, Anil et al 2016) and numerically (Miyamoto et al 1989, Thabet & Haldaen 2000, Kishi et al 2001, Abbas et al 2004, Cotsovos et al 2008, Saatci & Vecchio 2009, Kishi et al 2011,Ožbolt and Sharma 2011, Adhikary et al 2012, Cotsovos & Pavlović 2012, Pham and Hao 2017, Guo et al 2017, Zhao et al 2017). The majority of these investigations adopted drop-weight testing where the load was applied through a steel mass (i.e. striker) allowing to fall freely from a predefined height (depending on the desired loading rate) on to the mid-span of the subject specimen. A couple of examples of the available drop-weight tests set up are shown in Figs .2.6 and 2.7.

In order to reduce the localised damage exhibited near the impact region, the impact load is usually applied through the use of pads or platen (e.g. steel, rubber and ply). Different types of impactor and interface between the specimen and impactor have been adopted during these tests; e.g. a spherical (Kish et al. 2001) or hemispherical impact which come into direct contact with the specimen during impact (Fujikake and Soeun 2009, Zhao et al 2017) or a drop hammer with square hollow structural streel which come into contact with a steel plate resting on the top surface of the specimen (Saatci and Vecchio 2009). The duration of the impact is extremely short, usually at the order of few milliseconds and the intensity of the impact load increases rapidly from zero to a maximum value. The mass of the impactor used in the literature, varied from 98.7-600 kg and the impact velocity ranged from 1-9.3 m/s. Using suitable instrumentations, the variation of strain, displacement and acceleration at various points along the specimen length are recorded. Typical results obtained from the experiments include load-deflection curves, deformation profiles, time-history of the impact force, reaction forces and the velocity with which the steel impactor collides with the specimen during impact testing as well as crack formation and propagation up to failure. Information regarding crack patterns and deformation profiles is recorded (using a high-speed camera) after the application of external load and not throughout the impact. The results obtained from drop-weight tests are usually presented in the form of:

- Diagrams describing the variation of the Dynamic Increase Factors (DIFs), expressing the ratio of the maximum sustained load recorded during drop-weight testing ($maxP_d$) and the load-carrying capacity established under equivalent static loading (maxPs) (i.e. DIF = $maxP_d$ / $maxP_s$), with increasing loading rates ($\dot{P}$).

- Load–deflection curves describing the variation of the contact force (P_d) generated in relation to the deflection exhibited at the area of impact (δ).

- Cracking and deformation profiles exhibited along the specimen span at different stages of the loading process.

- Curves describing the variation with time (t) of the impact (P_d) and reaction (R_d) forces, the displacement (δ) at specific points on the impactor and along the span of

the beam as well as the strain (ε) developing at certain critical regions of the specimen.

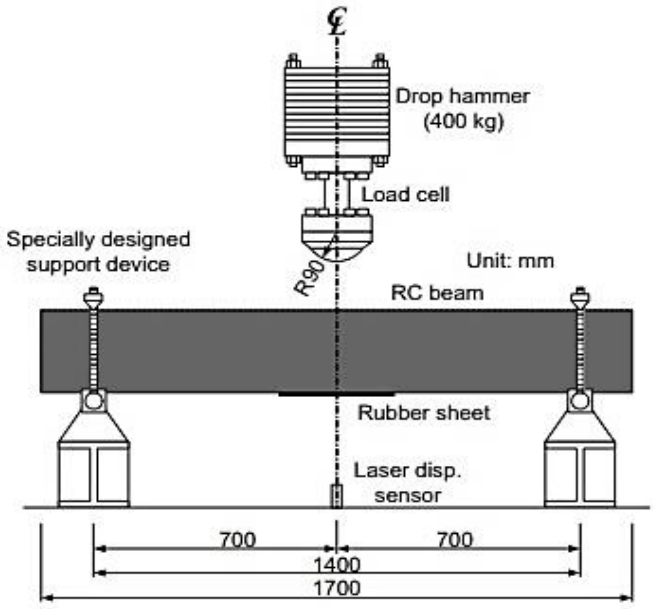

Figure 2-6 Drop hammer impact test setup (Fujikake, Soeun 2009)

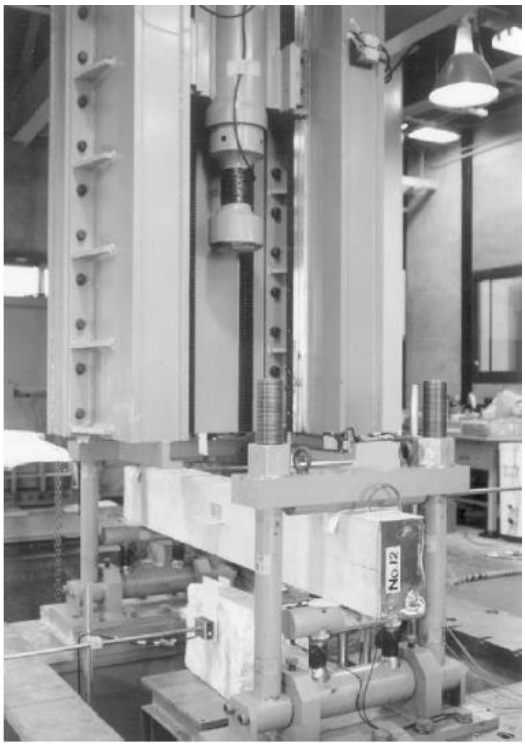

Figure 2-7 Experimental setups (Kish et al. 2001).

2.5.1 Dynamic increase factor and load-deflection curve

The variation of DIF and the load-deflection (P-δ) curves presented in Fig. 2.8a. reveal that increasing values of loading rate ($\dot{P}$) can lead to an increase in the maximum sustained load ($maxP_d$) and to a stiffer structural response. Typical load-deflection curves describing the behaviour of RC beams subjected to a point- load at mid-span for both impact and equivalent static loading are shown in Fig. 2.8b (Miyamoto et al. 1989).The latter curves describe an increase in the load-carrying capacity of the RC beam specimen when subjected to impact loading comparing to the case of static loading The variation of DIF and the load-deflection (P-δ) curves presented in Fig. 2.8a reveals that increasing values of loading rate ($P^{\cdot}$) can lead to an increase in the maximum sustained load ($maxP_d$) and to a stiffer structural response.

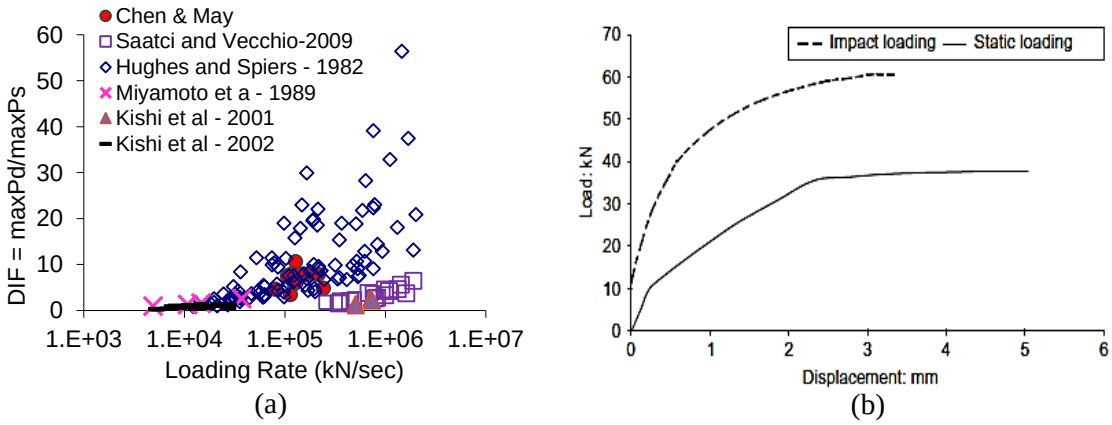

Figure 2-8 (a) Variation of DIF = $maxP_d$ / $maxP_s$ with increasing loading rates and (b) typical load deflection of concrete under static and impact loading (Miyamoto et al 1989)

It is evident from Fig.2.8a the experimental data available in literature suffers from significant scatter. This, in turn, reveals the in the inability of the experimental investigations to correlate the measured response to the actual physical state and strength characteristics of the specimen. For instance, the applied impact force P(t) at time t is usually obtained from the expression m a(t), where m is the mass of the steel impactor and a(t) is the measure deceleration value (of the impactor) *after* contacting the specimen. However, the deceleration continues well after the true load carrying capacity is reached with maxP(t) really corresponding to a physical state of the specimen characterised by disintegration of concrete and low residual load-carrying capacity (Abbas et al 2010, Cotsovos 2010). It is important to note that the residual load-carrying capacity (after

impact) is provided solely by the reinforcement mesh and post-failure mechanism through which the applied force is transferred to the supports. Hence true load-bearing capacity is likely to be significantly smaller than the maximum value of the applied load (i.e. maxP_t) recorded experimentally.

The values of strain rate in the critical early stages of the impact test were found to be considerably lower than the threshold established experimentally (over decades of testing) describing the variation of the concrete compressive and tensile strength under different strain rates. Thus, the increase in load-carrying capacity with the rate of loading observed in literature cannot be attributed to an increase in the material strength due to strain rate sensitivity. It should also be borne in mind that the terms failure and load-carrying capacity require careful qualification as it will first be necessary to establish the post-impact performance criteria (such as the residual strength required and the level of damage that can be tolerated) in order to arrive at meaningful estimates.

When considering the maximum sustained load of an RC beam under impact, it is important to identify up to what value of load intensity the beam behaves as a continuum owing to the level of damage within the concrete medium, beyond which the beam acts as a mechanism in order to transfer the loads to the support and its behaviour relies on post-failure mechanism in order to transfer the applied loads to the supports. Such phenomenon leads to large deformation and eventually total collapse of the element.

2.5.2 Cracking and deformation profile

Under impact loading, the initiation and extension of cracking occur immediately after the collision of the impactor and the specimen (Abbas et al. 2010). Cracking initiates at the lower surface of the mid-span region of the beam and almost immediately after the contact between the striker and the beam, propagate upwards (Hughes and Spiers 1982, Saatci and Vecchio 2009, Chen and May 2009, Abbas et al. 2010, Zhao et al.2017) which shows that the strains become tensile very early in the loading process (Abbas et al. 2010). Below a certain impact velocity, often, only flexural cracks form that penetrates deeply into the upper surface of the specimen (compressive region), (Hughes and Spiers 1982, Kishi et al.2002 and Abbas et al. 2010), (see Fig. 2.9). However, as the loading rate increases, diagonal shear cracks form and regardless of static shear failure modes, shear failure occurs

(Kishi et al 2002, Zhao et al.2017). Further increase of the impact velocity (and loading rate) will lead to the formation of shear-plug near the impact region with an angle approximately 45 degrees (Saatci and Vecchio 2009, Kishi and Mikami 2012, Zhao et al.2017) causing the response of RC beams deviating from their static counterpart (see Fig. 2.10). Diagonal shear cracks are generated in the mid-region of the beams underneath the region where the impact load is applied, these cracks became prominent as the impact velocity increased.

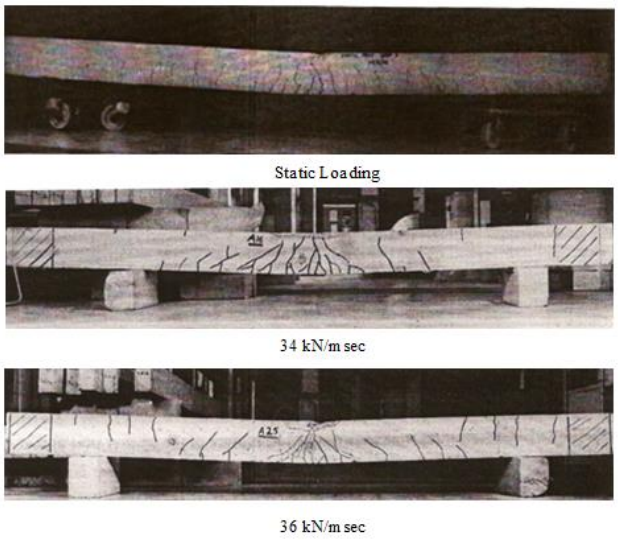

Figure 2-9 Crack pattern at failure of RC beams under various rates of loading established experimentally (Hughes and Spiers 1982).

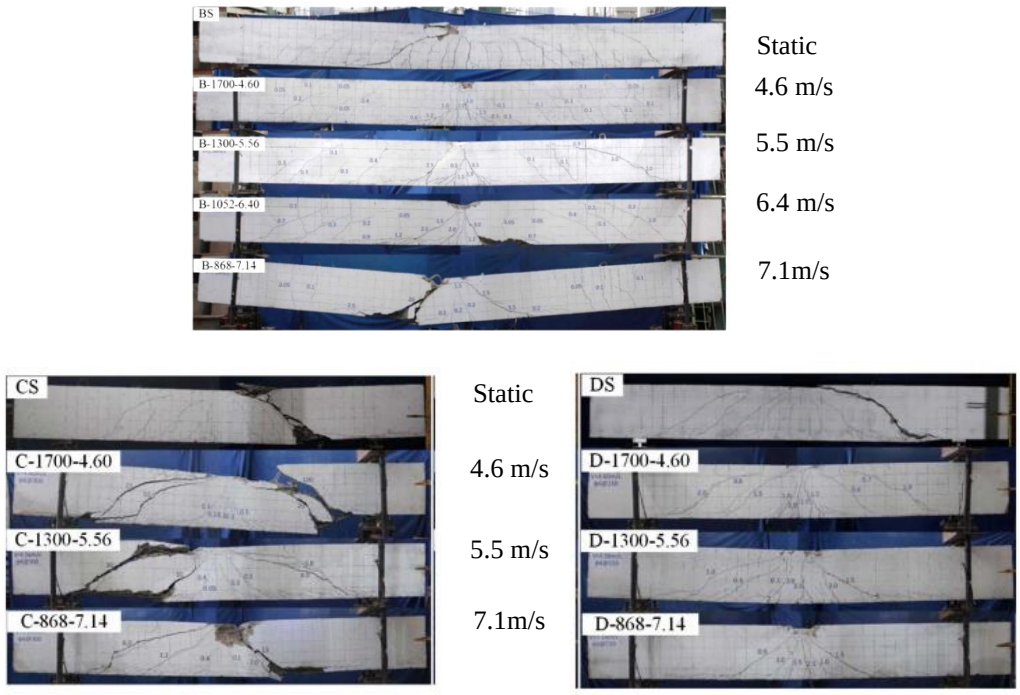

Figure 2-10 Crack pattern at failure of RC beams subjected to impact loading at different velocities (Zhao et al 2017).

As the rate and intensity of the applied load increases, the L_{eff} reduces and tends to concentrate around the impact region of the specimen, where the load is applied (Cotsovos 2010 and Zhao et al. 2017). A closer examination of the deflected shape of the beams reveals the appearance of a 'discontinuity' point marking the start of a sudden increase of the slope of the deflected shape, with the discontinuity moving towards the mid-span for increasing loading rates (Miyamoto et al. 1989). This is compatible with the crack patterns shown in Figs. 2.9 and 2.10, which clearly indicate that, as the rate of loading increases, cracking tends to concentrate around the impact region of the beam. It is also interesting to notice that another set of cracks initiate at the upper face of the beams, around the point of slope discontinuity, extending vertically downwards towards the bottom face.Overall, cracking is primarily concentrated within the area extending between the successive points of discontinuity which coincides with boundaries on either side of L_{eff}.

Based on the above, as the rate of applied loading increases and the discontinuity points gradually move closer to the mid-span (leading to a reduction of L_{eff}), an increasingly localised response is observed that needs to be accurately considered when assessing RC

structural performance under impact loading. In fact, under increasingly loading rates, it seems that the beam tends to deflect as a fixed-end member (rather than simply supported) with points of contraflexure (i.e. zero moments) being formed at the point where the bending moment changes from positive to negative. The above suggests that the fashion based on which the impact-induced stress wave travels through the concrete medium is irrelevant to the actual support conditions of the RC beam.

The above observation is consistent with what has been reported by other reporters (Hughes and Spiers 1982, Chen et al. 2006). The effect of boundary conditions on impact was studied by Hughes and Spiers 1982 carried out a comprehensive series of experiments with concentrated impact tests on pin-ended and simply supported beam specimens. They concluded that for the very short duration of the impact the response of RC beams is independent of the end conditions since the beam does not 'know' its end conditions until the wave travels the full distance from the impact region to the supports. It is noteworthy that the response of the RC specimens was similar regardless of their end support types (pin-ended or simply-supported). Furthermore, the experimental work of Chen and May 2006 revealed that the supports conditions had less influence on the impact force than the span length.

With increasing loading rates, RC beam specimens exhibit a more localised response, since the portion of the member reacting to the external load reduces in length as cracking (and often failure) occurs prior to the generated waves reaching the supports. The above phenomenon, which is evident from the developing crack patterns (see 2.4.2), combined with the inertia forces generated along the element span appears to underlie the mechanisms governing RC structural response (and failure modes) under impact loading (Cotsovos et al. 2008, Cotsovos 2010).

2.5.3 Failure modes

Previous studies (Cotsovos 2010 and Zhao et al. 2017) suggest that under high-velocity impact the failure mode, as well as the overall behaviour of the RC beams, are influenced by the effective length rather than the full span of the beams. Others (Kishi et al. 2002)

suggest that the failure modes under dynamic loading could be linked to the static shear/bending capacity ratio (i.e. ratio of static shear capacity to bending capacity)- if this ratio is less than 1, RC beams clearly collapse in shear while the failure modes are uncertain if this ratio is greater than 1. The amplification of peak reaction force due to high-velocity impact compared to the static shear load case was found to cause a shear mode of failure. Such an assertion clearly requires further data for verifications.

The observed shift is more profound in the case of slender RC beams characterised by a shear-span to depth ratio greater than five (i.e. $a_v/d > 5$). Under static loading such elements (even when containing the minimum amount of shear links) tend to exhibit ductile behaviour, with flexural cracking gradually extending along the whole element span and penetrating deep into the compressive zone with increasing levels of applied loading, ultimately resulting in a flexure form of failure (Kotsovos, 2014, Zhao et al., 2017). However, when subjected to impact loading slender RC beams tend to exhibit more localised response and cracking (Mutsuyoshi and Machida 1984), ultimately leading to more brittle (and often explosive) modes of failure (Cotsovos & Pavlović 2012). The experimental work of Saatci & Vecchio, 2009 suggested that failure modes were determined mainly by the static behaviour of subject specimens. The majority of the specimens exhibited flexural failure at mid-span while a few failed in shear at approximately third points. The shear failure at the latter points was attributed to the excitation of the third mode. The brittle transition in the mode of failure under high loading rates runs counter to the (Kulkarni and Shah, 1998) flexural failure beams at high rates. (Kulkarni and Shah, 1998) suggest that this contraposition result in the experiments could be interpreted due to the rate sensitivity of the different rates of steel used in their study. Nevertheless, as discussed in regardless of their failure modes and geometrical properties of RC specimens, when subjected to high-velocity obvious diagonal shear cracks develop near the impact point eventually forming a shear plug (see 2.4.2).

2.5.4 Inertia Effects

The dynamic equilibrium of the equation of motion requires the excitation of inertia forces that develop along the element span, acting in the opposite direction of impact load. These forces which are equal in magnitude to the mass of the target (in this case RC beam) times the

acceleration integrated over the volume of the target. The inertia forces tend to resist the movement of the beam in the direction of the transverse load (Cotsovos and Pavlović 2012) particularly during the initial stages of the exhibited response (Saatci and Vecchio 2009). The latter observation implies that the mass and geometric properties of a structural element, such as the span length of a beam, are important factors in resisting the impact load. Banthia, 1987 concluded that the inertial load governs the true bending load since the latter is derived from the difference between the effective inertial load (acting at the mid-span of the beam) and the applied impact load. Mutsuyoshi and Machida, 1984, argued that under high loading rates, the significant shift in the response (in the form of deflected shape) of RC beams (comparing to its equivalent static response) is attributed to the inertial forces. These inertial forces are presented by the beams as a result of high dynamic loading within a short period of time.

2.5.5 Impact velocity and loading rates

Impact response characteristics such as the maximum impact load, the impulse, the duration of impact load, the maximum mid-span deflection and the time taken for the stress wave reaching the supports and deflected shape are subject to an increase as the drop-height increases. When the drop-weight height increases (so as the loading rate), the subject specimen can suffer from local failure, characterised by crushed concrete near the impact region as well as formation of inclined cracks propagating from load point towards both sides of beam, forming a shear-plug (Fujikake et al. 2009, Miyamoto et al.1989) (see 2.4.2).Furthermore, under increasing loading rates, the energy absorption and the peak load were found to increase as well (Kulkarni and Shah 1998).

The effects of impact velocity were also studied by Bhatti et al.2009 and Zhao et al 2017. The work of Bhattie et al., 2009 suggested that under low impact velocity (i.e. 3.7 m/s), after unloading, the maximum mid-span displacement of RC beam decreased near to zero while for higher velocities (i.e. 8.4 and 9.3 m/s), residual displacement was exhibited by the beam. In other words, while the reaction forces were decreasing, a residual deflection was excited. The authors attributed such observation to the yielding of transverse reinforcement. From the above, it could be assumed that under high-rate loading, beyond certain rate of loading, the applied load is mainly resisted by the post-failure mechanism. Zhao et al 2017 attributed the formation of a shear-plug to the increase of impact velocity

and loading rate and suggested that increasing impact velocity increases both the moment and shear force on the critical section of the RC beam.

2.5.6 Longitudinal reinforcement

It is believed that the amount of longitudinal reinforcement affects the response of RC beams under impact loading. Fujikake et al. ,2009, conducted a series of drop-weight tests on under-reinforced RC beams while the shear reinforcement remained the same for all the subject specimens. It was noted that increasing the amount of tensile reinforcement can cause local failure in the impact region. In it was also found that increasing the compression reinforcement tends to reduce the localised failure. It was further concluded that the beams with a higher amount of longitudinal reinforcement exhibited flexural failure while the specimens with less amount of longitudinal reinforcement suffered from both flexural and local failure. The amount of longitudinal reinforcement not only affected the mode of failure but also the degree of localised failure. When a higher amount of compression reinforcement was used the localised failure tends to be more moderate and hence the resistance of the beam was increased.

2.5.7 Transverse reinforcement

It has been established experimentally that the number of stirrups used in the design of RC beams influences the magnitude of the impact load generated during impact as well the energy absorbed by the specimen as the transverse reinforcement resists the development and extension of cracking exhibited during the loading process (Hughes. and Spiers 1982, Saatci and Vecchio 2009, Bhatti et al. 2009). The above suggests that RC specimens with higher transverse reinforcement ratio are able to generate larger values of impact load and absorb more energy while the one with lower transverse reinforcement ratio might be damaged under the same or smaller value of impact forces. The available experimental data (Hughes and Spiers 1982, Saatci and Vecchio 2009, Bhatti et al. 2009, Banthia 1987) reveal that specimens with lower shear capacity suffered from large-scale damage under smaller impact loads than the specimens with higher shear capacity. Those beams were able to sustain more impacts and absorb more energy. The amount of shear reinforcement also influences the ductility and consequently the mode of failure (Adhikary et al., 2012). The

effect of transverse reinforcement ratio was also investigated by Adhikary et al., 2012. The work confirmed that the ultimate load-carrying capacity of the subject beams increased with the increment of shear reinforcement ratios. The RC beams with a high amount of transverse reinforcement ratio provided additional confinement to the core concrete and supplementing lateral reinforcement which leads to higher resistance (i.e. higher Dynamic increase factor DIF) to the catastrophic failure mode under loading rate greater than static loading by providing additional confinement to the core concrete and supplementing lateral reinforcement. Furthermore, Zhao et al., 2017 suggested that providing additional stirrups inhibit the development of shear cracks and increasing the amount of the latter can inhibit the development of inclined cracks and therefore prevent the shear failure however its influence of the early-stage response of the beam is insignificant.

Based on the above, shear mechanisms should also be considered for investigating the structural response of RC beams under impact loading. Regardless of whether the specimen exhibited flexural or shear failure during static loading, shear mechanisms should not be ignored.

2.5.8 Strain rate effects

The effects of loading rate on plain concrete were discussed in 2.3.2 and a summary of literature test data was presented expressing the trend established experimentally for concrete over decades of testing cylinders and prism describing the variation of the plain concrete strength (in compression and tension) with respect to different strain rates. It should be reminded that these experimental data reveal that the specimen strength is subject to an increase once certain thresholds of strain rates are surpassed. Furthermore, in section 2.3.2 it was argued that strain-rate effects are unlikely to result in a significant increase of concrete strength.

The formation and extension of crack pattern near the impact region immediately after the collision of the striker and the RC beam (see 2.4.2) show that the strains become tensile very early in the impact loading process. Therefore, it can be concluded that the strains recorded during testing do not correspond to concrete behaving as a continuum, but to a

portion of the beam that also contains significant cracking (Abbas et al. 2010). Hence, in reality, it can be assumed that the strain-rate record essentially expresses the speed at which the cracks develop, thus practically describing the rate of deformation for a certain area of concrete which has already failed. In the view of the above discussion, attributing the load-carrying capacity of RC structural elements under impact loading to strain-rate sensitivity is questionable.

2.5.9 Shear span to depth ratio

The shear span to depth ratio (a_v/d) has a significant effect on the mechanics underlying the behaviour of RC beams under static loading (Kotsovos 2013). This effect is visible when observing the cracking profiles and the mode of failure exhibited by simply supported beam specimens with different values of a_v/d subjected to three or four-point bending tests under increasing levels of applied loading (Kotsovos 2013). The behaviour of slender RC beams (with $a_v/d>5$), even when having a minimum amount of shear links, is ductile ultimately exhibiting a flexural mode failure. Shorter beams (with $a_v/d<5$) are more likely to exhibit a brittle (shear) mode of failure if they do not have a sufficient amount of transverse reinforcement. For the case of impact loading, the available experimental data obtained from drop-weight tests (see Fig. 2.11) clearly indicates that beams with larger values of a_v/d exhibit a higher increase of DIF = $maxP_d/maxP_s$. More specifically, the slenderer the RC beam (with $a_v/d > 5$) the higher the increase of maximum sustained load ($maxP_d$) it exhibits when subjected to increasing loading rates. This can be attributed to the fact that slender RC beams (with $a_v/d >5$) are usually characterised by smaller values of stiffness and larger deformability. This results in the development of higher inertia forces compared to those developing along the shorter beams. Furthermore, due to the larger length, the waves (generated in the impact region) require more time to reach the supports and consequently, under high rates of impact loading, failure may occur prior to the waves reaching the supports thus exhibiting more localised response.

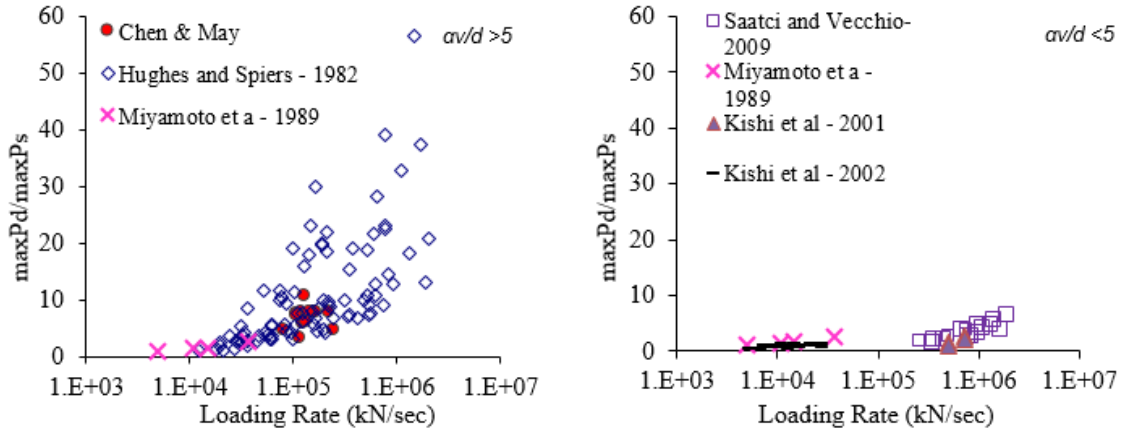

Figure 2-11 Variation of maximum sustained load during impact ($maxP_d$) in relation to the static load-carrying capacity ($maxP_s$) with increasing loading rate) (Hughes and Spiers 1982, Saatci and Vecchio 2009, Miyamoto et al. 1989, Kishi et al 2001,2002).

2.6 EFFECT OF AXIAL LOADING

As discussed in the previous section, a large number of experimental studies have been carried out to date (the results of which are available in the literature) investigating the response of RC beams under impact loading. However a limited studies have been carried out on establishing the behaviour of axially loaded RC members (beams and columns) when subjected to impact loading either experimentally (Huynh et al., 2015, Demartino et al., 2017, Remennikov and Kaewunruen ,2006, Louw et al., 1992[a,b], Feyerabend ,1988) or numerically (Tsang and Lam 2008, Thilakaranthna et al. 2010, Sharma et al. 2012, Madurapperuma and Wijeyewickrema, 2012, Chen et al., 2016). The following section aims at discussing the effect of axial loads on different aspects of the response of RC members when subjected to impact loading.

2.6.1 Impact force and load-deflection curves

A series of impact tests on High Strength Concrete (HSC) and Reactive Power Concrete (RPC) columns have been carried out by Huynh et al,2015. The reinforcement details of the subject specimens are shown in Fig. 2.12. Curves describing the variation of the impact load (generated in the contact area) with the mid-span deflection exhibited by RC columns during testing are shown in Fig. 2.13. The results in Fig. 2.13a refers to a specimen with no

axial force being imposed whereas those presented in Fig. 2.13b refer to an axially loaded specimen. The peak value of the impact force generated was obtained immediately after the collision of the striker onto the mid-span region of the RC column. At this moment the corresponding mid-span deflection was found to be small (see Fig. 2.13 b).

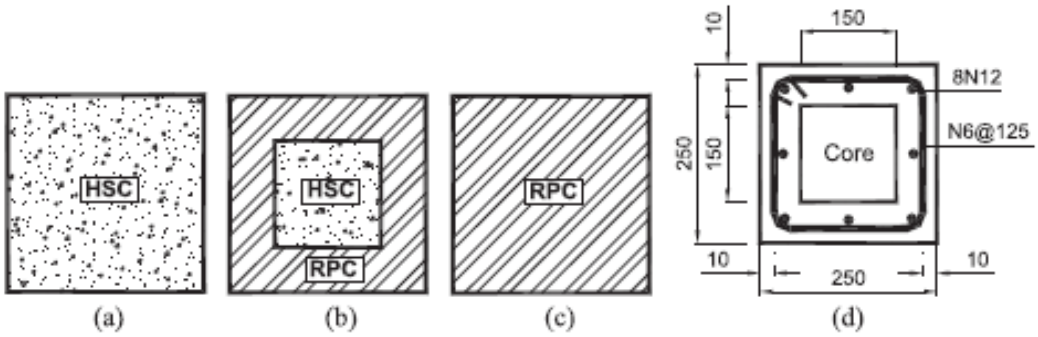

Figure 2-12 Schematic cross-section of the tested columns (a) HSC, (b) composite (HSC core-RPC shell), (c) RPC and (d) geometrical outline and reinforcing details of the specimens.

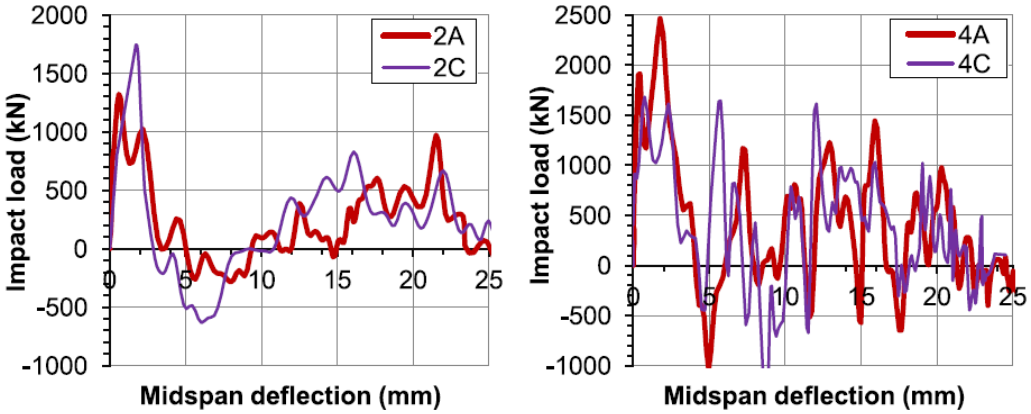

(a) (b)

Figure 2-13 Impact load versus mid-span deflection in the first drop test without (a) and with (b) axial compressive load

It is therefore believed that the axial compressive force applied onto the RC members (i.e. columns) increases the maximum induced impact force generated and the impact resistance (energy absorption ability) of RC members when subjected to low-velocity transverse impacts (Thilakarathna et al. 2010). This occurs due to the fact the axial compressive force applied onto the RC members increases the effective stiffness of these members for a given bending moment while at the same time resisting the formation and extension of cracking along the element span (the resulting in the generation of higher values of impact loading

as shown in Fig. 2.13). It is noted that the magnitude and eccentricity of the axial load have a significant influence on the exhibited failure mode as well as the cracking process the specimen undergoes during testing (Huynh et al. 2015).

2.6.2 Failure mode and crack pattern

It has been established that conventional RC columns are likely to experience shear failure under transverse impact loads (Remennikov and Kaewunruen, 2006). The initial stages of the exhibited response of the RC columns immediately after being subjected to hard impact is critical if the shear strength of the member should prove to be inadequate. Assuming shear failure does not occur during the initial stages of the specimen response the flexural resistance appears to dominate the exhibited response. The combination of the moment and shear developing along the element span shifts from a low moment-high shear value to a higher moment but much lower shear value. The initial high values of shear generated immediately after the impact load is imposed causes cracking that spreads rapidly as the stress waves generated in the impact region propagate towards the support (Eibl 1987) resulting in a reduction of flexural resistance (Louw et al. 1992). The eccentricity of axial compressive force determines whether the response is flexure-dominated (fail in flexural shear mode) or axial force-dominated (fail in brittle-shear mode) (Huynh et al. 2015).

The effect of axial loading on the crack process and the failure mode exhibited by high-strength concrete (HSC) RC column is shown in Figs. 2.14 and 2.15 (Huynh et al. 2015). It is seen that under both static and impact loading the failure mode of the RC column was flexural with the damage sustained being more extensive under impact loading. The consistency observed in the failure mode of the latter RC columns under static and impact loading is in contrary to the shift in the failure mode (from flexural/ductile to shear/brittle) exhibited by the slender RC beam specimens when subjected to increasing loading rates (i.e. from static to impact loading) reported by Mutsuyoshi and Machida ,1984 and Kulkarni and Shah 1998. The above contrast can be explained by considering the effect of axial loading on specimen response. The presence of axial loading (up to certain level) results in an increase of the static load-carrying capacity of RC beam/column members and a delay in the onset of flexural cracking especially in the case of RC beams without transverse reinforcement (ACI 318-14).

A shift in the failure mode of RC columns investigated by Huynh et al. 2015 is observed under impact loading when the compressive axial loading is applied (see Fig. 2.15b and c). The RC column subjected to axial loading exhibited a shear-brittle failure while the specimen without axial loading fails in a flexural-ductile manner with well-distributed fine cracks being formed in the mid-span region. The application and eccentricity of the applied axial force are also found to be a determining factor in the behaviour and performance of the columns under impact (see Fig. 2.15d and e). Nevertheless, the mode of failures indicated in Fig. 2.15 (Huynh et al. 2015) are inevitably associated shear cracks forming near the supports (i.e. point of contra-flexure). The latter is in agreement with the findings of Thilak et al., 2010 which suggested that excessive shear forces are generated at the contra-flexure points located close to the supports. This observation was cited as a potential reason for the failure of the columns.

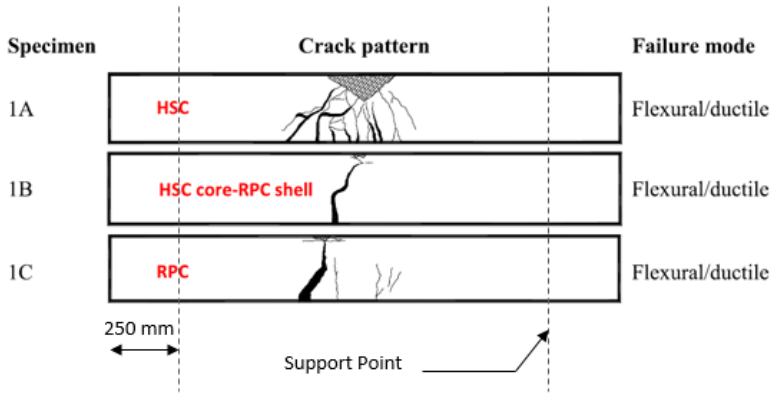

Figure 2-14 Patterns of cracks for the columns subjected to static test (Huynh et al. 2015)

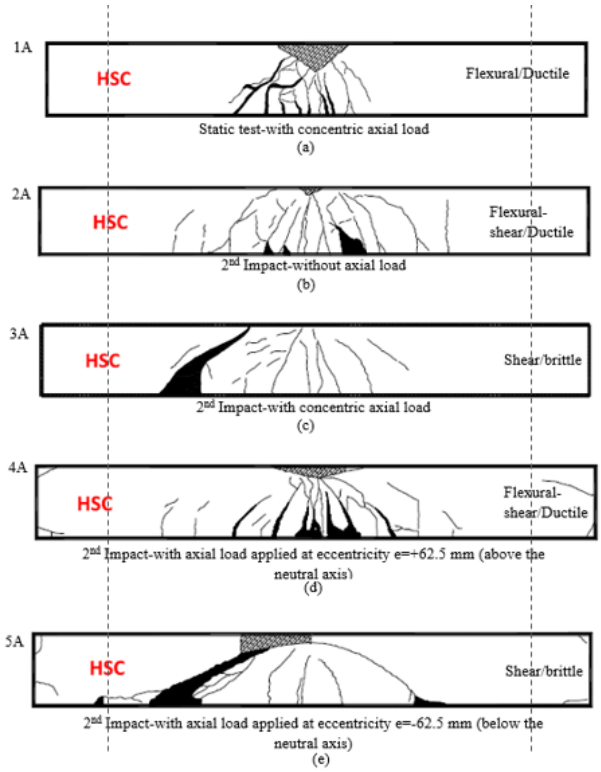

Figure 2-15 Patterns of cracks/damage in the columns after the 2nd impact test; failure mode after 2nd or 3rd impact or damage after 3rd impact (Huynh et al. 2015).

2.6.3 Transverse and longitudinal reinforcement

Reducing the stirrup spacing in RC column was found to result in an increase in ultimate impact strength (Louw et al. 1992). Furthermore, Madurapperuma and Wijeyewickrema, 2012 suggested that the increase in longitudinal reinforcement ratio alone may not effectively improve impact resistance and the subsequent damage sustained particularly for square columns as the amount of transverse reinforcement governs the lateral restraint against the buckling of the longitudinal bars. The effect of an increase in the amount of the longitudinal reinforcement on the impact resistance of columns is also significant particularly in a predominant flexural mode (Louw et al. 1992). The enhancing effect of steel ratio on the impact resistance of columns is in contrast with the numerical findings of Thilakarathna et al., 2010 as they suggested that the vulnerability of columns with axial loading can be reduced by choosing the design option with low amount of steel It was also reported that the contribution of the steel to mitigate the impact-induced damage is less pronounced as (under higher rates of loading) the reinforcement does not have enough time to react to the imposed impact load and hence to develop its full strength against impact by reaching the nonlinear range Thilakarathna et al., 2010.

2.7 LIMITATION OF EXPERIMENTAL DATA

Overall, drop-weight tests are difficult to conduct due to the high intensities and loading rates characterising the impact loads generated (which are considerably higher compared to those applied during equivalent static testing). Furthermore, the application of such loads results in the rapid development and propagation of cracking often leading to explosive (brittle) forms of failure which can in turn damage the instruments employed for measuring various aspects of structural response. Data obtained from such tests (describing usually the variation of maximum sustained load and mid-span deflection with increasing loading rates) is characterised by considerable scatter associated with a wide range of parameters (associated with the experimental setup and the design of specimen) which differ from test to test. This scatter predominantly reflects the difficulty in correlating the measured response to the actual physical state of the specimens considered; in fact, the measured maximum value of imposed load frequently corresponds to a specimen physical state characterised by a high level of concrete disintegration (Cotsovos 2010, Cotsovos & Pavlović 2012). This stage of structural response has minor significance as it usually depends heavily on post-failure mechanisms for transferring the applied loads to the specimen supports. In view of the above, the available test data cannot provide detailed insight into the mechanisms underlying structural response and can only qualitatively describe of the effect of loading-rate on certain aspects of specimen behaviour which are often measured after the impact load is applied (Cotsovos 2010, Cotsovos & Pavlović 2012).

2.8 REVIEW OF NUMERICAL STUDIES ON RC BEAMS

The majority of the numerical studies, (Miyamoto et al., 1989, Thabet & Haldaen, 2000, Kishi et al., 2001, Abbas et al., 2004, Cotsovos et al., 2008, Saatci & Vecchio, 2009, Kishi et al., 2011,Ožbolt and Sharma, 2011, Adhikary et al., 2012, Cotsovos & Pavlović, 2012, Pham and Hao, 2017, Guo et al, 2017, Zhao et al., 2017) on the dynamic response of RC beams under impact loading have been carried out through nonlinear finite-element analysis NLFEA which forms a safer and more efficient method (compared to drop-weight testing). The use of such packages allows the study of more complex structural forms (compared to the simple structural configurations studied experimentally) while providing a more detailed description of the exhibited response (i.e. stress and strain distribution, deformation profiles, failure modes and crack patterns) throughout the loading process.

2.8.1 Material model of reinforced concrete

A large number of material models have been proposed to date to describe the failure stress-strain behaviour of concrete. There are advantages and disadvantages associated with these models which mainly depend on their particular application. Plasticity models are often used to describe concrete material behaviour (Anil et al., 2016, Pham and Hao, 2017) to account for the plastic flow of concrete before crushing which account for the strain-rate effect and assumes damage softening after failure (Pham and Hao, 2017). The concept of strain-rate dependency was adopted by a number of researchers (Guo et al., 2016) in proposing a concrete material model. Elasto-plastic (Thabet and Haldane, 2000 and Kishi et al., 2011) and elasto visco-plastic models were also been used which their formulations are rate and history independent, however, they can be modified to allow for strain-rate sensitivity (Bicanic and Zienkiewicz, 1973). Liu 1985 proposed a modified elasto-plastic model that incorporated strain-rate sensitivity. It should be noted that *'softening'* region exhibited by elastic-plastic fracture model was neglected by a number of researchers such as Thabet and Haldane, 2000 which assumed that the residual stiffness and strength of concrete after pure crushing was significantly reduced and essentially the material behaved like granular material with confinement provided by the neighbouring concrete elements. The latter assumption is assumed to be more profound in the case of impact loading since due to the short duration of the loading the *'softening'* branch has no time to develop. On the other hand, authors such as Abbas et al.,2004 proposed a strain-rate sensitive visco-plastic model in which no *'hardening'* was considered for concrete and the post-failure behaviour (i.e. *'softening'* region) was described through an equipotential function. Cotsovos et al.,2008 adopted an orthotropic strain-rate independent model which consisted of both *'softening'* and *'hardening'* branch to account for the behaviour of concrete both before and after the peak-stress concrete. As the authors believed that the strain-rate dependency is based on a certain interpretation of the available experimental data, the validity of which was questioned (Cotsovos and Pavlovic, 2008[a, b, c], and Cotsovos, 2004) see section 2.5. However, the modelling adopted by the above authors were limited to RC structures that have been air-cured and exhibited low moisture content. Nevertheless, by assuming that the properties of concrete material are not dependant on the rates of loading (Saatci and Vecchio, 2009), the effect of the latter on the response of RC members was assumed to be attributed to the inertial response of the specimen mass which was included in the concrete modelling (Cotsovos and Pavlović, 2008[a, b, c], and Cotsovos, 2004).

2.8.2 The equation of motion and nonlinear solution analysis

When a structural form is subjected to an external force an internal action develops within the form which aims to resist the externally applied force. This field of internal forces develops as the result of the element deformation (U) and the structural motion. $F_{int}=K.U$ expresses the internal forces associated by the deformation of the specimens (where K is the element stiffness), $F_I=M.\ddot{U}$ (which oppose the velocity and acceleration) the inertia forces and $F_d=C.\dot{U}$ (which oppose the change of displacement (velocity) with time) the damping forces. Where M is the element mass, $\ddot{U}$ is acceleration, C is damping constant and $\dot{U}$ is the element velocity. The damping force F_d represents a percentage of the energy of motion that is dissipated. It is difficult to quantify the damping constant, C since it is assessed experimentally with a high factor of uncertainty as it depends on multiple parameters, the effect of which is not clear.

The choice of static or dynamic analysis depends on the rate of loading applied to an RC structure. When the external force is imposed at such a low rate that the acceleration and the velocity of the structure are insignificant, static analysis is used. As a result, the inertia and damping forces are ignored as well as they are also insignificant. The only internal forces that develop within the structural element are those resisting the deformation of the structure.

On the contrary, the dynamic analysis adopts the rate of the applied (external) loading under which the value of the associated acceleration and the velocity (of the structure) cannot be ignored. As a result, to the presence of all the internal forces (i.e. inertia and damping), the equation of equilibrium is no longer a simple algebraic equation but a second-order differential equation of motion.

$$M.\ddot{U}(t) + C.\dot{U}(t) + K(t).U(t) = R(t) \qquad \text{Eq. (2.1)}$$

where M is mass $U(t)$, $\dot{U}(t)$and $\ddot{U}$(t) are the displacement, velocity and acceleration respectively at time t, C is the structure's damping constant and R(t) is the applied load. The above equation is solved numerically through a number of methods (e.g. Houmbolt,

Newmark, Wilson and the a-method), (Bath 1996, Cook et al. 1989. All of which is based on the notation that, for each time step Δt, a solution may be achieved by transforming the second-order differential equation of motion into a simpler algebraic equation that can be easily solved. To achieve this, both velocity $\dot{U}(t)$and acceleration $\ddot{U}(t)$of the structure are expressed in terms of the change in displacement ΔU.

In all of the above methods, the Eq. (2.1) can be transformed into an equivalent static problem within a given time step as follow;

$$K^{*}\cdot\Delta U=\Delta P^{*} \qquad \text{Eq. (2.2)}$$

where: K^{*} : the effective stiffness matrix

ΔP^{*} : the effective load vector

The effective stiffness matrix K^{*} and the effective loading vector ΔP^{*} are functions of the structures stiffness matrix K and loading vector ΔP respectively, as well as the structure's mass M and damping C matrices and the time step used in order to solve Eq. (2.1) numerically. These expressions depend on the particular method used for the numerical solution of the equation of motion, in the current numerical investigation numerical method was used to solve the equation of motion and will be discussed in the following sections. In the nonlinear dynamic analysis, the solution of the finite element equations is obtained by employed employing explicit or implicit direct integration schemes

In the *explicit* method (Bathe 1996), at each time step, following the formation of the effective stiffness and the load vectors, the acceleration and the velocity is evaluated only once. Then, Eq. (2.2) is solved to obtain the displacement increment. The specified time-step in the explicit method must be extremely small so minimise the error and maximise the accuracy of the method. Since the construction of the effective stiffness and loading matrices is carried out only once (during each time step), then the solution of the equation of motion is evaluated only once. The latter is considered as the advantage of this method since the computational cost reduces significantly. However, the use of a small-time step may increase the overall computational cost of the whole problem especially if the problem

has a long duration. Moreover, the error at every time step is compiled and is added to the next time step, thus resulting in a continuous increase of the divergence between the numerical predictions and the actual behaviour of the structural element or structure analysed.

When using the *implicit* method, the solution process used in the explicit method described above is repeated until convergence is reached, i.e. until the difference between calculated and true values is small. For each iteration, the values of velocity and acceleration are assessed, the effective stiffness and loading matrices are constructed, and the equation of motion is solved in order to evaluate the displacement increment. If the residual force (the difference between internal and external forces) is too high, then, the residual force is reapplied to the system as an external load and the whole procedure is repeated. If the difference is smaller than a predefined value (convergence criteria) the solution procedure moves on to the next time step.

2.8.3 Newmark method

The Newmark family of approximation is used for the numerical solution of the equation of motion (see Eq.2.1). The integration scheme used in this method can be considered as an extension of the linear acceleration method (Bath 1996). The following assumptions are applied;

$$ {}^{t+\Delta t}\dot{U} = {}^{t}\dot{U} + [(1-\delta)\,{}^{t}\ddot{U} + \delta\,{}^{t+\Delta t}\ddot{U}]\Delta t \qquad \text{Eq. (2.3)} $$

$$ {}^{t+\Delta t}U = {}^{t}U + {}^{t}\dot{U}\Delta t + [(0.5-\alpha)\,{}^{t}\ddot{U} + \alpha\,{}^{t+\Delta t}\ddot{U}]\Delta t^2 \qquad \text{Eq. (2.4)} $$

when $\delta=1/2$ and $\alpha=1/6$, Eq. (2.3) and (2.4) correspond to the linear acceleration method. It should be reminded that oscillations in velocities and accelerations can sometimes be observed in implicit dynamic contact analysis particularly for high-speed impact problems. One of the methods currently adopted in this study to reduce such oscillations is to set the Newmark parameter $\alpha=0.5$. As mentioned before, Newmark is unconditionally stable and

is proposed as the constant-average-acceleration method (also called trapezoidal rule, TR), in which δ=1/2 and α=1/4 (Bathe 1996), see Fig. 2.16.

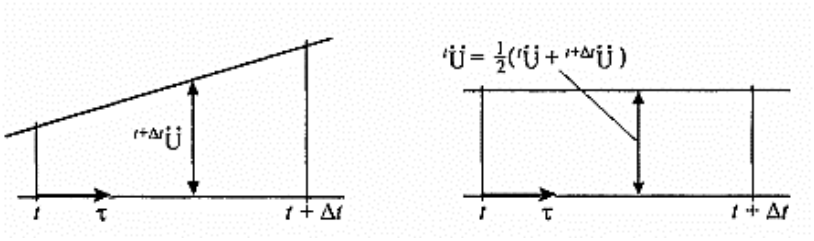

Figure 2-16 Linear acceleration method (left)-TR scheme (right), (Bathe 1996).

In addition to the above equations, for the solution of the displacements, velocities, and accelerations at time t+Δt, the Eq. (2.1) at time t+Δt is also used;

$$M.^{t+\Delta t}\ddot{U}+C.^{t+\Delta t}\dot{U}+K.^{t+\Delta t}U=^{t+\Delta t}R \qquad \text{Eq. (2.5)}$$

Considering the trapezoidal rule, which is mostly used, solving for $^{t+\Delta t}\dot{U}$ and $^{t+\Delta t}\ddot{U}$ from Eq. (2.3) and (2.4) in terms of $^{+\Delta t}U$, we solve for each time step

$$\left(\frac{4}{\Delta t^2}M+\frac{2}{\Delta t}C+K\right)^{t+\Delta t}U=^{t+\Delta t}R+M\left(\frac{4}{\Delta t^2}{}^{t}U+\frac{4}{\Delta t}{}^{t}\dot{U}+{}^{t}\ddot{U}\right)+C\left(\frac{2}{\Delta t}{}^{t}U+{}^{t}\dot{U}\right) \qquad \text{Eq. (2.6)}$$

And then calculate $^{t+\Delta t}\ddot{U}$ and $^{t+\Delta t}\dot{U}$. The complete solution procedure using the Newmark method is given as follows Bathe 1996);

Initial calculations:

1. Form stiffness matrix K, mass matrix M, and damping constant C
2. Initialize ^{0}U, $^{0}\dot{U}$, and $^{0}\ddot{U}$
3. Select time step Δt and parameters α and δ and calculate integration constants:

$$\delta \geq 0.50; \qquad \alpha \geq 0.25\,(0.5+\delta)^2$$

4. $a_0=\frac{1}{\alpha\Delta t^2}$; $a_1=\frac{\delta}{\alpha\Delta t}$; $a_2=\frac{1}{\alpha\Delta t}$; $a_3=\frac{1}{2\alpha}-1$;

$a_4=\frac{\delta}{\alpha}-1$; $a_5=\frac{\Delta t}{2}\left(\frac{\delta}{\alpha}-2\right)$; $a_5=\Delta t(1-\delta)$; $a_7=\delta\,\Delta t$

5. Form effective stiffness matrix $\widehat{K}$: $\widehat{K}=K+a_0M+a_1C$.

6. Triangularize $\widehat{K}$: $\widehat{K}$=LDL^{T}

2.8.4 Choosing between implicit and explicit formulations

The main criterion based on which the implicit or explicit formulations is selected is the time scale of the solution. The implicit method is unconditionally stable; therefore, it can use much larger time step comparing to the explicit method. However, the implicit method is iterative, and it involves the assembly and solution of a system of equations (Bath 1996). As a result, the computational time per load step is relatively high. The explicit method, on the other hand, uses much smaller time steps since it is conditionally stable. The latter implies that the time step for the solution has to be less than a certain critical time step, which depends on the smallest element size and the material properties. However, in contrast to the implicit method, it is non-iterative and involves no matrix solution, therefore it requires less computational cost per load step. For (both linear and) nonlinear static problems, the implicit method is the only option.

For low-speed dynamic problems, the solution is dominated by the lower frequencies of the structure since the solution time spans a period of time considerably longer than the time it takes the wave to propagate through an element. Most structural dynamics problems, such as certain metal forming problems, crush analysis, earthquake response and biomedical problems belong to this category of problems (ADINA 2017). If the explicit method is used for such problems the resulting number of time steps will be large, unless mass-scaling is applied, or the loads are artificially applied over a shorter time frame. While in the case of the implicit method, such modifications are not required. Hence, the implicit method is the optimal choice.

For high-speed dynamic problems, the solution time is comparable to the time required for the wave to propagate through the structure. Most wave propagation problems, explosives problems, and high-speed impact problems are categorised in this class of problems. For these problems, the number of steps required with the explicit method is not excessive. If the implicit method uses a similar time step it will be much slower and if it uses a much larger time step it will introduce other solution errors since it will not be capturing the pertinent features of the solution (but it will remain stable). Therefore, the explicit method is considered as the optimal choice.

It should be emphasised that a large number of dynamic problems e.g. crash problems, drop tests and metal forming problems cannot be fully categorised as wither low-speed or high-speed dynamic. In such cases both implicit and explicit methods are comparable. However, when the time step is relatively large (i.e. larger than the critical time step Δt_{cr}) and there are no convergence difficulties, the implicit method is considered as the optimal choice.

In the view of the above discussion, the implicit method with large time steps was adopted in the current numerical investigations. One of the factors that governed the choice of solution method was the order elements used for modelling the concrete medium, the latter will be discussed in Chapter 5. Higher-order elements e.g. 27 node brick elements are only available in the implicit analysis since in explicit method no suitable mass-lumping technique is available for these elements (ADINA 2017).

2.8.5 Nonlinear procedure

During each time step, the equation of motion governing the nonlinear dynamic problem considered is solved as a sequence of equivalent static problems through the use of the Newmark family of approximation methods. At the beginning of each iteration and based on the values of displacement, velocity and acceleration obtained from the previous iteration, the effective stiffness and load matrix are calculated, and an equivalent static problem is formulated (Kotsovos 2015). The equivalent static problem is solved through an iterative procedure based on the Newton-Raphson method (Kotsovos 2015). In full Newton Raphson iteration, the following algorithms are used:

$$^{t+\Delta t}K\ \Delta U^{(i)} = {}^{t+\Delta t}R - {}^{t+\Delta t}F^{(i-1)} \qquad \text{Eq. (2.7a)}$$

$$^{t+\Delta t}U^{(i)} = {}^{t+\Delta t}U^{(i-1)} + \Delta U^{(i)} \qquad \text{Eq. (2.7b)}$$

where: $^{t+\Delta t}K^{(i-1)}$: tangent stiffness matrix based on the solution calculated at the end of iteration (i-1) at time $t+\Delta t$

$^{t+\Delta t}R$: externally applied load vector at time $t+\Delta t$

$^{t+\Delta t}F^{(i-1)}$: nodal force vector corresponding to the element stresses due to the displacement vector $^{t+\Delta t}U^{(i-1)}$

$\Delta U^{(i)}$: Incremental displacement vector in iteration (i)

A characteristic of this iteration is that a new tangent stiffness matrix is calculated in each iteration, which is why this method is known as the *full* Newton-Raphson method. In full Newton-Raphson iteration, the computational cost per iteration is associated with the calculation and factorization of the tangent stiffness matrix. Since these calculations can be quite expensive particularly in large-order systems, the use of a modification of the full Newton-Raphson method can be effective (Bathe 1996). One such modification is to use the initial stiffness matrix ^{0}K in Eq.2.2 and thus operate on the equation:

$$^{0}K\ \Delta U^{(i)}=^{t+\Delta t}R-^{t+\Delta t}F^{(i-1)} \qquad \text{Eq. (2.8)}$$

With the initial condition $^{t+\Delta t}F^{(0)}=^{t}F$, $^{t+\Delta t}U^{(0)}=^{t}U$. In this case, only the matrix ^{0}K needs to be factorized, thus avoiding the expense of recalculating and factorizing many times the coefficient matric in Eq.2.7a. The above is referred to as the 'initial stress' method correspond to a linearization of the response about the initial configuration of the finite element system and may converge very slowly or even diverge (see Fig. 2.17a).

The iteration approach employed in the modified Newton-Raphson method is somewhat in between the full Newton-Raphson iteration and the initial stress method (see Fig. 2.17b). It involves fewer stiffness reformations than the full Newton-Raphson iteration and bases the stiffness matrix update on an accepted equilibrium configuration. The choice of time steps when the stiffness matrix should be updated depends on the degree of nonlinearity in the system response; i.e. the more nonlinear the response the more often the updating should be performed.

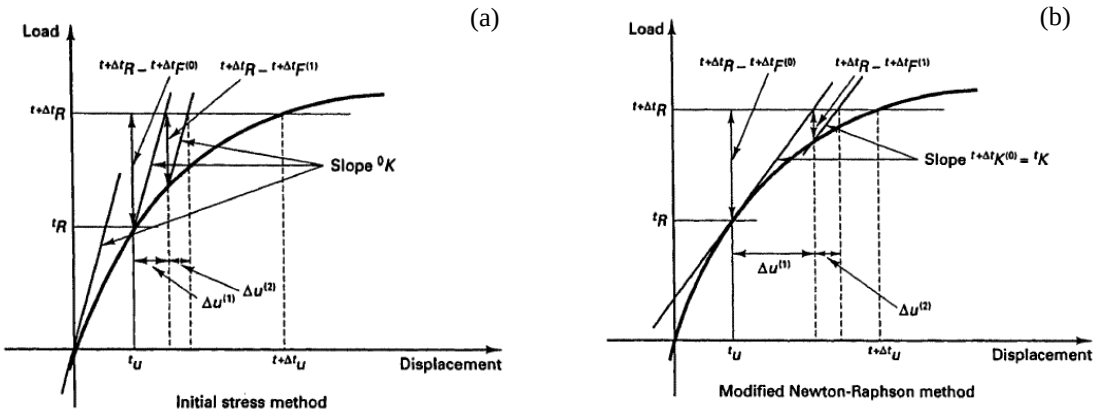

Figure 2-17 Illustration of initial stress and modified Newton-Raphson methods (Bathe 1996).

In modified Newton Raphson iteration, the following algorithms are used:

$$^{\tau}K\,\Delta U^{(i)} = {}^{t+\Delta t}R - {}^{t+\Delta t}F^{(i-1)} \qquad \text{Eq. (2.9a)}$$

$$^{t+\Delta t}U^{(i)} = {}^{t+\Delta t}U^{(i-1)} + \Delta U^{(i)} \qquad \text{Eq. (2.9b)}$$

where: $^{\tau}K$: tangent stiffness matrix at time τ, where $\tau \leq t$

Note that the stiffness matrix $^{\tau}K$ correspond to the last stiffness reformation. In ADINA, Stiffness reformations are performed only at the solution steps that the user specifies. Unless convergence has occurred, K [U] =R will not be satisfied at any stage of the iteration and hence a system of residual forces (i.e. Δf) can be assumed to exist. The latter may be viewed as a measure of the system's current departure from the required state of equilibrium. The total load is imposed incrementally, the iterative procedure commences once the load increment is imposed. In order to determine whether loading or unloading is taking place, each Gauss point is checked. Then, further checks are carried out to determine if any cracks close or open, or if any steel reinforcement yield or fail. Depending on the results of the previous checks, changes are introduced to the stress-strain matrices of the individual FE's and to the stiffness matrix of the structure. Convergence is checked locally at each Gauss point; this involves the use of the constitutive relations for the calculation of the stresses increments which correspond to the estimated values of the strain increments. Once the values of the strain and the corresponding stress increments become less than a small predefined value (i.e. convergence criterion) then convergence is accomplished.

When this is not achieved, the residual forces are calculated and are then re-imposed onto the FE model the RC form investigated until convergence is finally achieved.

2.8.6 Stability conditions

As mentioned before Newmark's approximations are unconditionally stable. This applies that by using any time step, the method remains stable and always yields to a solution. However, an unconditional stable solution does not necessarily provide an accurate result. In the sense that when using a large time step the solution provided by Newmark method may prove to be misleading and inaccurate (Bathe 1996). In such cases, the use of a smaller time step may give a different result from that obtained for a larger time step. In other words, although the stability of this particular approximation is independent of the time step used, the accuracy of the solution obtained is not. In order to ensure the accuracy of the solution, a number of test runs must be made, each time using a smaller time step, until the solutions obtained converge. An initial time step that can be used in the average-acceleration approximation is one-tenth of the period that corresponds to the largest eigenvalue (frequency) of the structure investigated.

2.8.7 Mesh size and finite-element modelling

The mesh size is an important parameter in numerical studies that significantly affect the computational time and the accuracy of the numerical predictions. A finer mesh may yield more accurate results but increases computational time significantly (Gue et al. 2017). As a result, often (Saatci and Vecchio 2009, Anil et al. 2016, Gue et al 2017, Pham and Hoa 2017, Gue et al. 2017) prior to conducting numerical simulations, a mesh density test is carried out in which a model is built using varying size elements and then a comparative preliminary analysis is conducted to ensure a suitable element size is adopted. The results of mesh convergence tests adopted in the above literature show a mesh size of approximately 10 mm yields to numerical convergence accurate predictions and the further reduction of element size has no significant influence on the results but increases the computational cost.

The element size used in the FE-modelling is usually dictated by the philosophy upon which the adopted FE package is based. The latter is influenced by the material model used and the volume of the specimens that were tested for obtaining the material models. Based on the above, a wide range of element shapes with different order of magnitudes have been adopted in FE modelling built to date. Anil et al. 2016 used a 10-node tetrahedron shaped element. Cotsovos et al. 2008, Kishi et al. 2011, Thabet and Haldane 2000, Pham and Hao 2017 adopted 8-node brick element with 1-point quadrature integration. In the numerical work of Abbas et al. 2004.RC Beam was modelled 20-noded isoperimetric elements. In another FE modelling conducted by Cotsovos and Pavlovic 2012, the 27-node brick element was used. The used a material model which was based on the data obtained from experiments on cylinder and which was assumed to constitute a material unit for which average material properties were obtained and hence the volume of these specimens provided a guideline to the order of the magnitude of the size of the FE.

2.8.8 Limitations of numerical studies

NLFEA forms a safer and more efficient method (compared to drop-weight testing) for investigating RC structural response under impact loading. To date, a range of NLFEA packages has been employed to study the RC structural response under impact loading. The use of such packages allows the study of more complex structural forms (compared to the simple structural configurations studied experimentally) while providing a more detailed description of the exhibited response (i.e. stress and strain distribution, deformation profiles, failure modes and crack patterns) throughout the loading process. However, the majority of the available NLFEA packages incorporate models of concrete behaviour, the derivation of which has been based on the regression analysis of test data obtained from static uniaxial compression and tension tests on plain concrete specimens (Cotsovos and Pavlovic 2008) [a,b]). Furthermore, they often assume that concrete material is strain-rate dependent (sensitive) and employ laws (in the form of dynamic increase factors) describing the variation (increase) of key material properties (e.g. modulus of elasticity, concrete compressive and tensile strength, yield and ultimate stress of steel) with strain-rate. The analytical formulation of these material models includes a number of parameters which are mainly linked to post-peak concrete characteristics such as strain softening, tension stiffening, and shear-retention ability. Such parameters are defined at the structural, rather than at the material level and attribute ductile characteristics to concrete behaviour not

compatible with its brittle nature and not justified by the available test data (Cotsovos and Pavlovic 2008[a,b]). As a result, the use of such parameters can affect the objectivity of the numerical predictions obtained since they require recalibration depending on the type of problem investigated.

2.9 DISCUSSION OF LITERATURE REVIEW

To date, a wide range of experimental and numerical studies have been conducted to investigate the dynamic response of RC beams under high-rate loading associated with impact problems. Although the experimental data available in the literature provides insight into the overall behaviour of RC structural forms under impact loading, it is not capable of describing the response quantitatively. This is due to the fact that the tests (drop-weight tests) are difficult to conduct. Another disadvantage of such tests is associated with the interpretation of the measured results. A large number of researchers believe that the observed increase in the load-carrying capacity of RC members with increasing loading rates is attributed to the strain-rate dependency of the material properties of concrete and the inertia forces that develop as the specimen reacts to the imposed load. Some researchers suggest that strain-rate sensitivity is associated with the post-failure behaviour of concrete attributing the observed shift in specimen behaviour with increasing loading rates to inertia, the nature of the problem at hand (a wave propagation problem within a highly nonlinear medium) and the ensuing localised response.

NLFEA packages employed for predicting RC structural response that adopts material models often not capable of accurately describing the triaxiality and brittleness characterizing concrete material behaviour. These material models rely on the definition of parameters associated with post-failure material behaviour which attribute ductile characteristics to concrete material behaviour which is not compatible with the available test data. Furthermore, the predictions obtained are influenced by the mesh size adopted, the type of FE elements employed to represent concrete. Furthermore, the material model adopted by FE packages assumes that concrete is strain-rate sensitive material.

The inability of material models to realistically describe the brittle nature and triaxially characterising concrete material behaviour can lead to inaccurate predictions, especially when considering impact problems. This is because as discussed before, during impact loading the concrete material has not enough time to react to the applied load, as a result, the RC member may not under-go the post-failure stage and any resistance provided by the member is mainly provided by the concrete and it is inevitable that concrete stiffness reduced significantly once the peak compressive strength is reached and this happens prior to post-failure stage. Although a number of experimental and numerical studies investigate the effect of axial loading on impact response of RC beam/column specimens the available information is not sufficient to provide a detailed insight into the effect of axial loading on the mechanics underlying specimen behaviour under impact loading. Nevertheless, the available data reveals that the presence of axial loading increases the load-carrying capacity of RC members under both static and impact loading as it delays the cracking process. The mode of failure exhibited by RC column under impact loading is influenced by the level of axial load applied. Under impact loading, the RC columns/beams subjected to axial loading exhibit shear-brittle failure while the same specimens without axial loading fail in a flexural-ductile manner with well-distributed fine cracks developing along their span. Axial loading and the eccentricity that characterizes its application can significantly affect the behaviour of the columns under the impact.

It was observed that in the presence of axial loading, reducing the spacing of the transverse reinforcement leads to a significant increase in the maximum sustained impact load while the increase in longitudinal reinforcement may not always enhance specimen behaviour. Further studies are required to investigate in detail the effects of reinforcement configuration on impact response. In the absence of axial loading increasing the (compressive) reinforcement increases the response significantly.

CHAPTER 3 - TESTING RC SLENDER BEAMS

3.1 INTRODUCTION

The available test data is often restricted to measurements of the contact force (generated in the impact region), the corresponding mid-span deflections and the reaction forces developing at the supports as well as observations of the specimen crack-patterns exhibited after the impact load is applied. However, such data are insufficient for studying in detail the causes underlying structural behaviour under impact loading as information concerning the variation of the deformation and cracking profiles throughout the loading process is often not captured during testing.

To this end, the work described herein attempts to produce experimental data that may help towards improving our understanding of the mechanics underlying the behaviour exhibited by slender RC beams when subjected to drop-weight testing. To achieve this, a series of drop-weight tests are carried out in order to study in detail certain important features of the response of six slender simply supported RC beam specimens when subjected to impact loading at their mid-span. Such features include the generated impact and reaction forces, the displacement of the drop-weight and specific points along the element span, as well as the values of strain (ε) and strain rate ($\dot{\varepsilon}$) measured at specific locations of the specimens throughout the loading process. The cracking and deformation profiles of the specimen at different stages of the loading process, as well as the failure modes, are also established as they provide information on the internal state of stress of each specimen. Furthermore, specimens already damaged under impact loading are also tested under static loading (by conducting 4-point loading tests). In the latter case, two concentrated loads are applied at a distance of 100 mm either side of the mid-span of the damaged RC beam specimens (in order to avoid applying the loads directly on the impact region of the pre-damaged specimens) and increased monotonically to collapse, in order to study the mechanisms through which the applied load is transferred to the supports. To achieve this, conventional instrumentation (e.g. LVDTs, accelerometers, strain-gauges and load-cells) is combined with a high-speed (HS) video camera, which has been proven to provide accurate measurements capable of describing in detail specimen behaviour throughout the loading

process (Abbas et al. 2010). The measurements obtained are finally compared to published test data obtained from similar specimens (i.e. slender RC beams with $a_v/d > 5$) under drop-weight loading.

This chapter documents the details of the experimental programme, including specimen properties, test setup and procedure, and instrumentations along with the discussion of the results.

3.2 OVERVIEW OF TEST PROGRAMME

The work presented herein is concerned with the investigation of the behaviour of six simply supported RC beams under drop-weight loading inducing moderate to high impact conditions. At first, for purposes of comparison, the behaviour of the specimens under static loading is experimentally established and assessed through the use of relevant design codes (e.g. Eurocode 2 2004). Also, some of the beam specimens damaged under drop-weight loading are also tested under static loading in order to assess their residual strength and stiffness. The test programme is outlined in Table 1.

3.2.1 Specimen characteristics

For all beams, the height (h) and width (b) of the cross-section was 200 mm and 100 mm respectively, whereas the full length (L) and the clear span (L_0) were 3.0 m and 2.7m, respectively (see Fig. 3.1). One of the beams was subjected to static 4-point loading (with the point loads being applied at a distance of 100 mm on either side of the mid-span) and all other beams to drop-weight loading at mid-span. In the case of impact loading, the shear span ($\alpha_v=L_0/2$) was 1.35m and the shear span to depth ratio was $\alpha_v/d= 7.9$ (>5). In the case of static loading, $\alpha_v= (L_0 - 0.2)/2 = 1.3$ m and $\alpha_v/d = 7.64$ (>5). The flexural and shear capacity under static loading were estimated as 18.9 and 24 kN for Type A and 20.4 and 26 kN for Type B respectively, using EC2 2004. The static load was applied in the form of displacement increments and increased monotonically to failure. The drop weight had a mass of 124 kg which was allowed to fall from different heights onto the mid-span region of each specimen in order to achieve different impact velocities as shown in Table 3.1. Two types of beam specimens were investigated (Type A and Type B) with different reinforcement detailing as shown in Table 2 and Fig. 3.1. A total of 13 tests were conducted

under both static and impact loading. It should be noted that the multi-impact tests on each specimen were terminated once the extent of the damage sustained (especially in the impact region) was such that did not allow the impact test to be carried out safely. Type A specimens had longitudinal reinforcement comprising two 10 mm diameter compression bars and two 12 mm diameter tension bars and 10 mm diameter stirrups at a spacing of 200 mm. The choice of stirrups size was not governed by design code requirements such as 'bent radius' due to limitations on the size of the beam cross-section and the diameter of the specimens available. Type B beams differed from Type A beams in that the compression reinforcement and the stirrups had an 8 mm (rather than 10 mm) diameter. The steel properties are shown in Table 3.3 where it can be seen that the yield stress (f_y) was 503 MPa, 609 MPa and 566 MPa for the 8 mm, 10 mm and 12 mm diameter bars, respectively, and Young's modulus E = 200 GPa. For all specimens, the 28-day compressive strength of concrete established from tests on 100 mm side cubes was f_{cu} = 27 MPa, whereas the splitting strength established tests on 300 mm long x 150 mm diameter cylinders was 1.88 MPa. The material and thickness of the pad used between the impactor and the specimen varied in an attempt to control the intensity and loading rate characterising the imposed impact load.

Table 1 Experimental Programme

Beam type		Test type	Test No.	Date	Support condition	Height of impacts (m)	Impact velocity (m/s)	Pad (thickness in mm)
A	A1	Static (undamaged)	1[a]	16-03-15	Simply Supported	-	-	Steel (40 mm)
	A2	Impact and Static (damaged)	2	17-02-15		0.5	3.16	Ply (15mm)
			3	17-02-15		1	4.42	
			4	17-02-15		1	4.42	Steel (15mm)
			14[b]	02-03-15		-	-	Steel (40 mm)
	A3	Impact	5	30-06-15		1	4.42	Steel (40mm)
			6	01-07-15		1.5	5.42	
B	B1	Impact and Static (damaged)	7	06-07-15	Simply Supported	1	4.42	
			8	06-07-15		1.5	4.42	
			9	07-07-15		1	5.42	
			15[b]	22-07-15		-	-	
	B2		10	14-07-15		1.5	5.42	
			11	15-07-15		2	6.26	Ply (35mm)
			16[b]	23-07-15		-	-	Steel (40 mm)
	B3	Impact	12	17-07-15		2	6.26	Ply (35mm)
			13	20-07-15		2	6.26	Ply (35mm)

[a] Static Tests on the undamaged specimen

[b] Static Tests on the pre-damaged specimen

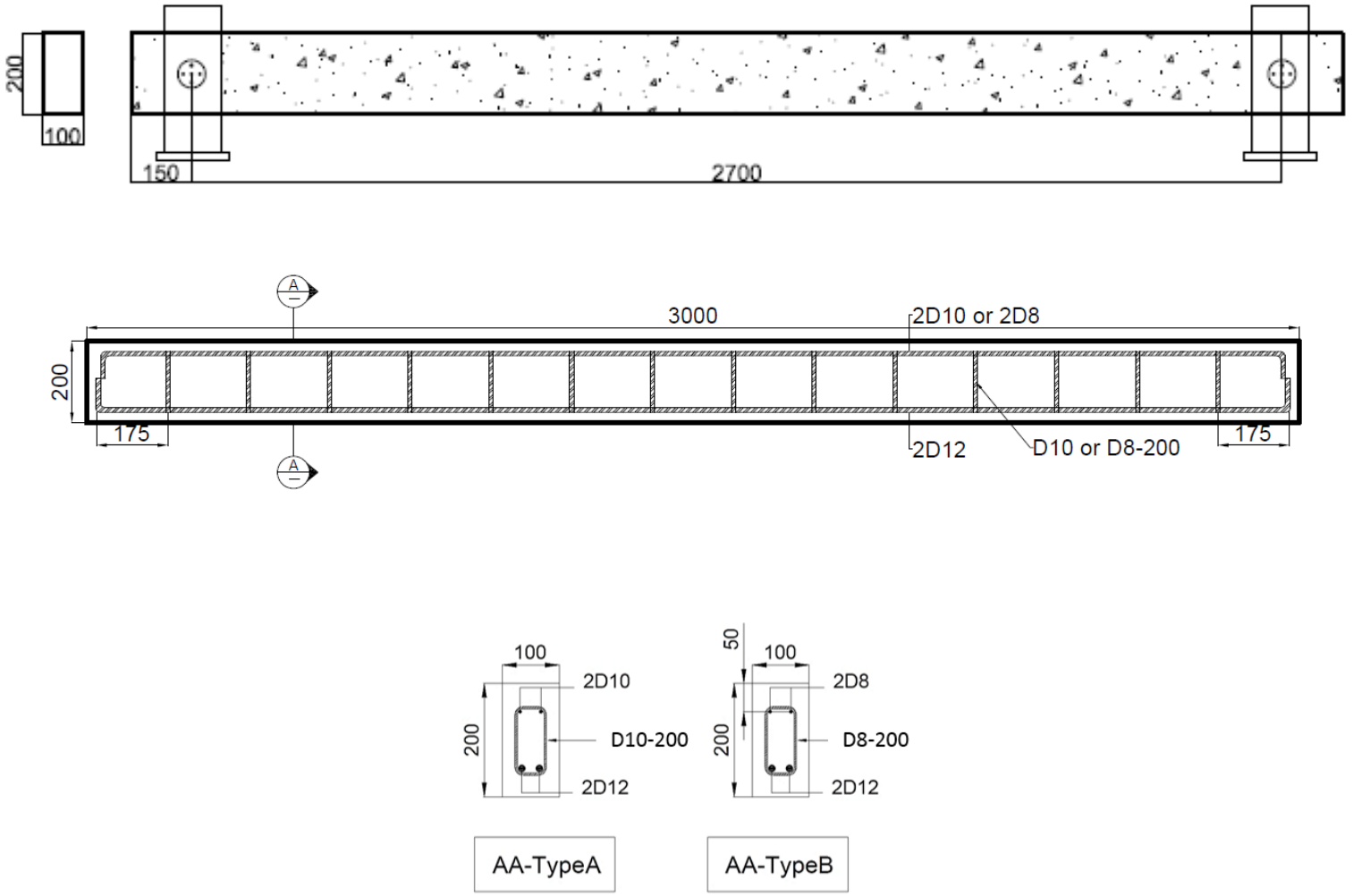

Figure 3-1 Design of the RC beam specimen (units are in mm)-cover 50 mm

Table 2 Reinforcement details of the RC beam specimens

Beam Type	Length (m)	Tension Steel A_s	Compression Steel $A_{s'}$	Stirrups	$\rho_w = A_{sw}/bs$
A	3	2x12φ	2x10φ	D10@200mm	0.785%
B	3	2x12φ	2x8φ	D8@200mm	0.502%

Table 3 Steel reinforcement mechanical properties

Rebar Size	12 mm	10 mm	8 mm
$f_{yield}(MPa)$	566	609	503
$f_{ult}(MPa)$	684	727	640
ε_{yield}	0.00283	0.003045	0.002515
ε_{ult}	0.12	0.14	0.11

3.3 EXPERIMENTAL SETUP EMPLOYED TO APPLY STATIC LOADING

The experimental setup employed for studying the behaviour of the (undamaged and damaged) RC beam specimens when subjected to static 4-point loading is presented in Fig. 3.2. Static loading was applied in the form of displacement increments to failure through the use of a 300 kN hydraulic jack. The level of loading applied was monitored via a load cell positioned above the hydraulic jack. The jack was supported by a steel beam on top which was in turn tied into the strong floor through two high strength steel bars with a diameter of 20mm. The concentrated loads were applied in two locations via a short rigid steel spreader beam (see Fig. 3.2), at a small distance (of 100 mm) from either side of the mid-span (instead of being applied as a single point load at mid-span) in order to avoid directly loading the impact region of the (pre-damaged) specimens. Two steel plates were used at the loading points in order to effectively distribute the concentrated loads applied on the top surface of the beam. This was intended in order to avoid the development of high-stress concentrations in these regions that could result in the development of localised cracking that can potentially affect the load-carrying capacity and the exhibited mode of failure of the specimen. During static testing, deflections were measured at mid-span through the use of a dial gauge due to the limitations associated with the availability of LVDTs at time. In addition, the crack patterns developing at different levels of loading were also established.

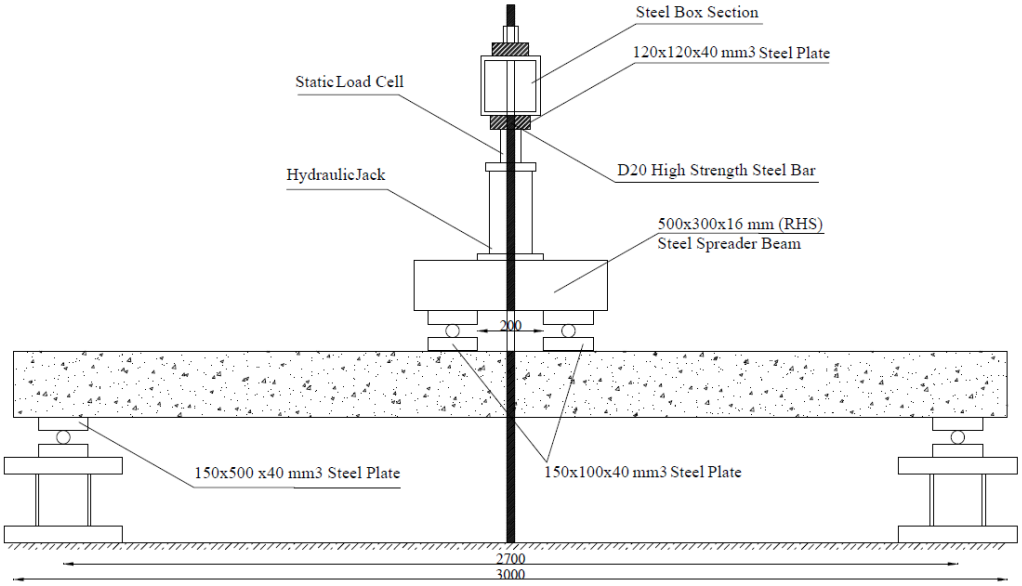

Figure 3-2 Setup used for static testing.

3.4 EXPERIMENTAL SETUP EMPLOYED FOR DROP-WEIGHT TESTING

The drop-weight testing rig presented in Fig. 3.3 is capable of delivering a steel drop-mass of 124 kg onto the mid-span region of the specimen from a maximum height of 4m. All specimens were tested as simply supported beams and were subjected to multiple drop-tests in order to study the behaviour exhibited during every impact. Steel pads were placed at the supports of the beams to avoid the development of high-stress concentrations that could lead to localised cracking in these regions. Plywood or steel pads were also used in the impact regions (at the interface between the impactor and the beam) to moderate the level of damage sustained at the top surface of the specimen during each collision and – to some extent – control the loading rate and intensity of the generated impact load during each drop test. Steel pads were used to achieve impact loads characterised by high values of loading rate ($\dot{P}$) and intensity ($\max P_d$) (high intensity impact testing) whereas plywood pads (or thin steel pads) were used to reduce the loading rate and intensity characterising the contact force developing in the impact region to achieve (moderate intensity impact testing). The term ‘moderate’ and ‘high’ intensity refers to the magnitude of impact force ranging from 50-150 kN and 150-300 kN, respectively.

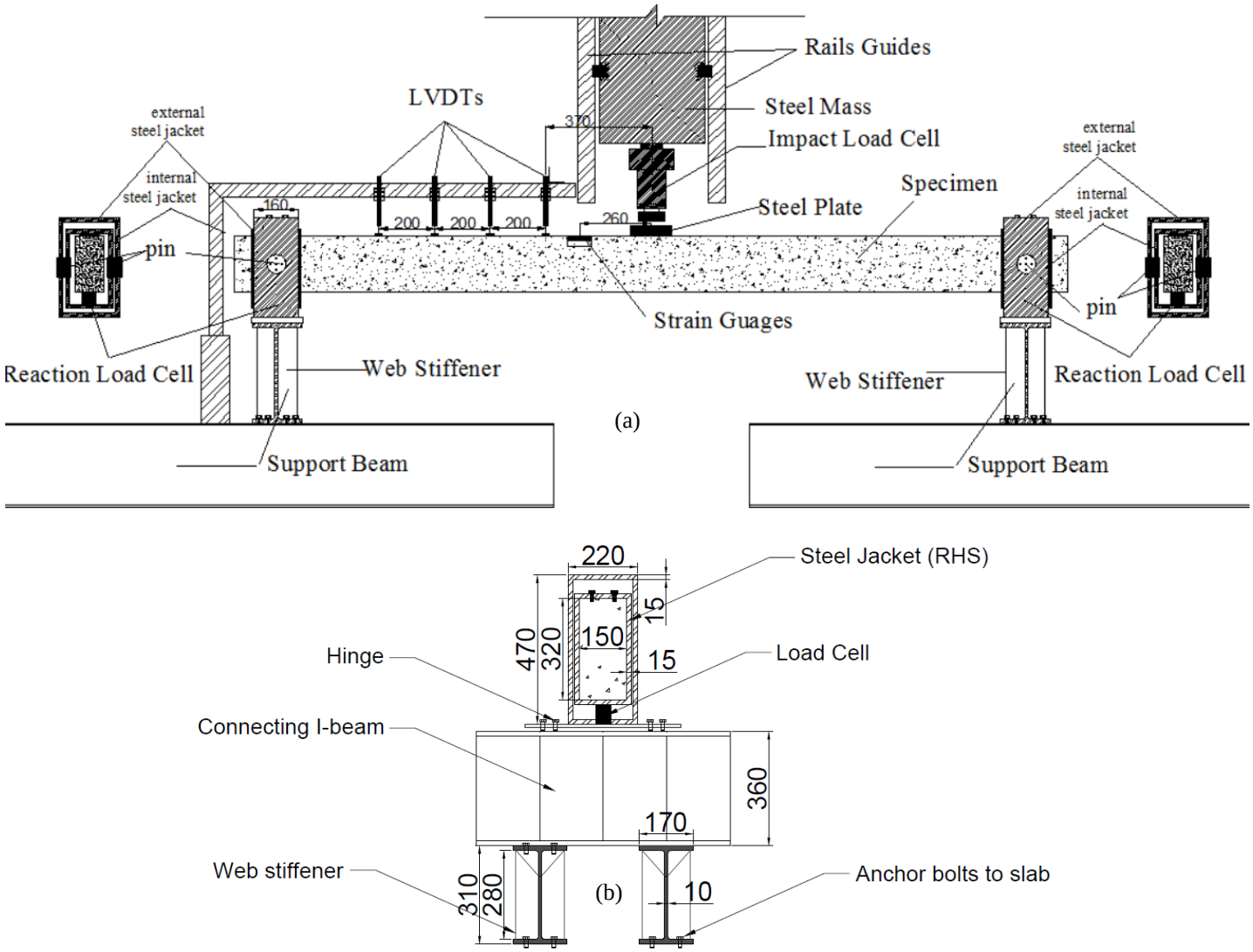

Figure 3-3 (a) Impact test setup at HWU, (b) support condition

The specimens were instrumented to measure the displacements, strains and strain rates at specific locations along the element span throughout the loading process, record the deformation and cracking profiles exhibited at different stages of loading as well as the time-history of the impact and reaction forces developing high-stressFigs. 3.4-3.6 show the position of the instruments used along the span of the specimens, which consist of the following items:

- Four Linear Variable Differential Transducers (LVDTs) were mounted at different locations along the element span (see Fig. 3.4) to measure the vertical displacement exhibited at these points. The LVDTs used were ACT3000C type manufactured by RDP group, with ±75 mm range with the maximum measurable frequency of 35 kHz. They are labelled as Ch-5, Ch-6, Ch-7 and Ch-8 (see Figs. 3.4 and 3.5a) and were mounted on a steel frame supported independently to the rest of the setup.

- Two dynamic load cells labelled Ch-9 and Ch-10 (see Fig. 3.4 and Fig. 3.5), were placed underneath each support to measure the variation of the reaction forces generated with time. Another dynamic load-cell (labelled Ch-11 in Fig. 3.4 and Fig. 3.5 and Fig. 3.6) was attached to the bottom of the drop weight and was used to measure the impact (contact) force generated during the collision of the drop-mass onto the specimen. The impact force was applied through the use of an impactor comprising a total mass of 124 kg (i.e. 98 kg steel plate, 18 kg load cell fitted with an adapter, 8 kg fixing plate and 2.032 kg impactor's spherical head).

- All the specimens in tests 5 to 13 were fitted with strain gauges installed in two locations. One of the strain gauges was mounted on the top (compressive) surface of the beam at a distance of 260 mm off the mid-span (Ch13 in Fig. 3.5). The second strain gauge was 50 mm attached bellow the first one on the side of the specimen (Ch14 in Fig. 3.4). Both strain gauges are used to measure longitudinal strains and corresponding strain rates in the compressive region of the beams.

- A data acquisition system was used capable of recording data at a sampling rate of 35 kHz per channel.

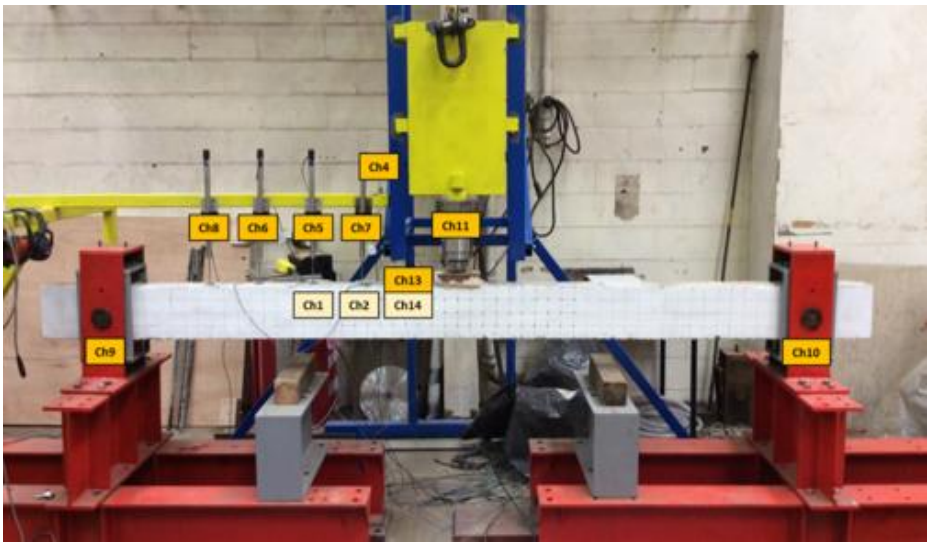

Ch1	Accelerometer
Ch2	Accelerometer
Ch3	-
Ch4	Accelerometer
Ch5	LVDT
Ch6	LVDT
Ch7	LVDT
Ch8	LVDT
Ch9	Load Cell
Ch10	Load Cell
Ch11	Load Cell
Ch12	-
Ch13	Strain gauge
Ch14	Strain gauge

Figure 3-4 Experimental setups used for conducting drop-weight testing and instruments used in order to record the behaviour exhibited by the RC beam specimens.

Finally, a high-speed camera was also used, which was set to record at a rate of 2000 frames per second (fps). The use of this camera aimed at confirming the measurements obtained from the instrumentation described above and compensating for the occasional loss of data. The photographic evidence was successful in providing a more detailed description of the specimen behaviour in the impact region by tracking the movement of a number of points marked in the form of a grid on the side surface of the specimen (see Fig. 3.4), the pad and the impactor. To achieve this, the videos recorded where digitised through the use of appropriate tracking software (Tracker 4.87 2014). The high-speed camera was also used to record in detail the development and the propagation of cracking in the impact region throughout the loading process.

3.4.1 Linear Variable Differential Transformers (LVDTs)

Four Linear Variable Differential Transformers (LVDT) were mounted to measure the displacements along the RC beam during impact (see Fig. 3.6). They are labelled as Ch4, Ch5, Ch7 and Ch8 on Fig. 3.5. They were bolted on a steel bar connected to the guide rail. The LVDTs used were ACT3000C type manufactured by RDP group, with ±75 mm range. The LVDTs were glued with Loctite superglue and Araldite glue (i.e. ARA-400001) to the top surface of the specimens through 3 mm square steel plates.

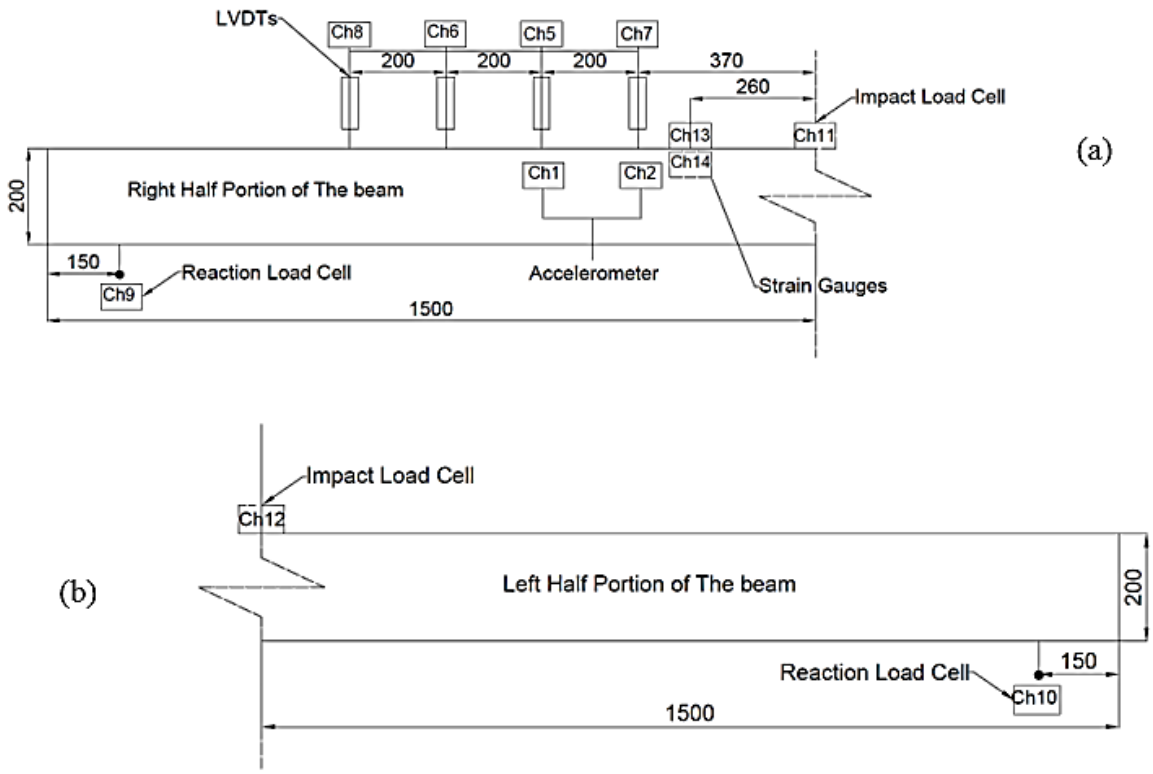

Figure 3-5 The position of the instruments used for recording specimen response during drop-weight testing (a) along the left and (b) along the right-hand side portion of the beams' span

Figure 3-6 Linear Variable Differential Transformers (LVDT)

3.4.2 Accelerometers

Three accelerometers were used for each impact test. Three accelerometers were used denoted as Ch1, Ch2 and Ch4. For tests ImpA2-a (i.e. tests 2-4), Ch1 and Ch2 were glued on the top surface of the specimen, at a distance 200 mm from the supports at either side to measure the accelerations induced due to impact. However, in order to improve the accuracy of the recorded acceleration data, their locations on the beam specimens were altered for tests 5-13) and they were mounted on the right-half portion of the specimens only. For these tests, the accelerometers were affixed to L-shaped aluminium brackets using mounting studs and screws. The brackets were then secured to test objects using Araldite glue, see Fig. 3.7a.

(a)

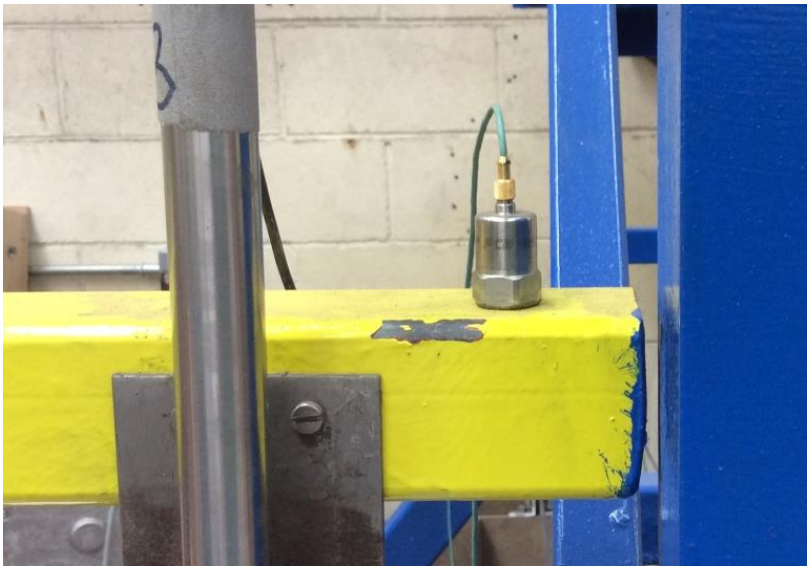

(b)

Figure 3-7 Accelerometers Ch2 and Ch1 (a) and Ch4 (b)

For all the tests, Ch4 was mounted on the steel bar (which was connected to the floor), to ensure the vibration of LVDTs are not excessive due to the impact. Ch4 was glued (using Loctite super glue) to the steel bar, see Fig. 3.8b. The location of the accelerometers on the test objects have been discussed in the preceding section. The accelerometers were ICP type piezoelectric accelerometers produced by PCB Piezoelectrics; they had a resonant frequency of 3000 Hz, measurement range of ± 500 g with overload limit of ± 2000 g.

3.4.3 Load-Cells

Two load cells were placed underneath each support to measure the reaction forces. They each had a 200 kN maximum load capacity, they were labelled as Ch9 and Ch10. One load cell was used to measure impact force and was attached to the impactor, with a total maximum force capacity of 2000 kN, denoted as Ch12. The three load cells were supplied by Novatech Measurements Limited. The 200 kN capacity load cells were calibrated before test under static load up to 200 kN using Denison Universal Testing Machine and the 2000 kN capacity load cell was calibrated up to 500 kN static load. In both calibrations, the static load was applied through steel plate for uniform distribution, see Fig. 3.8.

Figure 3-8 Transient Load Cell, Ch12 (Left)-Reaction load cell Ch10 (Right)

3.4.4 Strain Gauges

All the specimens in tests 5-13 were fitted with strain gauges placed at two locations of the test objects. One of the train gauges was affixed on the top (compressive) surface of concrete while the latter was secured underneath the former on the web of the beam to measure the strains in the longitudinal direction. The gauges used were Leadwire-integral P series, type PL-60-11 single element with a 60mm gauge length, gauge factor of 2.12 and 120±0.3Ω gauge resistance and 35 kHz sampling rate. They are manufactured by Tokyo Sokki Kenkyujo Co., Ltd. The gauges were set to operate in a quarter bridge configuration.

Prior to securing the gauges on test objects, the concrete surface was grinded using grinder and sandpaper and then was degreased using GC-6 Isopropyl Alcohol. The target area was then prepared using Silicon Carbide papers (i.e. Grit: 220A, 320A and 400) and M-prep conditioner A and Neutralizer 5A. In order to affix the gauges to the prepared surface, M-Bond 200 adhesive kit (containing catalyst-C) was used. Following this process, the strain gauges were covered with M-Coat FBT to prevent possible damages particularly to lead wires. The installation accessory products were manufactured by Micro-Measurements. Fig. 3.9 shows a photo of a glued gauge on the concrete top surface prior to the application of M-Coat FBT. To ensure the accuracy of the measured data, prior to the impact tests, the strain gauges were mounted on steel I-section and were calibrated.

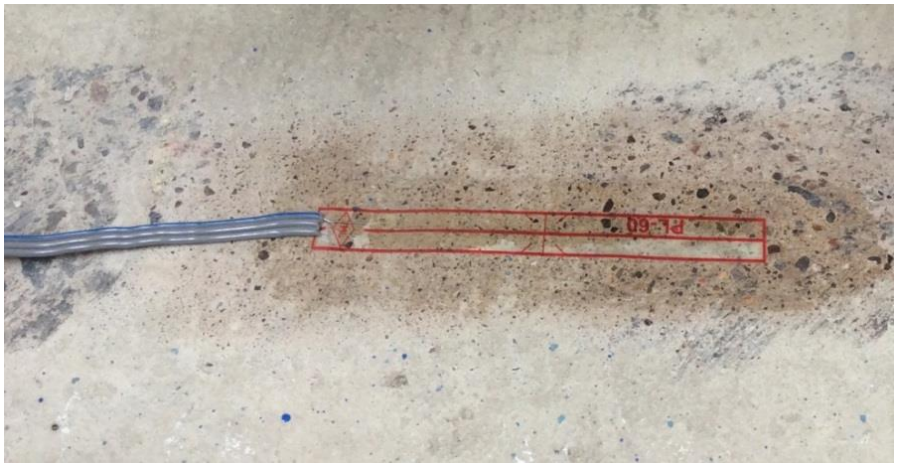

Figure 3-9 Strain gauge glued on concrete top surface

3.4.5 Data Acquisition system

The digital data was collected using a Micro Analog2-FE-MM40 data acquisition system manufactured by Fylde Electronic Laboratories Ltd. It accommodates maximum 40 channel analogue instrumentation system in 2U enclosure. The maximum sampling frequency of the data acquisition system is 500 kHz (for the entire unit), 14 channels were used for the purpose of this experimental investigation resulting in a sampling rate of 35 kHz per channels and the data are recorded by the channels in sequence. The numbers of channels assigned to instrumentations are as follow:

- Four accelerometers channels
- Four lead cell channels
- Two strain gauges channels
- Four LVDTs channels

The collected data were processed in real-time with DASYLab® software. The information regarding the data acquisition system and the connection boards can be found on the manufacture's website (http://www.fylde.com/).

The specifications of the connection boards used for the test programme are summarised in Table 4 below.

Table 4 Sensors specifications

Sensors	Type of Connection Board	No. of Available Channels	No. of Boards Used	Sampling Rate
LVDT's	FE-346-CA	4	2	35.714 KHz
Accelerometers	FE-376-IPF	3	2	35.714 KHz
Load Cells	FE-366-TA	3	2	35.714 kHz
Strain Gauges	FE-366-TA	2	1	35.714 kHz

3.4.6 High-Speed Camera

In order to obtain details of transient load, local failure (e.g. scabbing and spalling), crack propagation and deformation profile, a high-speed camera with a framing rate capacity of up to 5100 fps was used. The camera was supplied by MotionPro X™ and was supplied

with a total memory of 4 GB. MotionPro X software suite provided by the manufacturer was used to record images and/or video captured during each test. The high-speed camera had two BNC connectors for input and output of triggering and synchronization signals which connected the camera to the impactor. Through these connectors, the simultaneous recording of the transducers and the camera was achieved. For the current experimental tests, the camera was set to operate at a rate of 2000 frames per second. The pre-triggering time was set as 0.4 s and the camera recording was saved as a video.

3.4.7 Electronic Winch

The drop weight was raised to a specified height from which it was then dropped safely to the test object using an electronic release winch. As soon as sampling begins, the winch is released, and the steel mass is dropped on mid-span of the beam. In order to have simultaneous sampling and transient impact, the winch was connected to a trigger, see Fig. 3.10.

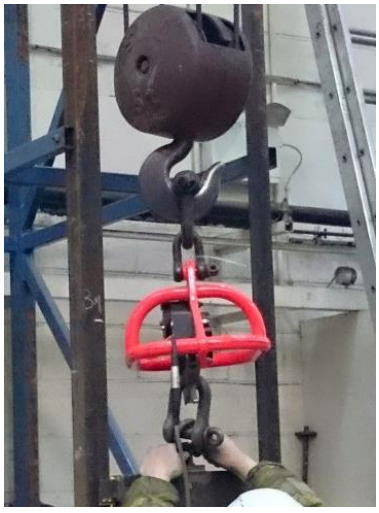

Figure 3-10 Crane and Electronic Winch Used for Lifting Up the Impactor (i.e. Steel Plate)

3.5 STATIC TEST RESULTS (UNDAMAGED SPECIMEN)

SS-A1 (Test Date: March 16, 2015; 1)

The behaviour of beam specimen A1 under static loading is presented in Fig. 3.11 in the form of a curve describing the relation between the applied load and the deflection recorded

at mid-span. This curve reveals that the beam exhibited ductile behaviour, with failure occurring after yielding of the longitudinal reinforcement bars at mid-span, resulting in the formation of extensive flexural cracking along its span that ultimately led to loss of load-carrying capacity due to failure in the compressive zone (associated with point A of the load-deflection presented in Fig. 3.11). This was in line with predictions of the design codes presently employed (Eurocode 2 2004) and a well-established assessment tool (Response-2000). Fig. 3.11 also shows the main cracks developing along the span of the specimen prior to failure. In the case of Type B, a similar type of behaviour is predicted by the codes and Response-2000 with a slightly lower load-bearing capacity (25 kN instead of 26 kN) due to the use of 8mm diameter longitudinal bars in the compressive zone instead of 10mm used in the case of Type A beams.

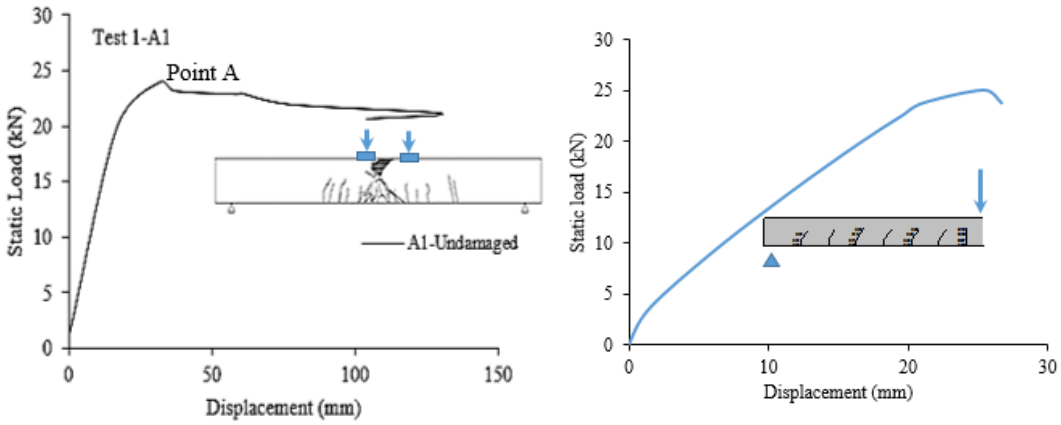

(a) (b)

Figure 3-11 Load-displacement curve and crack patterns (a) established experimentally for the case of specimen A1 (Type A) and (b) predicted by Response 2000 for specimens A1 and B1 when subjected to static 4-point bending testing.

3.6 IMPACT TEST RESULTS

ImpA2-a (Test Date: February 17, 2015; Contact- surface: 15mm Ply; Test 2)

The height of impact was 0.5 m and the specimen was impacted with a velocity of 3.16 m/s to a 15 mm ply. No significant damage was observed. Moderate flexural cracks developed in the tensile zone and compressive zone. The crack profile was symmetrical and propagated throughout the span. The impact test lasted for 1.40 s, several minor cracks developed on top and bottom of the specimen. Few diagonal cracks were observed near the

support. The crack pattern was not symmetrical along the length of the specimen. Ch7 was not properly in contact with the test object, as a result, the recorded displacement values were close to 0. Ch5 showed constant negative value for displacement which clearly does not describe impact-induced vibration; therefore, the readings obtained from Ch7 and Ch5 had to be discarded.

ImpA2-a (Test Date: February 17, 2015; Contact- surface: 15mm Ply; Test 3)

Localised damage was observed in which the concrete underneath the plate was disintegrated. The damage was more apparent on the left-half portion of the beam. Inclined cracks developed in tensile zone penetrating into the compressive region. The cracks widened and were concentrated in the mid-region. The crack profile was not symmetrical however, they were more apparent in the left-half portion of the beam. All the LVDTs were detached from their original mounting location at the early stage of the impact test; as a result, their recordings were discarded, see Fig. 3.12.

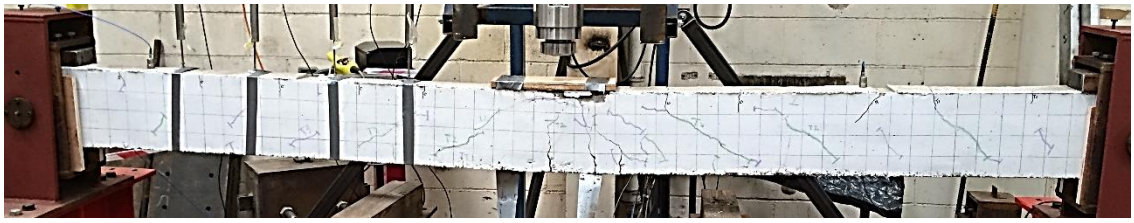

Figure 3-12 Crack pattern, deformation profile and localised damage Imp-A2-a, Test 3.

ImpA2-a (Test Date: February 17, 2015; Contact- surface: 15mm Ply; Test 4)

During Test 4 the specimen suffered significant damage. Concrete spalling was observed at the top and bottom of the concrete beam. The cracks (formed already during Tests 2 and 3) expanded in width and propagated from bottom to the top face of the specimen and there was an increase in their concentration around the region where the impact load was applied. Diagonal cracks formed resembling punching shear pattern; however, their formation was not symmetrical, see Fig. 3.13.

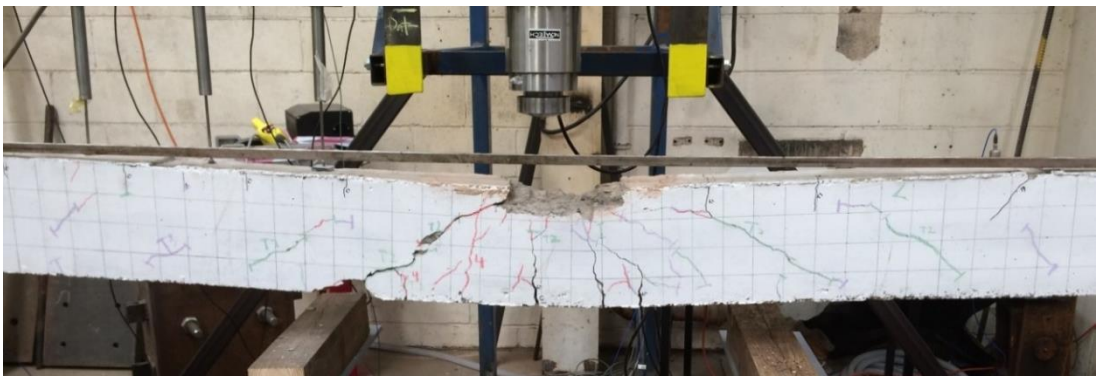

Figure 3-13 ImpA2-a-Test 4

ImpA3-b (Test Date: June 30, 2015; Contact- surface: 40mm Steel; Test 5)

The impactor was dropped to a 40 mm steel plate from a height of 1m with a velocity of 4.42 m/s. Following the impact, several cracks appeared at various locations near the point where the impact load was applied. Flexural cracks developed in both tensile zone and compressive zone along the central region of the beam specimen. Inclined cracks propagated from the tensile region towards the compressive zone of the beam near the point at which the steel plate was placed. The crack-profile was not symmetrical, more inclined cracks were observed in right half portion of the beam specimen. The observed damage was not significant, no significant spalling and/or concrete crushing (i.e. localised damage) was observed during the test (see Fig. 3.14). Through the use of the high-speed camera, it was observed that the specimen was subjected to multiple impacts, during the first impact, just before the striker hits the steel plate, it was slightly shifted to the right half portion of the beam, and in other words, the application of load was not eccentric. Right after the striker hits the steel mass, an uplift of the contact plate was observed, as a result in the second impact the steel mass also behaved as the striker. The sensitivity (i.e. gain) of the strain gauges was not accurately defined (i.e. connectivity and signal conditioning were not satisfied). The glue bonding between Ch5 and Ch8 and the metal-plated was destroyed as the result of the impact.

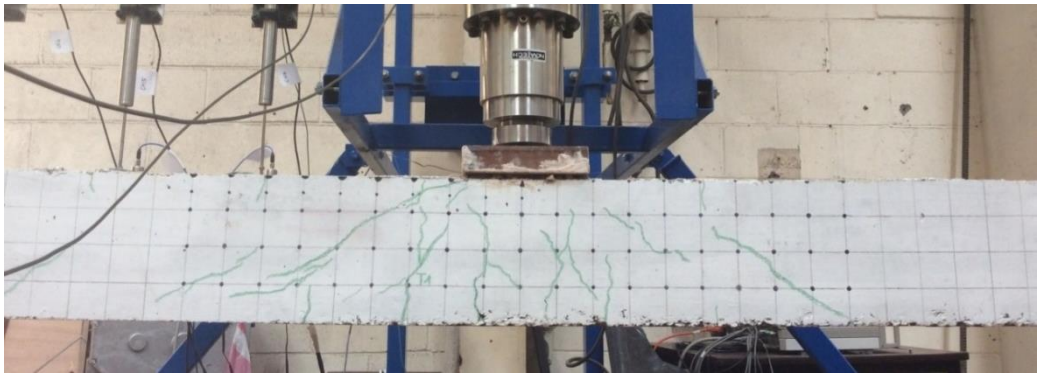

Figure 3-14 ImpA3-b-Test 5

ImpA3-b (Test Date: July 01, 2015; Contact-surface: 40mm Steel; Test 6)

The pre-damaged beam specimen was subjected to an impact velocity of 5.42 m/s. The existing inclined crack on the right half portion of the beam widened in width and led to a significant spalling and scabbing of concrete in compressive (near the point where the impact load was applied) and tensile zone respectively. The former resulted in bucking of compressive reinforcement while as the result of the latter effect, the bond between the steel reinforcement and concrete was removed. There were no new cracks observed, the existing ones widened slightly in width particularly the flexural cracks in the tensile region of the specimen. Similar to the previous test, the impact force application was not eccentric. There have been technical issues with the DASYLab software which caused loss of data. Example of such issues is observing spikes in the measurements and aliasing. The compressive reinforcement was exposed and buckled (see Fig. 3.15).

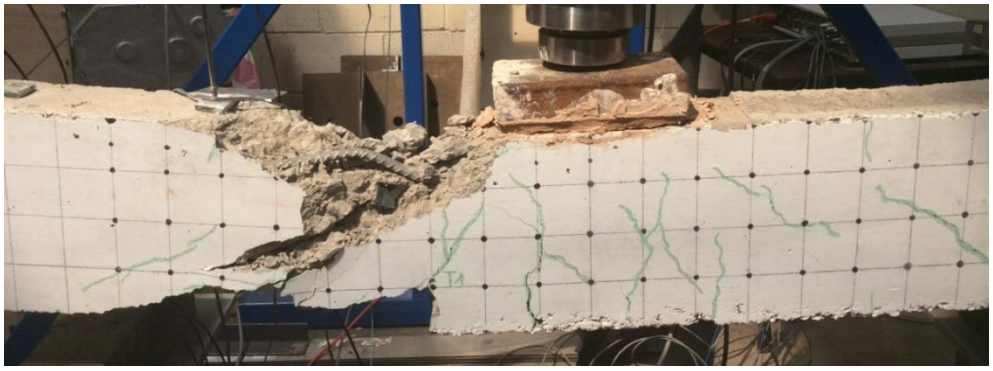

Figure 3-15 ImpA3-b-Test 6

ImpB1 (Test Date: July 06, 2015; Contact-surface: 40mm Steel; Test 7)

The steel-plated was impacted with a total velocity of 4.42 m/s. Flexural cracks were observed in the compressive and tensile region of the beam specimen concentrated in the central region of the beam (i.e. near the point of load application). Several inclined cracks were formed propagated from the tensile zone towards the compressive region of the beam. The crack-profile was symmetrical. No significant damage was observed. The crack which was formed between the first inclined crack and the middle flexural crack had larger width comparing to the rest of the cracks despite the fact that the diagonal crack on the right half portion of the beam formed prior to the latter crack. The width of the flexural crack underneath the impact load, in the tensile zone, was 2 mm, while the width of the neighbouring flexural crack (i.e. 100 mm away from the former crack) was 3 mm, see Fig. 3.16.

Figure 3-16 ImpB1-Test 7

ImpB1 (Test Date: July 06, 2015; Contact-surface: 40mm Steel; Test 8)

The pre-damaged specimen was impacted with an impact velocity of 5.42 m/s. The existing cracks widened in width; significant spalling was observed. Following the first contact between the impactor and steel plate, the latter was displaced as a result the application of impact load was not eccentric. The inclined cracks on the left half portion of the beam widened more significantly. The width of the flexural cracks forming in the tensile region of the beam was measured as large as 5 mm. New inclined cracks developed between the mid-span and the supports at either side of the beam. Several horizontal cracks (almost parallel to the longitudinal edge of the beam) appeared in the tensile zone underneath the steel plate intersecting with the inclined cracks propagating away towards either sided of the beam, the effect was more visible on right half portion of the specimen. Ch 5 and Ch 6 were detached. The width of the flexural crack underneath the impact load, in the tensile

zone, was 2 mm, while the width of the neighbouring flexural crack (i.e. 100 mm away from the former crack) was 3 mm. Ch2 was detached (see Fig. 3.17).

Figure 3-17 ImpB1- Test 8

ImpB1 (Test Date: July 07, 2015; Contact-surface: 40mm Steel; Test 9)

The striker was dropped from a height of 1 m (i.e. a total impact velocity of 4.42 m/s) to pre-damaged beam specimen. Following the first impact, the existing horizontal cracks widened in width combined with further opening of the intersected inclined cracks led to concrete scabbing in the tensile zone. The concrete in the compressive region, underneath the contact surface disintegrated further resulting in an increase in localised damage. The cracks were concentrated in the central region of the beam. The steel plate fell down as the bond between the contact surface and the impactor was damaged due to the impact. The steel plate was dropped to the cables connecting the instruments to the data acquisition, as a result, Ch4, Ch6, Ch8 were disconnected. The width of the flexural crack underneath the impact load, in the tensile zone, was 2 mm, while the width of the neighbouring flexural crack (i.e. 100 mm away from the former crack) was 3 mm (see Fig. 3.18).

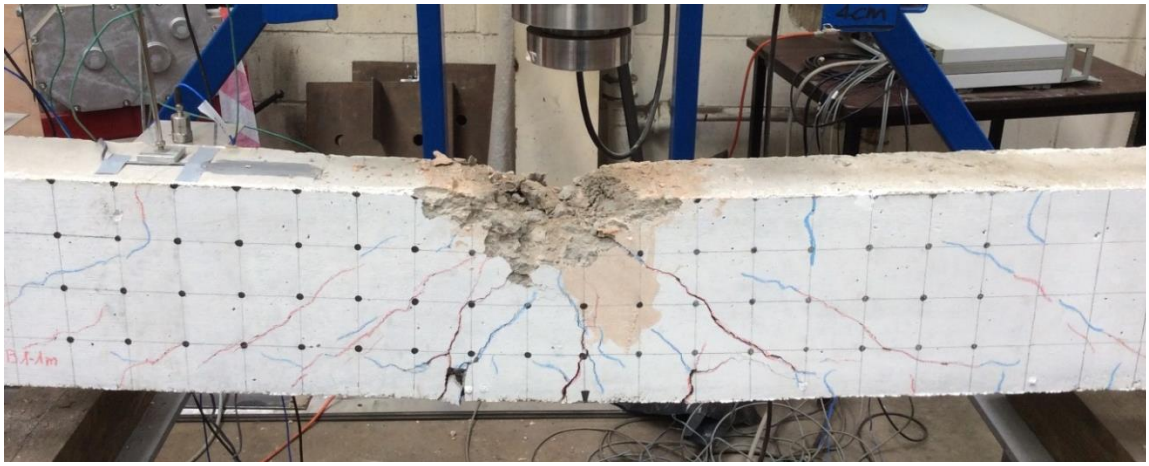

Figure 3-18 ImpB1-Test 9

ImpB2- a (Test Date: July 14, 2015; Contact-surface: 35mm Ply; Test 10)

The impact velocity was 5.42 m/s and the load was applied through a 25 mm Ply plate was used. The ply plated was displaced from its original position following the impact. Flexural cracks were observed in the tensile zone underneath the plate (see Fig. 3.19). No shear-plug-like cracks were formed. Few inclined cracks were observed near the point of load application and the supports, propagating from the compressive zone to the bottom region of the specimen. The crack profile was not symmetrical, and its formation was concentrated in the central region.

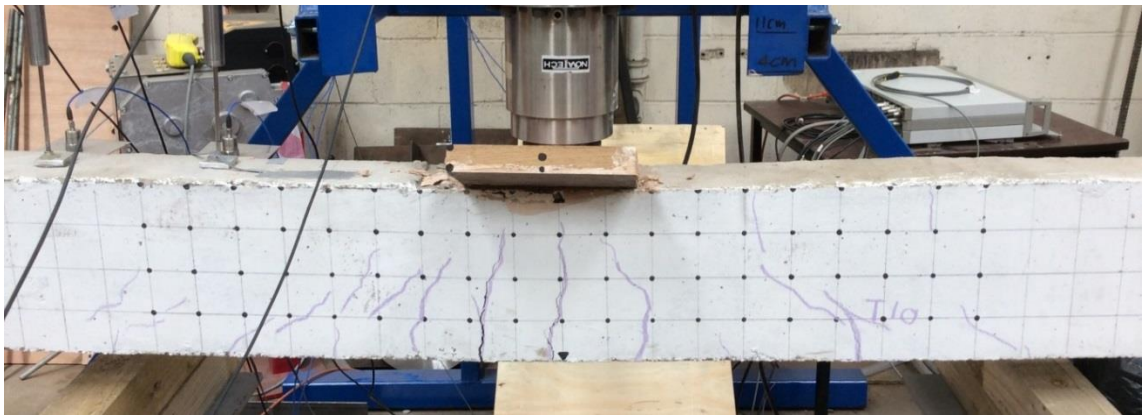

Figure 3-19 ImpB2-1-Test 10

ImpB2- a (Test Date: July 15, 2015; Contact-surface: 35mm Ply; Test 11)

The steel mass was dropped from a height of 2 m to the mid-span of the specimen, the beam was pre-damaged, and the impact velocity was 6.26 m/s. The impact load was applied through a 35 mm ply. Significant localised damage was observed near the point of load application. The existing cracks widened, particularly those flexural cracks that developed in the tensile region underneath the impact load. Diagonal cracks also developed around the localised damage in the compressive zone, they propagated away from the region to the tensile zone, and however, their length was not significant (see Fig. 3.20). As a result of the localised damage, the concrete cover was disintegrated. New flexural cracks appeared in the compressive zone between the mid-point and the beam supports. New inclined cracks developed propagating away from tensile zone penetrated into the compressive region; however, the new cracks concentrated near the mid-point of the beam specimen. The regions close to the support where the previous inclined cracks developed remained unaffected. Ch6 was detached.

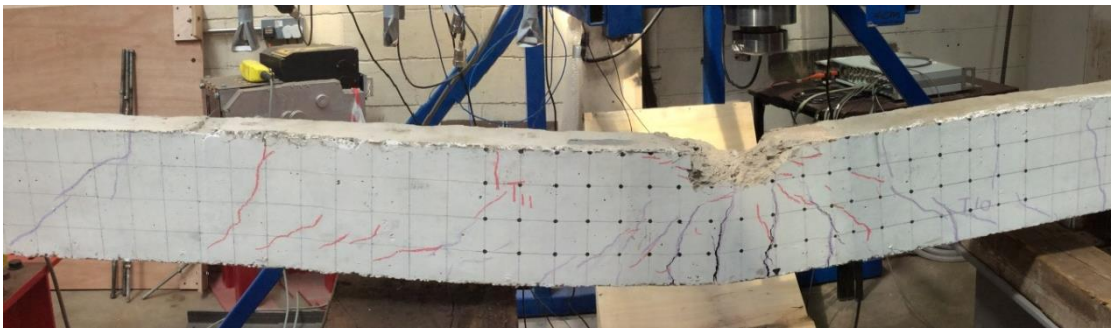

Figure 3-20 ImpB2-1- Test 11

ImpB3- b (Test Date: July 17, 2015; Contact-surface: 35mm Ply and 1mm Aluminium; Test 12)

The pre-damaged specimen was subjected to impact force with a velocity of 6.26 m/s, a composite contact surface was used consisting of 1 mm aluminium plate and 35 mm ply. The aluminium plate was glued to the latter and was placed on top of the ply plate. A few flexural cracks developed in the tensile region of the beam; several inclined cracks propagated away from the tensile zone to the point where the load was applied. Flexural cracks also appeared in the compressive region of the beam. Slight scabbing occurs which was more significant in right half portion of the beam adjacent to the ply plate. The crack

profile was not symmetrical and the development of inclined cracks in right half portion of the beam was more apparent. Ch5 was detached (see Fig. 3.21).

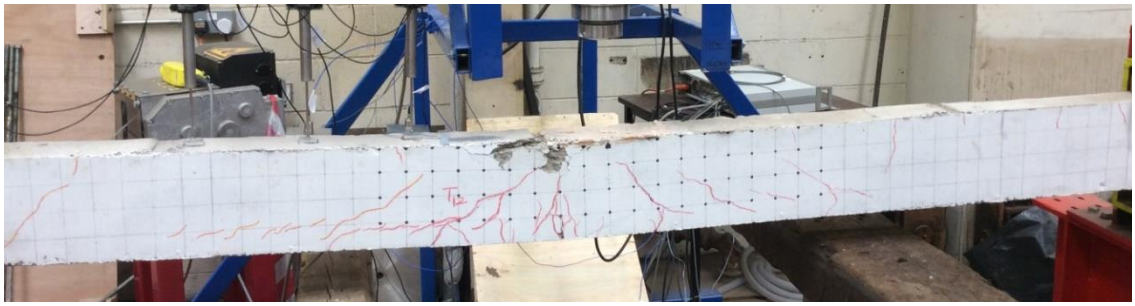

Figure 3-21 ImpB3-b-Test 12

ImpB3- b (Test Date: July 20, 2015; Contact-surface: 35mm Ply; Test 13)

The height of the impact was 1.5 meter leading to a total velocity of 6.26 m/s. The impact load was applied through a 35 mm ply. The existing localised damage (as a result of the previous impact) deteriorated, the compressive reinforcement was exposed, deflected and buckled (see Fig. 3.22). Scabbing was observed in the tensile zone on the left-half portion of the specimen. The flexural and inclined cracks opened further. The total deflection of the beam was more significant. Ch6 was detached; the quality of the recorded video was poor.

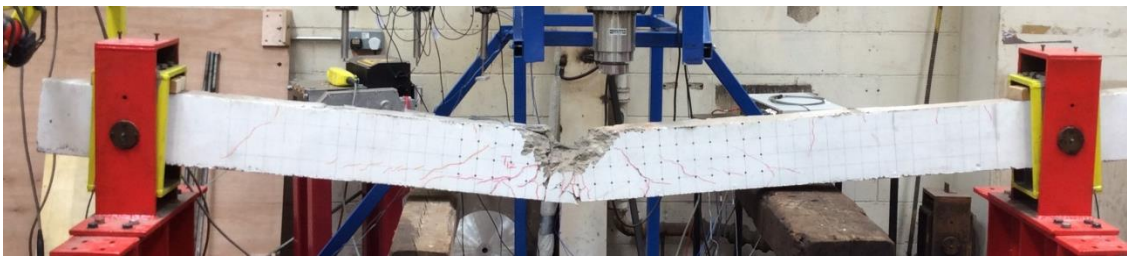

Figure 3-22 ImpB3-b-Test 13

3.7 STATIC TEST RESULTS (PRE-DAMAGED SPECIMEN)

In order to assess the residual load-carrying capacity of RC beam, specimens A2, B1 and B2, were tested under equivalent static loading. The test objects already suffered from impact-induced damage. The layout of the static test set-up has been already discussed in

section 5.8. The observed post-impact behaviour of the test objects subjected to equivalent static loading is summarised in the following section.

A2 (Test Date: March 2, 2015; 14)

Significant localised damage was observed near the point where the load was applied (i.e. pre-existing damage). The deflection of the beam increased significantly and the existing cracks in the tensile region of the beam specimen widened. The mid-span displacement was recording using only one dial-gauge placed underneath the mid-span of the beam. The concrete cover was disintegrated due to further localised damage and the compressive reinforcement was exposed and buckled, see Figs. 3.23-3.25 below. It should be noted that the curve shown in the figure does not start from zero, this may suggest that either a) the plate (which was used to distribute the applied force) was not fully in contact with the concrete surface and/or b) there was residual displacement in the beam as a result of being previously damaged. A comparison between un-damaged and damage load-deflection curve of specimen A2 is provided in section 3.9.

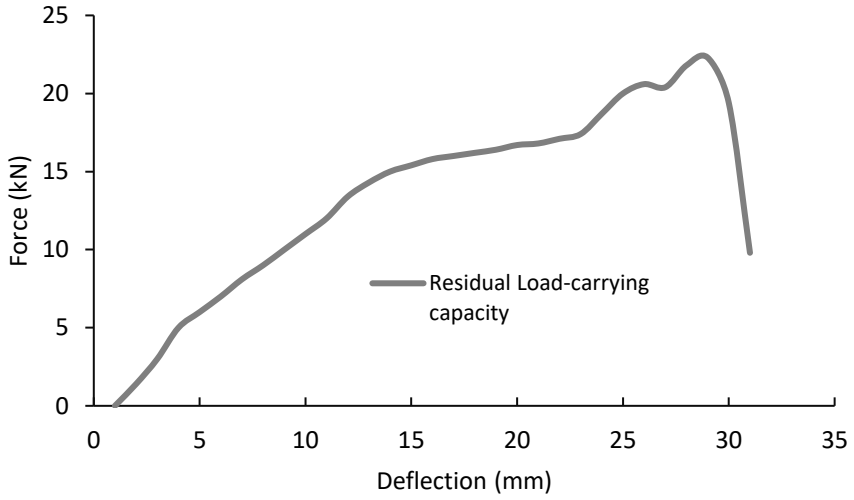

Figure 3-23 Static load-displacement (Test 14)

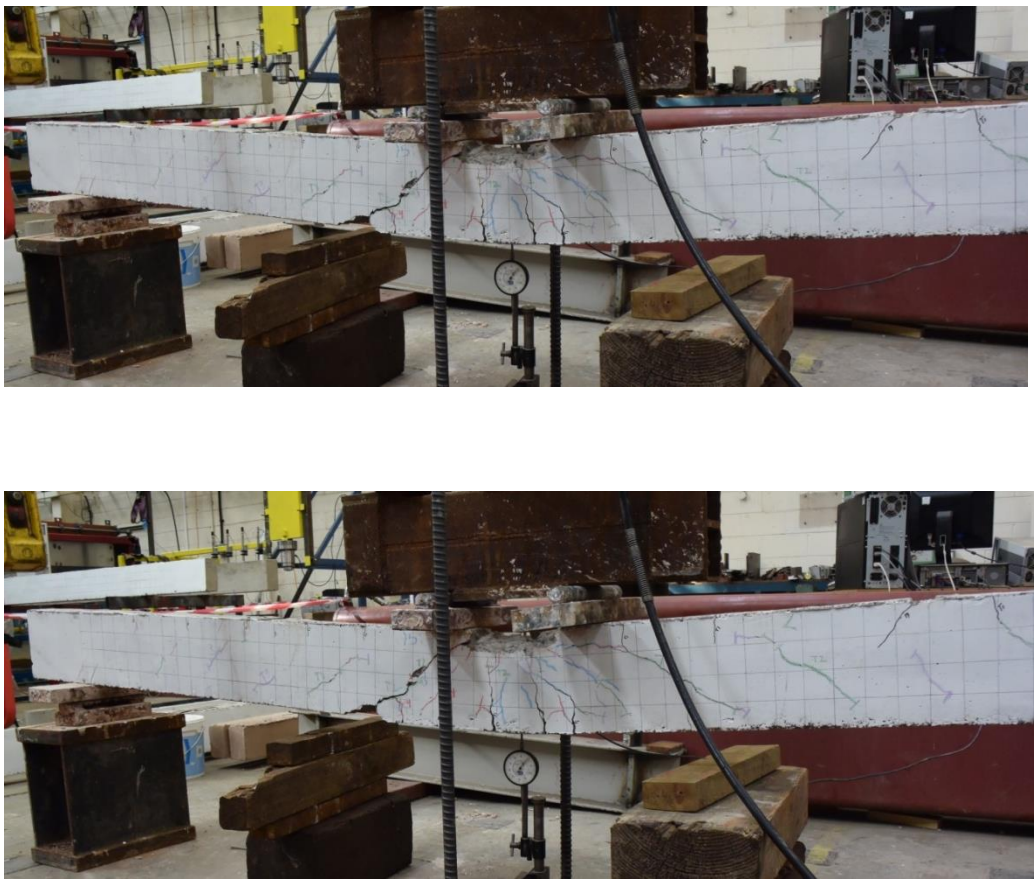

Figure 3-24 Specimen A2 (Top) prior to residual-static load application (Bottom) post static load application (Test 14).

Figure 3-25 Compressive reinforcement of A2-Test 14

A2 (Test Date: July 22, 2015; 15)

The deflection at the mid-span of the beam was recorded using dial gauges. Prior to the test, the existing flexural cracks in the tensile zone had a width of 5 mm, after the static test they widened to 7 mm. The width of the existing inclined cracks also increased. The deflection profile was not significant. The load-carrying capacity of the test object was

omitted as the damaged beam exhibited higher (residual) stiffness comparing to the undamaged specimen. This could be caused by applying the load too fast during the test or instrumentation (i.e. load cell) error.

B2 (Test Date: July 23, 2015; 16)

The concrete cover was disintegrated, inclined cracks penetrated deep into the damaged region (near the point of load application). The existing cracks widened the measured width of the flexural cracks in the tensile zone after the residual test was 5 mm, see Fig. 3.26.

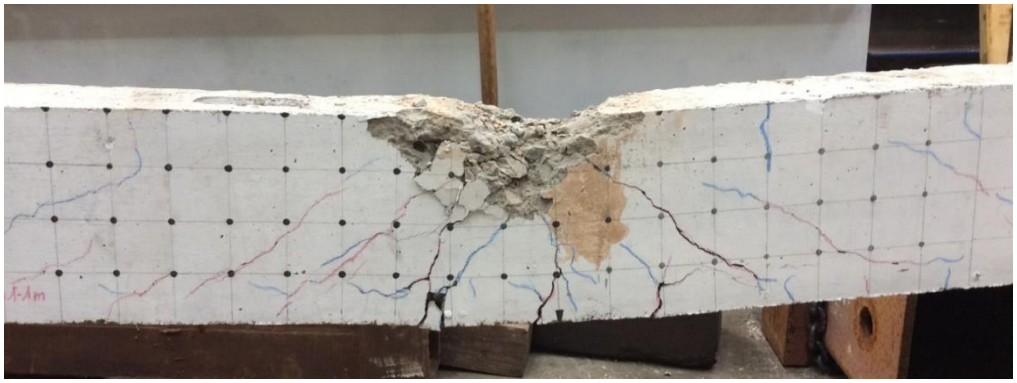

Figure 3-26 Test 16 following failure under static loading

3.8 BEHAVIOUR EXHIBITED DURING DROP-WEIGHT TESTING

During drop-weight testing emphasis is focused on recording certain aspects of the behaviour of the specimens throughout the loading process. These aspects include the impact and reaction forces generated, the displacement exhibited at specific points marked on the drop-weight and along the element span (see Fig. 3.4) as well as the values of strain developing locally in certain regions of the specimens. The cracking and deformation profiles exhibited by the specimen at different stages of the loading process as well as the mode of failure are also recorded as they provide an indication of the internal state of stress developing within the specimen. Depending on the type of pad used in the impact region (steel or ply) the impact tests performed can be categorised into two main groups; those generating high and medium (or moderate) values of loading rate ($\dot{P}$) and intensity ($maxP_d$) as shown in Table 5.

3.8.1 Impact force and support reactions

The curves presented in Figs. 3.27 and 3.28 show the variation of the impact and reaction forces recorded during the first 40ms (0.04s) of each impact (drop-weight) test, starting from just before the moment of contact between the impactor and the specimen and finishing when the values of the impact and reaction forces eventually become equal to a small fraction of their peak values. The curves describing the variation of the impact force with time reveal that it increases rapidly (immediately after the drop mass comes into contact with the specimen) to a maximum value and then quickly reduces. The overall duration of the impact force is less than 2ms and 10ms when conducting high intensity and moderate intensity impact tests respectively. It is interesting to notice that the form of these curves can be characterised by multiple peaks, likely to be associated with secondary impacts being exhibited between the specimens, the pads and the drop-mass during the loading process, as well as the cracking of the concrete medium in the impact region (scrubbing). The curves describing the time history of the reaction forces reveal that the latter forces start increasing with a delay compared to the contact forces generated in the impact region. This delay is associated with the time required by the stress waves, generated during impact, to reach the supports. It is also interesting to notice that the curves describing the time history of the reaction forces are characterised by multiple peaks due to the secondary impacts mentioned earlier and the oscillation exhibited by the specimen.

On the basis of the curves presented in Figs. 3.27 and 3.28 certain key values are established such as the peak values (intensity) of the impact ($maxP_d$) and reaction ($maxR_d$) forces generated during testing and the corresponding time at which these values are attained (t_P and t_R respectively), the average loading rate ($\dot{P} = maxP_d / t_P$) and the time interval (delay) between the peak impact and peak reaction force ($\Delta t_{P\text{-}R} = t_R - t_P$). These values are summarised in Table 5. It is noted that in some cases data is missing due to the instrumentation failing to trigger when conducting the impact tests (e.g. tests 6 and 8). In the latter cases, the emphasis is focussed on the information provided by the photographic evidence recorded by the HS camera.

In tests 5 to 9, 40mm (rigid) steel pads were used at the impact region (positioned between the steel drop-mass and the top surface of the specimens) and as a result the impact forces generated were characterised by higher values of loading rate and intensity (high-intensity impact tests) compared to those recorded from the tests conducted using plywood or 15mm thick steel pads (resulting in softer impacts; moderate intensity impact tests). The test data obtained from the high intensity impact tests reveals a considerable difference between the peak values of the impact ($maxP_d$) and reaction ($maxR_d$) forces associated with the large portion of the impact energy (introduced by the impactor) which is lost (absorbed/dissipated) due to the damage (cracking) suffered by the specimen. In the case of tests 2 to 4 and 10 to 13, the impact (contact) forces generated are characterised by lower values of loading rate and intensity (due to the use of softer pads). Furthermore, the recorded values of $maxP_d$ and $maxR_d$ are similar, denoting that the level of impact energy lost is significantly lower (compared to that lost during high-intensity impact testing) as the loads applied in the impact region are largely transferred, through the specimens, to the supports without significant losses. This suggests that higher values of loading rate and intensity result in higher levels of damage being sustained along the span of the specimens. It is also worth noticing that the delay ($\Delta t_{P\text{-}R} = t_R - t_P$) between the time at which $maxP_d$ and $maxR_d$ are attained increases as the intensity of the impact force and the level of damage sustained by the specimens also increases (see the results in Table 5 for tests 3 and 4 as well as 10 and 11). Increasing levels of cracking results in the stress waves, generated at the impact region, to travel at lower speeds through the concrete medium towards the supports due to the plane of the developing cracks essentially forming barriers to the stress wave. This is evidenced by the values of $\Delta t_{P\text{-}R} = t_R - t_P$ provided in Table 5 for tests 3 and 4 as well as 10 and 11.

In addition to the above, it is interesting to note that the impact force (P) generated during drop-weight testing appears to be primarily associated with the velocity with which the drop-mass collides onto the specimen as well as the pads used in the impact region and not with the physical state of the specimen and the level of damage sustained along its span. On the other hand, the values of the reaction forces (R) generated appear to be significantly affected by the level of damage sustained by the specimen as well as the mechanisms that are activated for transferring the applied loads to the supports. Based on the above it can be suggested that the peak value of the reaction force ($maxR_d$) in relation to the maximum impact force generated ($maxP_d$) – expressed by $maxR_d$ / $maxP_d$ – and the delay between

the time at which $maxP_d$ and $maxR_d$ are attained ($\Delta t_{P\text{-}R} = t_R - t_P$) can potentially serve as practical indicators of the physical state and the level of damage sustained by RC beam specimens during each drop test.

Table 5 Key values established based on the curves describing time-histories of the impact and reaction forces generated during each drop-weight test

	Test No.	Pad	H (m)	$maxP_d$ (kN)	t_I (ms)	$\dot{P}$ (kN/ms)	$maxR_{d,9}$ (kN)	$maxR_{d,10}$ (kN)	$maxR_{m,9}$ / maxPd	$maxR_{m,10}$ / maxPd	t_p (ms)	$t_{r,10}$ (ms)	$t_{r,9}$ (ms)	$\Delta t_{10}=t_r-t_m$ (ms)	$\Delta t_9=t_r-t_m$ (ms)
A1	1[a]	(Static)													
A2	2	15mm ply	0.5	29.6	4.90	6.04	11.3	15.9	0.38	0.54	2.9	10.54	9.67	7.64	6.77
	3	15mm ply	1	113.7	2.20	51.6	32.5	40.5	0.29	0.36	4.17	9.21	9.24	5.04	5.07
	4	15mm steel	1	112.3	4.66	24.09	45.4	47.3	0.40	0.42	2.1	12.81	12.23	10.71	10.13
	14[b]	(static)													
A3	5	40mm steel	1	267.0	0.52	509.5	40.31	37.0	0.15	0.14	0.36	7.76	7.93	7.24	7.41
	6	40mm steel	1.5	-	-	-	-	-	-	-	-	-	-	-	-
B1	7	40mm steel	1	367.1	0.265	1385.5	44.8	42.5	0.12	0.12	0.38	8.20	8.54	7.82	8.16
	8	40mm steel	1.5	-	-	-	-	-	-	-	-	-	-	-	-
	9	40mm steel	1	-	-	-	-	-	-	-	-	-	-	-	-
	15[b]	(Static)													
B2	10	35mm ply	1.5	118.6	1.97	60.2	56.9	49.6	0.48	0.42	4.05	9.66	9.91	5.61	5.86
	11	35mm ply	2	117.6	4.30	27.3	60.8	55.2	0.52	0.47	4.65	10.72	10.58	6.07	5.93
	16[b]	(Static)													
B3	12	35mm ply	2	-	-	-	-	-	-	-	-	-		-	-
	13	35mm ply	2	124.5	1.93	64.5	57.4	58.8	0.46	0.47	2.18	10.92	10.89	8.74	8.71

[a] Static Test
[b] Residual Static Test

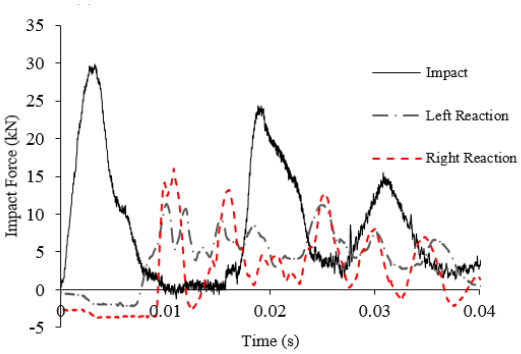

(a) Test 2 –A2

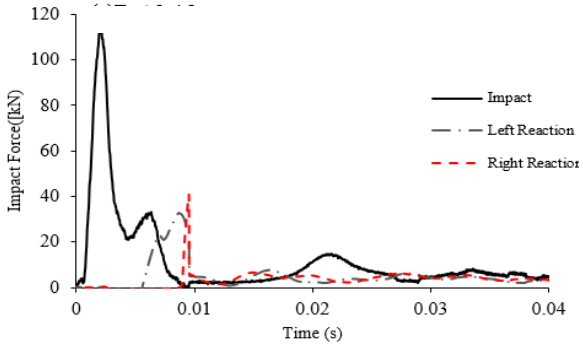

(b) Test 3 –A2

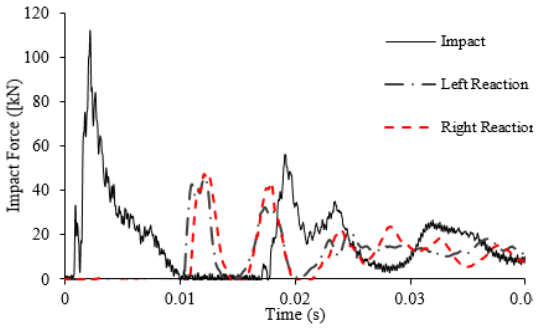

(c) Test 4-A2

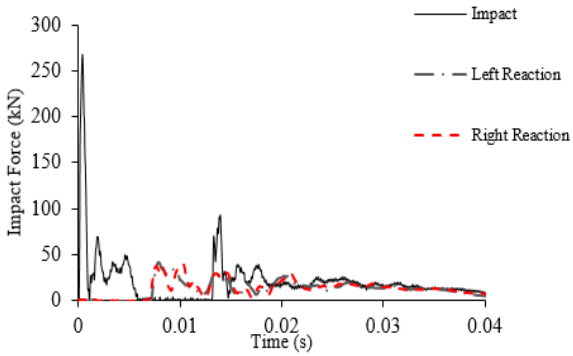

(d) Test 5-A3

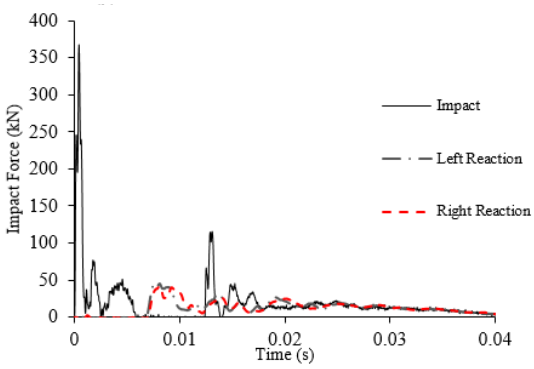

(e)Test 7-B1

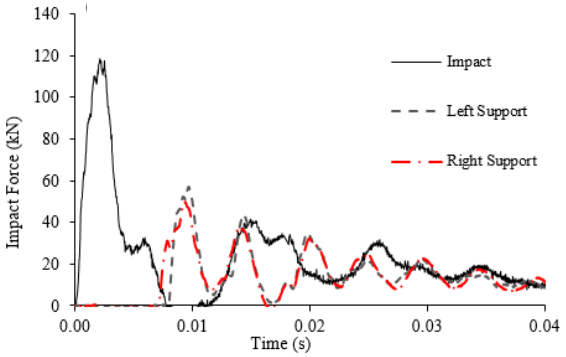

(f)Test 10-B2

Figure 3-27 Impact and reaction force-time histories recorded during different drop-weight tests at different loading rates and intensities (Tests 2-10).

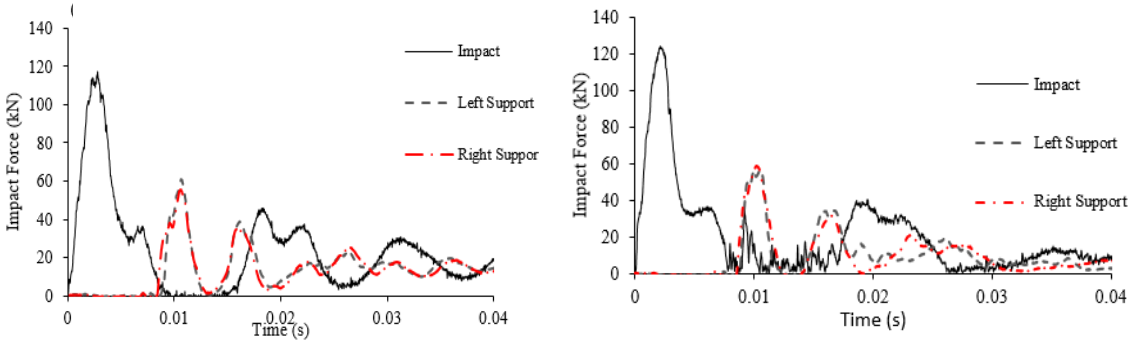

(a)Test 11-B2 (b)Test 13-B3

Figure 3-28 Impact and reaction force-time histories recorded during different drop-weight tests at different loading rates and intensities (Tests 11 and 13).

3.8.2 Displacement data and deformation profiles

During testing the vertical displacement exhibited at specific points along the span of the specimen in the region between the locations at which the load is applied (mid-span) and the left-hand-side support is measured through the combined use of LVDTs (see Fig. 3.29) and the high speed (HS) camera. A total of four LVDTs (Ch-8 to Ch-11, see Fig. 3.4) were used in Tests 2 to 9 and three (Ch-9 to Ch-11, see Fig. 3.4) for Tests 10 to13 (as one of the LVDTs – Ch-8 – was damaged during test 4). Figs. 3.29 show a comparison between the displacement time histories measured by the LVDT (at a distance of 370 mm from the mid-span) with that obtained from the HS camera for tests 5, 7 and 10. Good agreement is observed between the two sets of measurements. The curves in Fig. 3.29 reveal that after initial contact between the impactor and the specimen, the deflection exhibited by the specimen increases to a maximum value and after fluctuating for a short period of time it obtains its residual value (the latter essentially depending on the level of damage sustained). It is interesting to notice that maximum deflection is attained well after the peak impact load is achieved. Figs. 3.30 to 3.33 show the time-histories of (i) the displacement recorded by the LVDTs along the span of the beams (see Ch-6 to Ch-9 in Figs. 3.4 and 3.5) and (ii) the contact force generated at the impact region. From the latter curves, it is clear that when the maximum impact load ($maxP_d$) is attained the deflection exhibited by the RC beam, even at mid-span, is a small fraction of the maximum displacement exhibited by the same specimen after the impact load is applied. This confirms that during the initial stages of the loading process (prior to attaining $maxP_d$) the specimens exhibit localised response with

the impact load applied essentially being resisted by a small portion of the beam's span concentrated in the mid-span region.

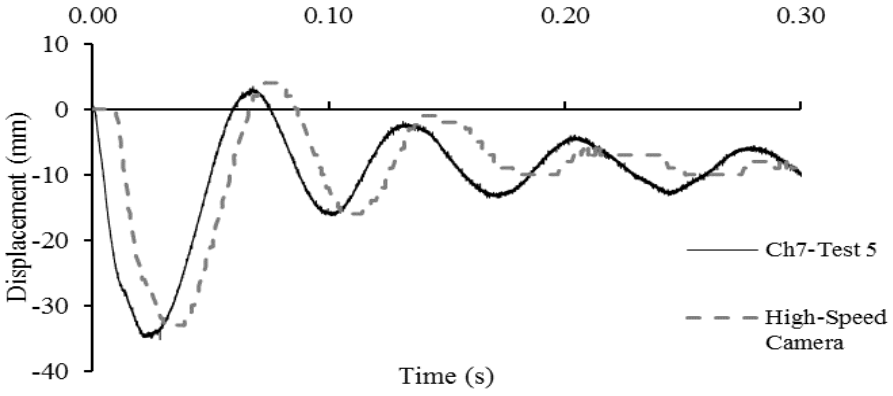

(a)

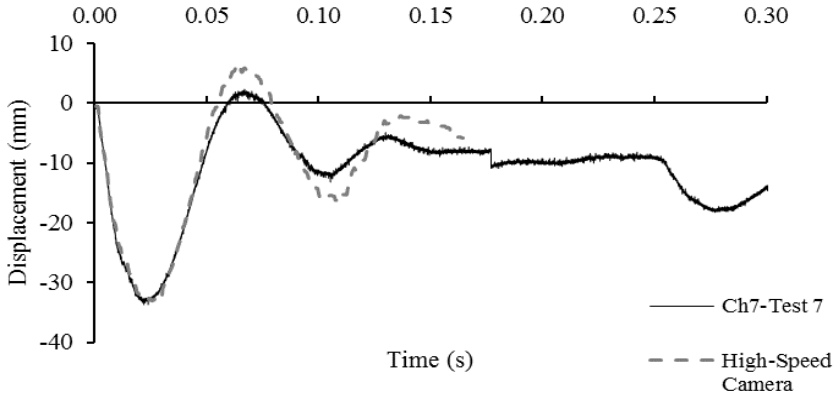

(b)

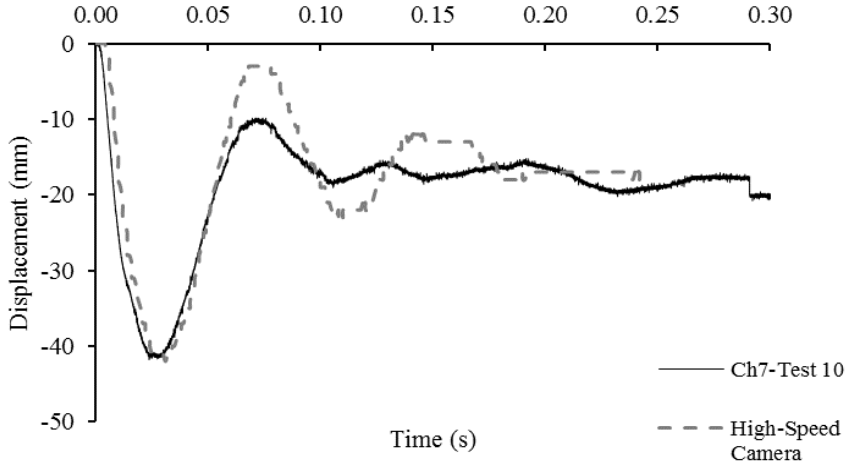

(c)

Figure 3-29 Correlation between the displacement time histories obtained during dropped-weight testing from the LVDT (CH-7) and the analysis photographic evidence obtained from the HS camera for (a) Test 5, (b) Test 7 and (c) Test 10.

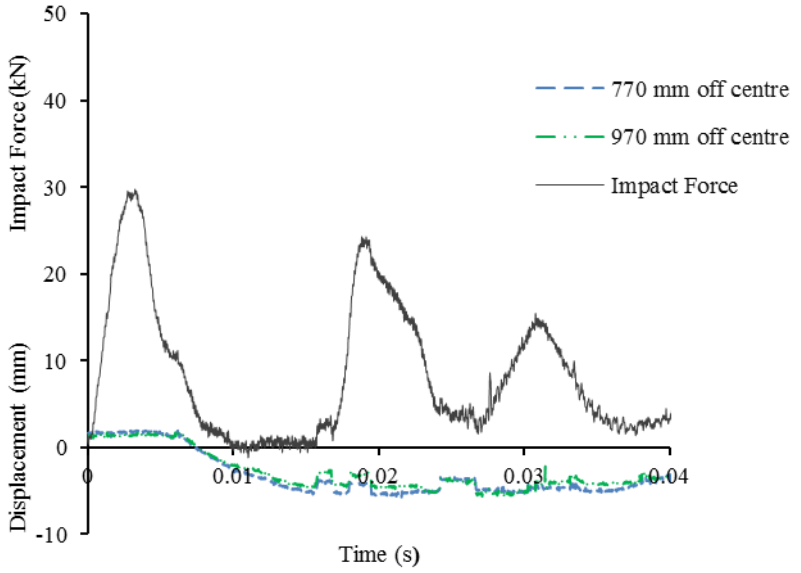

(a) Test 2

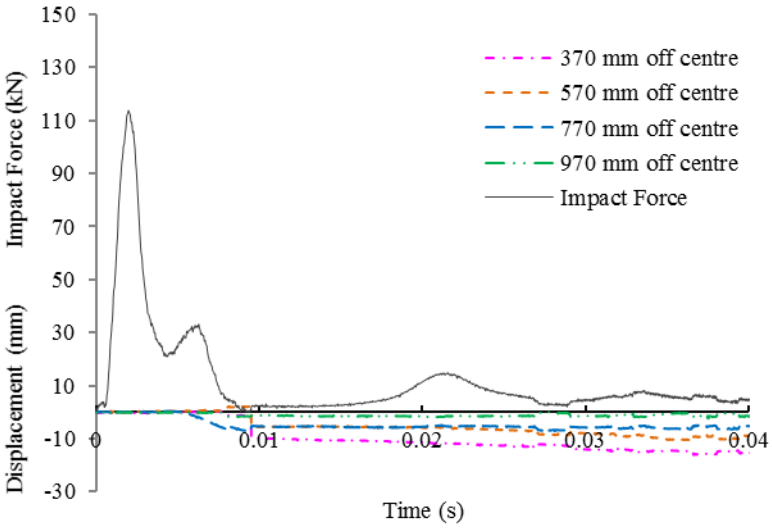

(b) Test 3

Figure 3-30 Impact force and displacement time histories recorded during Tests 2 and 3.

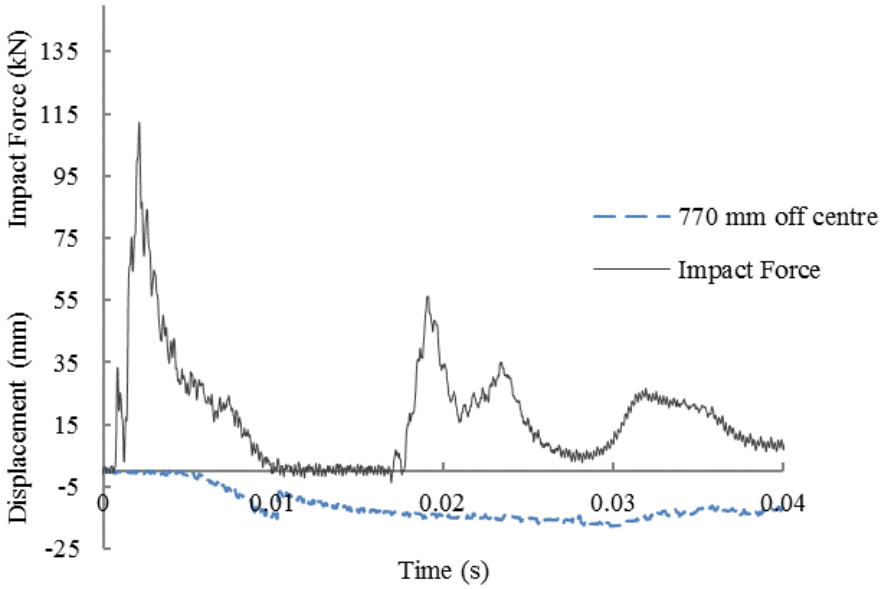

(a) Test 4

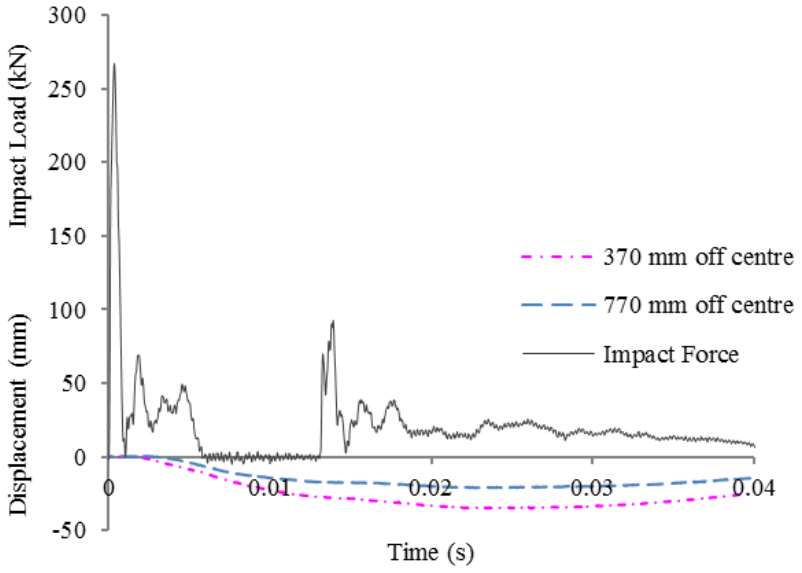

(b) Test 5

Figure 3-31 Impact force and displacement time histories recorded during tests 4 and 5.

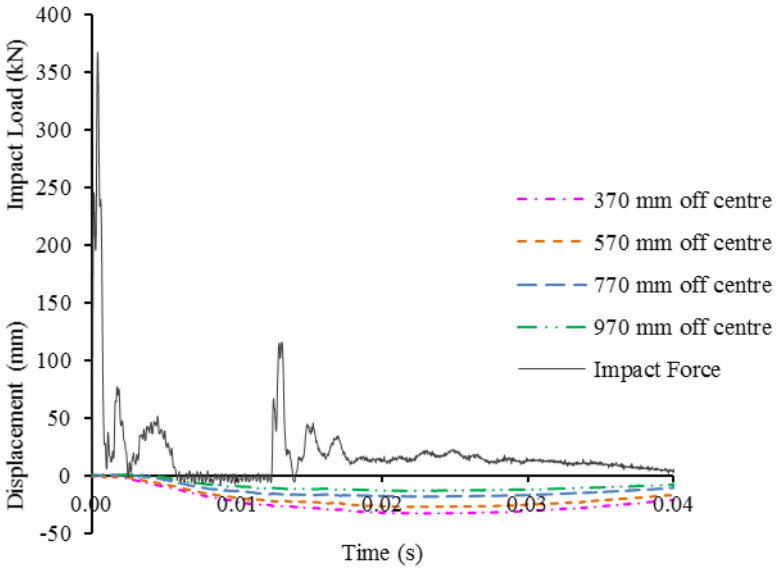

(a) Test 7

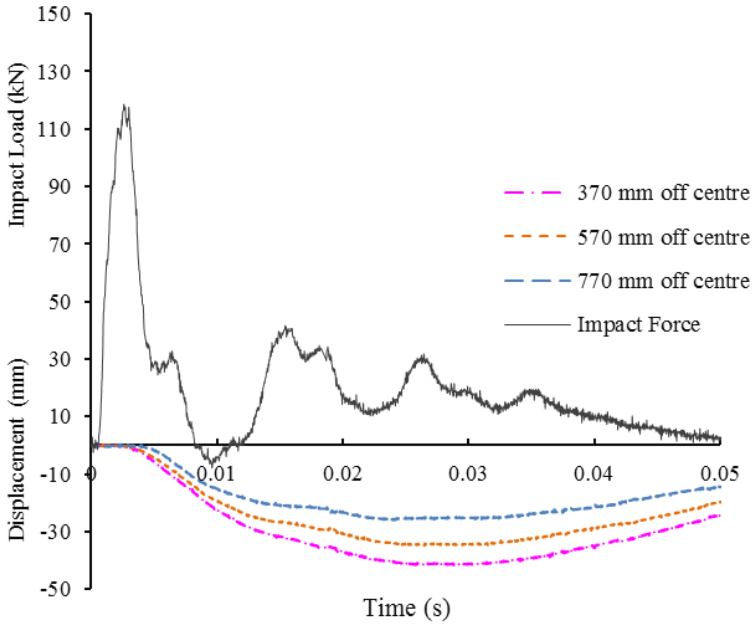

(b) Test 10

Figure 3-32 Impact force and displacement time histories recorded during tests 7 and 10.

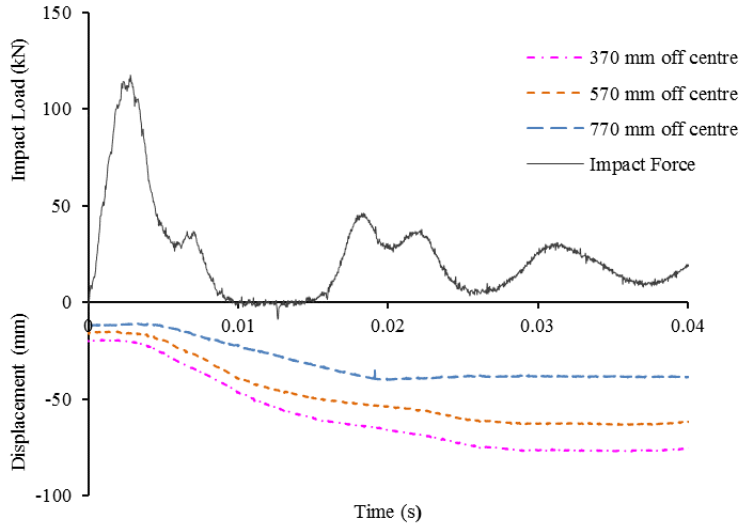

(a) Test 11

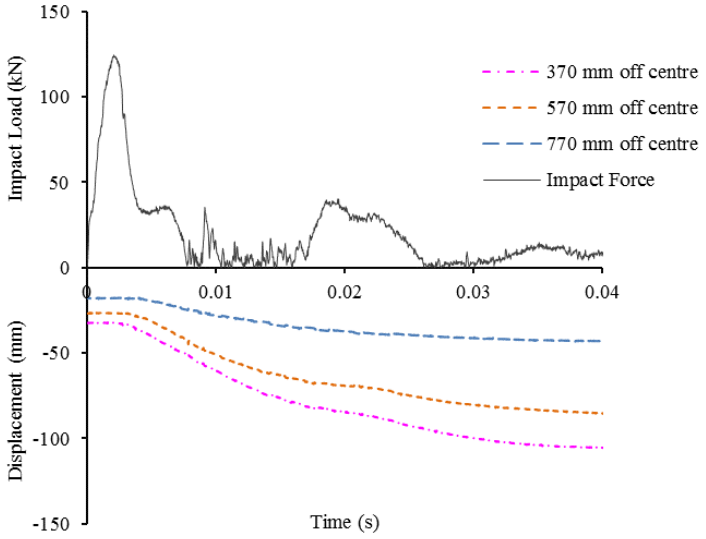

(b) Test 13

Figure 3-33 Impact force and displacement time histories recorded during tests 11 and 13.

The variation of the vertical deflection measured during tests 5,7,10 and 11 (through the combined used of the high-speed camera and the LVDTs) at different points along the portion of the span of the beam between the mid-span (impact) region and the left-hand side support are presented in Fig. 3.34 (a- d). These curves once again demonstrate that the problem at hand is a wave propagation problem as the points closer to the impact (mid-span) region start moving first. As the stress waves move away from the impact region the points located further away from the mid-span also start moving. This provides evidence

of the localised response exhibited by the RC beams specimens immediately after the initial contact between the impactor and the specimen.

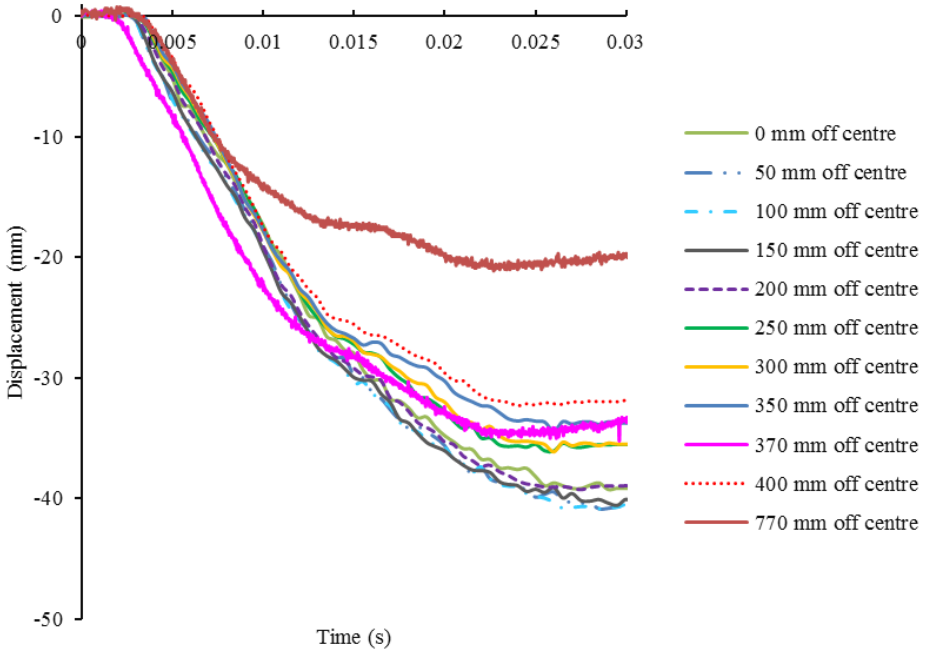

(a) Test 5

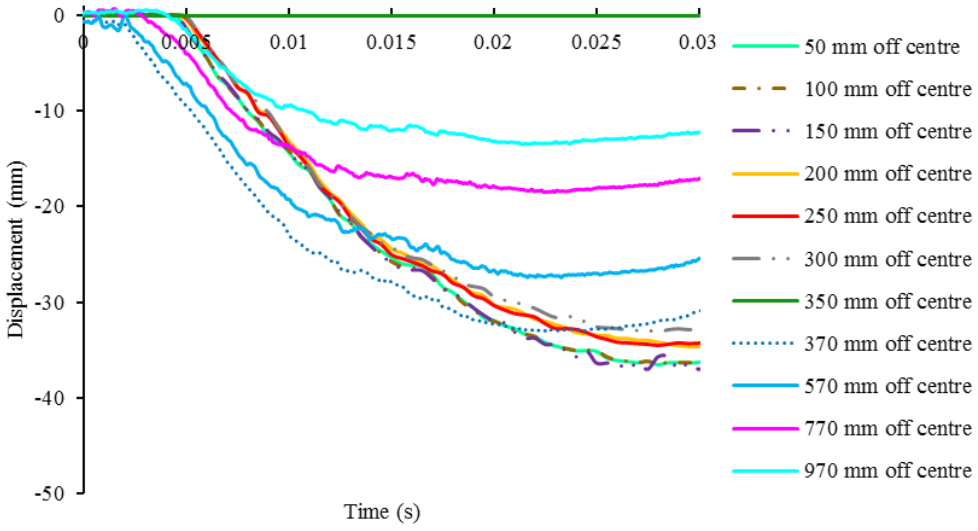

(b) Test 7

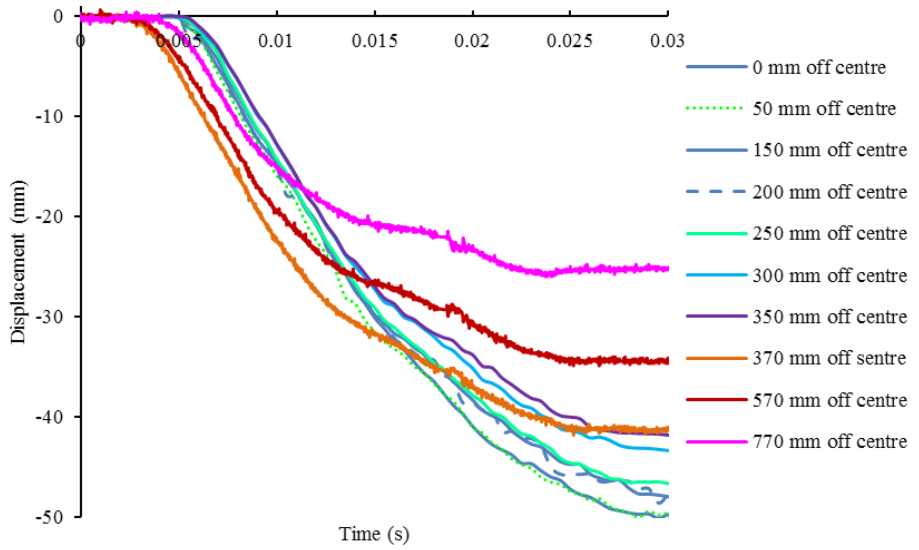

(c) Test 10

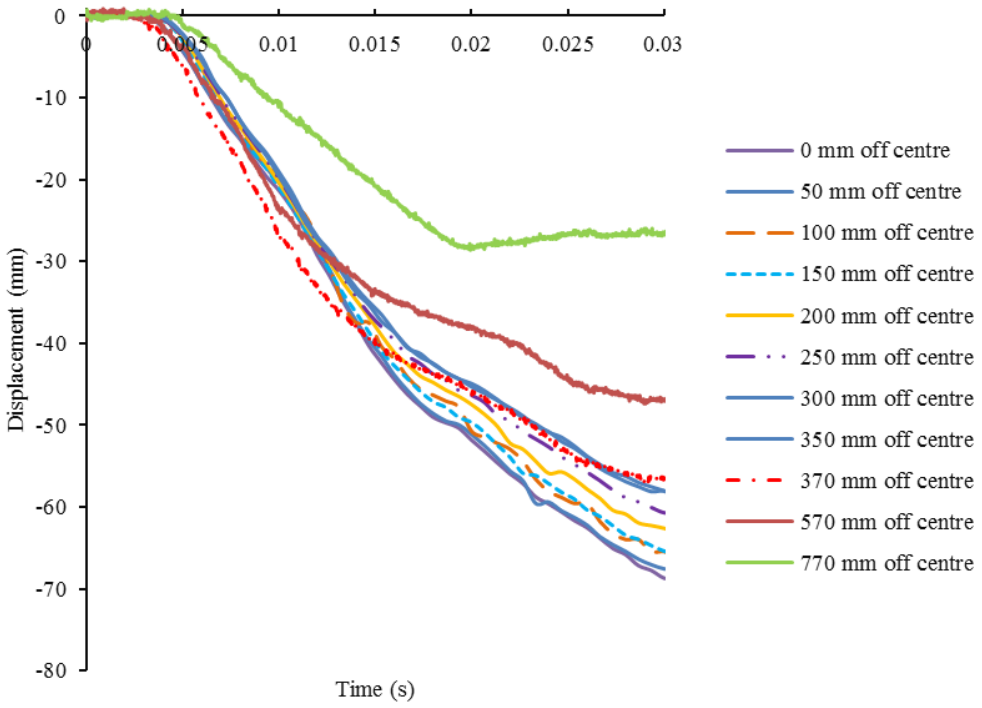

(d) Test 11

Figure 3-34 Variation of the vertical deflection of a series of points at different locations along the beam span established through the combined use of the HS camera and LVDTs for the case of different impact tests

The localised response can be also observed form the deformation profiles (presented in Fig. 3.35) exhibited along the span of the beam between the mid-span and the right-hand-side support when subjected to high (tests 5 and 7) and medium (tests 10 and 11) intensity impact testings.Some inconsistencies associated with the deflection values presented in Fig. 3.36 are considered to be associated with the ability of the photographic technique to always provide accurate measurements for small values of deflection (of the order of a few mm) and as a result, only the general trends of these deformation profiles are considered herein. On the basis of these deformation profiles it can be seen, yet again, that during the initial stages of the loading process (until $maxP_d$ is attained) the RC beams exhibit localised response since essentially only the portion of the span of the specimen close to the impact region reacts to the imposed load. However, when the maximum value of deflection at mid-span is attained (well after $maxP_d$ is reached) the full length of the specimens deforms exhibiting global response. It is interesting to note that for the case of Test 7, which is characterised by higher values of intensity and rate of impact loading, the localised response is more prominent as the maximum values of deflection associated with $maxP_d$ are considerably higher compared to those established in the case of Test 10 (the latter being characterised by lowers levels of intensities and rates of loading).

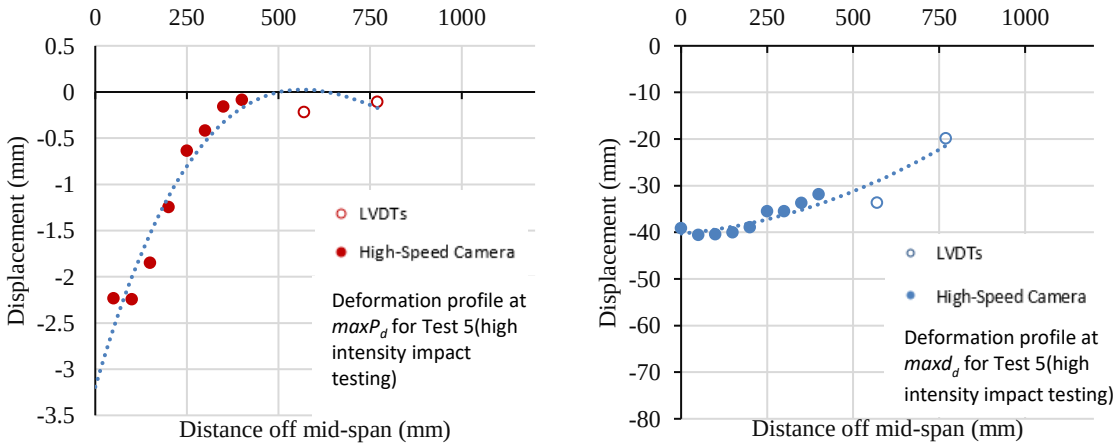

(a) Test 5

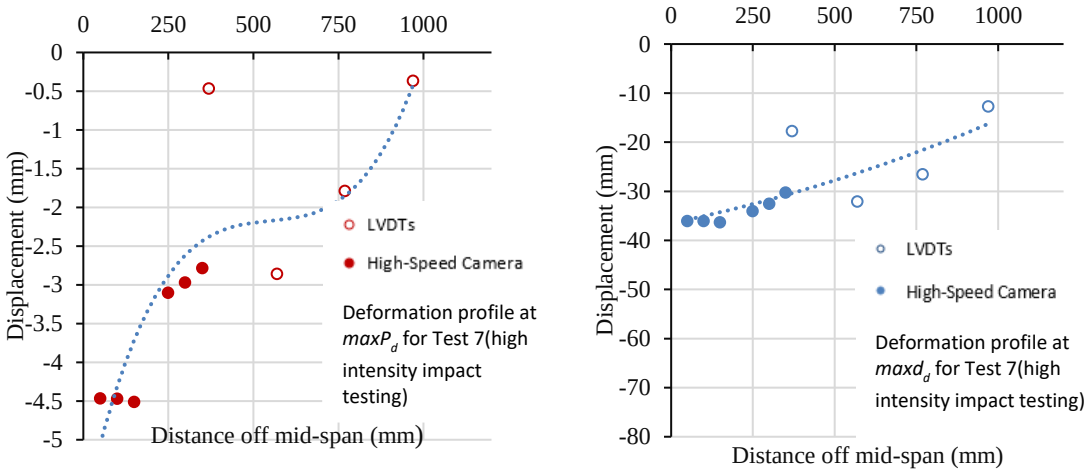

(b) Test 7

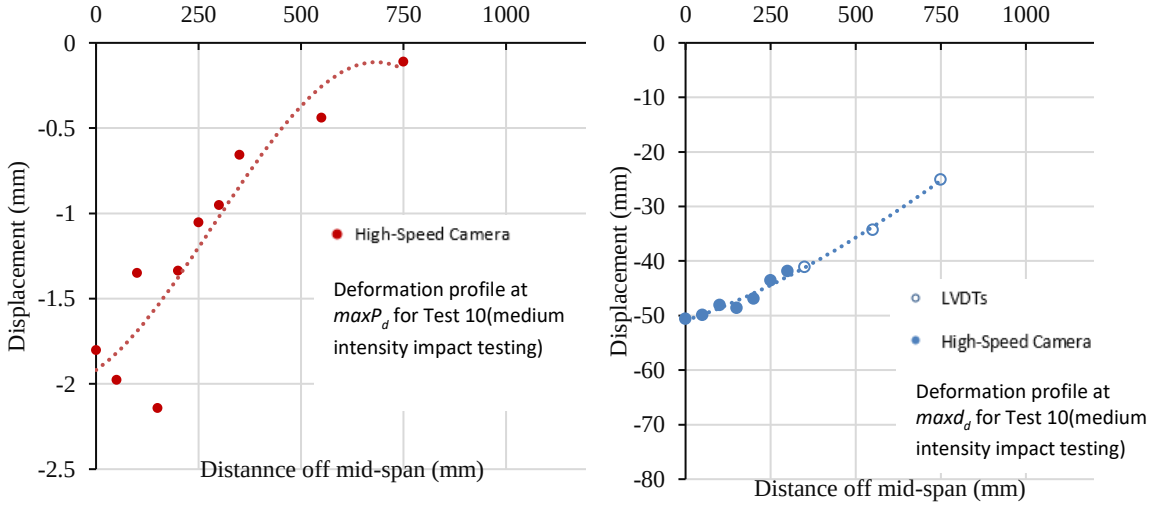

(c) Test 10

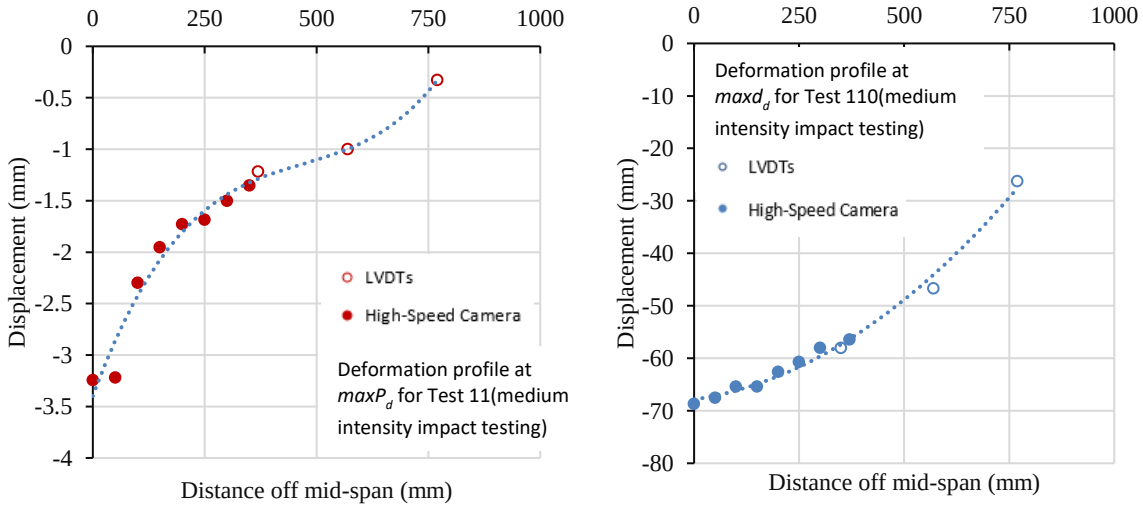

(d) Test 11

Figure 3-35 Deformation profile exhibited by the RC beam specimen established through the combined use of a high-speed camera and LVDTs when $maxP_d$ and $maxd_d$ are attained for the case of Tests 5,7,10 and 11.

3.8.3 Strains and strain rates

The variation of the strain values recorded by the strain-gages (Ch-13 and Ch-14, see Figs. 3.4 and 3.6) located on (or close to) the top surface of the beam (acting in compression) at a distance of 260 mm form mid-span are presented in Fig. 3.36 for Tests 5,7,10 and 11 respectively. The associated strain rate values were also calculated (see Fig. 3.37). It is interesting to observe that the latter strain rates (associated with compression) are small, not exceeding a maximum value of 0.6 s^{-1}.

The strains and the associated strain rates (acting normal to the specimen cross-section) were also measured along the height of the beams at the mid-span region. This was achieved by analysing (digitising) the photographic data obtained from the HS camera in order to establish the change in distance between a number of points marked in the form of a grid (see Figs. 3.38 and 3.39) on the side surface of each specimen tested. The strains acting normal to the specimen cross-section at the impact (mid-span) region and the associated strain-rate values calculated for Tests 5 and 7 (associated with high-intensity impact testing) and Tests 10 and 11 (associated with medium intensity impact testing) are presented in the form of time-histories in Fig. 3.40.

The curves depicted in Fig. 3.39 and 3.40 reveal that the peak values of strain are attained a few msec after the impactor comes into contact with the specimen, approximately at the same time at which the impact load achieves its peak value ($maxP_d$) and not when the maximum deflection ($maxd_d$) is achieved (well after $maxP_d$ is attained). This essentially suggests the development of higher internal actions during the initial stages of the loading process when localised response is exhibited. It is interesting to notice from the curves in Fig. 3.39 that positive values of strain (associated with tension) are exhibited throughout the whole height of the specimen cross-section. Negative values of strain (associated with compression) are only measured by the strain-gauges close to the top surface of the specimen (see Fig. 3.38) even during the initial stages of the loading process. It is noted that the photographic method employed herein cannot be used to measure the values of strain between points G and H as the displacement exhibited by these points are very small. This shows that cracking develops and propagates deep in the compressive zone even before the impact load attains its peak value.

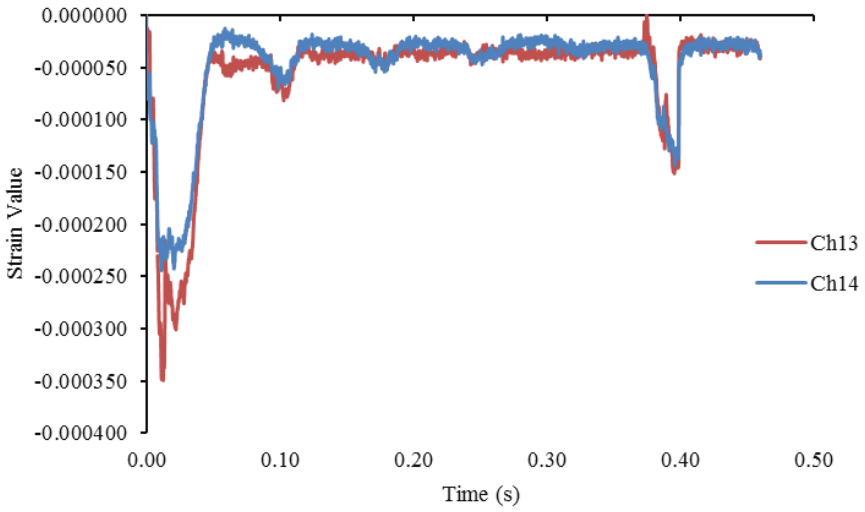

(a) Test 5

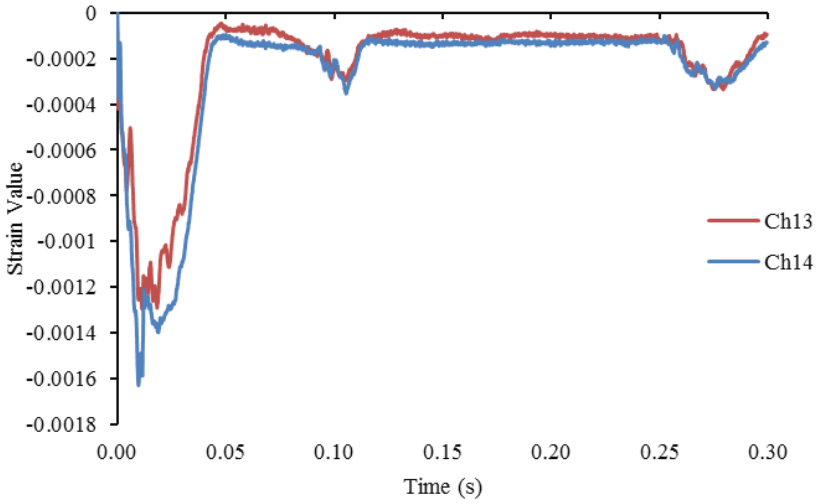

(b) Test 7

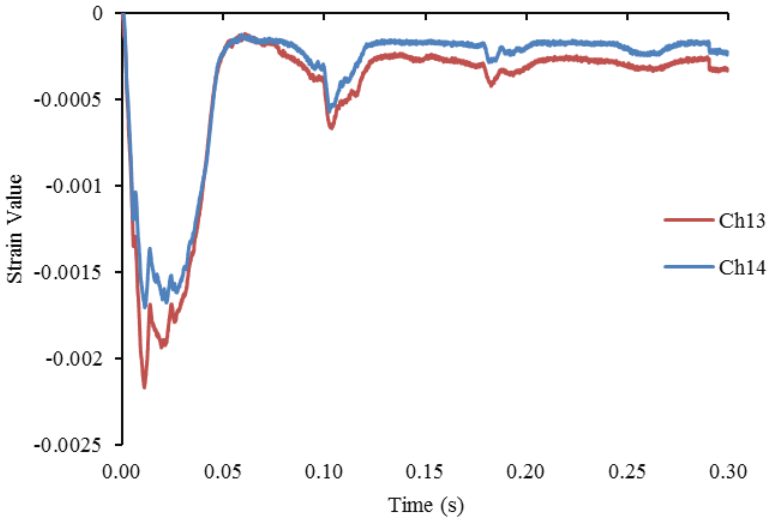

(c) Test 10

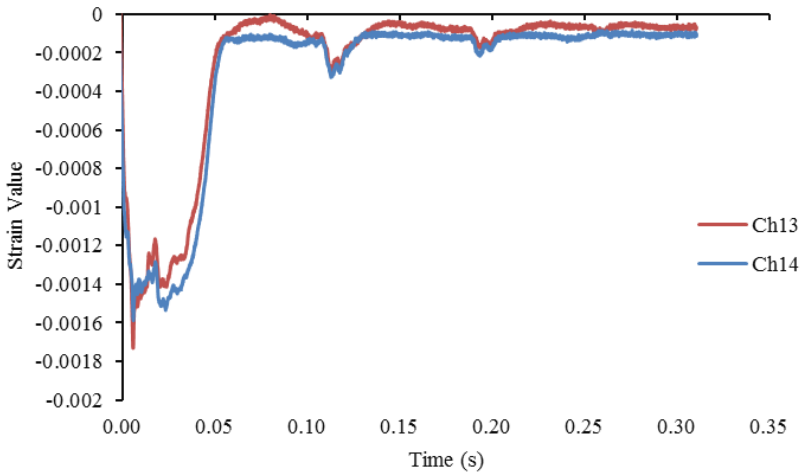

(d) Test 11

Figure 3-36 Variation of strain measurements obtained from the strain gauges during impact testing.

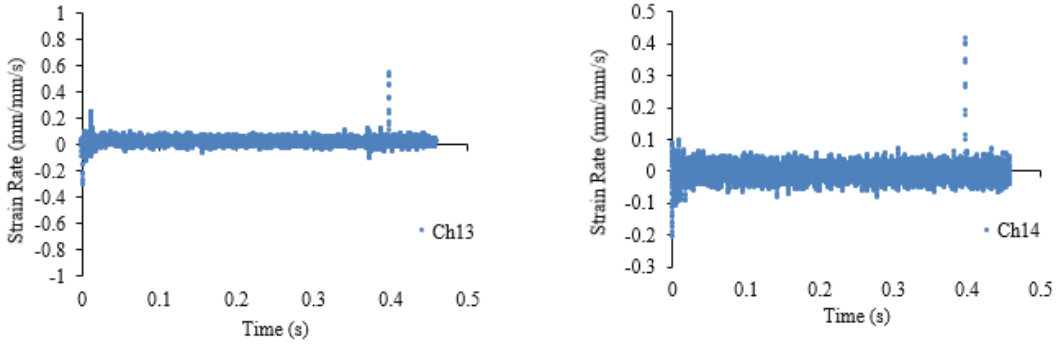

(a) Test 5

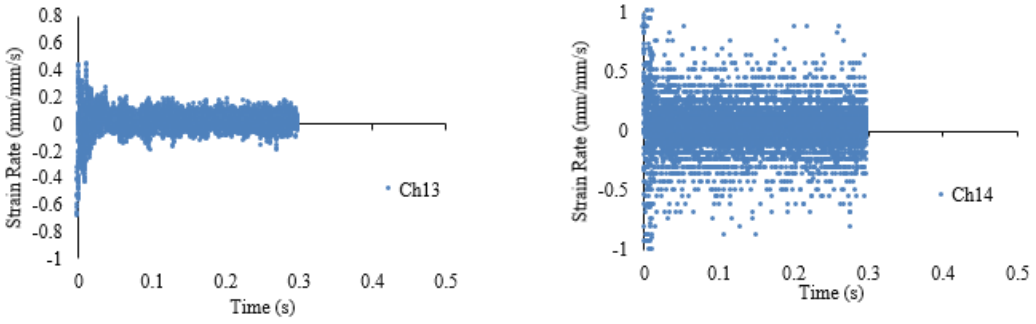

(b) Test 7

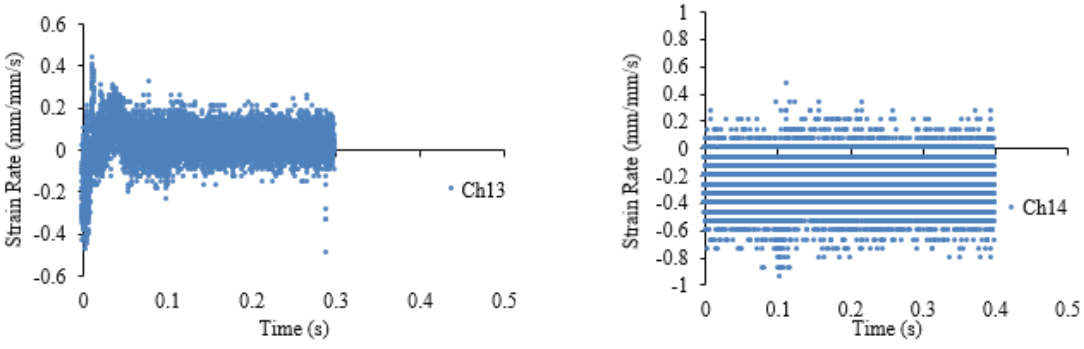

(c) Test 10

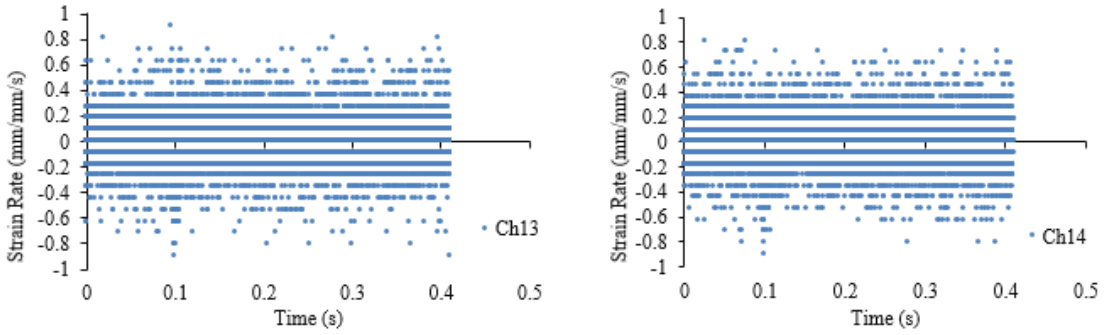

(d) Test 11

Figure 3-37 Variation of strain-rates measurements obtained from the strain gauges during impact testing.

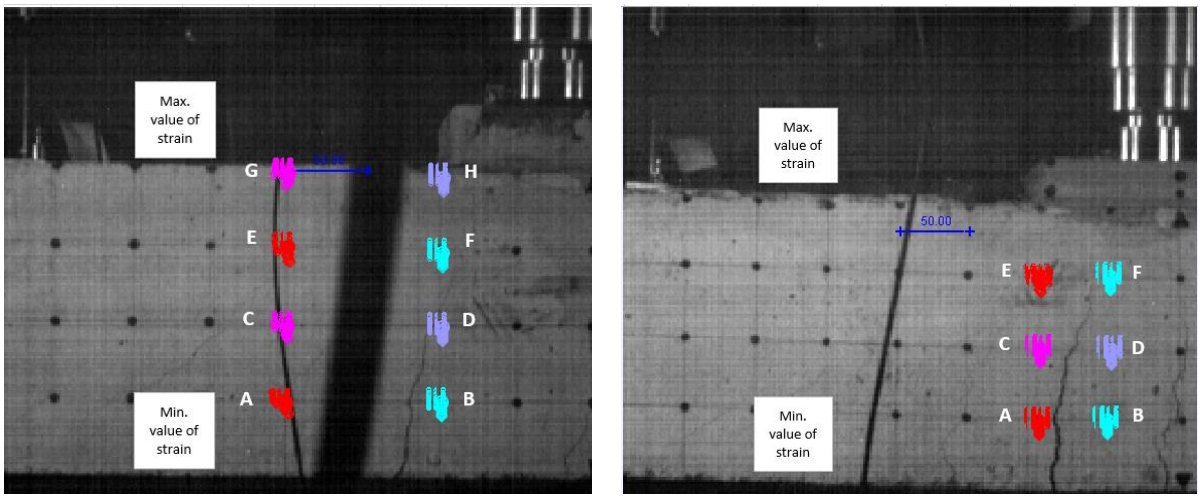

(a) Test 5 (high loading rate)

(b) Test 10 (low loading rate)

Figure 3-38 Locations at which the strain and associated strain rates are calculated along the element height at mid-span (impact region) in the case of (a) Test 5 (similar to Test 7) and (b) Test 10 associated with the application of high and medium intensity impact loading respectively.

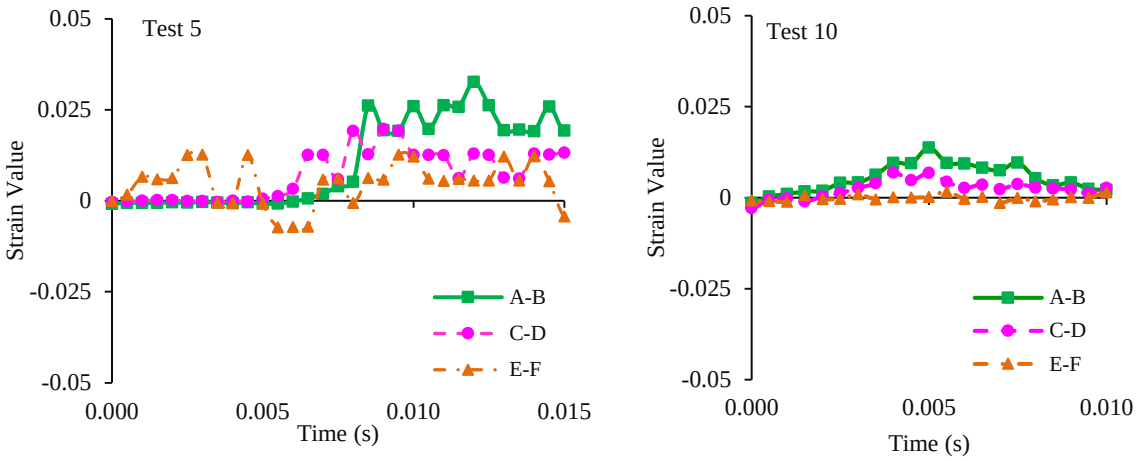

(a) Test 5 (high loading rate)

(b) Test 10 (low loading rate)

Figure 3-39 Curves describing the time histories of strain along the height of the specimen's cross-section close to the impact (mid-span) region between the points presented in Fig. 3.38 for (a) Test 5 and (b) Test 10.

The curves presented in Fig. 3.40 are also used to estimate the values of the strain-rate exhibited at the top (acting in compression, see Fig. 3.40a and c) and bottom (acting in tension, see Fig. 3.40b and d) surface of the specimen at the mid-span region. The values of the strain-rate have been obtained by measuring the change in the strain values in Fig. 3.35 (between two points) with respect to time. The maximum values of the strain rate are 0.6 sec^{-1} to 10 sec^{-1} at the top and bottom surface of the beam respectively for Test 10 (medium intensity impact testing) while these values increased significantly to 0.4 sec^{-1} and 20 sec^{-1} in the case of Test 5 (high-intensity impact test). Nevertheless, it is important to point out that the high tensile values of strain rate observed in Test 5 are mainly associated with the development of flexural cracking in the mid-span region that penetrated deeply into the compressive zone during the initial stages of the loading process (i.e. before $maxP_d$ is attained). As a result, it could be suggested that high values of strain-rate in the region of the specimen acting in tension reflect the rate at which the cracks widen rather than the actual deformation of the concrete medium itself.

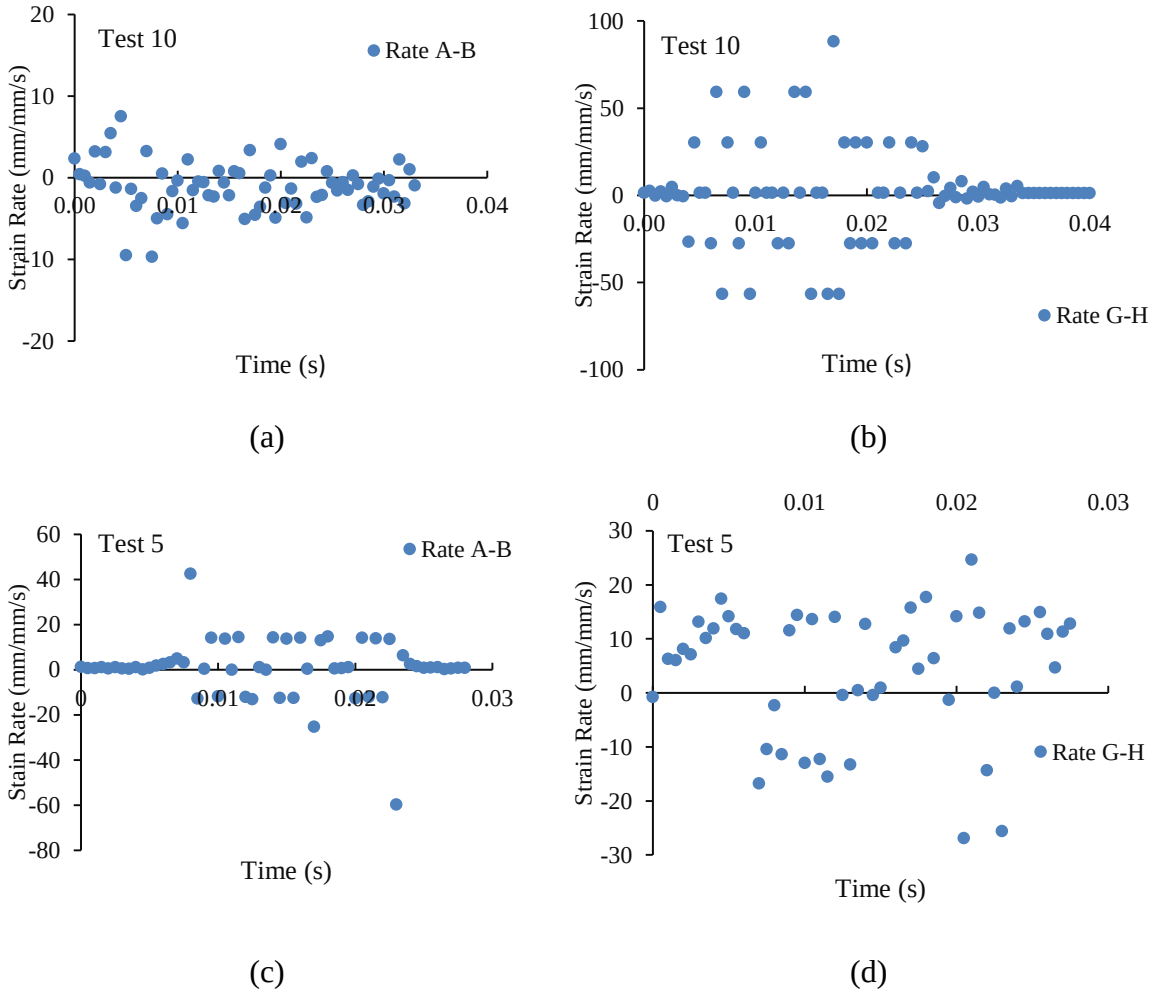

Figure 3-40 Variation with time of the strain-rate exhibited at the top (between points G and H) and bottom (between points A and B) face of the beam at mid-span for (a) Test 5 and (b) Test 10.

3.8.4 Cracking process and exhibited mode of failure

Frames obtained from the high speed (HS) camera at different stages of the loading process during high (tests 7) and moderate (test 10) intensity impact testing are presented in Fig. 3.41 and 3.42 respectively. The high-speed camera focuses on the left-hand side portion of the subject specimens, between the mid-span region and the left support. The frames presented in Fig. 3.41 show the cracking process exhibited immediately after the impactor comes into contact with the top surface of the RC beam at mid-span. From these photos, it is observed that flexural cracks form and quickly penetrate deep into the compressive zone very early in the loading process, prior to the contact (impact) force attaining its peak value ($maxP_d$). This can be seen from Fig. 3.34 which shows the variation with time of the contact force (generated in the impact region) and the deflections measured by the LVDTs located along the span of the beam. From these curves, it is clear that when the maximum impact load ($maxP_d$) is attained the deflection exhibited by the RC beam is a small fraction of the

maximum deflection exhibited by the specimen after the impact load is applied. The fact that cracking is exhibited early in the loading process, prior to maxP_d being achieved, confirms (once again) that the specimen exhibits localised response with only a small portion of the beam span, concentrated in the mid-span region, reacting to the imposed load.

Under static loading all specimens considered in this study are predicted to exhibit ductile behaviour characterised by distributed flexural cracking gradually penetrating deeply into the compressive zone with increasing levels of applied load, ultimately resulting in a ductile, flexural type of failure. Under impact loading, however, the cracking developing is more localised, exhibited primarily around the mid-span region (the area where the impact load is applied) often resulting in a more brittle and sometimes explosive form of failure. Furthermore, another set of cracks initiate at the upper face of the beams, at a certain distance from the mid-span, which extend vertically downwards towards the specimens' bottom face (see Fig. 3.43 to 3.46). These crack patterns are in line with the results of previous experimental (Hughes & Spiers 1981, Miyamoto et al. 1989, Kishi et al 2001 and 2002, May & Chen 2006, Saacti & Vecchio 2009) and numerical (Cotsovos et al. 2008, Cotsovos & Pavlović 2012) work and essentially define the region of the RC beam (effective length, L_{eff}) reacting to the imposed impact load.

After the maximum impact force (maxP_d) is attained (i.e. t_p = 0.38 msec and 4.05 msec for tests 7 and 10 respectively, see Fig. 3.41 and 3.42), cracks that have developed up to this stage continue to increase in width and further extend into the compressive zone as the deflection of the RC beam continues to increase due to inertia. In some cases, the cracking sustained results in extensive disintegration of the concrete medium resulting in the RC beams to depend on residual (post-failure) mechanisms for transferring the applied load to the supports. When conducting consecutive drop-weight tests on the RC beam specimens, cracks that form during the initial test continue to widen and extend with every drop test, resulting in an increase in residual displacement, ultimately leading to the collapse of the specimen (see Fig. 3.43 to 3.46). As a result, it can be suggested that the cracking forming during the first impact appears to be critical concerning how the specimen will behave during the following impacts. Examples of crack patterns forming on specimens A3, B1, B2 and B3 (see Tables 1 and 5) after being subjected to consecutive drop-weight tests are

shown in Fig. 3.43 to 3.46. Based on the above it becomes evident that it is difficult to establish when the specimens have actually failed (i.e. stopped behaving as RC member and started depending on residual load mechanisms for transferring the applied load to the supports). Therefore, the peak load measured during each test should not be confused with the load-carrying capacity of the RC members studied.

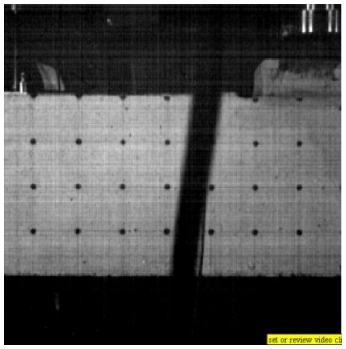

(immediately before contact)

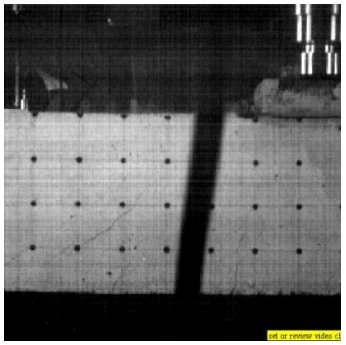

t_p= 0.38 msec (at $maxP_d$)

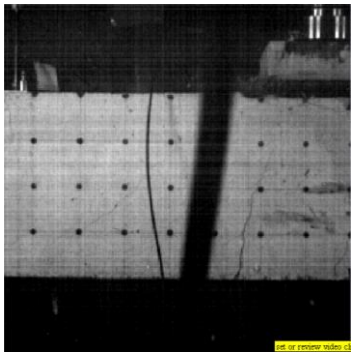

t =1msec (uplift of the impactor)

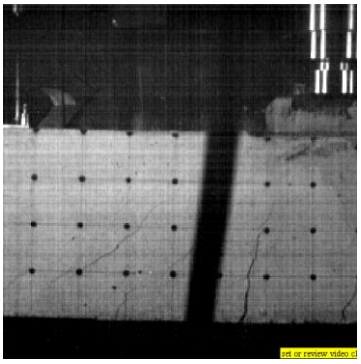

$t_{d,max}$ =22 msec (at maximum mid-span deflection)

Figure 3-41 Cracking process that the specimen undergoes throughout the loading process during Tests 7 (high-intensity impact testing)

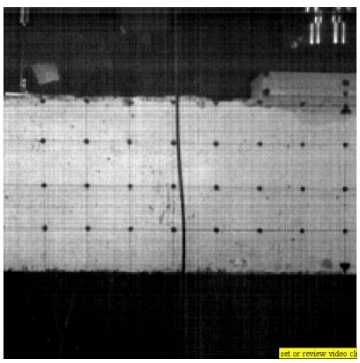

(pre-contact)

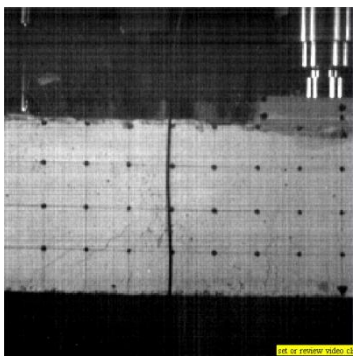

t_p=4.05 msec

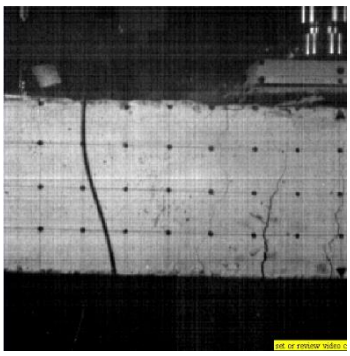

t=8.5 msec (uplift of the impactor)

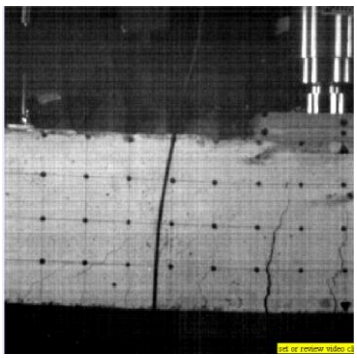

t_{d_max}=28.msec (at maximum mid-span deflection)

Figure 3-42 Cracking process that the specimen undergoes throughout the loading process during (a) Tests 7 and (b) 10 (moderate intensity impact testing)

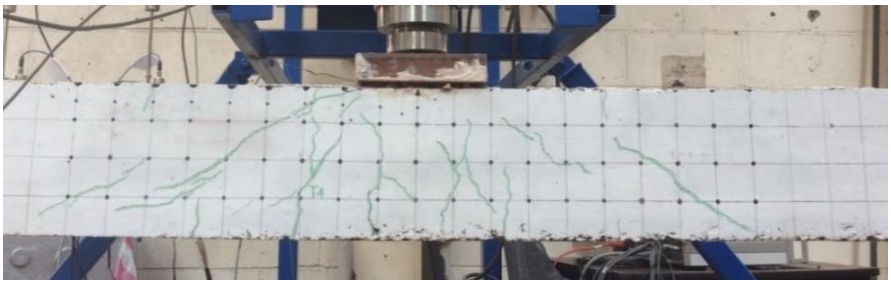

(a) 1st impact

(b) 2nd impact

Figure 3-43 Cracking exhibited by specimen A3 after (a) the first (Test 5, see Table 5) and (b) the second drop test (Test 6, see Table 5)

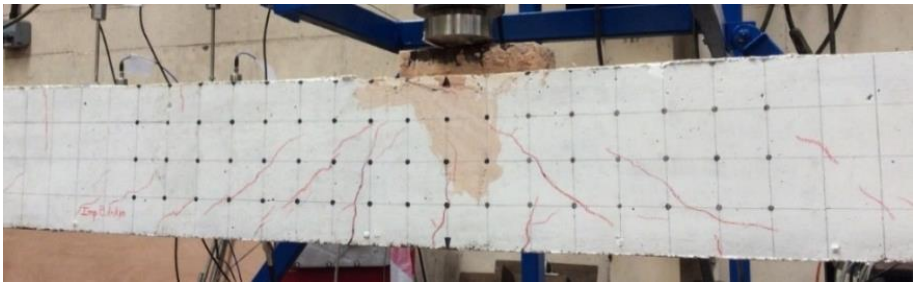

(a)-1st impact

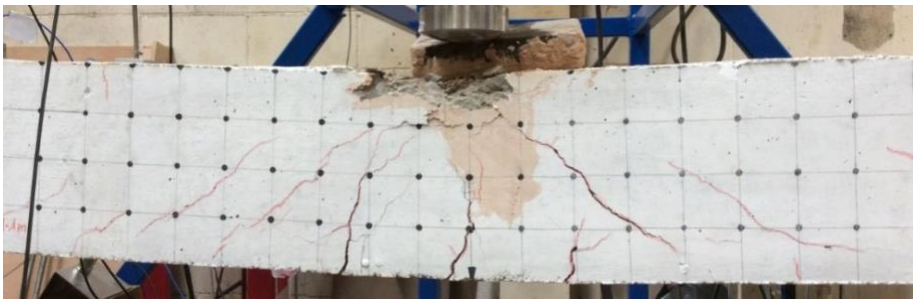

(b)-2nd impact

(c)-3rd impact

Figure 3-44 Cracking exhibited by specimen B1 after the (a) first (Test 7, see Table 5), (b) second (Test 8, see Table 5) and (c) third drop test (Test 9, see Table 5)

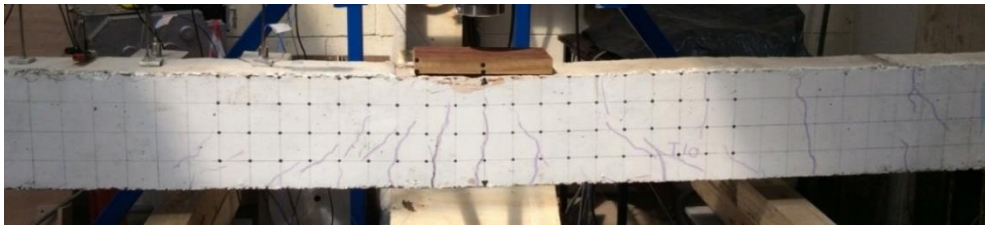

(a)-1st impact

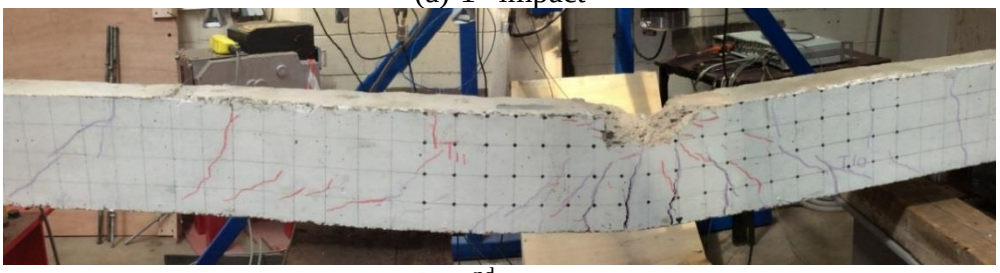

(b)-2nd impact

Figure 3-45 Cracking exhibited by specimen B2 after the (a) first (Test 10, see Table 5) and (b) second drop test (Test 11, see Table 5)

(a)-1st impact

(b)-2nd impact

Figure 3-46 Cracking exhibited by specimen B3 after the (a) first (Test 12, see Table 5) and (b) second drop test (Test 13, see Table 5)

3.9 BEHAVIOUR OF PRE-DAMAGED SPECIMENS UNDER STATIC LOADING

In order to assess the overall behaviour exhibited by the RC beams after being subjected to multiple drop-weight tests, specimens A2, B1 and B2, are tested under equivalent static loading applied monotonically to failure as described in section 3.2. The curves in Fig. 3.47 show the relationship between the applied load and the deflection exhibited at mid-span for specimen B2. The figure also includes the load-deflection curve for the undamaged specimen A1 for purpose of comparison. It should be noted that any initial (residual) deflection that the specimens had prior to static testing is presently ignored. As already described in section 4, specimen A1 exhibited ductile behaviour, with failure occurring after yielding of the longitudinal tensile reinforcement bars at mid-span and the formation of extensive flexural cracking along its full span that ultimately led to the loss of load-carrying capacity due to the failure of the compressive zone. The pre-damaged specimens exhibited a flexural but brittle mode failure. During the consecutive impact tests, the latter specimens suffered extensive cracking in the contact area (scrubbing) resulting essentially in a reduction of the specimen cross-section at the mid-span (impact) region and exposing the longitudinal compressive reinforcement bars. As a result, during static testing, the compressive force developing due to bending at mid-span is sustained by the compressive reinforcement rather than concrete which has essentially disintegrated and may only be capable of providing some support to the steel bars against buckling. Eventually, this

support diminishes, and the compressive reinforcement suffers buckling resulting in a flexural, yet brittle mode of failure. It may be noted that the damaged specimens B1 and B2 exhibited higher load carrying capacities than specimens A1 (undamaged) and A2 (damaged) due to the error in the data recorded, hence omitted from the figure. It should also be noted that specimens B1 and B2 were significantly deformed prior to them being subjected to static testing (see Fig. 3.45b and 3.46b). Therefore, their ability to undertake the applied load may also be attributed to post-failure mechanisms for transferring the applied load to the supports.

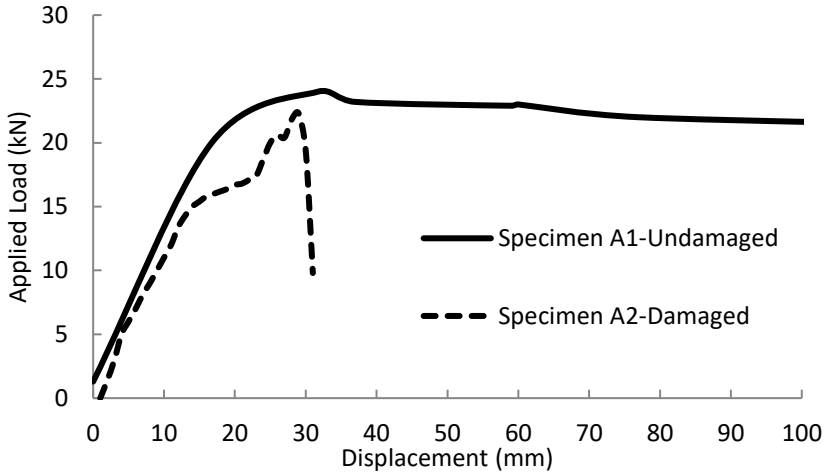

Figure 3-47 load-displacement curves describing the behaviour between un-damaged (A1) and pre-damaged (A2, B1 and B3) specimens when subjected to static four-point bending tests.

3.10 DISCUSSION-DESIGN IMPLICATIONS

The data presented in Fig. 3.48 have been extracted from Cotsovos & Pavlović (2008[a,b,c]). They have been obtained from tests carried out on concrete prisms under uniaxial compression and tension, respectively, through the use of the Split Hopkinson Pressure Bar (SHPB) apparatus and describe the variation of concrete strength with the rate of loading. From the figures, it can be seen that an increase in specimen strength is exhibited once certain thresholds of strain rate are surpassed. These are approximately 100 s-1 and 10 s-1 for uniaxial compression and tension, respectively. Comparing these thresholds with the values of strain rate characterising RC behaviour under drop-weight loading – presented in Fig. 3.37 – shows that strain-rate effects are unlikely to result in an increase of concrete strength that could, in turn, affect beam structural behaviour.

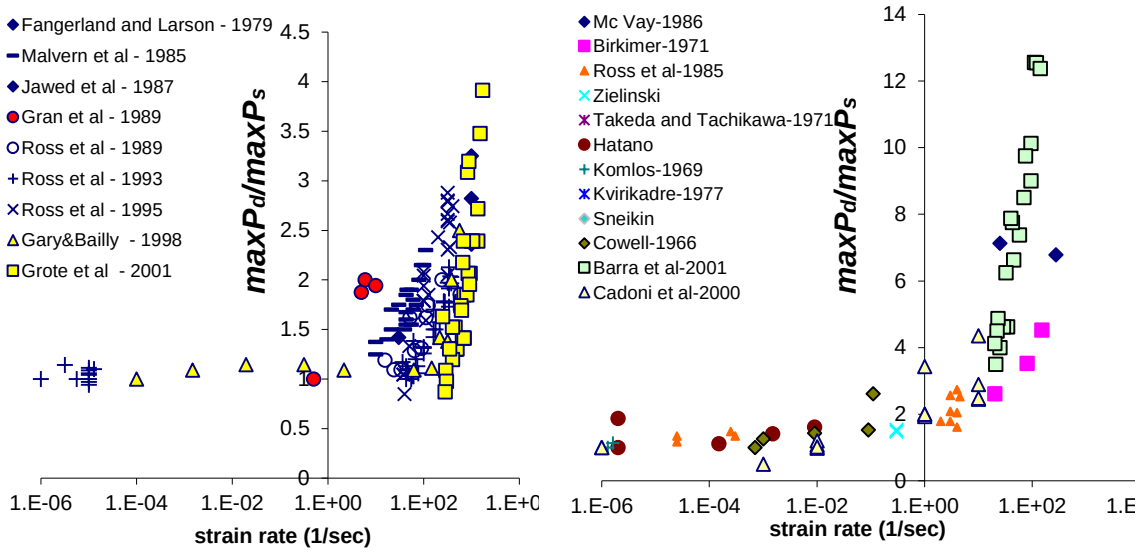

(a) (b)

Figure 3-48 Experimental data obtained from experiments conducted on plain concrete specimens subjected to high rates of uniaxial (a) compression and (b) tension loading

It is also of interest to note that, as discussed in 3.8.1 and shown in Fig. 3.34, the impact force attains its peak value soon after contact of the drop-weight with the beam. Once this load value is attained, from the deformation profiles of the beams shown in Fig. 3.35, it is can be seen that deflection reduces rapidly with the distance from mid-span and becomes practically zero well before the supports. Moreover, as indicated in Figs. 3.43 and 3.44, the location at which the deflection diminishes to zero is marked by the presence of a vertical crack which initiates at the top face of the beam and extends downwards. Therefore, it would appear from the above that resistance to the applied load is essentially provided by the portion of the beam extending, on either side of the mid-span, to the cross-section where vertical cracking initiates at the top face and extends downwards. This portion, termed L_{eff}, has been suggested to be linked with the increase of the peak value of the applied load with the rate of loading (Cotsovos et al. 2008, Cotsovos 2010, Cotsovos &Pavlović 2010).

During testing, the strain developing along the specimen span (normal to the beam cross-section) reaches its peak value at the same time at which the impact load attains its maximum value ($maxP_d$), shortly after the impactor collides onto the beam at mid-span. The data presented in Fig. 3.34 shows that the displacement recorded along the span of the RC beam specimens when $maxP_d$ is achieved is only a small fraction of the maximum

deflection ($maxd_d$) measured at mid-spam. This, in combination with the observation that flexural cracking forms and extends deep into the compressive zone of the specimens during the initial stages of the loading process, prior to achieving $maxP_d$, demonstrates that the beams exhibit localised response confined to the portion of the element span around the mid-span (impact) region. This localised response significantly affects the mechanics underlying the behaviour (as well as the cracking process) of the subject specimens as the length of the beams reacting to the imposed load is characterised by a smaller shear span as well as different boundary conditions compared to those of the whole specimen when subjected to equivalent static loading. This is evidenced by the differences characterising the crack patterns observed under impact and equivalent static loading. After peak load ($maxP_d$) is attained the specimens continue to deform reaching a maximum deflection at mid-span considerably higher compared to that corresponding to $maxP_d$. During this phase of the loading process, the response becomes gradually increasingly global due to the damage suffered locally at mid-span and the fact that the waves generated in the impact region reach the supports resulting in the full span of the beam reacting to the imposed load.

It has been well established that the shear span to depth ratio (a_v/d) has a significant effect on the mechanics underlying the behaviour of RC beams under static loading (Kotsovos 2014). The behaviour of slender RC beams (with $a_v/d>5$), even when having a minimum amount of shear links, is ductile ultimately leading to a flexural mode failure. Shorter beams (with $a_v/d<5$) are more likely to exhibit a brittle (shear) mode of failure if they do not have a sufficient amount of transverse reinforcement. For the case of impact loading the available experimental data obtained from drop-weight tests (see Fig. 3.49) clearly indicates that slender RC beams (e.g. $a_v/d > 5$, see Fig. 3.49) exhibit a higher increase of maximum sustained load ($maxP_d$) with increasing loading rates compared to shorter specimens characterised by smaller values of a_v/d (e.g. $a_v/d < 5$, see Fig. 3.49a). This can be attributed to the fact that in the case of the more slender specimens, due to their longer span, the waves generated in the impact region require more time to reach the supports and consequently, when subjected to high rates of impact loading, cracking (and potentially failure) may occur prior to them reaching the supports. As a result, the specimens exhibit more localised response with only a portion of their span (effective length, L_{eff}) essentially reacting to the imposed load. This localised response, the fact that L_{eff} does not form a simply-supported beam (since its end conditions can be assumed fully or partially fixed) in combination with the inertia forces developing along the element span appear to

significantly affect the mechanics underlying the behaviour of the subject specimens under impact loading.

Available (mainly military) design codes (TM5-855-1 (1998) employ equivalent simple lumped mass-spring systems for modelling individual structural elements with distributed mass and loading. The equivalence is based upon energy approximations that rely on a deflected shape (e.g. Associated with the first eigenvector or the deflected shape under equivalent static loading) which assumes that the full length of the RC beam reacts to impact loading. The above methodology relies on a number of simplifications concerning both material behaviour and structural response. These include the use of simple uniaxial material laws, the description of post-failure behaviour, empirical amplification factors attributed to the strain-rate sensitivity of concrete behaviour and steel, assumptions concerning the deformed shape of the structural elements and the use of elastic or elasto-plastic laws for describing structural behaviour. Such assumptions appear largely incompatible with the experimentally established deformation and cracking profiles recorded during testing as they do not allow the existing assessment methods to account for the localised response exhibited by slender RC beam specimens during the initial stages of the loading process (until $maxP_d$ is attained). However, the test data obtained justify the assumptions adopted by a simplified assessment method proposed in previous studies (Cotsovos et al. 2008, Cotsovos 2010, Madjlessi & Cotsovos 2016) that links the observed shift in structural response to the localised behaviour exhibited with increasing rates of applied impact loading.

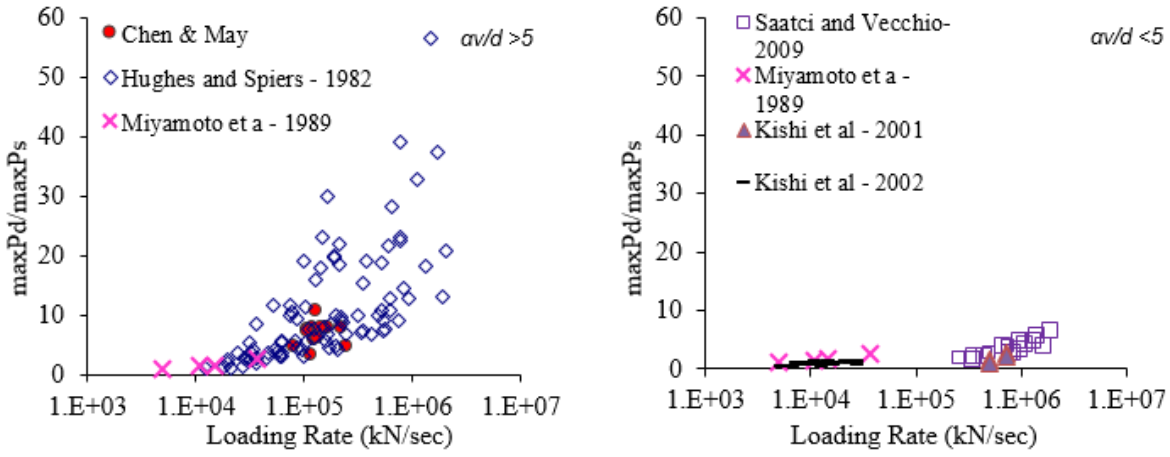

Figure 3-49 Variation of maximum sustained load during impact ($maxP_d$) in relation to the static load-carrying capacity ($maxP_s$) with increasing loading rates for the case of RC beam specimens with values of a_v/d (a) greater than 5 and (b) less than 5

3.11 CONCLUSIONS

The test data and relevant observation describing the response of the RC beam specimens during drop weight testing compared to their counterparts established from static testing reveals significant differences, which confirms the findings of published experimental and numerical studies carried out on similar slender RC beam specimens. Under impact loading, the RC beam specimens are capable of withstanding higher values of loading compared to their load-carrying capacity established under static loading, while at the same time exhibiting a stiffer response. During the initial stages of the loading process, the response of the RC beams appears to be more localised as its middle portion seems to deform more than the rest of the specimen span. In addition, the analysis of the photographic evidence collected from the high-speed camera reveals that under high-rate loading flexural cracking appears at the bottom face of the mid-span area and extends rapidly towards the upper face of the beam almost immediately after the collision of the impactor with the RC beam.

Based on the analysis of the high-speed camera record and the strain values, it can be concluded that high values of strain rate in the mid-span area of the beam are exhibited once the concrete medium suffers considerable cracking and, as a result, these high strain rates do not correspond to a concrete material but are linked to post-failure behaviour of the cracked area of the beam. The values of strain rate in the critical early stages of the impact test were found to be considerably lower than the threshold established experimentally (over decades of testing) describing the variation of the concrete compressive and tensile strength under different strain rates. Thus, the increase in load-carrying capacity with the rate of loading observed in the present study cannot be attributed to an increase in the material strength due to strain rate sensitivity. It should also be borne in mind that the terms failure and load-carrying capacity require careful qualification as it will first be necessary to establish the post-impact performance criteria (such as the residual strength required and the level of damage that can be tolerated) in order to arrive at meaningful estimates.

Based on the above, the assumptions adopted by the relevant (mainly military) design codes appear to be incompatible with the behaviour exhibited by the RC beam specimens

presently considered (especially during the critical initial stages of the loading process) as they do not allow the assessment methodology to account for the true nature of problem at hand (a wave propagation problem within a highly nonlinear material) and the localised response exhibited. This raises concerns regarding the validity of the predictions provided by these codes and the effectiveness of the obtained design solutions. Finally, it is interesting to note that a newly proposed assessment method, that links the observed shift in structural response to the localised behaviour exhibited with increasing rates of applied impact loading, is found capable of providing predictions in agreement with the test data recorded. It is important to mention that the latter method is still under development.

CHAPTER 4 -EXPERIMENTAL ANALYSIS OF RC SHORT BEAMS

4.1 INTRODUCTION

In the previous chapter, the effects of high-rate loadings on slender RC beams with a shear span-to-depth ratio *greater* than five (i.e. $a_v/d > 5$) was investigated. From the analysis of the test data (obtained through dropped-weight testing), the parameters influencing the mechanics underlying the impact response were established. The portion of the beam span reacting to the imposed load – referred to as effective length (L_{eff}) – as well as the inertia forces generated as the specimen deformed were found to be the main factors contributing to the shift in the response of the RC specimens. The slender RC beams appeared to exhibit a localised response during impact testing. It was further established that the increase in load-carrying capacity with the rate of loading cannot be linked to an increase in the material strength due to strain rate sensitivity. This was due to the fact that the measured values of strain rate during impact testing were considerably lower than the threshold established experimentally over decades of testing describing the variation of the concrete compressive and tensile strength under different strain rates.

The current chapter focuses on the experimental investigation of short RC beams with a span-to-depth ratio *less* than five (i.e. $a_v/d < 5$). The primary objective of the current experimental investigation is to study the influence of the reduced span-to-depth ratio characterising the beam specimens considered in the present chapter as well as the amount of shear reinforcement provided on certain important aspects of the exhibited behaviour. Such aspects include the generated impact and reaction forces, the displacement exhibited by the drop-weight (hammer) and specific points along the element span as well as the values of strain (ε) and strain rate ($\dot{\varepsilon}$) developing locally in certain key regions of the specimens throughout the loading process. For this purpose, nine RC beams were fabricated and subjected to consecutive drop weight tests. Through the use of a high-speed camera, cracking and deformation profiles exhibited by each specimen at different stages of the loading process as well as the failure modes were also recorded as they provide an indication of the internal state of stress developing within each specimen. In order to

determine the residual stiffness and strength of damaged specimens, which were already subjected to impact loading, static loading was conducted after impact tests. The static loading was applied monotonically at the mid-span of the subject specimens until collapse. The main focus of the current study is to investigate in detail the effects of reduced span-to-depth ratio as well as the design details of stirrups on the overall structural response of the RC beam specimens. To achieve this, a combination of conventional instrumentation (e.g. LVDTs, accelerometers, strain-gauges and load-cells) as well as a high-speed video camera are used. The measurements obtained are finally compared to published test data gathered from the specimen with higher values of span-to-depth ratio (i.e. slender RC beams with $a_v/d > 5$) when subjected to drop-weight testing.

4.2 OVERVIEW OF TEST PROGRAMME

A total of nine RC beams were cast for the purpose of this test programme six of which were subjected to multi-impacts and three we tested under equivalent static loading to establish the static behaviour of the test specimens prior to impact loading. The results obtained from static tests form a benchmark in relation to the impact response of the RC beams. Relevant design codes (EC2) were used to design and analyse the test specimens. The flexural and shear capacities of the specimens are shown in Table 6.

Table 6 Predicted load bearing capacity of beams C-E under static loading

Specimen type	Calculated static load-carrying capacity associated with flexural capacity by EC2 P_f (kN)	Calculated design shear capacity of concrete by EC2 (EC2) $V_{Rd,c}$(kN)	Calculated shear resistance of the stirrups by EC2 (EC2) $V_{Rd,s}$(kN)
C	70	38	-
D	153	38	180
E	130	38	128

In order to assess the residual load-bearing capacity and the stiffness of the specimens, following each impact test, the damaged specimens were also tested under equivalent static loading. Table 7 shows a summary of the test programme carried out in this study.

Table 7 Experimental Programme

Specimen	Beam type	Test programme	Support conditions	Test No.	Date	Height of impacts (m)	Impact velocity (m/s)	Pad (mm)	Pad dimension
SD	D	Static (undamaged)	Simply-Supported	i[1]	27-Jul-16	-	-	13 Steel	185x185x13
ImpD-a		Impact and Static (damaged)		1	11-Aug-16	1	4.43	10.4 Steel	275x140x10.4
				2	12-Aug-16	1.5	5.42	10.4 Steel	
				3	24-Aug-16		5.42	10.4 Steel	
				4	02-Sep-16		5.42	10.4 Steel	
				5	06-Sep-16		5.42	10.4 Steel	
				6	06-Sep-16		5.42	10.4 Steel	
				I*	19-Oct-16	-	-	13 Steel	
ImpD-b				16	07-Mar-17	2	6.26	13 Steel	185x185x13
				17	07-Mar-17		6.26	13 Steel	
				18	07-Mar-17		6.26	13 Steel	
				19	07-Mar-17		6.26	13 Steel	
SC		Static (undamaged)		ii[1]	12-Oct-16	-	-	13 Steel	
ImpC-a	C	Impact and Static (damaged)		7	12-Sep-16	1.5	5.42	10.4 Steel	275x140x10.4
				8	12-Sep-16		5.42	10.4 Steel	
ImpC-b				14	08-Nov-16	2	6.26	25 Steel	150x150x25
				15	08-Nov-16	1.5	5.42	25 Steel	
SE	E	Static (undamaged)		iii[1]	26-Oct-16	-	-	13 Steel	185x185x13
ImpE-a		Impact and Static (damaged)		9	21-Sep-16	1.5	5.42	10.4 Steel	275x140x10.4
				10	21-Sep-16	1.5	5.42	10.4 Steel	
				11	26-Sep-16	1.5	5.42	10.4 Steel	
				12	04-Oct-16	1.5	5.42	25 Steel	
				13	04-Oct-16	1.5	5.42	25 Steel	150x150x25
				II*	02-Nov-16	-	-	13 Steel	185x185x13

[1] Static Test

* Residual Static Test

4.3 SPECIMEN CHARACTERISTICS

A total of nine RC simply supported beams (i.e. 3 pairs of 3 specimens) were cast for the current test programme. The height (h) and width (b) of the specimen cross-section was 300 mm and 150 mm respectively, whereas the full length (L) of the beams was 2.5 m and the clear span between the supports was 1.7m, see Fig. 4.1. Each beam was subjected to static or impact load concentrated at its mid-span and the shear span (a_v) was 0.85 m. Under static loading condition, the load was applied monotonically to failure in the form displacement increments. During drop weight testing a drop steel mass allowed to fall onto the mid-span of the specimen from the heights of 1, 1.5 and 2 m with the initial velocities of 4.43, 5.42 and 6.26 m/s respectively.

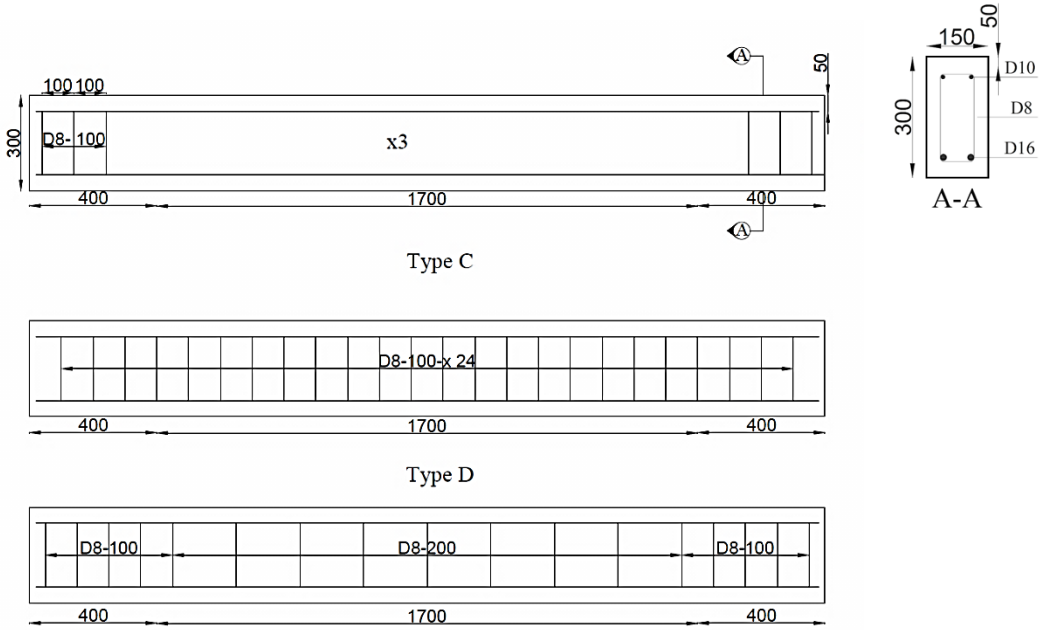

Figure 4-1 Design of RC beam specimen (units are in mm)-Cover is 50 mm (top and bottom)

The test specimens are labelled as C, D and E based on the amount of shear reinforcement used, see Fig. 4.1. All the three types of specimens were reinforced with two 10 mm diameter bars in compression and two 16 mm diameter steel bars in the tension with a cross-sectional area of 78.53 mm^2 and 201.06 mm^2 respectively with 8 mm diameter stirrups. The shear reinforcement ratio ($\rho_{w=Asw/bs}$) was 0.16%, 0.64 % and 0.45% for type C, D and E respectively (see Table 8).

Table 8 Reinforcement details of subject specimens

Beam type	Tension Steel	Compression Steel	Flexural Reinforcement Ratio (%)	Stirrups	Transverse Reinforcement Ratio (%)
C				6x8φ	0.16
D	2x16φ	2x10φ	1.24	24x8φ	0.64
E				17x8φ	0.45

4.4 MATERIAL PROPERTIES

A ready-mix concrete with a nominal cubic strength of 45 MPa was used to cast the specimens 30 days prior to testing. The mean cubic strength of the 100 x 100 mm^2 cube was measured through uniaxial compressive test 30 days after casting. The splitting tensile tests were conducted on plain concrete cylindrical specimens (with a height of 300 mm and a diameter of 150 mm) to establish concrete material behaviour in tension. The mean splitting strength ($f_{t,sp}$) of the concrete was established experimentally at 6.18 MPa. The yield strength of steel reinforcement was 545 Mpa and 500 Mpa for 10mm and 16 mm respectively (through the tensile testing machine) with the young modulus of 200 Gpa (see Fig. 4.2). Tables 8 and 9 provide the material properties of the concrete and steel used for casting the RC beam specimens tested under both static and impact loading(s).

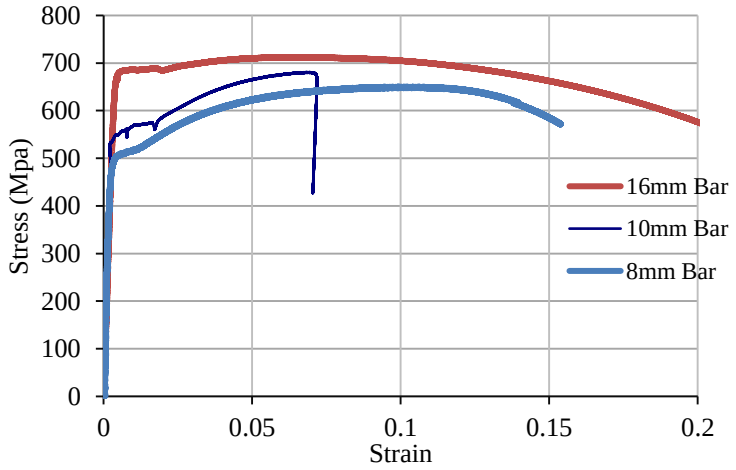

Figure 4-2 Material properties of steel reinforcement

Table 9 Material properties of concrete

Specimen	Date	$f_c(Mpa)$	$f_t(Mpa)$
Cube 1	05 Aug 2016	44.93	-
Cube 2	05 Aug 2016	45.68	-
Cube 3		43.65	-
Cube 4		47.62	-
Cube 5	07 Mar 2017	46.74	-
Cube 6		40.83	-
Cube 7		48.38	-
Cylinder 1	05 Aug 2016	-	6.321
Cylinder 2	05 Aug 2016	-	6.99
Cylinder 3	07 Mar 2017	-	5.23

Table 10 Material properties of steel reinforcement

Rebar size	8 mm	10 mm	16 mm
$f_{ult}(Mpa)$	572	668	712
$f_{yield}(Mpa)$	501	495	682
ε_{ult}	0.102	0.071	0.075
ε_{yield}	0.004	0.002	0.006

4.5 EXPERIMENTAL SETUP EMPLOYED FOR DROP-WEIGHT TESTING

Prior to conducting the drop-weight testing, the specimens were tested under static loading. The details of the test setup, as well as the static test programmes, have been discussed in Chapter 3 section 3.5. Concerning the drop-weight testing, a drop-weight testing rig was used capable of delivering a steel impact of 120 kg onto the impact region with a maximum velocity of 7 m/s. The setup employed is presented in Fig. 4.3. It should be noted that the setup used for the impact test of RC slender beams (see Chapter 3) was modified to account for a shorter span of short beams discussed herein. All of the specimens were simply supported and tested under multiple drop-tests to investigate how the exhibited behaviour varied with every collision. Steel pads were placed at the supports on top of the beam cross-section so that the uplift is reduced as much as possible. The experimental programme is described in Table 11.

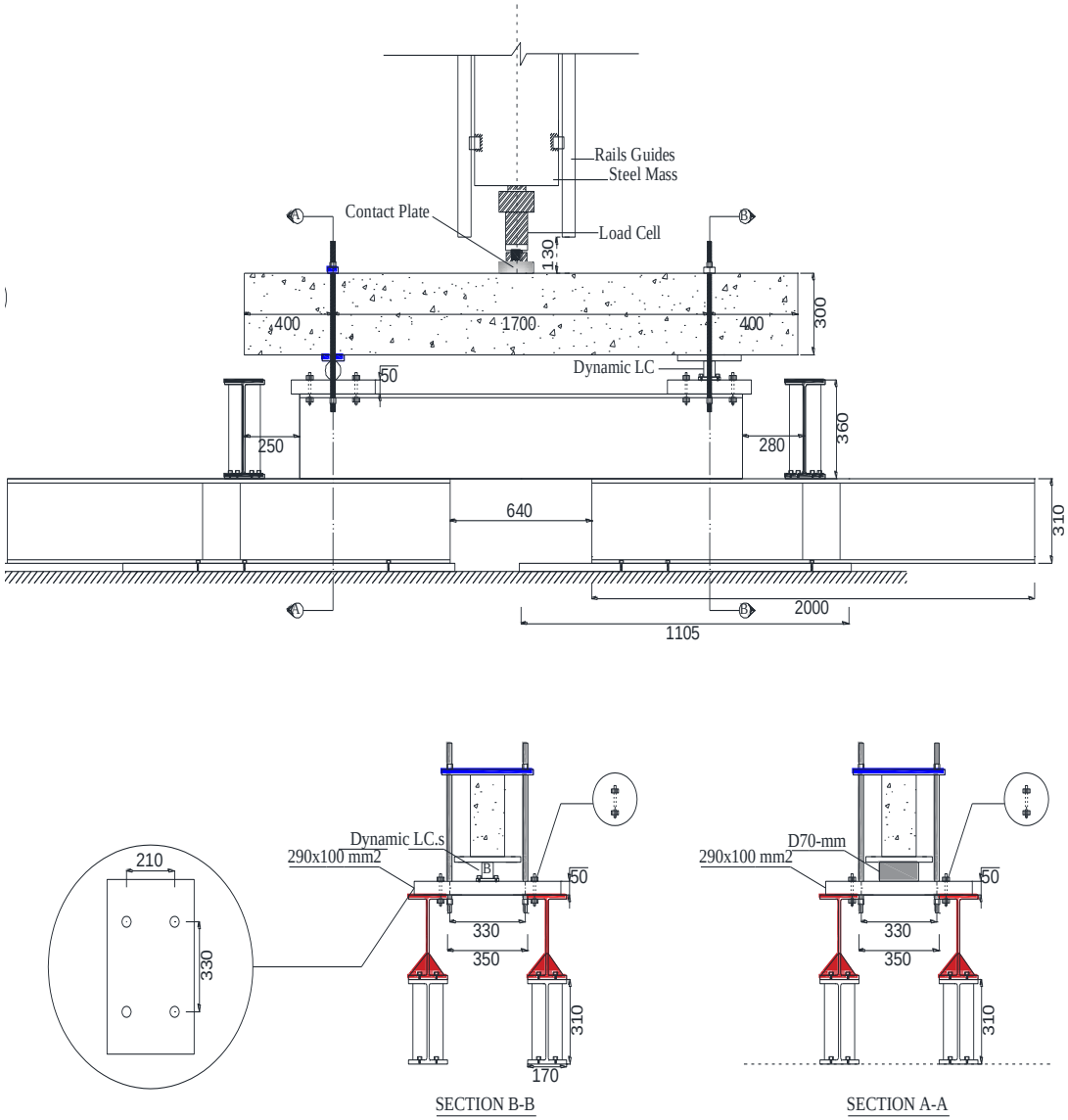

Figure 4-3 Experimental set up used for conducting drop weight testing

The specimens were instrumented to capture the displacements, accelerations, deformation profile, crack pattern, impact force and support reactions. Figs. 4.3a and 4.3b show the position of sensors along the length of the specimens, which consisted of the following.

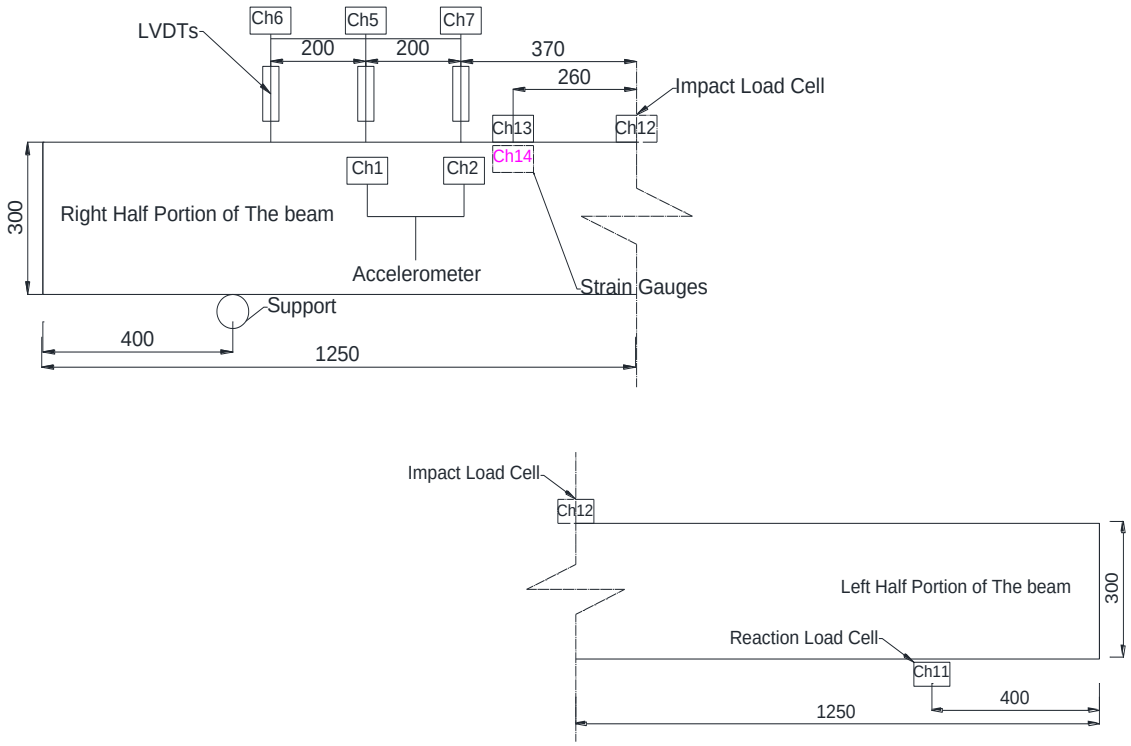

Figure 4-4 Arrangement of instrumentations along (a) right half portion and (b) left half portion of the beam

Three Linear Variable Differential Transformers (LVDT) mounted at different locations along the element span to measure the displacement exhibited at these points throughout the length. They are labelled as Ch5, Ch6 and Ch7 on Fig. 4.4 and mounted on a steel bar connected to the guide rail.

Three accelerometers were used for each impact test. Three accelerometers were used denoted as (Ch1, Ch2 and Ch4). Ch1 and Ch2 were affixed to an L-shaped aluminium brackets fixed to L-shaped aluminium brackets, on the right-half portion of the specimens near the top portion of the specimen (see Fig. 4.5).

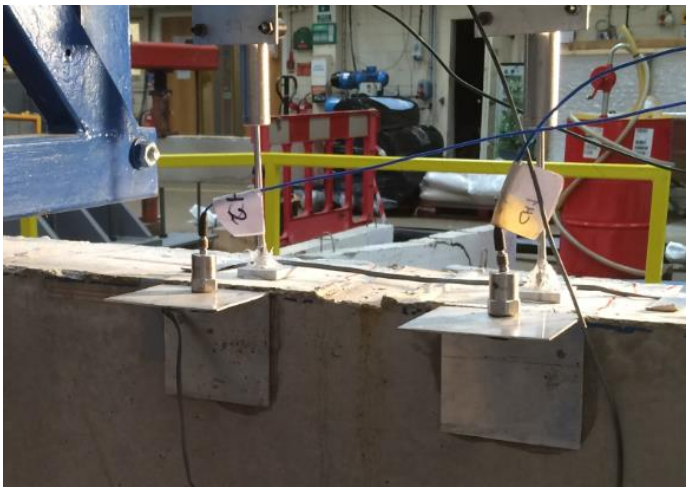

Figure 4-5 Arrangement of accelerometers (Ch1 and 2) placed on RC specimens

A load cell was placed underneath the support to measure the reaction forces and was labelled as Ch11. One load cell was used to measure impact force and was attached to the bottom of the impactor (see Ch12). The specimens were fitted with strain gauges installed at two locations of the test objects. One of the train gauges was mounted on the top (compressive) surface of the concrete while the latter was secured underneath the former on the web of the beam to measure the strains in the longitudinal direction. A data acquisition system was used capable of recording data at a sampling rate of 35 kHz per channel. Finally, a high-speed camera was used operating at a rate of 2000 frames per second. The latter was aimed to confirm previous measurements, monitor crack pattern and the deformation profile as well as compensate for the loss of data. The above was achieved by tracking a series of dots (generates on the face of the subject specimens through gridlines prior to impact test) using a video analysis software (i.e. Tracker).

4.6 SPECIMEN BEHAVIOUR UNDER STATIC LOADING

The static behaviour of the types of test specimens (types C, D and E) are presented in Fig. 4.6a expressed in terms of the magnitude of the applied load versus the deflection at mid-span. The results show that RC beams type D and E exhibit ductile behaviour (i.e. performed higher value of displacement comparing to type C), which is characterised by yielding of the longitudinal reinforcement mainly at mid-span. The latter results in the formation of extensive cracking that ultimately led to the loss of static load-carrying capacity of the tensile and compressive zone. On the other hand, the behaviour of specimen

type C failed in a brittle manner mainly to do the formation of inclined/shear cracks extending from the support and penetrated deep into the compressive region. The load-carrying capacity of the specimens C, D and E were 82.67, 150.89 and 128.08 respectively. Fig. 4.6b shows the crack pattern during the loading process and is compatible with the load-displacement curve obtained earlier in terms of ductility.

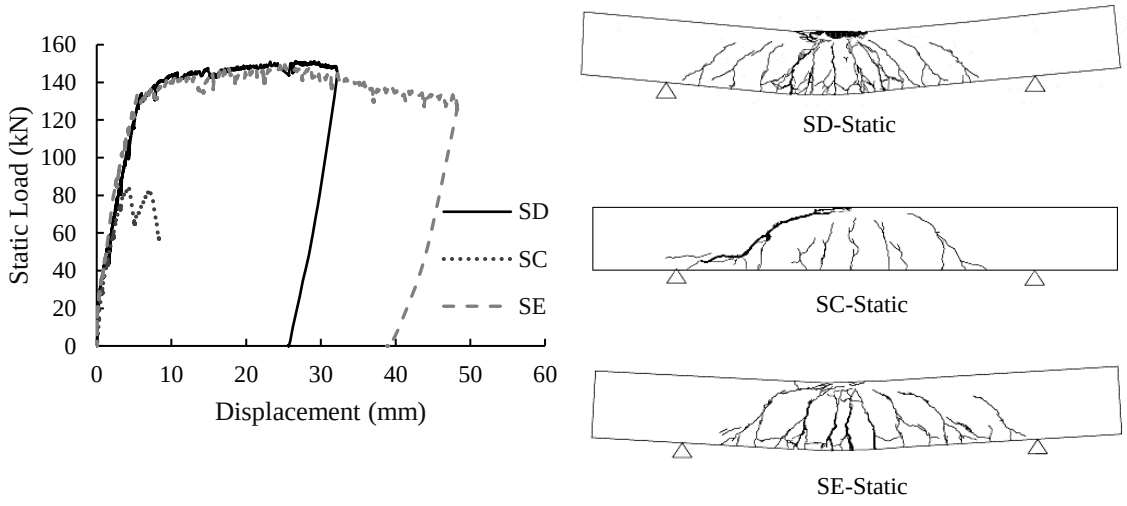

(a) (b)

Figure 4-6 Static test results (a) load-displacement curves (b) crack pattern

4.7 SPECIMEN BEHAVIOUR DURING IMPACT LOADING

During and after impact tests different aspects of the response exhibited by the RC beams were recorded. Such as the maximum sustained load and support reactions generated during impact, mainly focusing on the effects of multi-impacts on the values of the loads. Other information studied include the value of displacement exhibited by mid-span and specific points along the element span as well as the values of strain developing locally in certain (critical/key) regions of the specimens throughout the loading process. Cracking and deformation profiles exhibited by the specimen at different stages of the loading process as well as the failure modes are also recorded as they provide an indication of the internal state of stress developing within the specimen. Damaged specimens, already subjected to impact loading, are tested under static loading monotonically applied at the mid-span until a collapse in order to determine the residual stiffness and strength of the specimen.

4.7.1 Impact force and support reactions

The peak values of measured data including the maximum impact forces (P_{max}), corresponding peak times (t_{max}), loading rate ($\dot{P}$), maximum resultant reaction forces (R_{max}), the time corresponding to maximum support reactions (t_r), and the time interval between peak impact load and support load (Δt) are presented in Table 12. It should be noted that information regarding impact force is missing in some of the impact tests due to instrumentation errors (tests 2, 3, 9 14 and 15). Figs. 4.7-4.10 depict the impact and reaction time-histories recorded during the first 0.02 s of the impact tests.

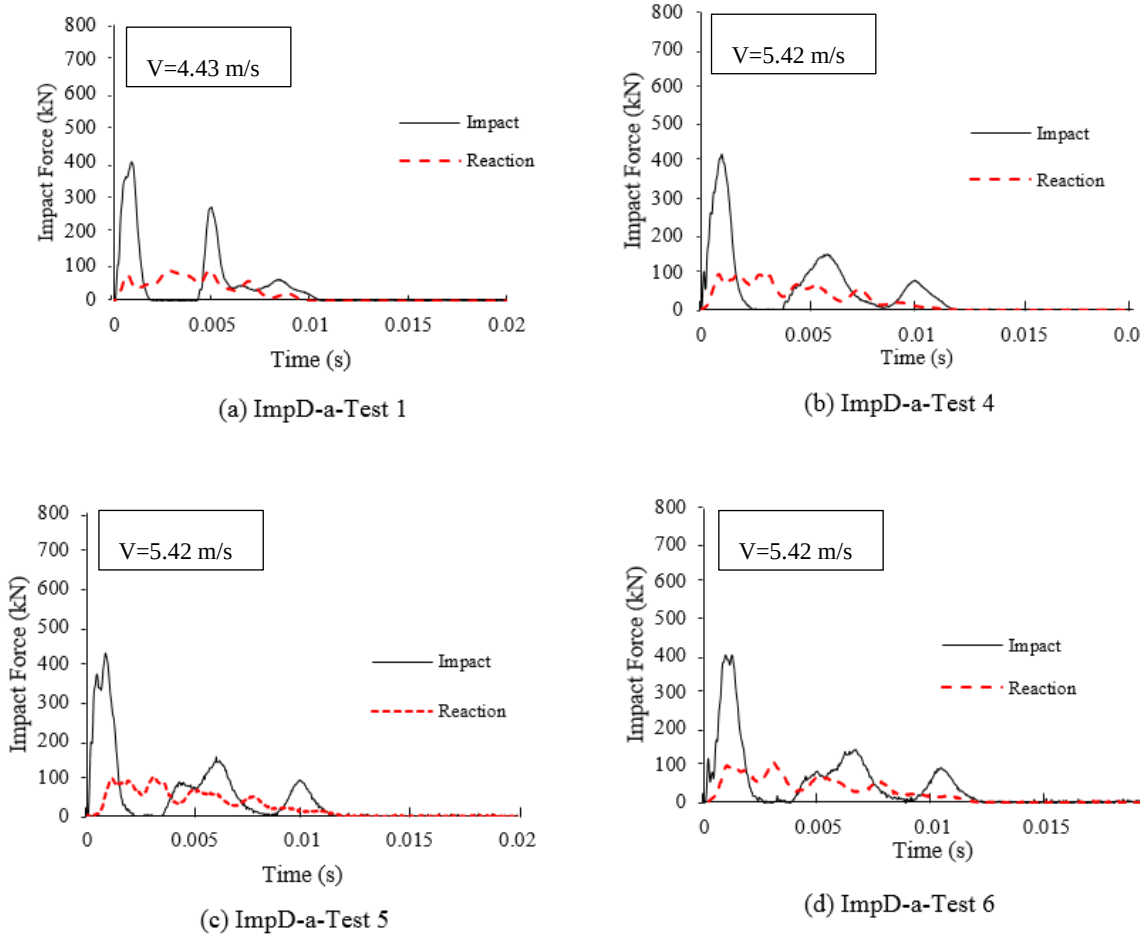

Figure 4-7 Impact and reaction force-time histories recorded during different drop-weight tests on specimen D-a

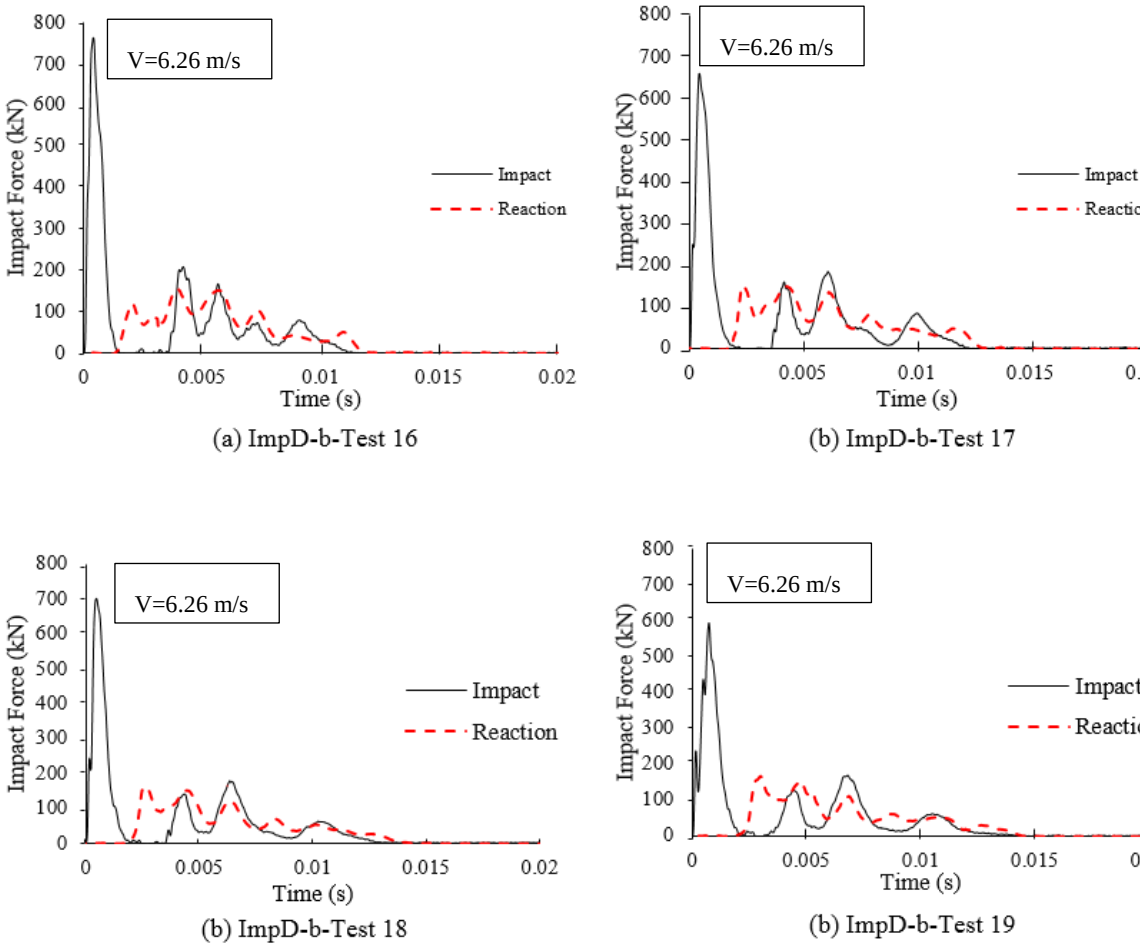

Figure 4-8 Impact and reaction force-time histories recorded during different drop-weight tests on specimen D-b

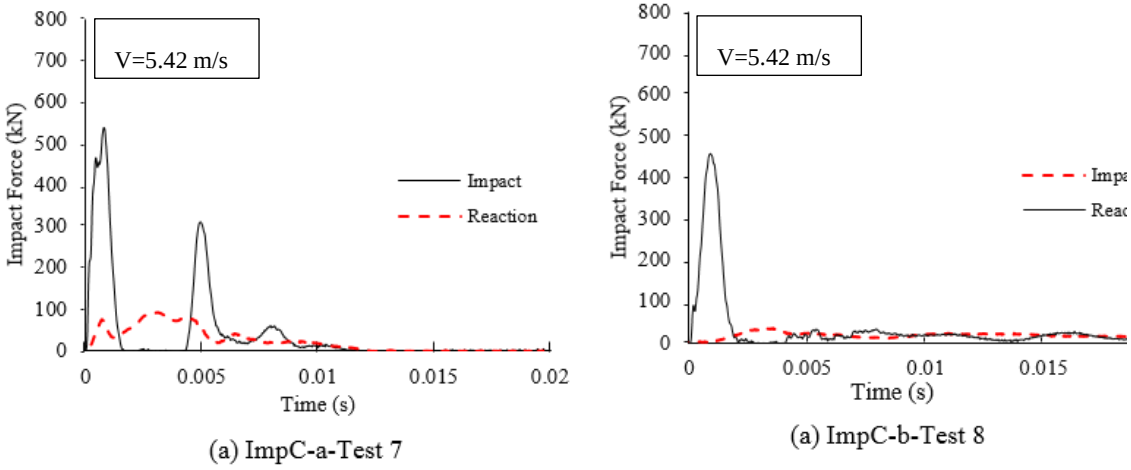

Figure 4-9 Impact and reaction force-time histories recorded during different drop-weight tests on specimen C-a

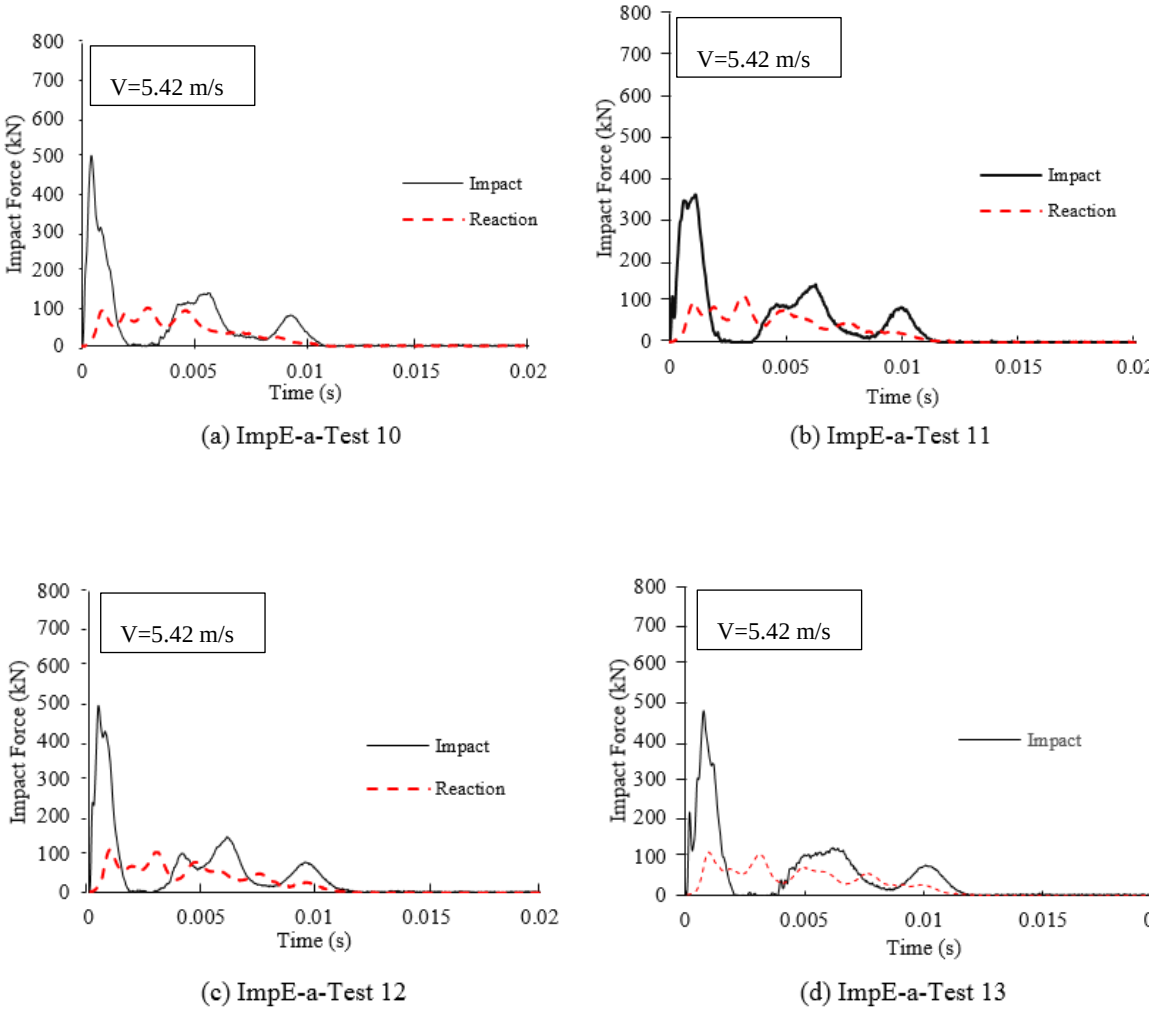

Figure 4-10 Impact and reaction force-time histories recorded during different drop-weight tests on specimen E-a

Type D-a- Fig. 4.7 shows the impact and reaction time-histories recorded during tests 1, 4, 5 and 6 on specimen D-a. The value of the peak impact force obtained during the initial impact (i.e. test 1) is 401 kN. There was an insignificant increase in the value of the peak impact force recorded during the subsequent impacts (i.e. 418 and 430 for tests 4 and 5 respectively) comparing to the initial one, while during the last impact (i.e. test 6) the impact forces reduced to 400 kN which was approximately equal to the value of impact force obtained from initial impact test (i.e. test 1). In other words, the magnitude of the impact force obtained during the subsequent impacts had an increase of 4% and 7% comparing to the initial one. Considering the rate of loading, test 1, exhibited the highest value of loading rate (i.e. 1302 kN/ms, while the latter was reduced to 703, 1193 and 1270 kN/ms for tests 4, 5 and 6 respectively.

The peak value of the reaction force for test 1 was approximately 70 kN peak values of the latter are close with an insignificant difference in tests 4, 5 and 6, see Table 12. The above suggests that the value of peak impact forces were approximately 4 times greater than the peak value of reaction forces. However, such a difference between the two values is more apparent during the initial impact test in the sense that the ratio of impact to reaction load was measured as 5.6.

Furthermore, it is worth to point out the existence of a time lag in the impact and reaction time-histories is insignificant. This suggests that the max impact force and reaction force occurred approximately at the same time. The maximum time lag was recorded during test 5 (i.e. 0.5 s) while the latter was at a minimum during test 1 (i.e. 0.016 s).

Type D-b- The impact and reaction time histories of impact tests 16-19 on specimen D-b are shown in Fig. 4.8. It is apparent that the magnitude of the peak impact forces obtained from tests 16-19 is considerably greater than those exhibited by specimen D-a. The maximum value of impact force was 760 kN for the initial impact test on specimen D-b (i.e. test 16) while this value had a reduction of approximately 13%, 8% and 20% in tests 17, 18 and 19 respectively. A summary of the recorded peak values of impact forces and reaction forces is provided in Table 6. The peak value of the reaction force was measured as approximately 117 kN during test 16 while the latter was increased to 150,160 and 165 kN for tests 17, 18 and 19 respectively. The ratio of the impact to reaction load was at the maximum value (i.e. 6.5) for Test 16 and at a minimum value (i.e. 3.5) for Test 19. It is interesting to note that, the time lag observed during impact tests on specimen D-b is more apparent to those recorded during tests on specimen D-a. The delay between the peak value of the impact force and reaction force was measured as 1.67 s for test 16 and this value was increased to 1.93, 2.1 and 2.3 s for tests 17, 18 and 19 respectively.

Specimen C-a- The difference between the peak values of the impact force and reaction force measured during the first (Test 7) and second test (Test 8) was insignificant i.e. 495 and 458 kN for tests 7 and 8 respectively, see Fig.4.9. However, the peak value of reaction forces reduced dramatically (i.e. approximately 53 %) during the second impact). The value of the loading rate recorded during Test 7 was measured as 660 kN/ms, the latter was increased to approximately 870 kN during the second impact (Test 8). The time lag between

the peak value of impact force and reaction force was insignificant (i.e. 0.011) for Test 7 while this value was more apparent (i.e. 2.52 s) during Test 8. See Table 12.

Specimen E-a- Similar to specimens D and C, the peak value of the impact force was at a maximum during initial impact test (i.e. Test 10) and decreased during the subsequent impacts. A similar observation applies to the value of loading rate which was 2260 kN/ms for the initial test and was reduced by 57, 31 and 58% in tests 11, 12 and 13 respectively. On the contrary, the peak value of the reaction force was increased during the subsequent impacts and attained its maximum value of 112 kN during the final test on specimen E-a (i.e. Test 13). The difference between the values of time lag in all the 4 impact tests was insignificant.

Table 12-Impact test results

Specimen	Beam type	Test programme	Test No.	P' (kN/s)	P' (kN/ms)	$P_{Imp,max}$ (kN)	$P_{support,max}$ (kN)	Ratio of Impact to reaction load	$t_{p,impact}$ s	$t_{p,impact}$ ms	$t_{max,impact}$ s	$t_{max,support}$ s	Δt ms
SD	D	Static (undamaged)	i	-	-	-	-	-	-	-	-	-	-
ImpD-a		Impact and Static (damaged)	1	6206646	6206.6	401.0	71.1	5.6	6.46E-05	0.06461	0.00062	0.00068	0.06
			2	-	-	-	-	-	-	-	-	-	-
			3	-	-	-	-	-	-	-	-	-	-
			4	694851	694.9	417.6	94.6	4.4	6.01E-04	0.60106	0.00098	0.00110	0.12
			5	1193142	1193.1	429.4	98.8	4.3	3.60E-04	0.35990	0.00087	0.00117	0.30
			6	1269841	1269.8	400.0	97.6	4.1	3.15E-04	0.31500	0.00098	0.00103	0.05
			I	-	-	-	-	-	-	-	-	-	-
ImpD-b			16	1076068	1076.1	760.8	116.3	6.5	7.07E-04	0.70700	0.00043	0.00211	1.68
			17	1280363	1280.4	658.8	149.4	4.4	5.15E-04	0.51456	0.00046	0.00239	1.93
			18	2105045	2105.0	701.0	161.4	4.3	3.33E-04	0.33300	0.00052	0.00262	2.10
			19	1705888	1705.9	593.1	165.7	3.6	3.48E-04	0.34770	0.00074	0.00307	2.32
SC	C	Static (undamaged)	ii	-	-	-	-	-	-	-	-	-	-
ImpC-a		Impact and Static (damaged)	7	659477	659.5	494.6	75.3	6.6	7.50E-04	0.75000	0.00073	0.00074	0.01
			8	870424	870.4	457.8	35.5	12.9	5.26E-04	0.52600	0.00095	0.00348	2.52
ImpC-b			14	-	-	-	-	-	-	-	-	-	-
			15	-	-	-	-	-	-	-	-	-	-

SE	E	Static (undamaged)	iii	-	-	-	-	-	-	-	-	-	-
ImpE-a		Impact and Static (damaged)	9	-	-	-	-	-	-	-	-	-	-
			10	947928	947.9	501.0	93.4	5.4	5.29E-04	0.52850	0.00043	0.00106	0.63
			11	964227	964.2	351.0	95.8	3.7	3.64E-04	0.36400	0.00090	0.00108	0.19
			12	1548154	1548.2	480.4	105.4	4.6	3.10E-04	0.31030	0.00046	0.00097	0.51
			13	949269	949.3	478.4	112.0	4.3	5.04E-04	0.50400	0.00078	0.00101	0.23
ImpE-b			II	-	-	-	-	-	-	-	-	-	-
			-	-	-	-	-	-	-	-	-	-	-

Fig. 4.11 demonstrates the variation of DIF $maxP_d/maxP_s$ or $max\delta_d/ max\delta_s$ with respect to loading rates. Type C with no shear reinforcement along the span, exhibited a higher value of load-carrying capacity with DIF value approximately equal to 2.75, while Type D with the highest value of shear reinforcement ratio is associated with the lowest value of DIF (see Fig. 4.11a). In terms of the amount of deformation the RC beams suffered from during impact loading, Type D with the highest amount of transverse reinforcement exhibited the least ductility under impact loading, while the weakest specimen i.e. Type C had the largest value of DIF (see Fig. 4.11b).

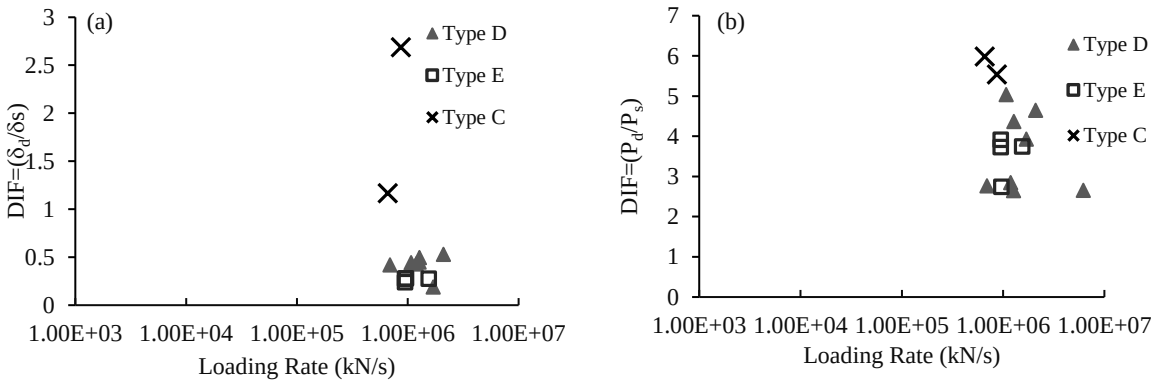

(a) (b)

Figure 4-11 Variation of (a) DIF = $maxP_d$ / $maxP_s$ and (b) max δ_d/max δ_d with increasing loading rates

4.7.2 Displacement data and deformation profile

The vertical displacement exhibited at specific points along the span of the beam was measured through the combined use of LVDTs and a high speed (HS) camera and appropriate tracking software (i.e. Tracker©), Tracker 4.87. (2014). The points were marked every 50 mm off the mid-span of the specimen between the impact region and the left-hand-side support, see Fig. 4.12.

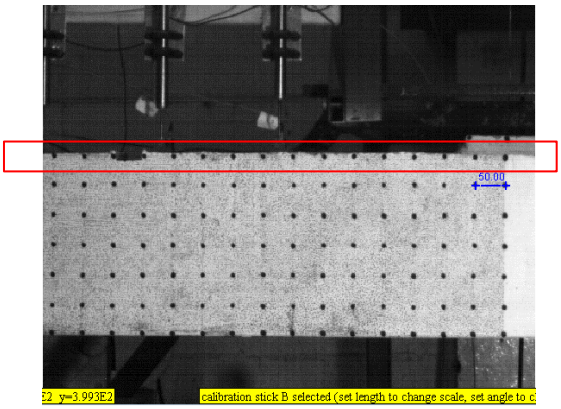

Figure 4-12 Specified points marked every 50 mm off the mid-span along the right-hand portion of the RC beam

In total three LVDTs were used in all the tests Located at a distance of 570, 770 and 370 mm off the mid-span and are labelled as Ch5, Ch6 and Ch7 respectively, see Fig. 4.3. The comparison between the displacement time histories recorded through LVDTs during the impact tests, with those obtained from the HS camera for tests 7, 10, 12 and 16, is shown in Fig. 4.13 (a-d). The curves reveal the deformation of the specimens after the initial contact between the striker and the specimen. The deflection exhibited by the beam specimen increases rapidly to a maximum negative value and shortly after, it obtains its residual value.

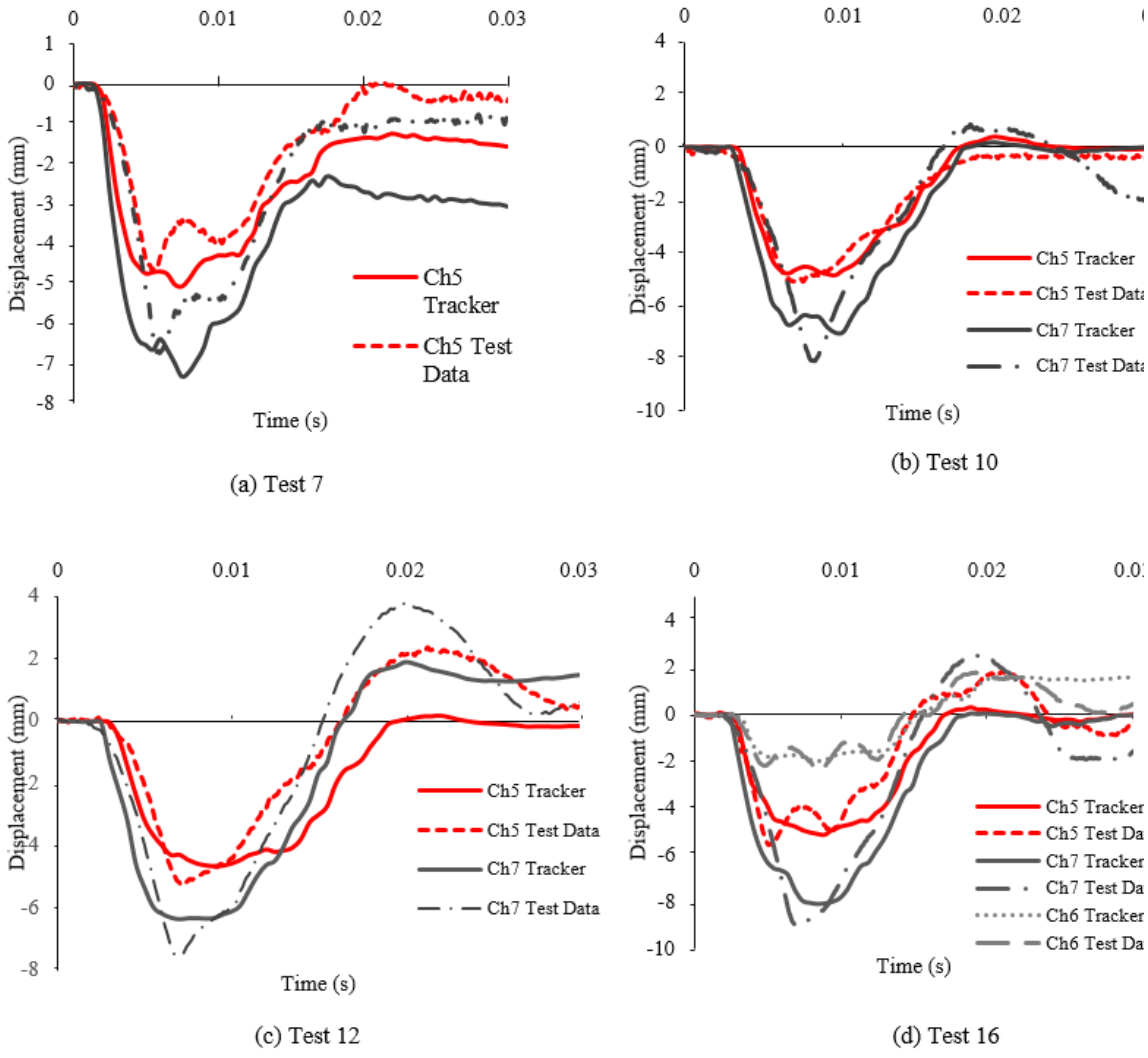

Figure 4-13 Correlation between the displacement time histories obtained during dropped-weight testing and the analysis of high-speed video recordings

The variation of the vertical deflection measured during tests 4, 7, 10, 12 and 16 (through the combined used of the high speed camera and the LVDTs) at different points along the portion of the beam specimen between the mid-span (impact) region and the left-hand side

support of the specimen are presented in Fig. 4.14 (a-d).Examination of these curves reveals that the points closer to the impact (mid-span) region start moving first, the latter indicates that the problem at hand is a wave propagation problem and the stress waves move away from the impact region the points located further away from the mid-span also start moving. This provides evidence of the localised response exhibited by the RC beams specimens immediately after the initial contact between the striker and the specimen. Considering the value of the maximum displacement, the obtained data reveals that as the height of the impact increases, the specimen tends to deform with higher values of displacement.

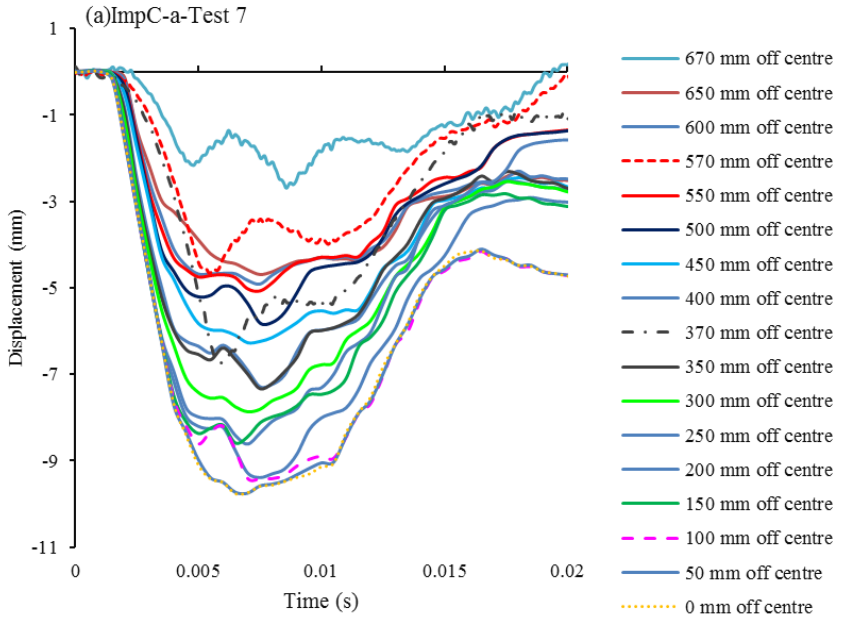

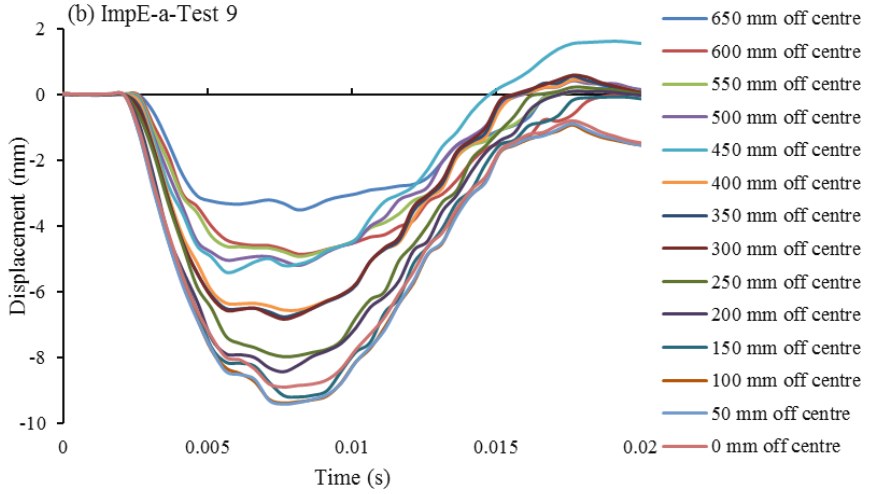
(b) ImpE-a-Test 9
Displacement (mm)
Time (s)
650 mm off centre
600 mm off centre
550 mm off centre
500 mm off centre
450 mm off centre
400 mm off centre
350 mm off centre
300 mm off centre
250 mm off centre
200 mm off centre
150 mm off centre
100 mm off centre
50 mm off centre
0 mm off centre

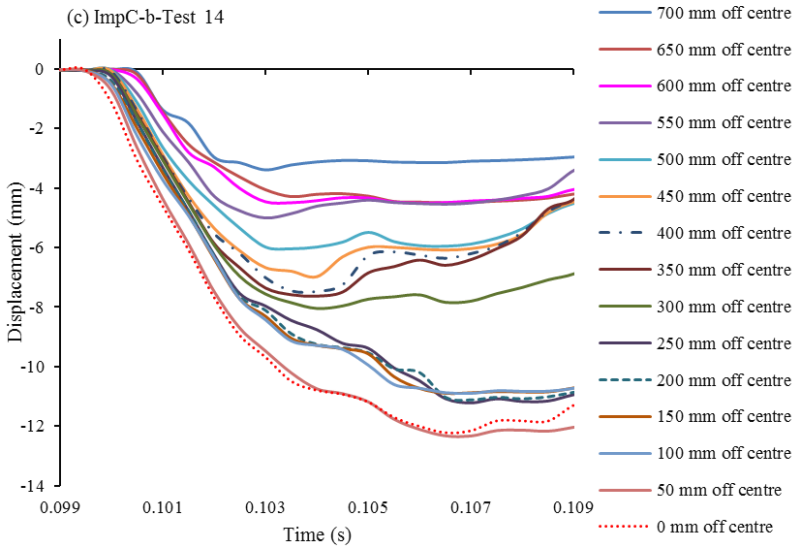
(c) ImpC-b-Test 14
Displacement (mm)
Time (s)
700 mm off centre
650 mm off centre
600 mm off centre
550 mm off centre
500 mm off centre
450 mm off centre
400 mm off centre
350 mm off centre
300 mm off centre
250 mm off centre
200 mm off centre
150 mm off centre
100 mm off centre
50 mm off centre
0 mm off centre

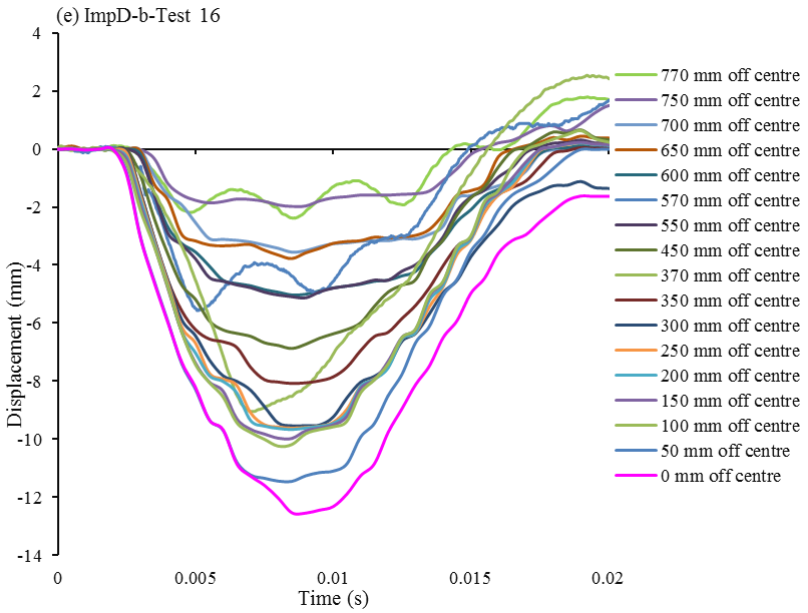

Figure 4-14 Variation of the vertical deflection of a series of points along the beam span located at distances ranging between 0 to 970 mm from the point of impact (mid-span) established through the combined use of a high speed camera and LVDTs for the case of a (a) medium (Tests 4 and 7) and (b) high (Tests 10, 12 and 16) intensity impact test.

Furthermore, the localised response can be also observed form the deformation profiles (Fig. 4.15 (a-h)) exhibited along the span of the beam when subjected to medium (Tests 4 and 7) and high intensity (Tests 10, 12 and 16) impact testing (tests 7 and 10 respectively). The deformation profile of the specimen obtained at maximum impact load, suggest that immediately after the contact of the striker and the specimen, the value of the displacement is very negligible. In other words, the time at which the deformation of the RC beam attains its maximum value does not correlate with the time at which the applied impact load reaches a peak value. On the basis of these deformation profiles, it can be seen that during the initial stages of the loading process – until maxP_d is attained – the RC beam specimens exhibit localised response since essentially only the portion of the span of the RC element close to the impact region react to the imposed load. However, when the maximum value of deflection at mid-span is attained the full length of the specimens reacts to the applied load.

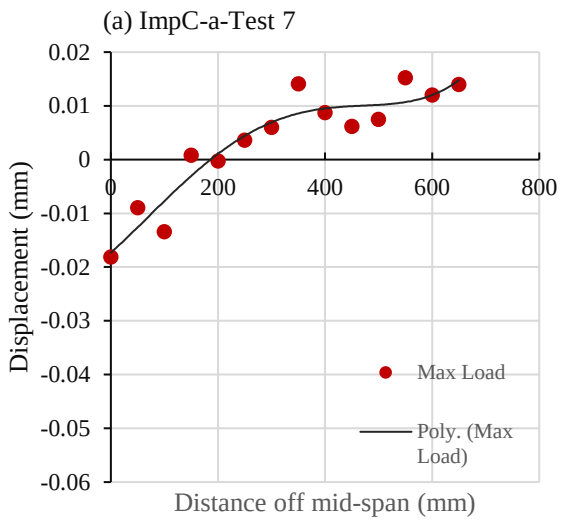
(a) ImpC-a-Test 7
Displacement (mm)
Distance off mid-span (mm)
Max Load
Poly. (Max Load)

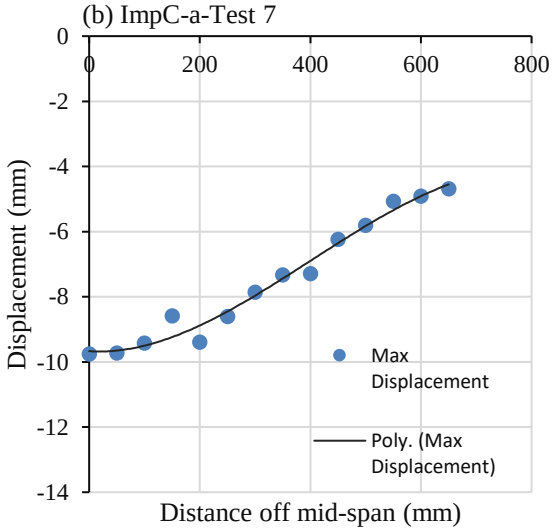
(b) ImpC-a-Test 7
Displacement (mm)
Distance off mid-span (mm)
Max Displacement
Poly. (Max Displacement)

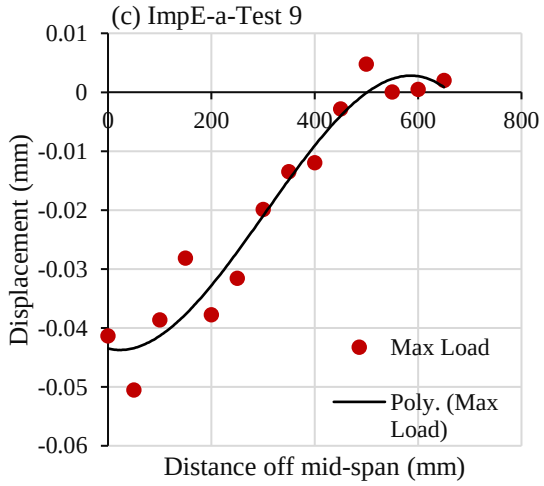
(c) ImpE-a-Test 9
Displacement (mm)
Distance off mid-span (mm)
Max Load
Poly. (Max Load)

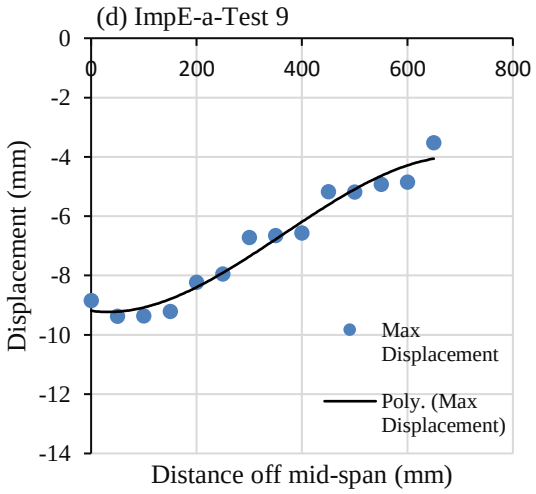
(d) ImpE-a-Test 9
Displacement (mm)
Distance off mid-span (mm)
Max Displacement
Poly. (Max Displacement)

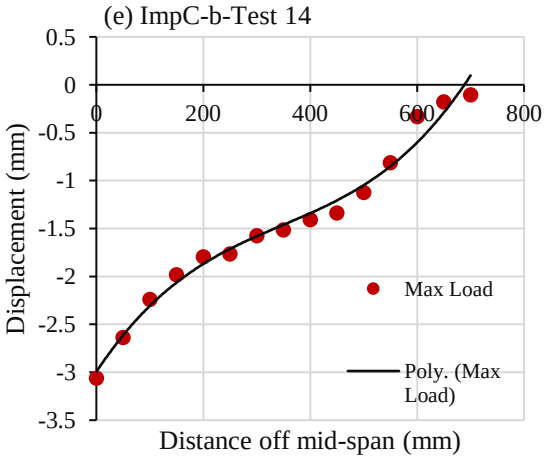
(e) ImpC-b-Test 14
Displacement (mm)
Distance off mid-span (mm)
Max Load
Poly. (Max Load)

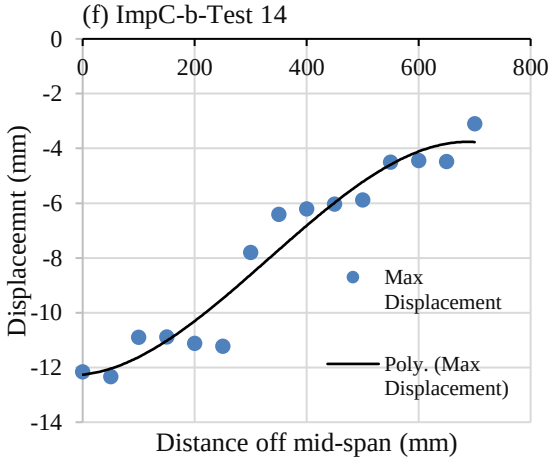
(f) ImpC-b-Test 14
Displaceemnt (mm)
Distance off mid-span (mm)
Max Displacement
Poly. (Max Displacement)

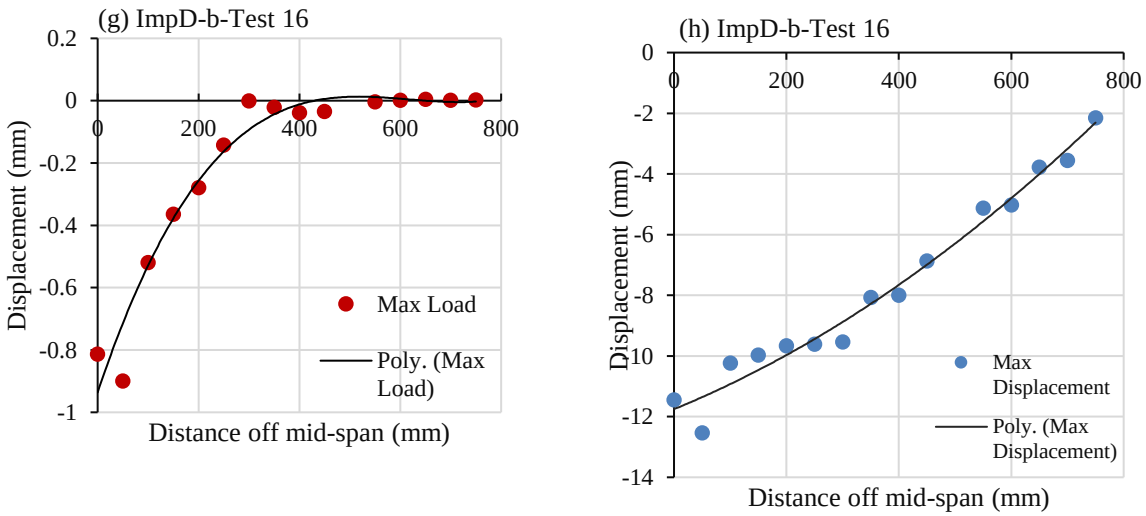

Figure 4-15 Deformation profile exhibited by the RC beam specimen established through the combined use of a high-speed camera and LVDTs when the maximum sustained force is attained and when maximum deflection is achieved for the case of (a) medium (Tests 4 and 7) and (b) high (Tests 10,12 and 16)intensity impact test.

4.7.3 Strain and strain rates

Fig. 4.16 show the variation of the strain and strain rate values recorded by the strain-gages (Ch13 and Ch14) located on the top surface of the beam (acting in compression) at a distance of 260 mm form mid-span (see Fig. 4.16) for Tests 4, 7, 10, 12 and 16. The strains and the associated strain rates were also measured throughout the height of the cross-section of the beam at the mid-span region of the beams through the use of the high-speed camera by measuring the change in distance between points on the specimen span.

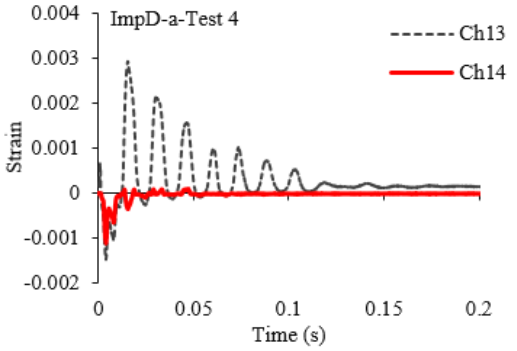
ImpD-a-Test 4
Ch13
Ch14
Strain
Time (s)

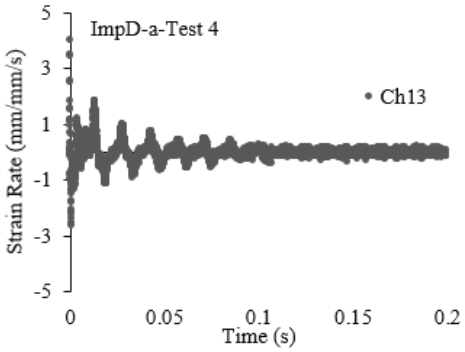
ImpD-a-Test 4
Ch13
Strain Rate (mm/mm/s)
Time (s)

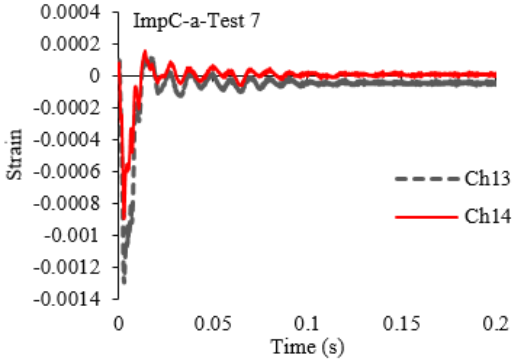
ImpC-a-Test 7
Ch13
Ch14
Strain
Time (s)

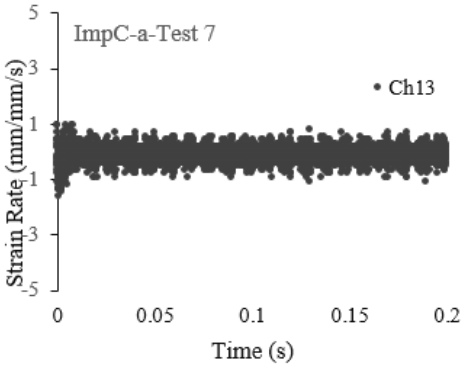
ImpC-a-Test 7
Ch13
Strain Rate (mm/mm/s)
Time (s)

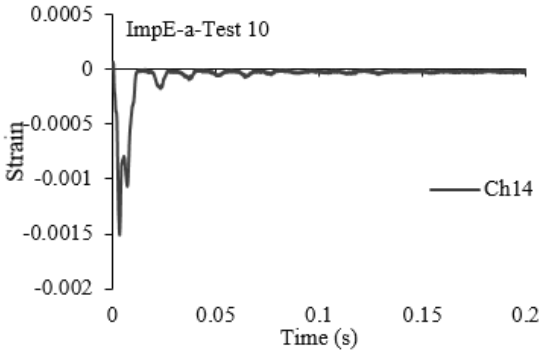
ImpE-a-Test 10
Ch14
Strain
Time (s)

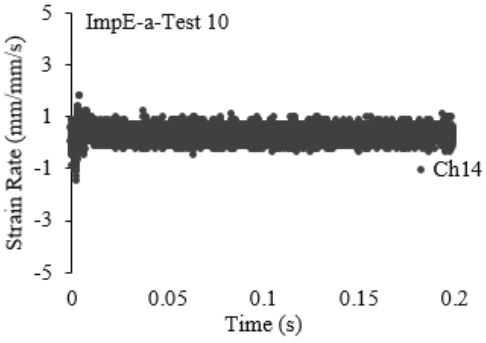
ImpE-a-Test 10
Ch14
Strain Rate (mm/mm/s)
Time (s)

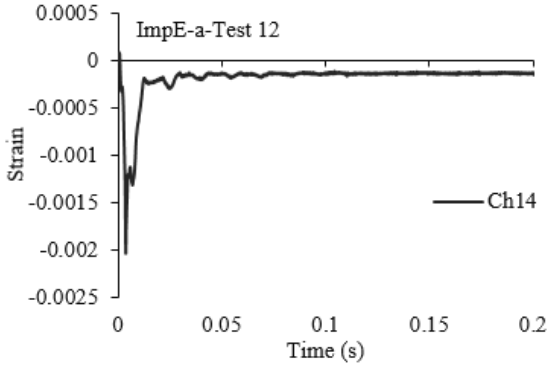
ImpE-a-Test 12
Ch14
Strain
Time (s)

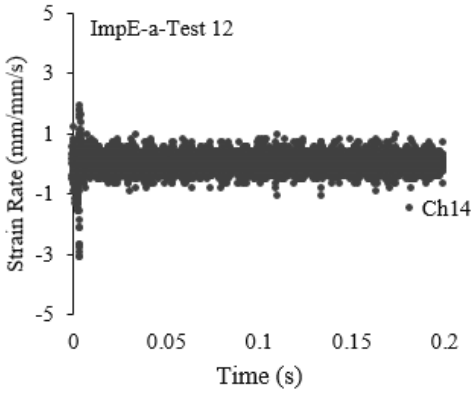
ImpE-a-Test 12
Ch14
Strain Rate (mm/mm/s)
Time (s)

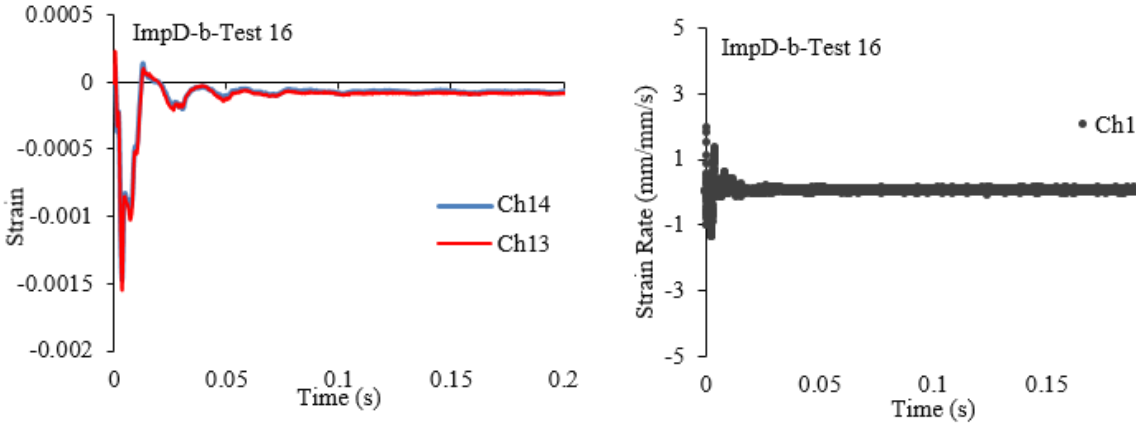

Figure 4-16 Variation of strain and strain rates measurements obtained from the strain gauges

Fig. 4.17 and Fig. 4.18 represent the variation of strain and strain rate values along the flexural crack near the impact region in the form of time histories obtained from Tests 4,7,10,12 and 16 through the analysis of high-speed camera recordings. Fig. 4.17 reveal that at the time at which the impact load reaches its maximum value (marked with dashed lines), the value of the strain is negligible for Test 4,10,12 and 16. However a few msec after the first contact between the striker and the specimen, the strain values increases to a maximum peak value. The time lag between t_{max} (i.e. the time corresponding to the peak value of impact) and the time that the stress wave reached each point (i.e. at which the strain values are measured) is marked as Δt in the figures. The latter has a value equal to zero for Test 7 which suggests the stress waves reaches the specified points (A-N) approximately at the same time as t_{max}. On the other hand, the time lag is more apparent in tests 12 and 16.

Furthermore, the variation of stain- time histories presented in Fig. 4-17 (a-d) reveal that the strain values measured at different distances with respect to impact region (i.e. A-B, C-D, E-F, G-H, I-J, K-L and M-N) do not initiate at the same time. The latter is an indication of a wave propagation problem along the height of the beam cross-section.

It is interesting to notice from the curves in Fig. 4-17 that compressive strain i.e. G-H (associated with negative values) are only exhibited close to the top surface of the specimen even during the initial stages of the loading process. This shows that cracking develops and propagate deep in the compressive zone even before the impact load attains its peak value. The strain curves presented in Fig. 4.17 are also used to estimate the values of strain rate exhibited at the top (acting in compression) and bottom (acting in tension) surface of the specimen at mid-span.

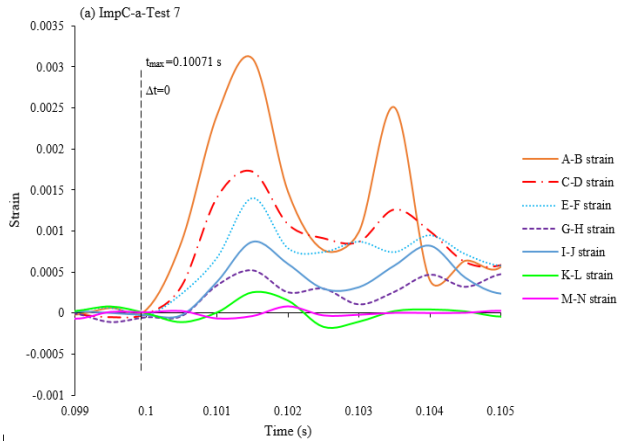
(a) ImpC-a-Test 7
t_{max}=0.10071 s
Δt=0
Strain
Time (s)
A-B strain
C-D strain
E-F strain
G-H strain
I-J strain
K-L strain
M-N strain

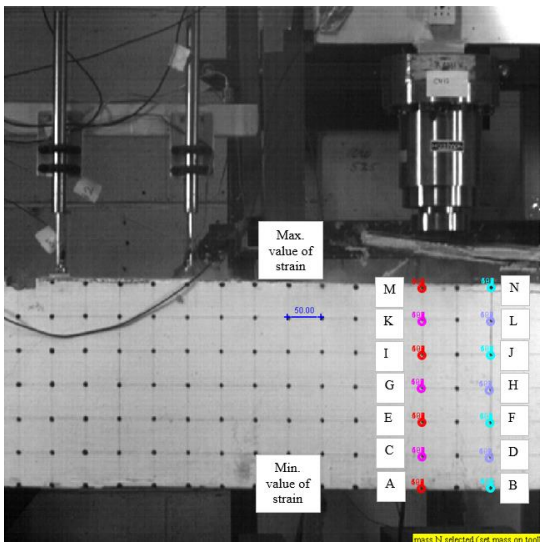
Max. value of strain
Min. value of strain
M
N
K
L
I
J
G
H
E
F
C
D
A
B

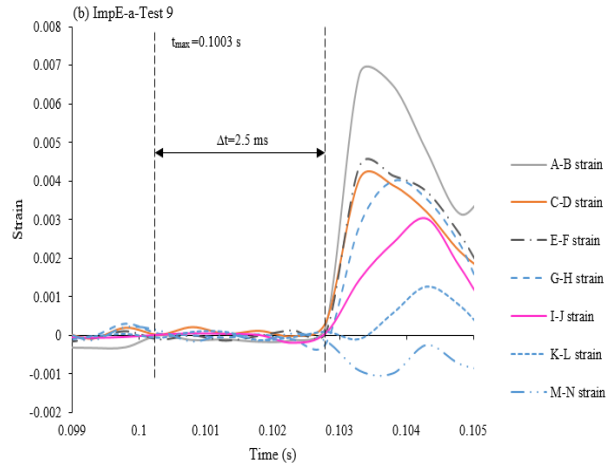
(b) ImpE-a-Test 9
t_{max}=0.1003 s
Δt=2.5 ms
Strain
Time (s)
A-B strain
C-D strain
E-F strain
G-H strain
I-J strain
K-L strain
M-N strain

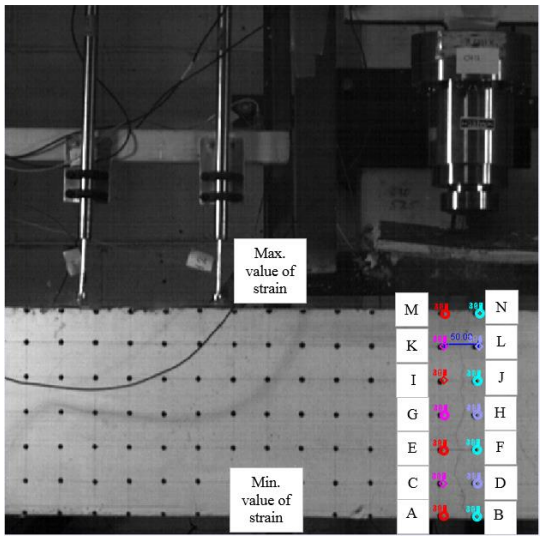
Max. value of strain
Min. value of strain
M
N
K
L
I
J
G
H
E
F
C
D
A
B

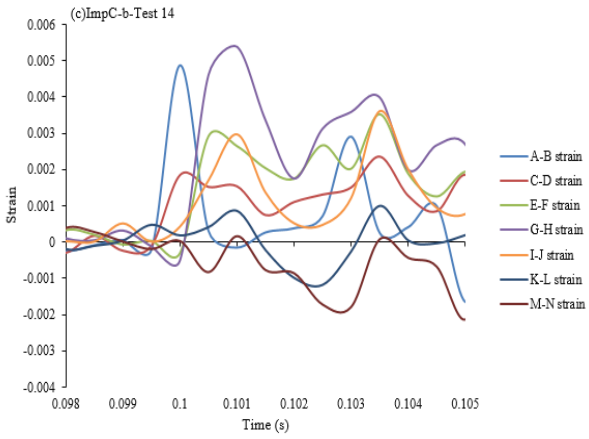
(c)ImpC-b-Test 14
Strain
Time (s)
A-B strain
C-D strain
E-F strain
G-H strain
I-J strain
K-L strain
M-N strain

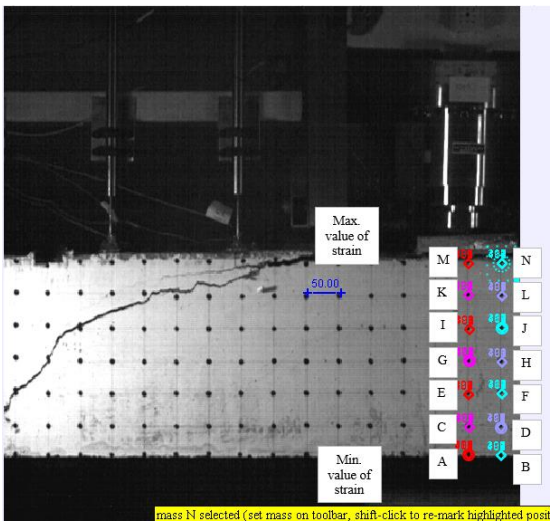
Max. value of strain
Min. value of strain
M
N
K
L
I
J
G
H
E
F
C
D
A
B
mass N selected (set mass on toolbar, shift-click to re-mark highlighted posit

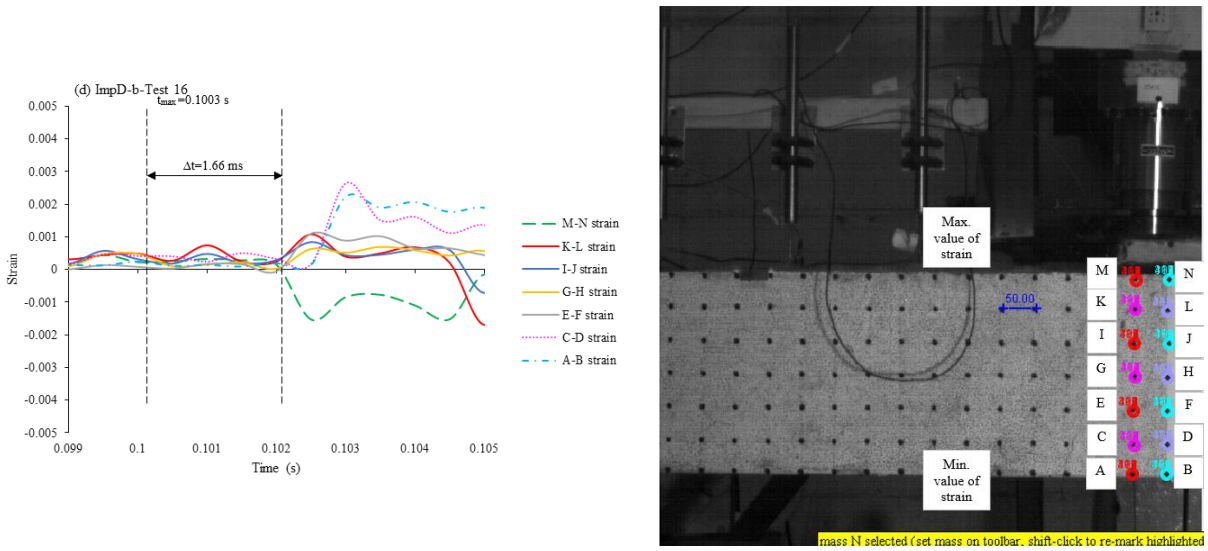

Figure 4-17 (Left) Locations at which the strain was calculated along the element height accompanied by the variation of (Right) strain with time at these locations

Regarding the value of strain rate, the maximum strain at the tensile region of the beam (i.e. A-B) was at 15,7,15,10.5 and 4.6 for Tests 4,7,19,12 and 16 respectively while the corresponding strain values corresponding to the compressive (top) region (i.e. M-N or k-L) were measured at 30,3,6,5 and 4.6 for Tests 4,7,10, 12 and 16 respectively (see Fig. 4.18).

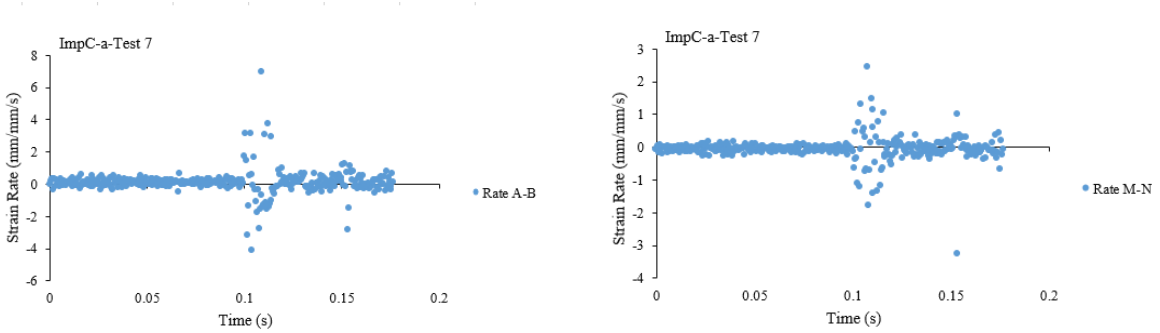

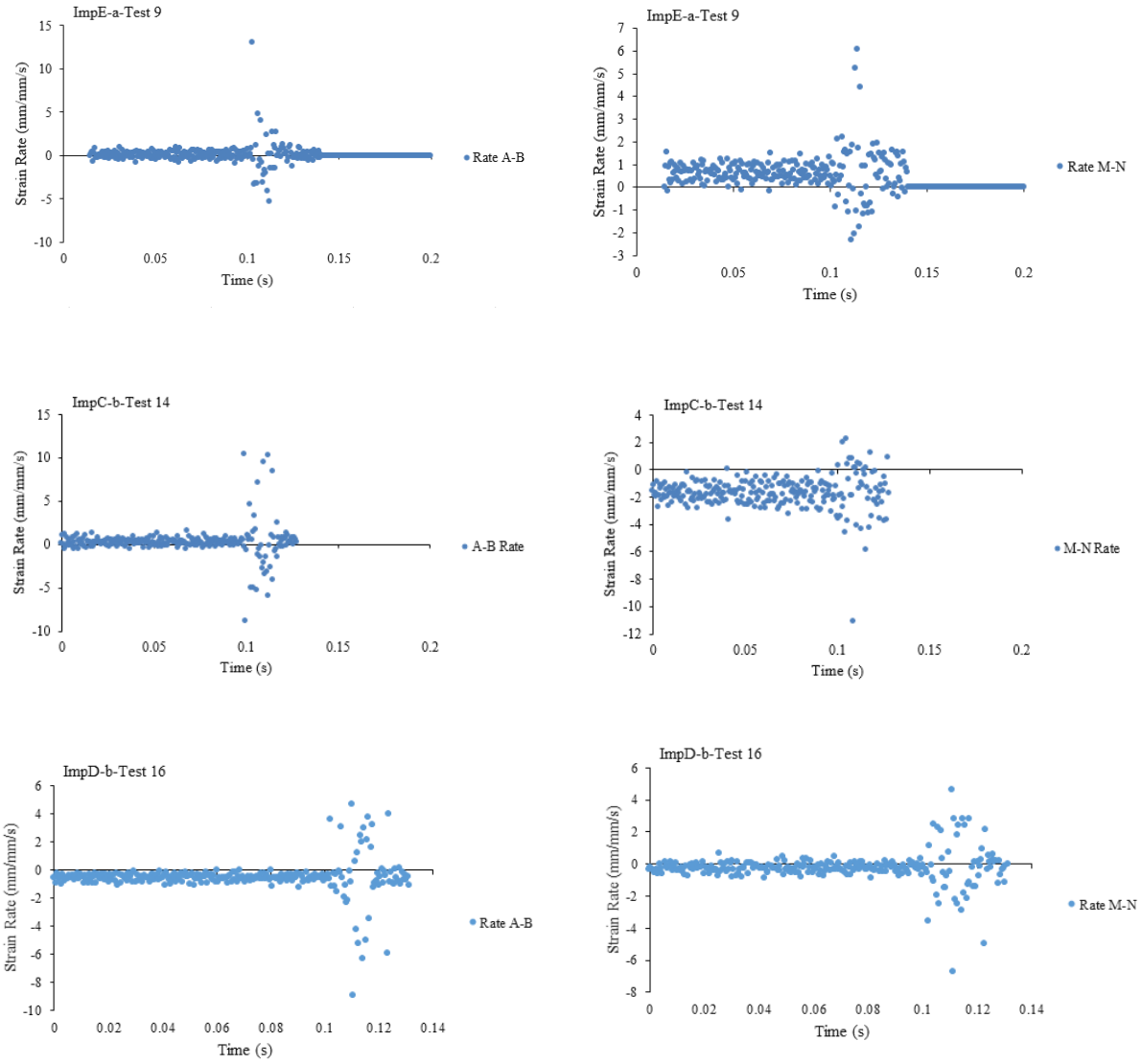

Figure 4-18 Strain rate time history calculated at the top and bottom of the beam cross-section

4.7.4 Cracking process and exhibited mode of failure

The variation of vertical displacement with respect to time measured at specific points along the left-hand portion of the specimen (see Fig. 4.14) in relation to impact time-history obtained from Tests 4,7 and 16 are presented in Fig. 4.19. During the first impact (i.e. peak), the value of displacement measured is insignificant, the maximum value of the displacement was achieved only after the second contact between the striker and the specimen. The latter suggests that the impact-induced stress waves do not reach the points until the subsequent impacts (2nd or 3rd) take place. Furthermore, the value of maximum displacement indirectly influenced by the height from which the impactor is dropped.

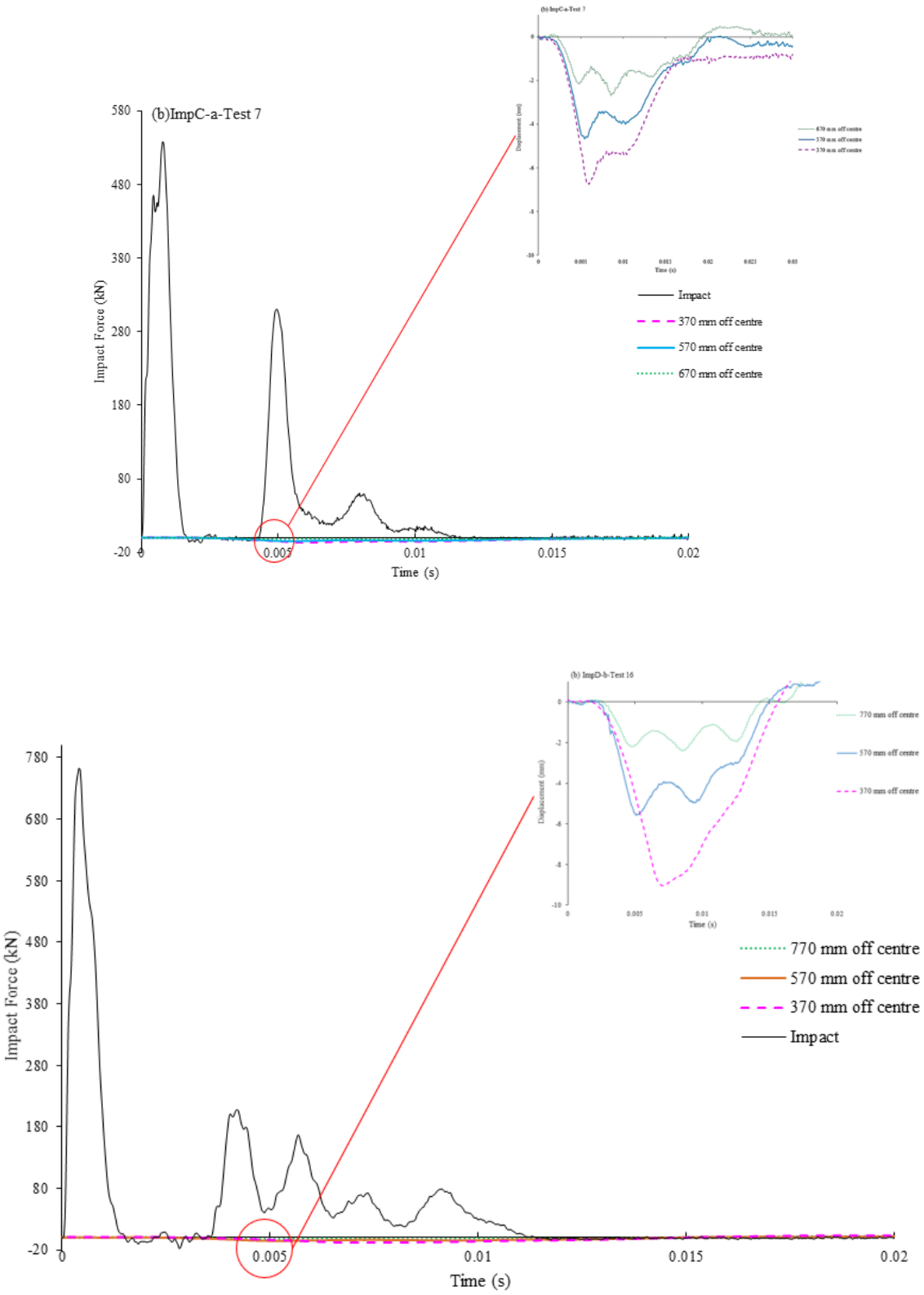

Figure 4-19 Impact force and displacement time history at maximum load (a) Test 7, (b) Test 16.

Fig. 4.20 shows the crack exhibited after the static, dropped-weight testing and residual static testing of RC specimens C, D and E. Different stages of the loading and cracking process measured during tests 7,9,14 and 16 are presented in Fig. 4.21 in the form of frames.

The latter were obtained from analysing high-speed video recordings. Adopting the assumption that the overall crack patterns developing are approximately symmetrical the high-speed camera mainly focuses on the left-hand side portion of the subject specimens (between the mid-span region and the left support). The frames presented in Fig. 4.21 show the cracking process exhibited immediately after the impactor comes into contact with the top surface of the RC beam at mid-span. From these photos, it is observed that flexural cracks form and penetrate deep in the compressive zone very early in the loading process. After the maximum impact force is attained (i.e t_{max} = 0.10071,0.10030,0.1005 and 0.108 s for tests 7,9,14 and 16 respectively), the latter cracks increase in width and extend even further into the compressive zone. It is interesting to note that the cracking pattern observed during impact tests are globalised in the sense that the entire span of the test objects reacted to the applied impact load. The latter is compatible with its static counterpart. As can be seen from Fig. 4.20 the crack pattern associated with the static loading do not depart significantly from impact loading.

SD-Static

ImpD-a-1st Impact-Test 1

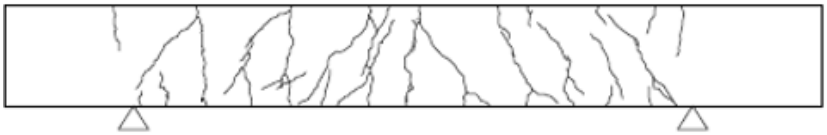

N/A

ImpD-a-2nd Impact-Test 2

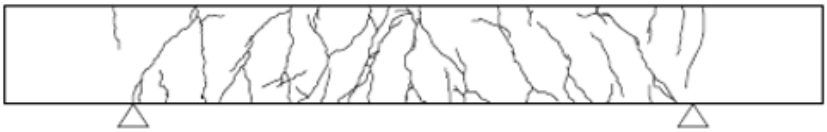

N/A

ImpD-a- 3rd Impact-Test 3

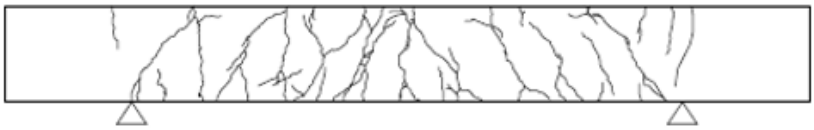

704 kN/ms

ImpD-a- 4th Impact-Test 4

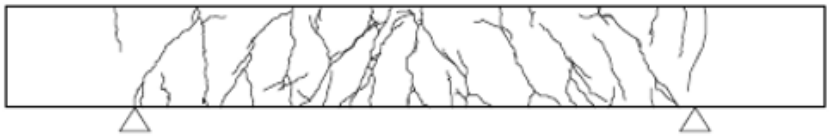

1194 kN/ms

ImpD-a- 5th Impact-Test 5

1270 kN/ms

ImpD-a- 6th Impact-Test 6

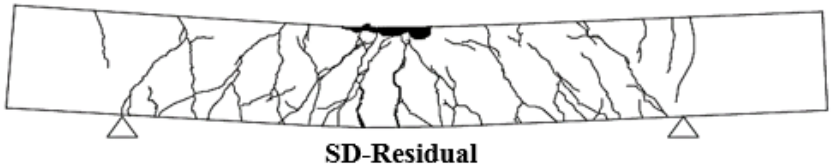

SD-Residual

ImpD-b- 1st Impact-Test 16

ImpD-b-2nd Impact-Test 17

ImpD-b-3rd Impact-Test 18

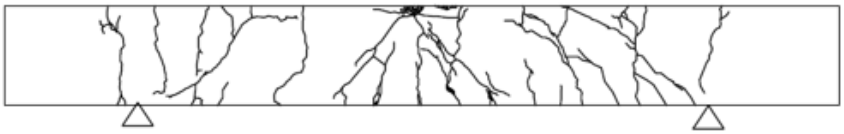

ImpD-b-4th Impact-Test 19

SC-Test

660 kN/ms

ImpC-a-1st Impact-Test 7

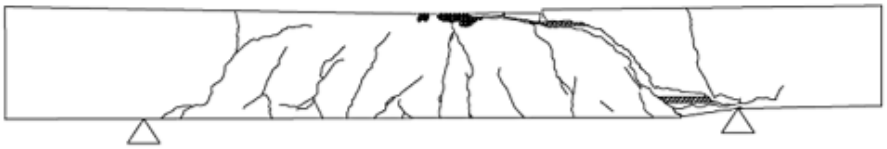

870 kN/ms

ImpC-a-2nd Impact-Test 8

N/A

ImpC-b-1st Impact-Test 14

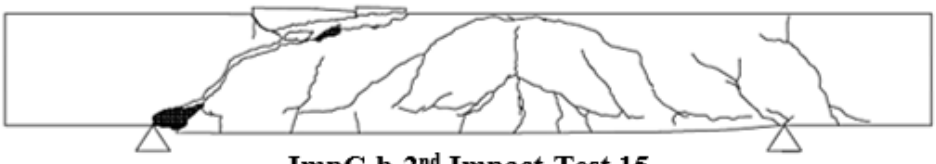

N/A

ImpC-b-2nd Impact-Test 15

SE-Test

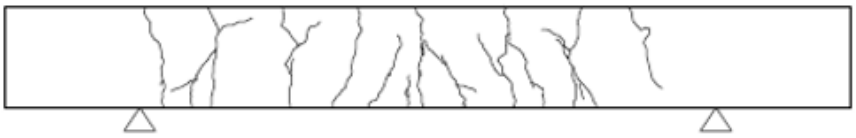

N/A

ImpE-a-1st Impact-Test 9

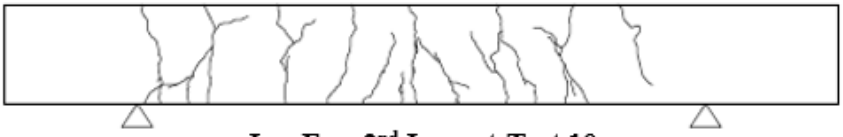

948 kN/ms

ImpE-a- 2nd Impact-Test 10

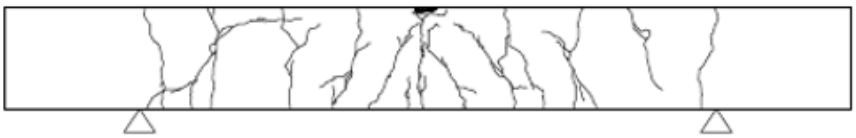

965 kN/ms

ImpE-a-3rd Impact-Test 11

1548 kN/ms

ImpE-a-4th Impact-Test 12

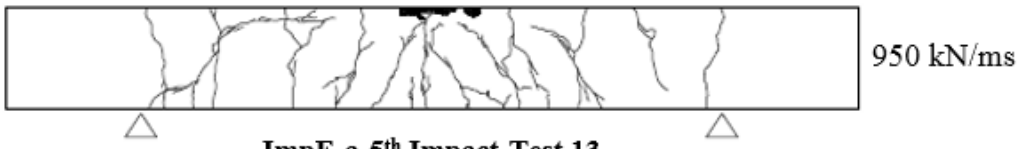

ImpE-a-5th Impact-Test 13

SE-Residual

Figure 4-20 Cracking (localised) failure

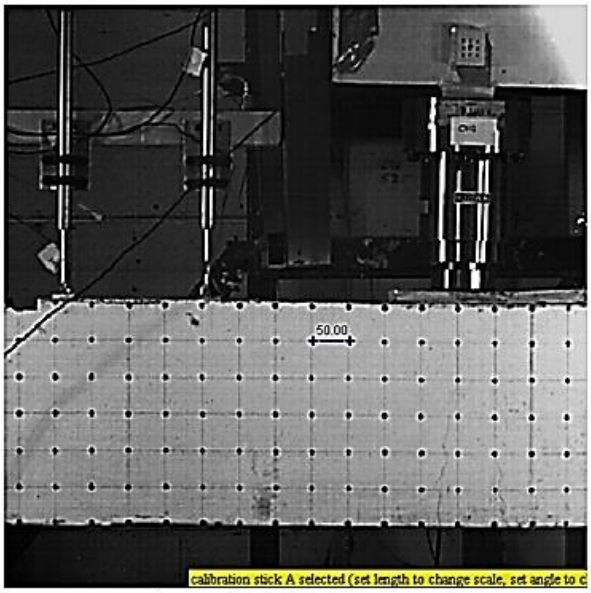

(Immediately before contact)

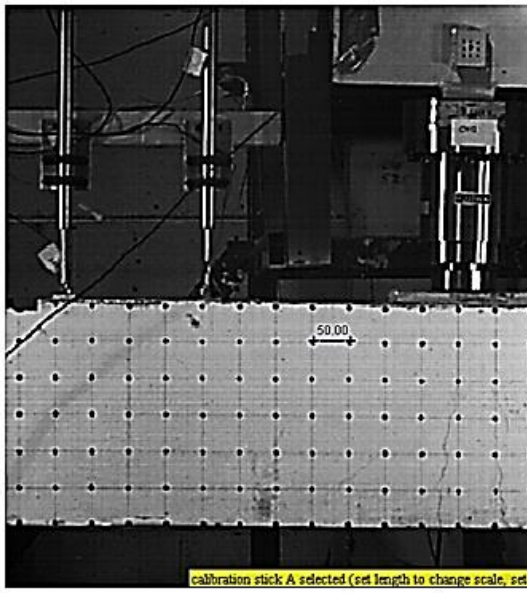

t_{max}= 0.73 msec (at *max*P_d)

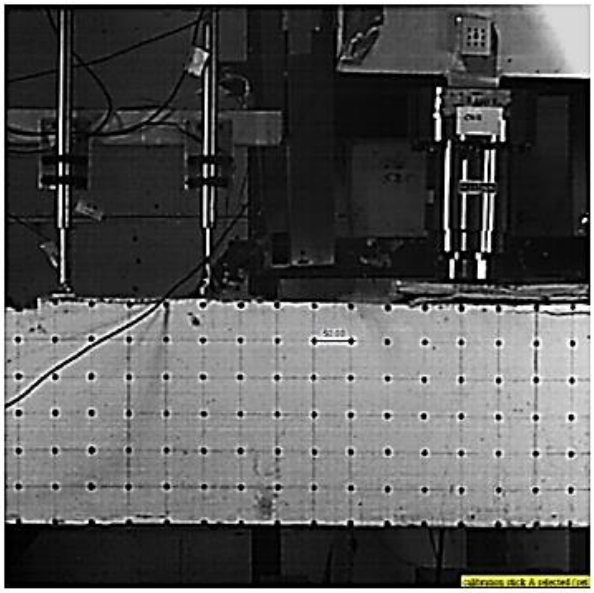

t= 11.8 msec (uplift of the impactor)

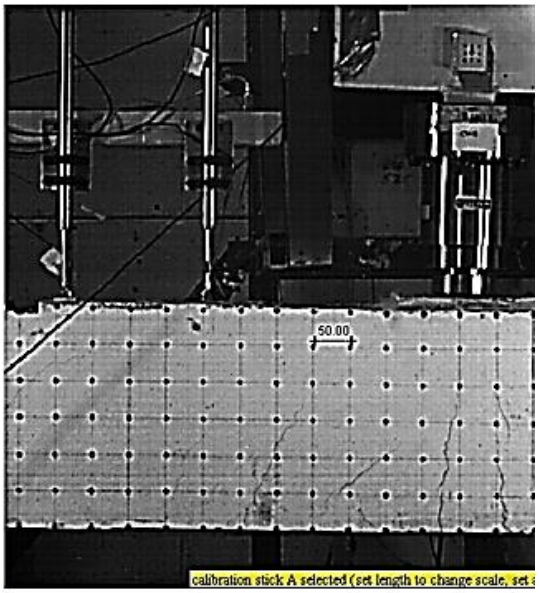

t=7 msec (at maximum mid-span deflection)

(a) Test 7

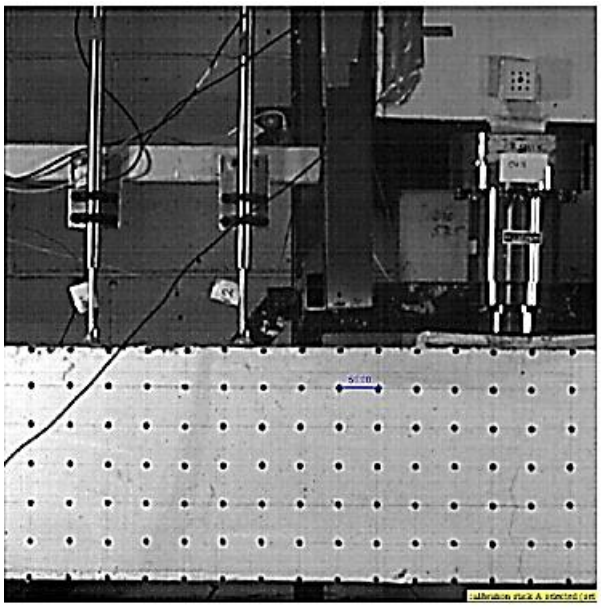

t= N/A (1/2 P_{max})

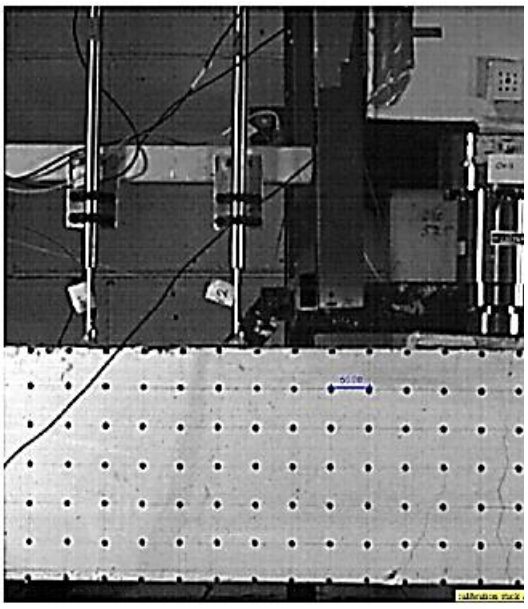

t_{max}= N/A (P_{max})

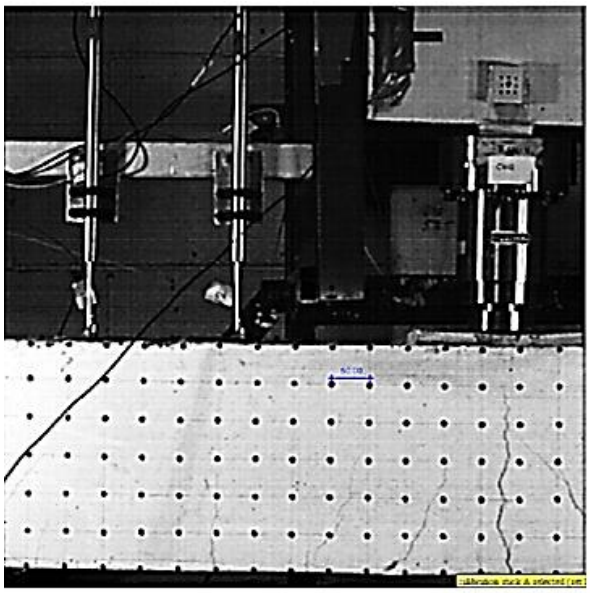

t_{max}= 7.6 msec (δ_{max})

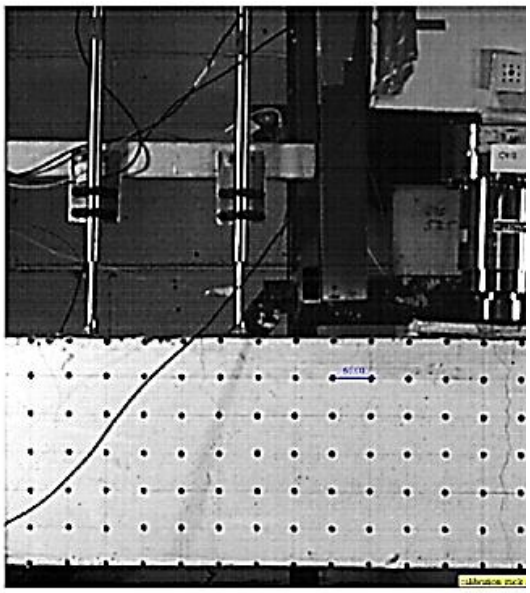

t=N/A (Unloading)

(b) Test 9

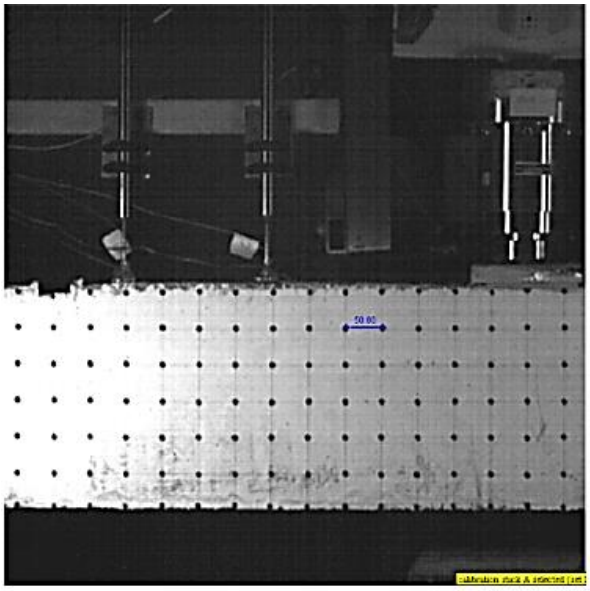

t= N/A (1/2 P_{max})

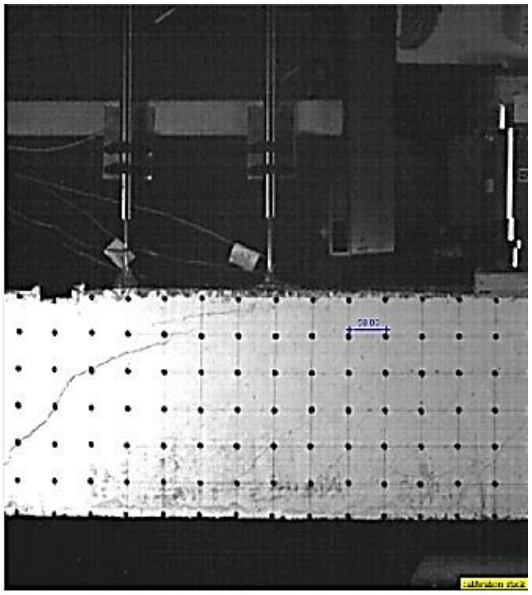

t_{max}= N/A s (P_{max})

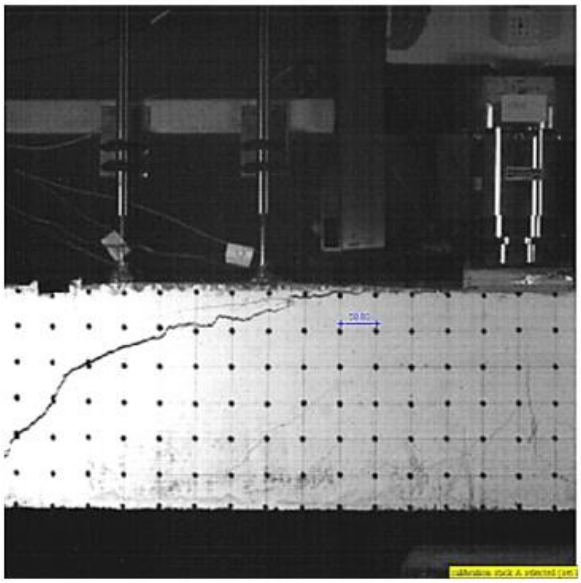

t_{max}= 107 msec

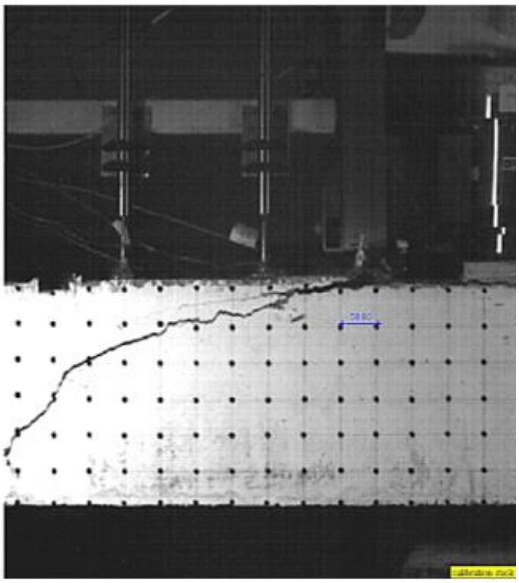

t=N/A (Unloading) s

(c) Test 14

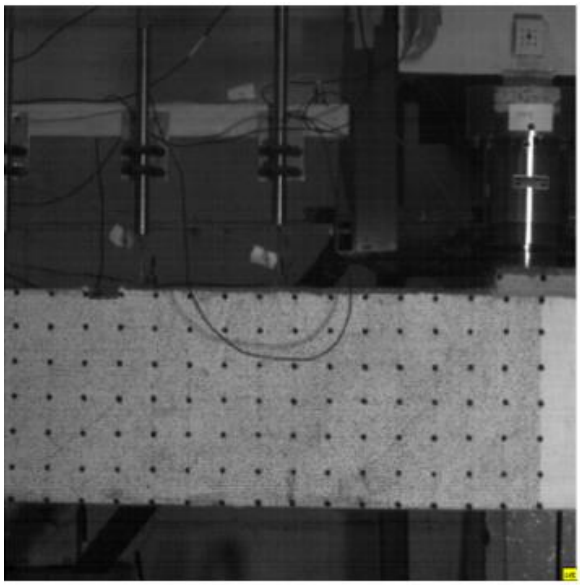

t= 0.1001 s (1/2 P_{max})

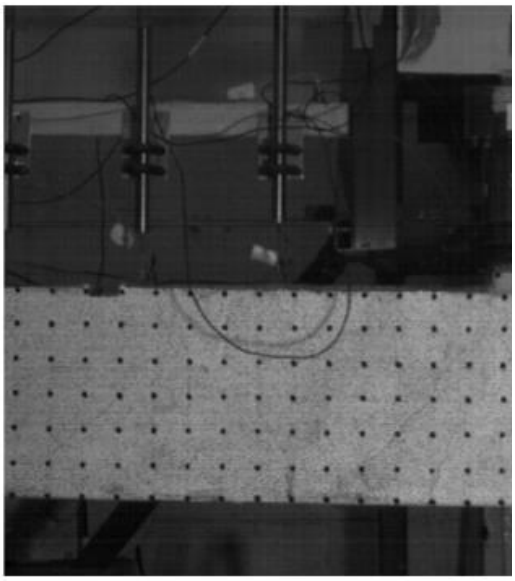

t_{max}= 0.1003 s (P_{max})

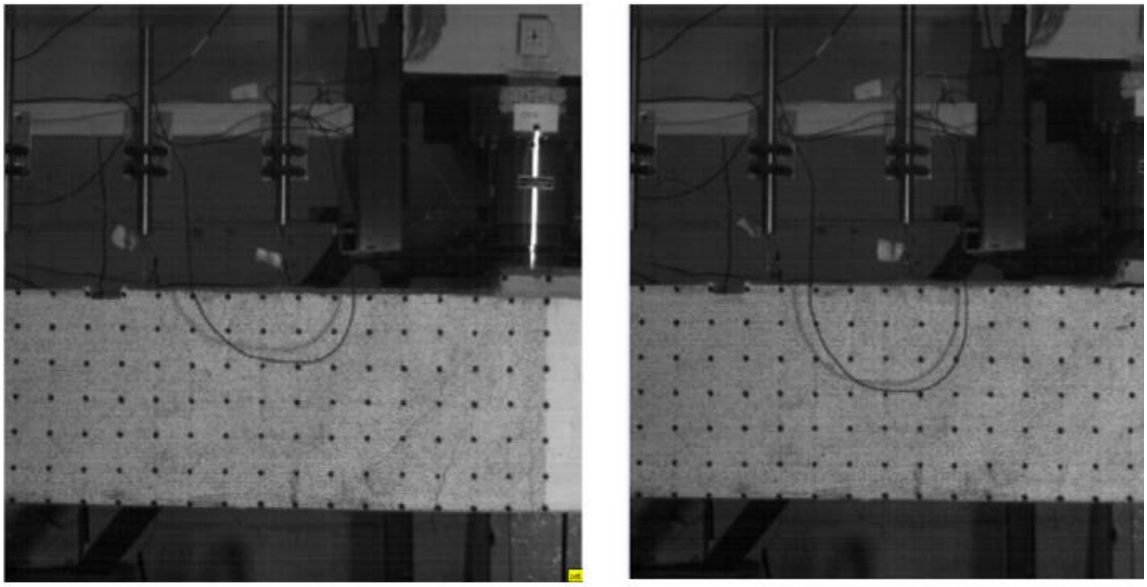

(d) Test 16

Figure 4-21 Cracking process that the specimen undergoes throughout the loading process during (a) Test 7 (b) Test 9 (c) Test 14 and (d) Test 16

4.8 BEHAVIOUR OF DAMAGED SPECIMENS UNDER STATIC LOADING

In order to assess the residual load-carrying capacity of RC beam, specimens D and E were tested under equivalent static loading. Fig. 4.22 shows the reduction of static capacity and stiffness of specimens D and E. These specimens were pre-damaged since they had already been subjected to drop-weight testing. When subjected to static testing the existing cracks sustained during drop weight testing began to widen with increasing levels of applied static loading. The mid-span displacement was recording using an LVDT placed underneath the mid-span of the beam specimen. The concrete cover on the top surface of the specimen gradually further disintegrated and the compressive reinforcement became exposed. Once the applied a load reached a certain level of loading the compressive reinforcement buckled due to the absence of concrete to restrain them. Overall, although the pre-damaged RC beams exhibit a load-carrying capacity close to that established by the undamaged specimen the overall stiffness of the specimen and ductility characterising their behaviour are considerably reduced due to the level of damage (cracking) sustained and the disintegration of the concrete in the compressive region.

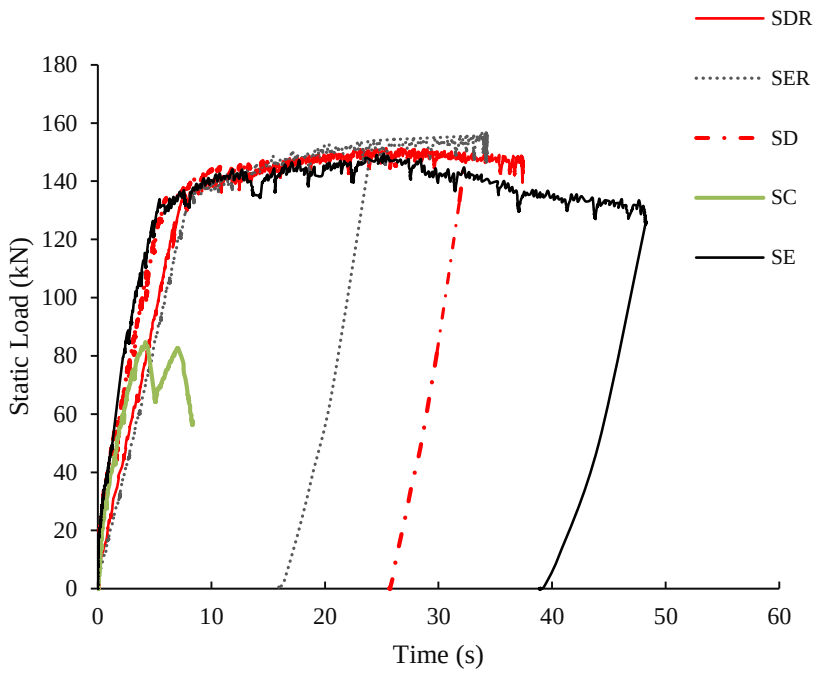

Figure 4-22 Comparison between the static and residual capacity of the specimen

4.9 DISCUSSION

The following section focuses on the comparison between the behaviour of (i) the slender beams (characterised by values of a_v/d = 6.75) described in Chapter 3 and (ii) the shorter beams (characterised by values of a_v/d = 2.83) discussed in the current chapter characterised when subjected to impact loading. Overall, it was observed that in the case of the slender beams the value of the maximum sustained load ($maxP_d$) recorded during impact testing was significantly higher compared to their load-carrying capacity ($maxP_s$) under equivalent static testing. This difference (between $maxP_d$ and $maxP_s$) is significantly smaller in the case of the shorter specimens considered. The latter findings are presented graphically in Fig. 4.23 expressing the variation of the dynamic increase factor (DIF=$maxP_d/maxP_s$) with the loading rate. The factors attributing to this shift in specimen behaviour are discussed below.

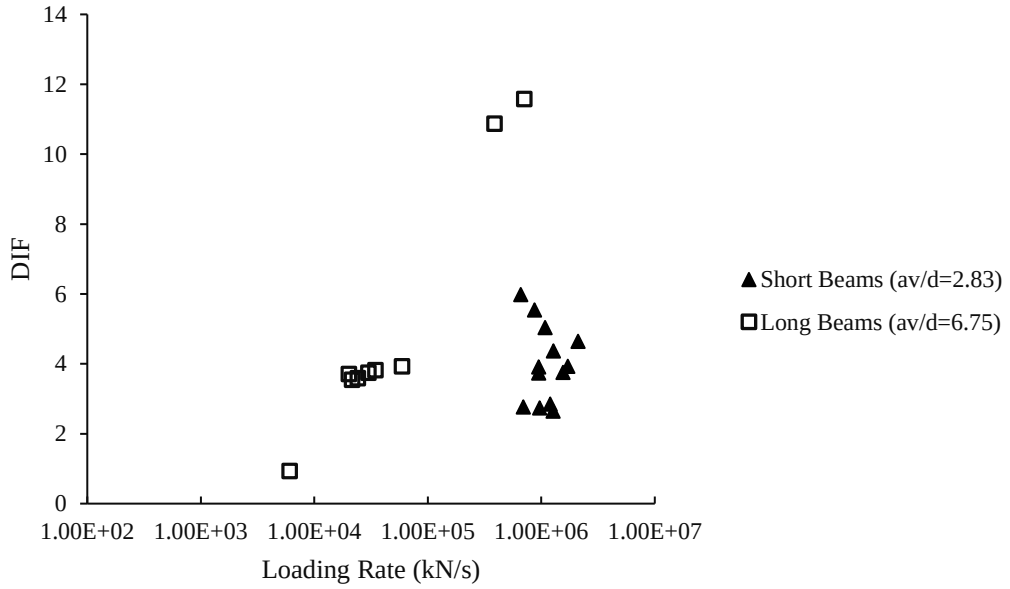

Figure 4-23 Variations of DIF with increasing loading rate

As discussed in Chapter 3, slender RC beams exhibit a higher increase in maximum sustained load ($maxP_d$) when subjected to increasing values of loading rate compared to that observed in the case of the shorter RC beams considered in the present chapter. This can be explained when considering the problem at hand (the collision of the drop-mass onto the RC beam specimen) as a wave propagation problem during which the stress-waves generated during in the impact region travel towards the supports through a highly nonlinear medium (full of discontinuities and cracks) such as concrete. In many cases (depending on the loading rate) failure (or cracking) can often occur prior to these waves reaching the supports resulting in a localised response.

In the case of the shorter beams, less time is required for these waves to reach the supports (due to the smaller distance that they are required to travel) and as a result, a larger portion of the span of the specimen (i.e. L_{eff}) reacts to the imposed impact load. Therefore, the response exhibited by the short beams when subjected to impact loading tends to be more global. Based on the above the increase in the length of the effective length (i.e. the portion of the span of the beam reacting to the imposed impact load) can lead to a reduction of the value of the *DIF* in the case of the shorter beams (see Fig. 4.23).

Shorter beams (characterised by $a_v/d < 5$) are more likely to exhibit a brittle (shear) mode of failure if they do not have a sufficient amount of transverse reinforcement. The latter is often accompanied by the formation of inclined/shear cracks, forming immediately after impact (see Fig. 4.21c) penetrating rapidly deep into the compressive region near the impact region. Such cracks are more likely to occur in the case of short beams with an insufficient amount of shear links. Furthermore, the cracking patterns observed along the span of the short beams when subjected to impact loading are similar to those formed during equivalent static loading. The above can be linked to the global response exhibited by the short beams under both static and impact loading due to the fact that the full span of these specimens appears to react to the imposed load. The slender beams under impact loading were generally found to exhibit a more ductile response leading to the formation of flexural cracks on top and bottom face of the beam, see Figs. (3.42-3.45). However, the cracking was significantly more localised concentrating primarily around the impact region. Furthermore, it was observed that only a portion of the specimen span reacted to the imposed load. This reduction in the length of the specimen reacting to the imposed impact load results in a significant shift in specimen behaviour with increasing loading rate compared to that established under equivalent static loading. As a consequence, the mode of failure becomes more brittle (and often explosive) as the rate of loading increases.

During the impact testing of the short beams, cracking initiates almost immediately after the collision of the steel impactor onto the beam and extends rapidly upwards. This is confirmed by both the photographic evidence and the strain record, which shows that the strains become tensile very early in the loading process. Therefore, it can be concluded that the strains recorded during testing do not correspond to concrete behaving as a continuum, but to a portion of the beam that also contains significant cracking. Thus, in reality, the strain-rate record essentially expresses the speed at which the cracks propagate or widens, thus practically describing the rate of deformation for a certain area of concrete which has already failed. As a consequence, attributing the increase of the beam's load-carrying capacity to the strain-rate sensitivity, which characterises the material properties of concrete, becomes questionable at least for the case investigated in the present study.

After subjected to impact loadings the specimens exhibit no steel buckling on the top surface (acting in compression) and therefore it can be assumed that they still have a residual load-carrying capacity. Static tests were performed on two pre-damaged beams in

order to investigate the remaining residual load-carrying capacity and deformation ability. Beam Types D, E (containing higher amounts of shear links) failure was exhibited at loads close to those associated with flexural capacity. Specimens type C (containing fewer amounts of shear links) exhibited shear failure.

It is interesting to note that the magnitude of the maximum impact load measured during initial (first) impact did not change significantly when the specimens were subjected to consecutive impacts (i.e. 2nd, 3rd and etc). However, the same was not observed in the case of the peak value of the peak reaction forces. The latter value reduced significantly with every consecutive impact test. Such significant dissipation of energy can be due to the formation of cracking or yielding of the reinforcement, since as discussed before the ductility of the short beams were found to be insignificant, the cracking is more likely to be associated with the reduction of maximum peak reaction forces. It is worth pointing out that the crack-widths developing along the specimen span directly influences the ratio of the impact to reaction load in the sense that the larger the crack widths developing results in higher ratios to be measured.

4.10 CONCLUSIONS

A total one nine short RC beams were tested under static or impact loading. The experimental data recorded was then compared with that obtained from impact tests carried out on longer slender beams. The focus of the investigation was to study in detail the effects of shear span-to-depth ratio as well as the shear reinforcement on the structural response of members when subjected to impact loading. Emphasis focuses on the differences observed in the deformation and cracking profiles developing under different stages of the loading process, the mode of failure exhibited, the magnitude (intensity) of the impact and reaction forces generated during testing.

In the case of the slender beams, the value of the maximum sustained load ($maxP_d$) recorded during impact testing was significantly lower compared to their load-carrying capacity ($maxP_s$) specimens under equivalent static testing. This difference (between $maxP_d$ and $maxP_s$) the is significantly smaller in the case of the shorter specimens considered.

The number of stirrups provided in the short beams should be carefully considered particularly under impact loading as it governs the mode of failure. Nevertheless, even in the case of beams with no shear links, the overall response tends to be global and the cracking process and mode of failure appears to be similar to that observed under equivalent loading.

High values of strain rate in the mid-span area of the beam are exhibited once the concrete medium suffers considerable cracking. As a result, these high values of strain rates do not describe concrete material behaviour but are linked to post-failure behaviour of a cracked area of the beam.

The strain rate exhibited during the critical early stages of impact testing (immediately after the impact load is applied) were found to be lower than the threshold established experimentally over decades of testing describing the variation of the concrete compressive and tensile strength under different strain rates. Thus, the increase in load-carrying capacity with the rate of loading observed in the present study cannot be attributed to an increase in the material strength due to strain rate sensitivity.

The terms failure and load-carrying capacity require careful qualification as it will first be necessary to establish the post-impact performance criteria (such as the residual strength required and the level of damage that can be tolerated) in order to arrive at meaningful estimates. This is particularly important in design terms and clear performance criteria similar to those employed in the design of RC structures under static loading (BSI, 2004) need to be established for impact conditions.

The digitisation and photogrammetric analysis process employed in the present work produced data that are in good agreement with the displacement and strain measurements, confirming the viability of high-resolution high-speed photography and its particularly useful role in validating data generated by conventional instruments such as strain gauges and deflection transducers.

CHAPTER 5 NUMERICAL INVESTIGATION

5.1 INTRODUCTION

Published data (Cotsovos *et al.*, 2008, Cotsovos, 2010, Saatci and Vecchio, 2009, Kishi *et al.*, 2011, Abbas *et al.*, 2010, May *et al.*, 2006, Cotsovos and Pavlović, 2012) obtained from drop-weight experimental tests on RC beams indicates that the response under impact loading differs significantly from that established during equivalent static testing, resulting in an increase of the maximum sustained load and a reduction in the portion of the beam span reacting to the impact load. However, there is considerable scatter making it difficult to ascertain the effect of loading rate on various aspects of RC structural responses. Crucially, most of the available test data obtained from drop-weight tests conducted on RC beam specimens is associated with a *post*-impact specimen physical state often characterised by significant concrete disintegration and low values of residual stiffness and load-carrying capacity. To address this, a dynamic NLFEA-based parametric study was carried out to assess the true ultimate limit state (ULS) and associated load-carrying capacity exhibited by the specimens when subjected to different loading rates.

Due to the limitations associated with the available experimental data, a numerical investigation is carried out in this chapter studying the effects of loading rate and intensity on the behaviour of different RC structural beams when subjected to impact. The study focuses on identifying the fundamental reasons for the experimentally observed shift in specimen behaviour (i.e. the apparent increase in strength and stiffness) when a certain threshold of loading rate is exceeded. A description of the nonlinear iterative solution procedure adopted by the program adopted, the method used for modelling cracking, the constitutive model adopted to describe concrete material behaviour, the RC structural forms investigated as well as the failure criteria employed are initially provided. This is then followed by the presentation and analysis of the predictions obtained describing the behaviour of the RC beam specimens considered in this chapter under static and high rate (impact) loading conditions.

5.1.1 Limitations of existing NLFEA packages

NLFEA forms a safer and more efficient method (compared to drop-weight testing) for investigating RC structural response under impact loading. To date, a range of NLFEA packages has been employed to study the RC structural response under impact loading. The use of such packages allows the study of more complex structural forms (compared to the simple structural configurations studied experimentally) while providing a more detailed description of the exhibited response (i.e. stress and strain distribution, deformation profiles, failure modes and crack patterns) throughout the loading process. However, the majority of the available NLFEA packages incorporate models of concrete behaviour, the derivation of which has been based on the regression analysis of test data obtained from static uniaxial compression and tension tests on plain concrete specimens (Cotsovos and Pavlovic 2008 [a,b]). Furthermore, they often assume that concrete material is strain-rate dependent (sensitive) and employ laws (in the form of dynamic increase factors) describing the variation (increase) of key material properties (e.g. modulus of elasticity, concrete compressive and tensile strength, yield and ultimate stress of steel) with strain-rate. The analytical formulation of these material models includes a number of parameters which are mainly linked to post-peak concrete characteristics such as strain softening, tension stiffening, and shear-retention ability. Such parameters are defined at the structural, rather than at the material level and attribute ductile characteristics to concrete behaviour not compatible with its brittle nature and not justified by the available test data (Cotsovos and Pavlovic 2008 [a, b]). As a result, the use of such parameters can affect the objectivity of the numerical predictions obtained since they require recalibration depending on the type of problem investigated.

5.1.2 Aims of the current numerical investigation

The current numerical investigation aims to;

(i) Achieve further insight into the mechanics underlying RC structural response under the increasing rate of impact loading by providing predictions which are complementary to the available test data.

(ii) Conduct parametric studies realistically accounting for the (brittle) material behaviour of concrete and the characteristics of the problem at hand (a wave propagation problem within a highly nonlinear medium) in order to assess the true load-carrying capacity of the beam specimens under increasing loading rates and intensities.

5.2 GENERAL ASPECTS OF THE FE MODEL PRESENTLY ADOPTED

In this study, the numerical investigation is carried out using a well-established commercial finite element software ADINA V.9.3.1. ADINA shares a number of characteristics with RCFINEL (Kotsovos 2014) which has been found capable of providing realistic predictions concerning the response of a wide range of RC structural configurations under static and dynamic loading. The material model employed by ADINA for describing concrete behaviour stems from the analysis of experimental data obtained from tests conducted on concrete cylinders under triaxial loading conditions (Kotsovos 2014). It is fully defined by a single material parameter - the uniaxial cylinder compressive strength f_c and accounts for the brittle nature and triaxiality characterising concrete material behaviour.

The smeared-crack approach is adopted for modelling cracking. The development of a crack is followed by immediate loss of load-carrying capacity in the direction normal to the plane of the crack. At the same time, the shear stiffness is also reduced drastically to about 10% of its value before the occurrence of the crack. Each integration point can develop up to three cracks. The above will be described in more detail in the following sections.

5.2.1 Modelling material behaviour

As mentioned before, the concrete material model employed by ADINA (ADINA 2017) stems from the experimental data obtained from tests conducted on concrete cylinders under triaxial loading conditions (summarised by Kotsovos and Pavlović 1995, Kotsovos 2015) and it describes concrete material behaviour as brittle. It is referred to in ADINA as 'data fitted concrete material model' and is considered to realistically account for the brittle nature and the triaxiality which characterises concrete material behaviour. Its formulation is characterised by both simplicity (fully brittle, with neither strain-rate nor load-path dependency, fully defined by a single material parameter - the uniaxial cylinder compressive strength f_c) and attention to the actual physical behaviour of concrete in a structure. The model is based on the work of Kotsovos and Pavlović, (1995). The subject model has been successfully used to predict the behaviour of plain concrete prisms under increasing rates of uniaxial compressive and tensile loading (Cotsovos and Pavlović 2008 [a,b]). The predictions obtained from the latter studies suggest that the observed shift in plain concrete specimen behaviour under high rates of compressive and tensile loading is mainly attributed to parameters associated with structural response (i.e. inertia, boundary

conditions imposed and the geometry of the specimens) as well as the characteristics of the problem at hand (a wave propagation problem within a highly nonlinear medium) rather than to strain-rate sensitivity of material properties of concrete. Due to the assumptions underlying the development of the latter model the predictions obtained are always conservative (safe) and can potentially be used for design purposes with more confidence.

Based on the interpretation of the available test data provided by Kotsovos and Pavlović (1995) and Kotsovos and Spiliopoulos (1998[a,b]), the following material characteristic can be attributed to plain concrete;

- it can be assumed as an isotropic material with a nonlinear behaviour in compression followed by a brittle post-peak behaviour, which is characterised by an abrupt loss of load-carrying capacity once the ultimate strength is achieved.

- beyond peak load, the values of the Poisson's ratio can become greater than 0.5, therefore concrete can no longer be considered to be a continuous medium.

- micro-cracking fracture processes underlie the compressive behaviour of concrete up to failure. Macro-cracking (associated with localised failure of the material) is associated with the fracture processes occurring during failure. Micro-cracks are considered to extend in the direction of the maximum compressive principal stress and macro-cracks are considered to form orthogonal to the maximum tensile principal stress developing just prior to cracking.

- No appreciable stress-strain hysteresis loop occurs during unloading and reloading.

- failure can be captured in the stress space by a failure surface. Practically failure can occur first in all possible triaxial states of stress except the fully compressive triaxial stress state.

- proper characterisation of concrete behaviour requires the description of general triaxial stress-states, which are conveniently interpreted by the octahedral stresses.

- stress path independence characterises the experimental data that define the failure surface and stress-strain curves.

- The mechanical properties are considered independent of the loading rate.

- All material constants can be related to the uniaxial compressive strength of a cylinder specimen.

Based on the above, the data fitted concrete material model consists of;

i. A nonlinear experimental based stress-strain law in compression that is combined with a linear behaviour when concrete unloads/reloads and is in tension (see Fig. 5.1)
ii. An experiment-based stress failure surface function that defines when either cracking or crushing occurs in concrete (see Fig. 5.2)
iii. A post-failure response for cracking based on a smeared crack approach that allows cracks to close and reopen (see Figs. 5.3-5)

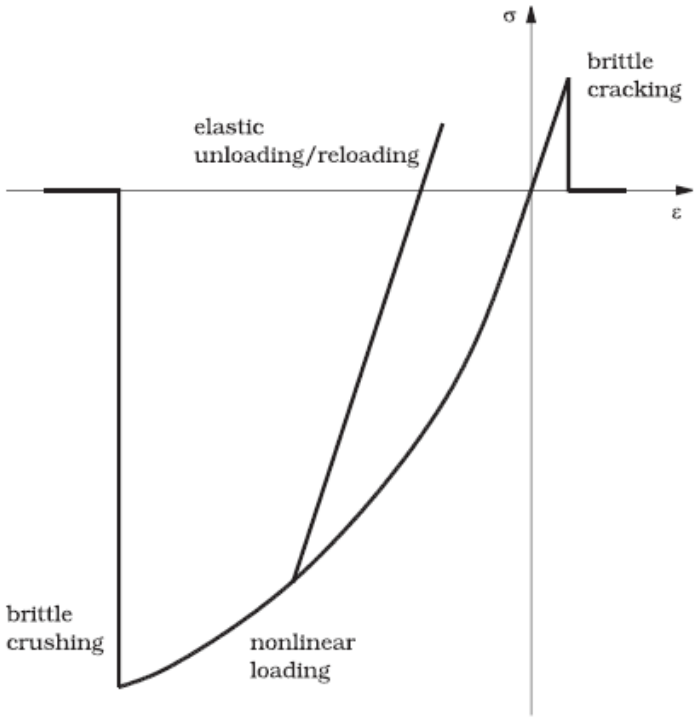

Figure 5-1 Stress-strain behaviour of the data fitted concrete material model (ADINA 2017).

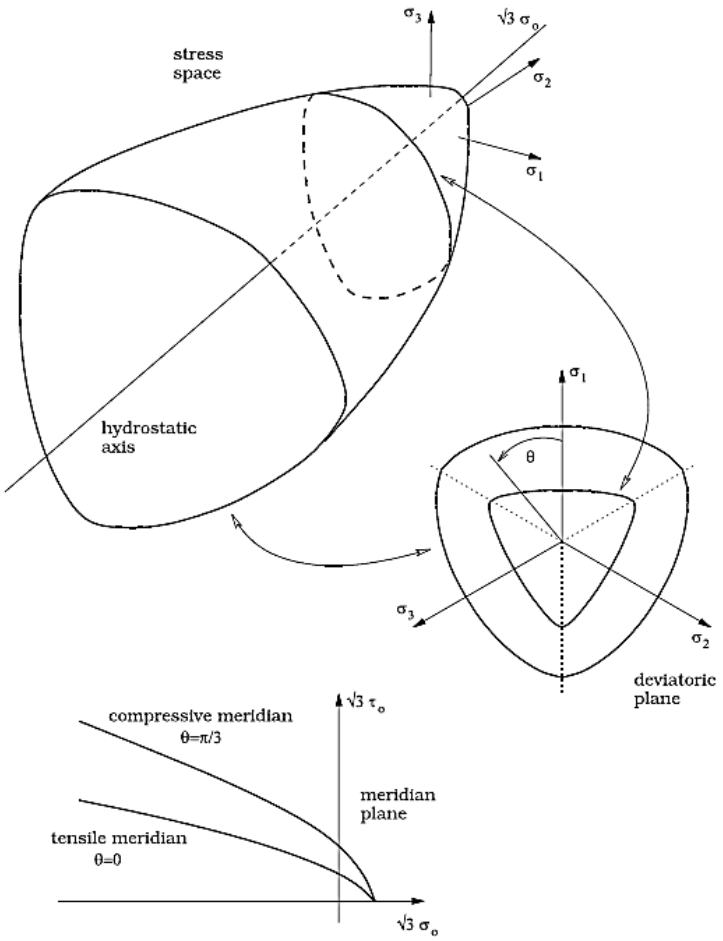

Figure 5-2 Failure surface of the data fitted concrete material model (ADINA 2017).

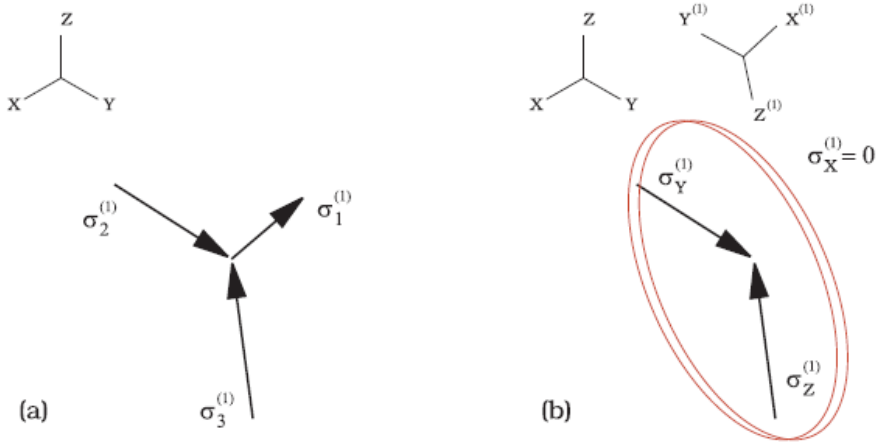

Figure 5-3 First crack formation of the data fitted concrete material model (a) before, and (b) after.

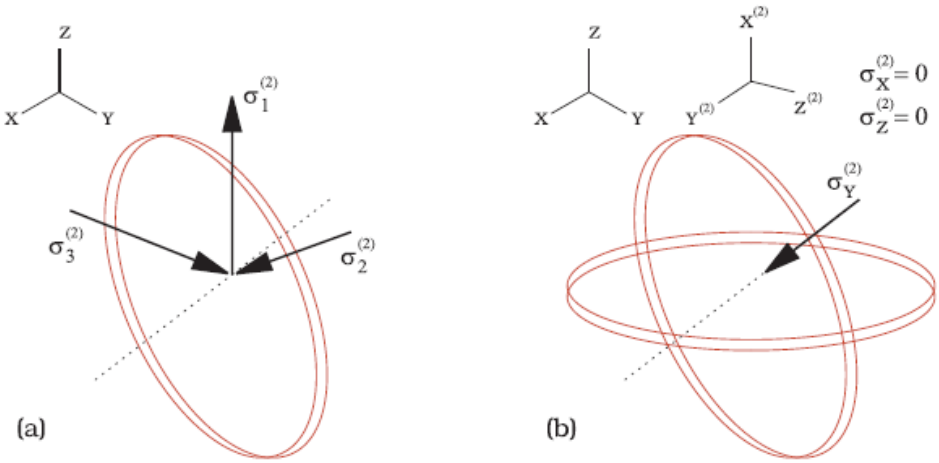

Figure 5-4 Second crack formation of the data fitted concrete material model (a) before, and (b) after.

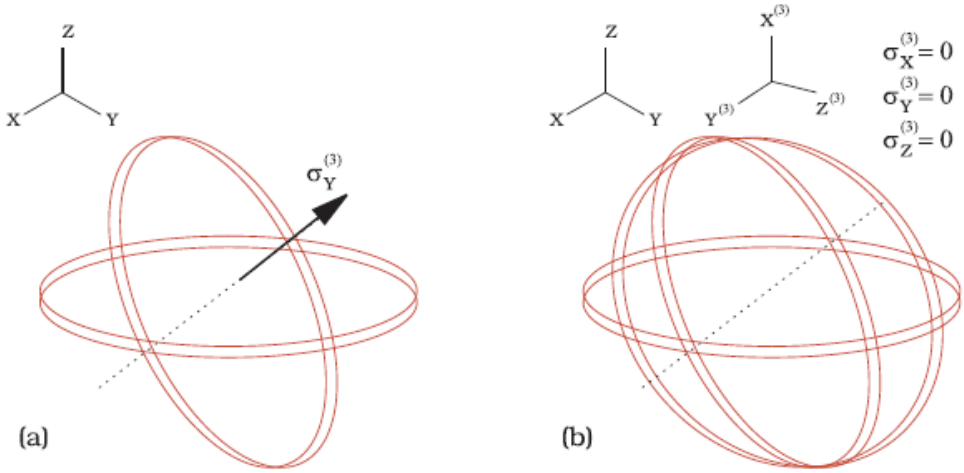

Figure 5-5 Third crack formation of the data fitted concrete material model (a) before, and (b) after.

The experimental data reported by Kotsovos et al. 1996 and 1998 is presented in terms of the octahedral normal and shear stresses (σ_0, τ_0), their corresponding octahedral strains (ε_0, γ_0) and the uniaxial cylinder compressive strength f_c material constant. Any stress state is a point in the stress space that can be represented by the principal stresses (σ_1, σ_2, σ_3) or, equivalently by the stress invariants (I_1, J_2, J_3) which are defined as;

$I_1=\sigma_{ii}=3\sigma_m$ first stress invariant, Eq. (5.1)

$J_2=\frac{1}{2} s_{ij}\, s_{ij}$ second deviatoric stress invariant, and Eq. (5.2)

$J_3=\det S_{ij}$ third deviatoric stress invariant Eq. (5.3)

where σ_{ii} and s_{ij} are the stress and deviatoric stress tensors respectively and σ_m is the mean stress. These stress quantities are related via the following expression;

$$\sigma_{ii}=s_{ij}+\sigma_m \delta_{ij} \quad \text{Eq. (5.4)}$$

where δ_{ij} is the Kronecker delta. A more convenient way (which is also geometrically intuitive) to express a stress state is by (I_1, J_2, ϑ) or (σ_0, τ_0, ϑ)

$$\vartheta=\frac{1}{3}\arccos\left(3\sqrt{3}\,J_3/2(J_2)^{3/2}\right) \quad \text{Eq. (5.5)}$$

Where ϑ is the angle of similarity (or Lode angle) on a deviatoric stress plane (i.e., any plane orthogonal to the hydrostatic axis), such that $0\leq \vartheta\leq\pi/3$. The octahedral normal and shear stresses are defined as;

$$\sigma_0=1/3I_1=\sigma_m \quad \text{Eq. (5.6)}$$

$$\tau_0=\sqrt{\frac{2J_2}{3}} \quad \text{Eq. (5.7)}$$

In ADINA (ADINA 2017), the data fitted concrete material model is defined by a single, material parameter-the uniaxial cylinder compressive strength f_c.

One of the featured of the data fitted concrete material adopted in the current numerical investigation is the inclusion of tension softening after cracking (see Fig. 5.6). The latter is assumed to follow a linear stress-strain curve and therefore, will replace the default brittle cracking behaviour. The tension softening is possible only for the one and two-crack state. In the one-crack state tension softening applied to $\sigma_X^{(1)}$, while in the two-crack state both $\sigma_X^{(2)}$, $\sigma_Z^{(1)}$, will follow the tension softening behaviour. The tension softening behaviour is defined by the fracture energy value and the characteristic length of the concrete model so as to ensure a numerical solution that is not dependent on the concrete's finite element mesh. The former is defined as the area under the tensile stress-displacement curve and can be taken as the length of the element along the direction perpendicular to the first crack plane and is depicted as ELEN in Fig. 5.6.

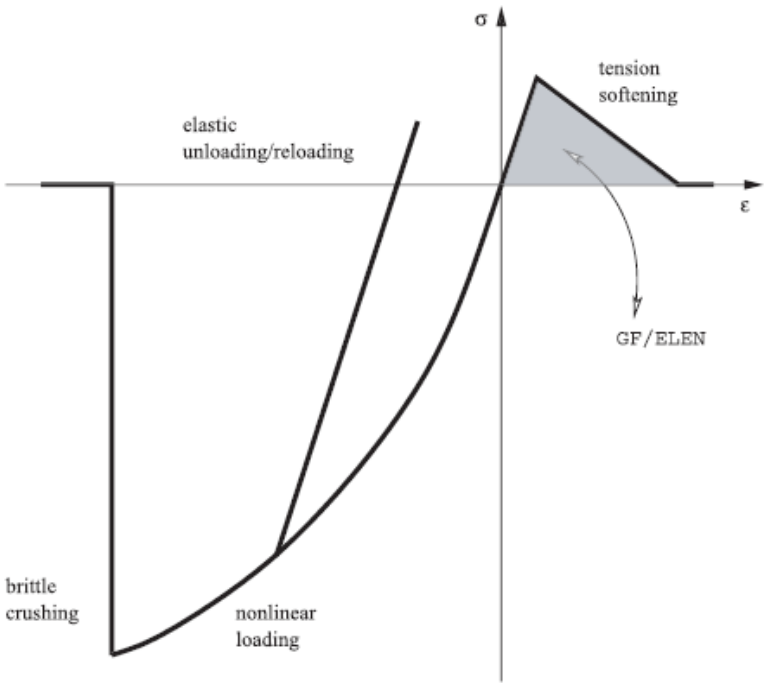

Figure 5-6 Stress-strain behaviour of the data fitted concrete material model

A simple bilinear elasto-plastic hardening model is employed for describing the behaviour of steel (see Fig. 5.7). Concrete and steel material behaviour is assumed to be independent of the loading-rate and full bond is assumed in order to describe the interaction between steel and concrete.

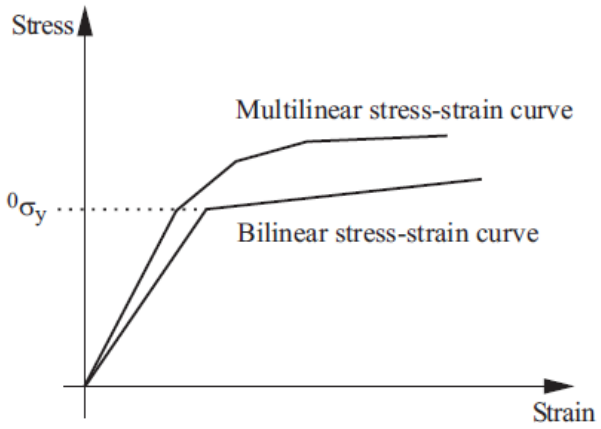

Figure 5-7 von Mises model

5.2.2 Modelling of cracking

The smeared-crack approach is adopted for modelling cracking. A crack forms when the stress developing in a given part of the structure (stresses are calculated at the integration point of the FE model employed) corresponds to a point in the principal stress space that

lies outside the predefined failure surface of concrete material, thus resulting in localised material failure. This failure takes the form of a crack and is followed by immediate loss of load-carrying capacity in the direction normal to the plane of the crack. At the same time, the shear stiffness is also reduced drastically to a small percentage (about 10%) of its previous value (before the occurrence of the crack). However, it is not set to zero in order to minimize the risk of numerical instabilities during the execution of the solution procedure, as explained elsewhere (Kotsovos 2015). It should be noted that each integration point can develop up to three cracks. The smeared crack approach, which governs part of the post-failure behaviour of the data fitted concrete material model follows a 'non-orthogonal fixed crack' type of modelling, that is, one that defines the crack planes of an integration point when they first occur such that they stay valid for the remaining of the simulation and where the crack planes are not necessarily orthogonal to each other. The modelling of a crack starts after cracking is detected by the failure surface function and hinges on the idea that concrete retains its strength only on the defined crack planes, which indicates a brittle type of cracking.

The criterion that identifies when a crack can be closed is dictated by comparing strain values along the direction of the stress that caused the formation of the crack. For the one- and two-crack cases, the direction is perpendicular to their corresponding crack planes, while for the fully cracked state it is along the line that defines the intersection of these two crack planes. In order to close a crack, the current strain value must be compressive and smaller than the strain value present when the crack was formed. An integration point presenting a closed crack can in a future time step remain with the closed crack or fail again. When failure is detected by the failure surface function, the corresponding integration point can either reopen the closed crack or crush. Note that cracks are assumed to be history-dependent and, therefore, a reopened crack will have the orientation defined when it was initially opened.

The other possible post-failure behaviour of the data fitted concrete material model is crushing, which characterises the brittle nature of concrete when subjected to compression. Crushing occurs when all the principal stresses (i.e. σ_1, σ_2, σ_3) are compressive and is modelled as a complete and permanent loss of load-carrying capacity and, therefore, all the stress components are set to zero (see Fig. 5.8). For numerical reasons, the corresponding

constitutive matrix is defined as the one for the fully cracked state but in the global coordinate system (ADINA 2017).

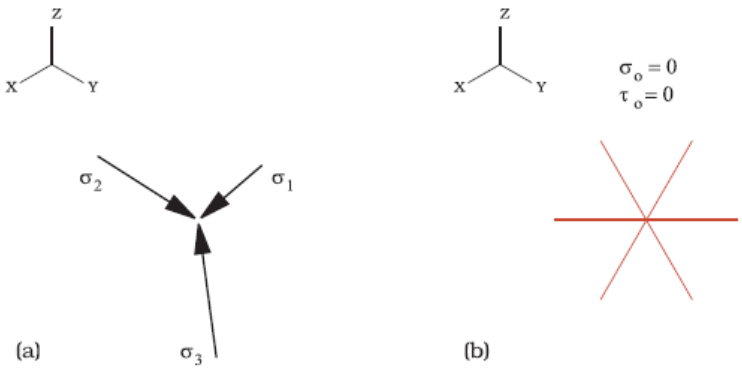

Figure 5-8 Crush modelling of the data fitted concrete material model (a) before, and (b) after.

5.2.3 Failure surface

The failure surface adopted through which the ultimate strength values of concrete is defined is derived from curves that best fit the experimental data portrayed in τ_0/f_c- σ_0/f_c plots. These data are presented on meridian planes which are considered as any planes that contain the hydrostatic axis and is defined by a constant angle of similarity. They are also presented on deviatoric planes, the latter is perpendicular to the hydrostatic axis and is defined by octahedral normal stress which is constant. It should be noted that due to the nature of the data, most of the relations that follow are only valid when the stress units employed are N/mm^2 or MPa. Below the failure surface function adopted for the brittle concrete material model in ADINA is presented;

$$g= \tau_0-\frac{0.944 f_c}{r}\left(TP-\frac{\sigma_0}{f_c}\right)^{0.724}-SPf_c=0 \qquad \text{Eq. (5.8)}$$

where: r : elliptic function

TP : percentage of f_c that represents the amount of tensile hydrostatic stress allowed by g such that $0.05 \leq TP \leq 0.1$

SP : percentage of f_c that represents the amount of additional octahedral shear stress allowed by g such that $0.0 \leq SP \leq 0.05$

If g > 0, then the stress state of concrete is ‘outside’ the failure surface and it is indicating that failure has occurred either in the form of a crack or crush. The cross-section of the failure surface that best fits the experimental data is defined by elliptic function This failure surface portrays a somewhat triangular cross-section for tensile and small compressive octahedral normal stresses, which tends to change to a somewhat circular cross-section for larger compressive octahedral normal stresses, which tends to change to a somewhat circular cross-section for larger compressive octahedral normal stresses (see Fig. 5.2). It should be noted that both TP and SP provide some level of flexibility to the failure surface by ‘stretching’ it in different directions. The former parameter ‘stretches’ the surface along the tensile side of the hydrostatic axis, while the latter ‘dilates’ it on the deviatoric plane.

5.2.4 Contact surface and contact algorithms

The interaction between the *‘concrete’* specimen and the *‘steel’* impactor was modelled in ADINA through the contact surface. Contact is ADINA is modelled using contact groups, contact surfaces, contact segments and contact pairs, as explained in detail in this section. In the current numerical investigation, 3D contact groups are adopted. A 3D contact surface is made up of a group of 3D contact faces (segments) either on solid elements (adopted for the current problem at hand), shell elements, plate elements or attached to rigid nodes. Fig. 5.9 illustrates a typical 3D contact surfaces and contact pair.

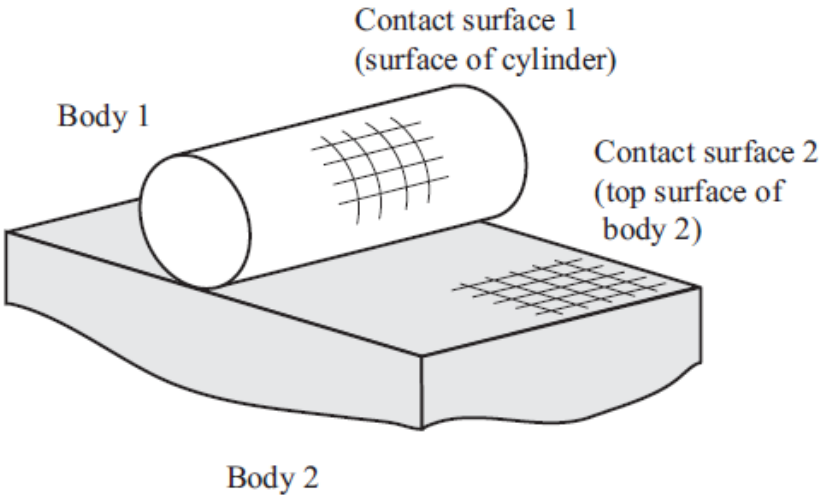

Figure 5-9 Typical contact surfaces and contact pair (ADINA 2017).

Two contact surfaces that may come into contact during the solution form a contact pair. One is aimed to be the ‘contactor surface’ and the other is selected as the ‘target surface’. Within a contact pair, the nodes of the contactor surface are prevented from penetrating the segments of the target surface, and not vice versa, see Fig. 5.10.

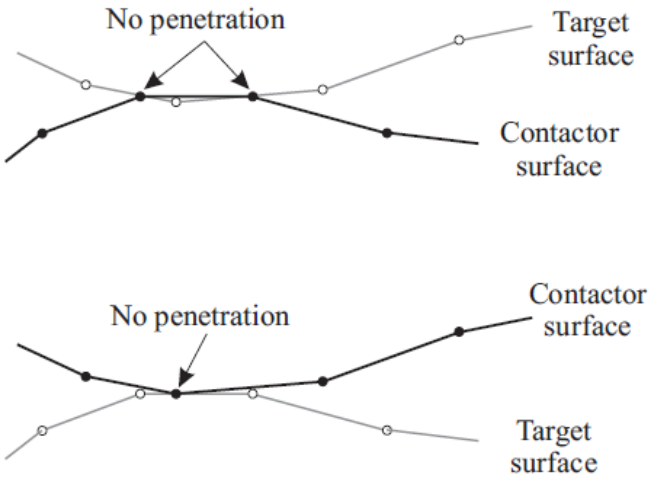

Figure 5-10 Contactor and target selection (ADINA 2017).

When considering two surfaces coming into contact, one surface is set as the ‘contactor surface’ and the other is as the ‘target surface’. The nodes of the contactor surface are prevented from penetrating into the segments of the target surface, and not vice versa, see Fig. 5.10. Furthermore, at least one of the two surfaces must not be rigid. If one surface is rigid, in most cases this surface should be the target surface. Rigid surfaces have no underlying elements and therefore no flexibility apart from rigid body motions. All their nodal degrees of freedom must be either fixed, have enforced displacement, or be rigidly linked to a master node. The normal contact conditions can be expressed as (Bathe 1996);

$$g \geq 0; \quad \lambda \geq 0; \quad g\lambda = 0 \qquad \text{Eq. (5.9)}$$

where: g : a gap

λ : normal contact force

Different algorithms may be used for describing the contact boundary condition. ADINA has a general Coulomb type friction model. For friction, a non-dimensional friction variable τ can be defined as;

$$\tau=\frac{F_T}{\mu\lambda}$$ Eq. (5.10)

where: F_T : tangential force

μ coefficient of friction

In this numerical investigation in an attempt to accurately and realistically simulate the impact problem, contact conditions were implied with friction, the standard Coulomb friction condition is used in contact modelling as follow;

$|\tau|\leq 1$ and $|\tau|<1$ implies $\dot{u}=0$ while $|\tau|=1$ Eq. (5.11)

implies sign $(\dot{u})$=sign (τ)

where $\dot{u}$: sliding velocity

In Coulomb friction, the friction coefficient can be constant or calculated from one of the several predefined friction laws (Bathe 1996). It should be noted that in the static analysis, the sliding velocity $\ddot{u}$ is calculated by dividing the incremental sliding displacement by the time increment, as a result, time is not a dummy variable in static frictional contact problems.

If it is more important for the nodes of one surface not to penetrate the other, then that surface should be the contactor. This factor is usually important when one surface has a much coarser mesh than the other (see Fig. 5.11). In this case, the coarse surface should be the target. In the case of the rigid contact surface, it can be a slave to a master node through which the motion of the rigid surface is controlled. Rigid links can be conveniently used between the master node and all the nodes on the rigid surface.

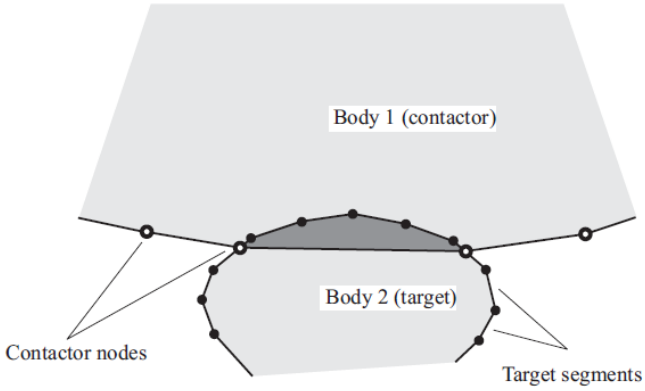

Figure 5-11 Effect of incorrect contactor-target selection due to the mesh density (ADINA 2017).

In ADINA three contact solution algorithms for implicit analysis are provided; (i) constraint-function method, (ii) segment (Lagrange multiplier) method and (iii) rigid target method. Each contact group must belong to one of these three contact algorithms with or without friction. The constraint-fiction method was adopted as the contact algorithms in the current implicit analysis in which constraint functions are applied to enforce the no-penetration and the frictional contact conditions (see Fig. 5.12). Then the inequality constraints are replaced by a normal constraint function as follows;

$$w(g,\lambda)=0.5\,(g+\lambda)-\sqrt{\left(\frac{g-\lambda}{2}\right)^2+\varepsilon_N} \qquad \text{Eq. (5.12)}$$

where: ε_N : a small user-defined parameter (default value of 1.0×10^{-12})

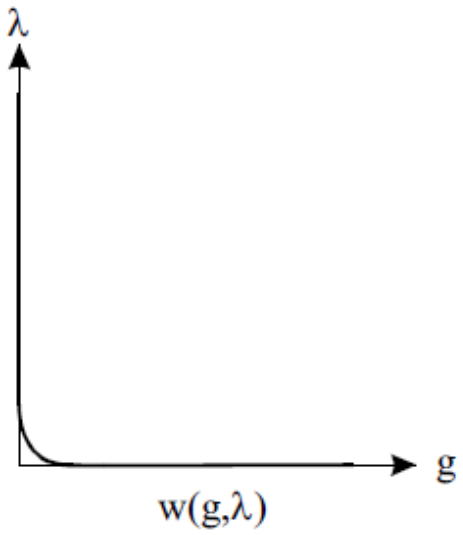

Figure 5-12 Constraint function for normal contact (ADINA 2017).

Note that the above function involves no inequalities and is smooth and differentiable.

5.2.5 Constraint equations

The contact condition adopted for modelling the contact surface in section 5.2.4, was enforced by constraint equations. In ADINA, two basic types of constraints between degrees of freedom can be imposed. The first type as the following form;

$$U_k = \sum_j (\beta_j U_j) \qquad \text{Eq. (5.13)}$$

where: U_k : Dependant (or slave) degree of freedom which is controlled by U_j

U_j : Multiple independent (master) degrees of freedom

β_j : factors

An alternative form of constraint has the form

$$\sum_j (\beta_j U_j) = 0 \qquad \text{Eq. (5.14)}$$

Where none of the U_j degrees of freedom is made dependent in other words there are no slave degrees of freedom. In such a case, the constraint is imposed using Lagrange Multipliers. The basic constraints of Eq. (5.13) are only approximately satisfied in an explicit analysis, since imposing the constraint exactly requires a non-diagonal mass matrix. The number of independent degrees of freedom is reduced by each constraint of the first type, while each general constraint of the second type increases the number of degrees of freedom by one (by adding a Lagrange Multiplier). Hence it is recommended by ADINA (ADINA 2017) to use Eq. (5.13) when possible. However, there are limitations regarding this, such as when a slave degree of freedom is only related to master's degrees of freedom. The example below illustrates such limitation as follow (ADINA 2017);

$U_{2(z)} = U_{1(z)} + 3\theta_{1(x)}$ ←valid constraint

$U_{3(z)} = U_{2(z)} + U_{1(z)} - 4\theta_{2(x)}$ ←invalid constraint

Note that the DOF $U_2(z)$ is already dependent, as a result, the problem with the second constraint could be resolved by manually applying the first constraint to obtain:

$$U_{3(z)} = 2U_{1(z)} + 3\theta_{1(x)} - 4\theta_{2(x)}$$

The convergence criteria adopted in the current numerical investigation is 'energy and force/moment'. Since in both static and dynamic analysis a contact surface was defined, the contact force convergence criterion is also used in addition to the above criteria. The convergence in equilibrium iterations is reached when the following inequalities are satisfied (ADINA 2017);

$$\frac{\left\|t+\Delta t\mathrm{R}-t+\Delta t\mathrm{F}^{(i-1)}\right\|_2}{\mathrm{RNORM}} \leq \mathrm{RTOL}$$ For the translational degree of freedom Eq. (5.15)

$$\frac{\left\|t+\Delta t\mathrm{R}-t+\Delta t\mathrm{F}^{(i-1)}\right\|_2}{\mathrm{RMNORM}} \leq \mathrm{RTOL}$$ For the rotational degree of freedom Eq. (5.16)

where: RTOL : user-specified force convergence tolerance

RNORM : user-specified reference force norm

RMNORM : user-specified moment norm

Note that in the above convergence criteria the residual norm is measured against a user-specified maximum residual value; for instance, the force criterion could be interpreted as (norm of out-of-balance loads) ≤ RTOL x RNORM, where TOL x RNORM is equal to the user-specified maximum allowed out-of-balance load.

Since contact surface groups were presented in the analysis the following additional criterion is used in measuring convergence;

$$\frac{max\left(\left\|\mathrm{R}_c^{(i-1)} - R_c^{(i-2)}\right\|_2, \left\|\Delta\lambda^{(i)} - \Delta\lambda^{(i-1)}\right\|_2\right)}{max\left(\left\|R_c^{(i-1)}, \mathrm{RCONSM}\right\|_2\right)} \leq \mathrm{RCTOL}$$ Eq. (5.17)

where:	$R_c^{(i-1)}$	:	contact force vector at the end of iteration (i-1)
	$\Delta\lambda^{(i)}$	:	incremental Lagrange multiplier vector at the end of iteration i.
	RCONSM	:	reference contact force level used to prevent possible division by zero
	RCTOL	:	user-specified contact force convergence tolerance

Convergence might not occur when the maximum number of iterations is reached or when the solution is diverging.

5.3 STRUCTURAL FORMS INVESTIGATED

The structural forms and case studies adopted in the current numerical investigation are presented in Table 11. The structural forms adopted in this study have different design details (i.e. amount of transverse reinforcement) and based on their shear-span-to-depth ratio can be categorised as slender (Hughes & Speirs 1982 and the slender beams presented in Chapter 3) and short (Saatci and Vehicco 2009 and the short beams presented in Chapter 4. The geometrical specifications, design details and material properties of the specimens investigated are depicted in Table 11 and Fig. 5.13 and Fig. 5.14. Specimens C2, D1 and E1 (Hughes and Speirs 1982) have an a_v/d =7.7 (C2 and D1) and an a_v/ d=4.3 (E1). Specimens A and B (slender beams presented in Chapter 3) have a_v/d = 9, Specimens SS0a-SS3a and C, D and E (short beams presented in Chapter 4) have a_v/d of 4.2 and 3.4 respectively. Specimens with $a_v/d > 5$ are considered as slender while RC members with $a_v/d < 5$ are referred to as short beams. Prior to impact analysis of RC beams considered, static analyses have been carried out to form a benchmark for the numerical predictions and to be used as a form of validation against their experimental counterparts.

Table 11 RC specimen adopted in the FE analysis

										Top Rebars			Bottom Rebars			Shear Rebars		
	Beam ID	f_c	h	b	d	a	L	a_v/d	Dia. of bar	p%	f_y	Dia. of bar	p%	f_y	Dia. of bar	p%	f_y
		Mpa	mm	mm	mm	mm	mm		mm	%	Mpa	mm	%	Mpa	mm	%	Mpa
Hughes & Spiers (1982)	C2	45	200	100	175	1350	3000	7.7	6	0.32	460	12	1.29	460	6	0.27	460
	D1					1350	3000	7.7	6	0.32		16	2.29		6	0.27	
	E1					900	1800	5.4	6	0.32		12	1.29		6	0.25	
Saatci & Vecchio (2009)	SS0a	50.1	410	250	357	1500	4880	4.2	30	1.58	464	30	1.58	464	6	0	605
	SS1a	44.7														0.1	
	SS2a	47														0.2	
	SS3a	46.7														0.3	
Heriot-Watt Slender beams	A	30	200	100	150	1350	3000	9	10	1.04	609	12	1.50	566	10	0.73	503
	B								8	0.66					8	0.47	
Heriot-Watt Short beams	D	45	300	150	250	850	2500	3.4	10	1.04	570	16	1.60	529	8	0.39	550
	C															0	
	E															0.27	

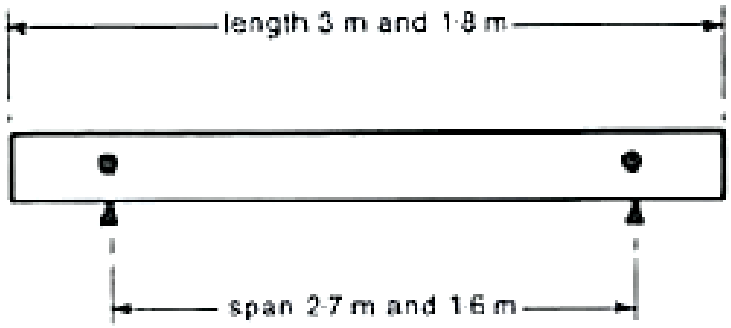

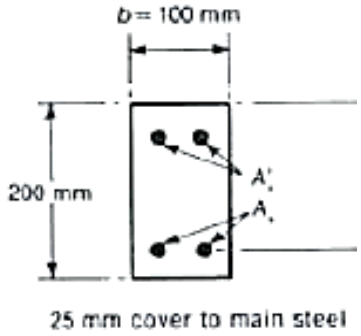

Hughes & Spiers (1982)

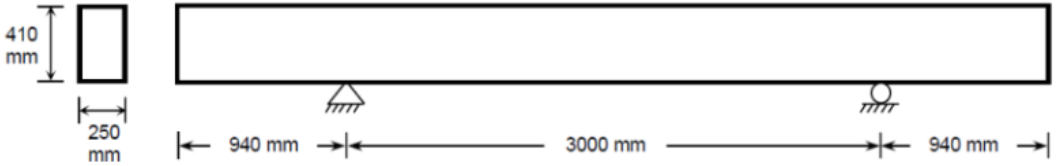

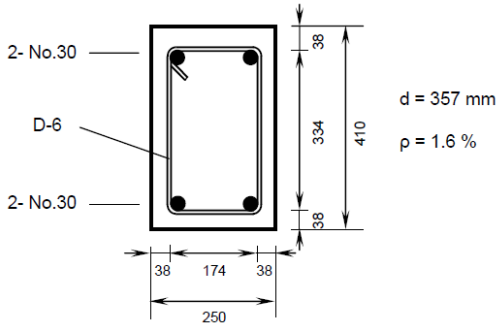

Saatci & Vecchio (2009)

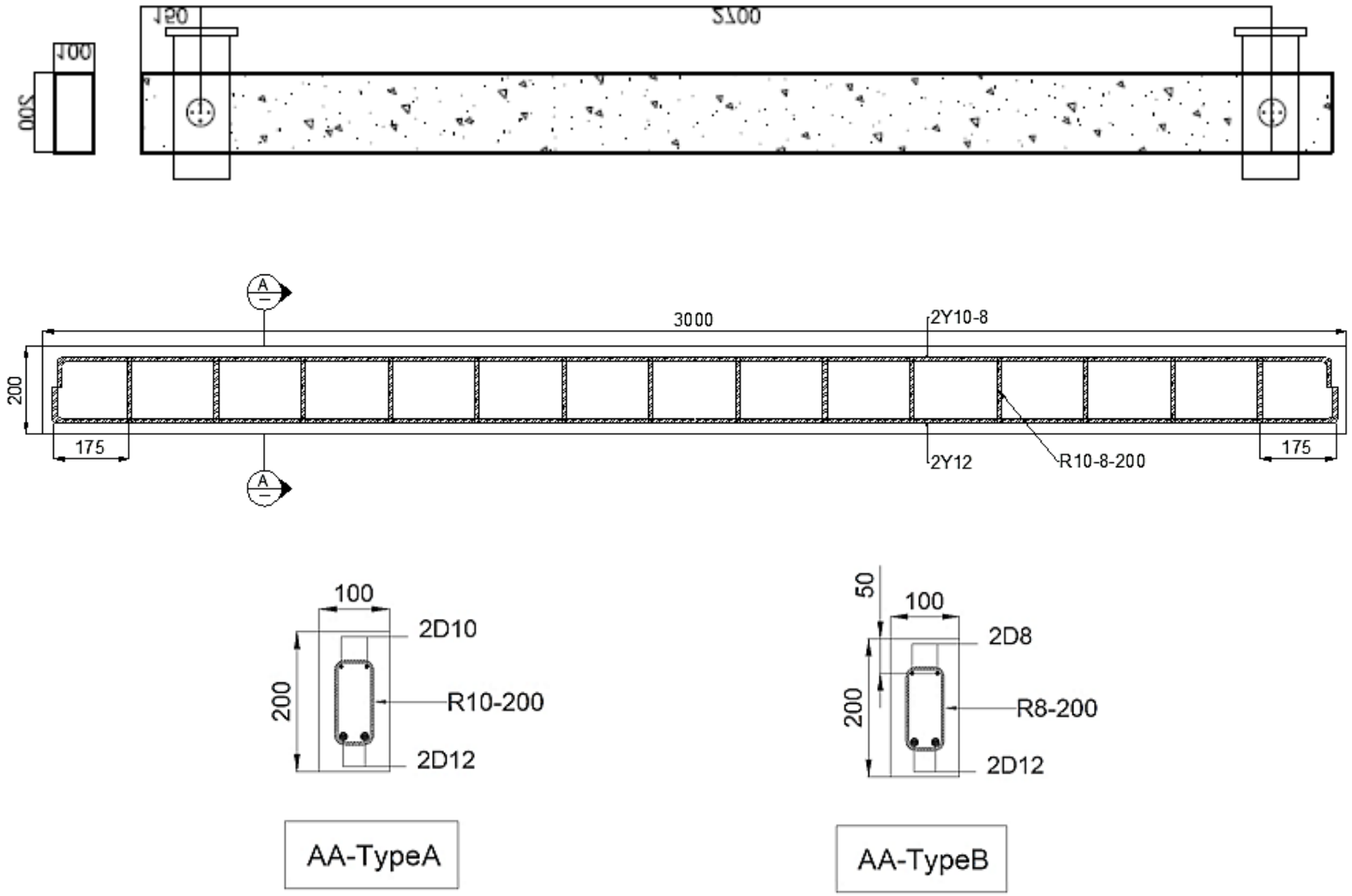

Figure 5-13 Heriot-Watt Slender beams (presented in Chapter 3)

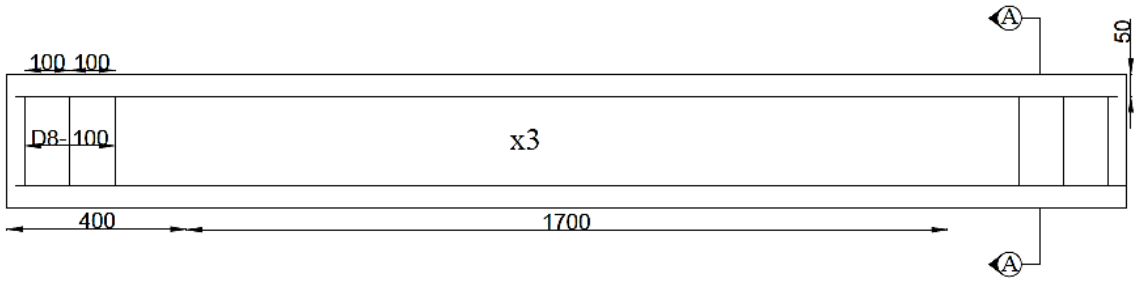

Type C

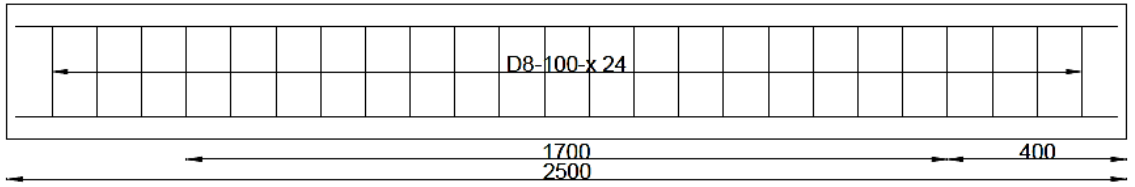

Type D

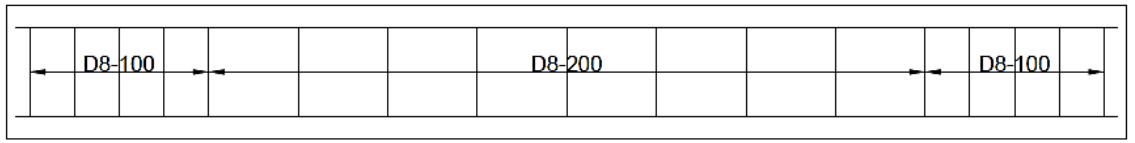

Type E

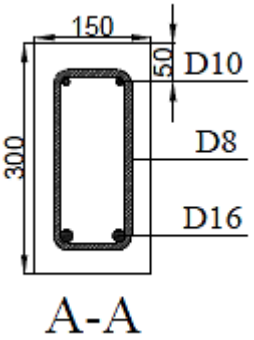

Figure 5-14 Heriot-Watt short beams (presented in Chapter 4)

5.4 FE MODELLING OF THE PROBLEM AT HAND

Concrete is modelled using a mesh of 27-noded brick elements (which adopt a 3x3x3 integration rule). The use of this element is considered to provide a more accurate description of the stress distribution developing within the specimen considered throughout the loading process (ADINA 2017) without requiring the use a denser FE mesh of 8-noded brick elements (often adopting a typical element size of 5mm, Cotsovos et al 2008). Each 27-noded element had an edge size of approximately 40 mm, see Figs. 5.15 and 5.16. Due to the double symmetry characterising the problem at hand, only a quarter of the RC beam is modelled with suitable boundary conditions.

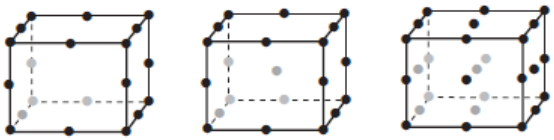

Figure 5-15 20-, 21-& 27-node elements

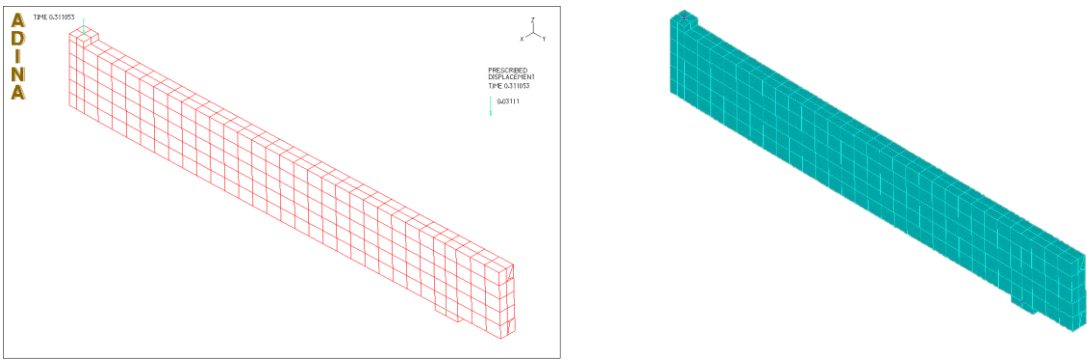

(a)

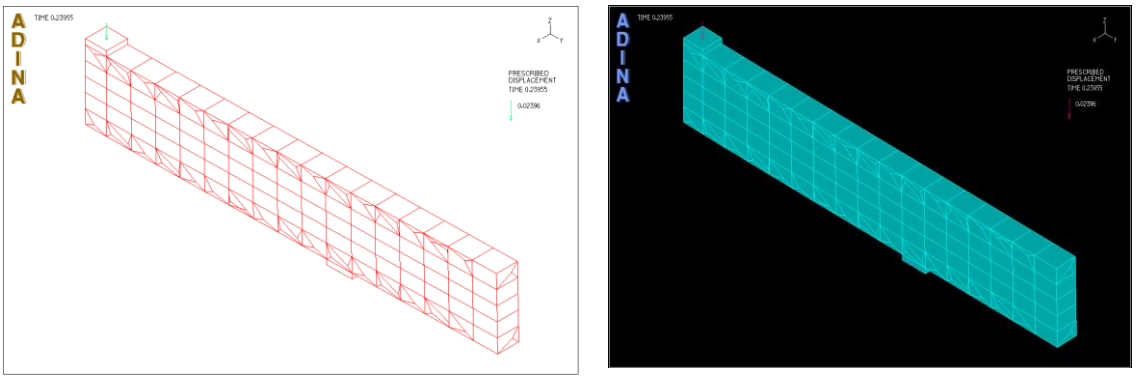

(b)

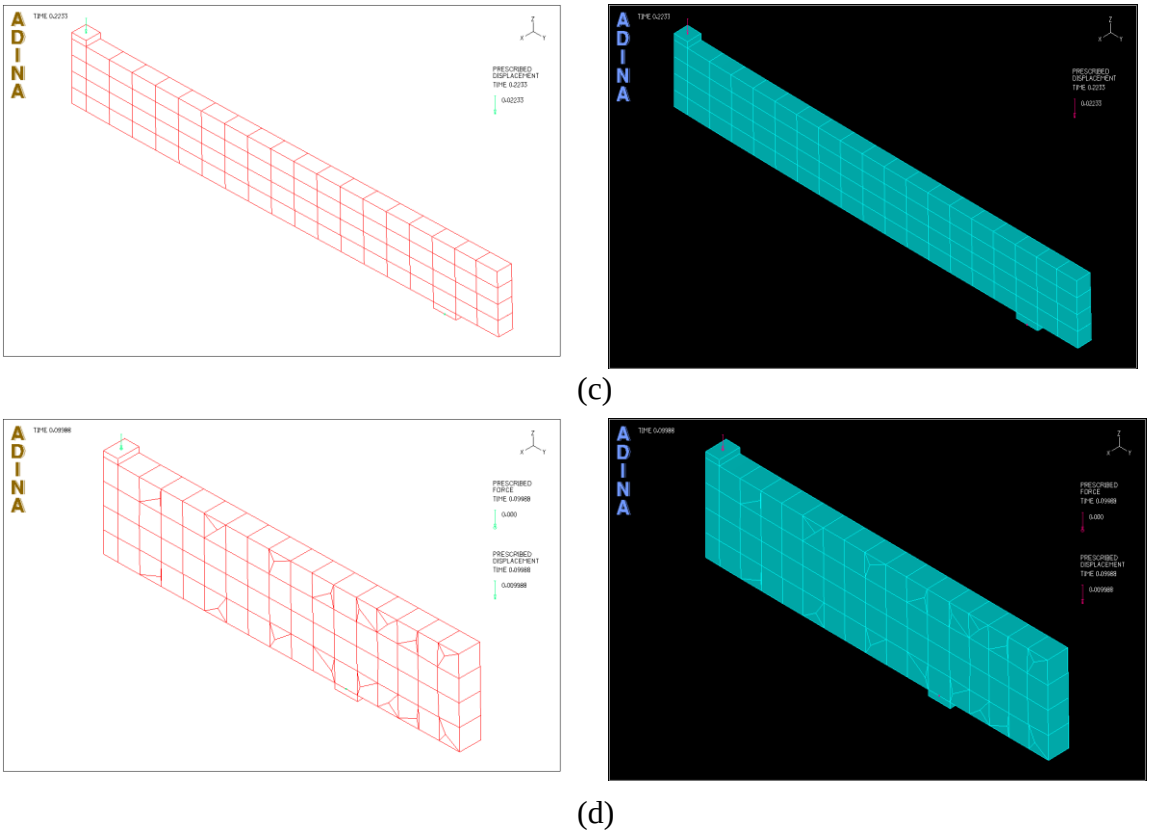

Figure 5-16 Brick elements adopted in ADINA to model concrete-(a) Hughes and Speirs (1982),(b) Saatci and Vecchio (2009),(c) HW-Long beams Type A and (d) HW-Short beams Type E

The steel reinforcement bars are modelled as 3D truss elements of appropriate cross-sectional area. The reinforcement bars are embedded in the concrete model using rebar elements/truss elements which are automatically connected to any 2D or 3D solid mesh in which truss elements lie. This connection is automatically formed by ADINA using constraint equations implemented during the generation of the data file. For each rebar line, the programme finds the intersection point of the rebar line and the faces of the 3D elements. ADINA then generates nodes at these (intersection) points and generates truss elements that connect the successive nodes. The constraint equations are defined by ADINA between the generated nodes and three closest corner nodes of the 3D element faces, Figs. 5.17 and 5.18.

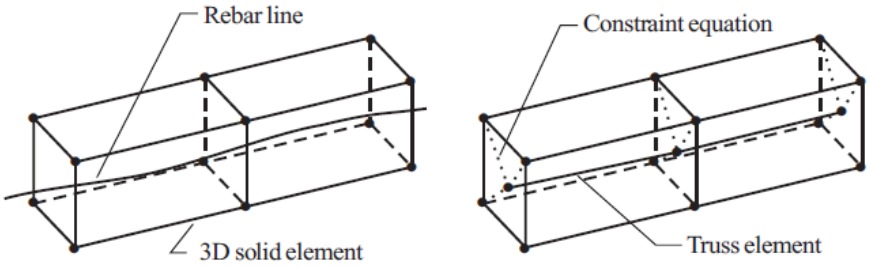

Figure 5-17 Rebar in 3D truss, 3D solid elements before data file generation (left) and after data file generation (right).

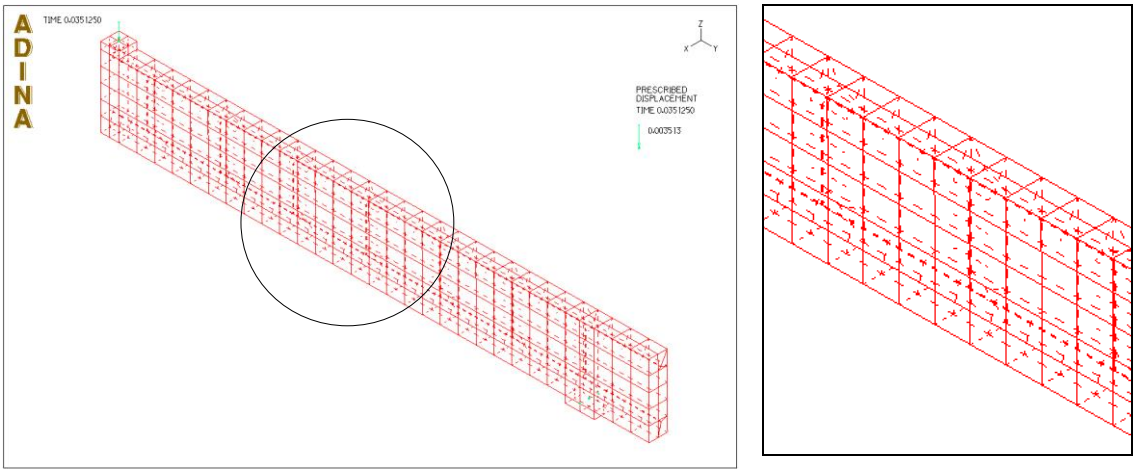

(a)

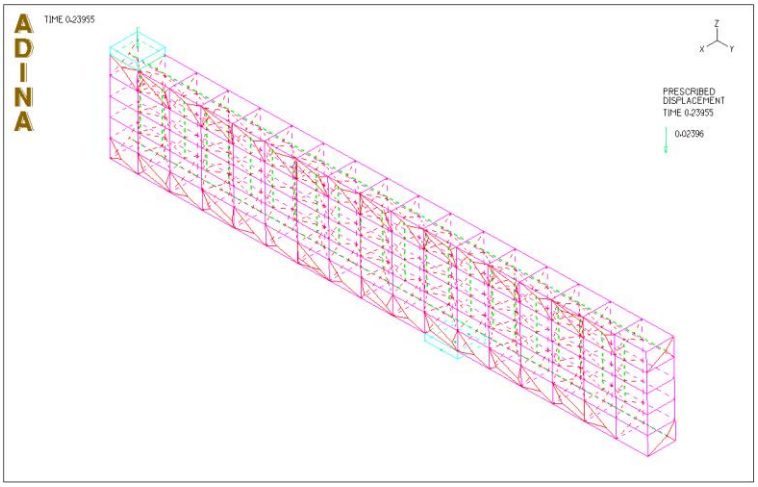

(b)

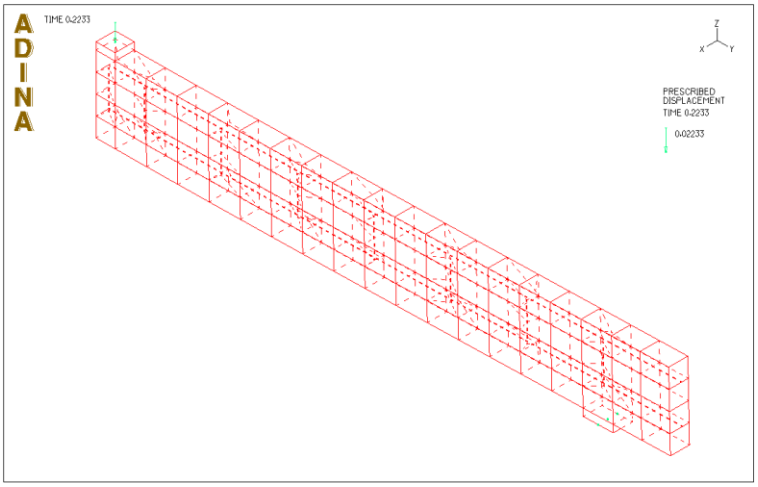

(c)

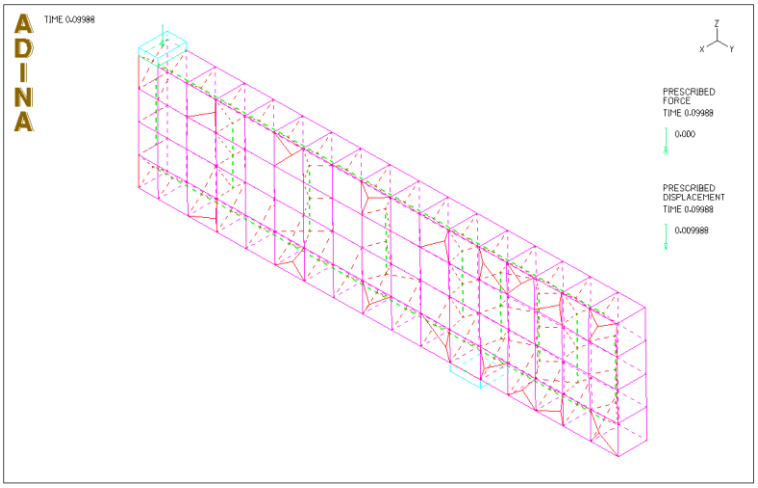

(d)

Figure 5-18 Rebar/truss elements adopted by ADINA to model steel-(a) Hughes and Speirs (1982),(b) Saatci and Vecchio (2009),(c) HW-Long beams Type A and (d) HW-Short beams Type E

5.5 LOAD APPLICATION

When studying numerically, the dynamic response of the RC beams subjected to impact loading, instead of applying the actual time-history of the contact force generated during each drop-test (see Fig. 5.20) the latter load is applied in the form of load-increments onto the mid-span of the beam through a steel plate (similar to the plate used in the contact region when conducting the drop tests). In doing so the form of the load is simplified (idealised) so that it is still characterised by the same intensity and average loading rate as the actual contact force recorded during testing. When carrying the numerically study the load is applied in two ways:

- The value of the applied load increases linearly at a constant rate until the load-carrying capacity of the RC beam is reached and failure occurs (see Fig. 5.19).

- The form of the imposed impact load is described by a simplified force-time function which consists of an ascending and a subsequent descending branch, in which the rate of loading (associated with the ascending branch) is assumed equal to the rate of unloading (of the descending branch).

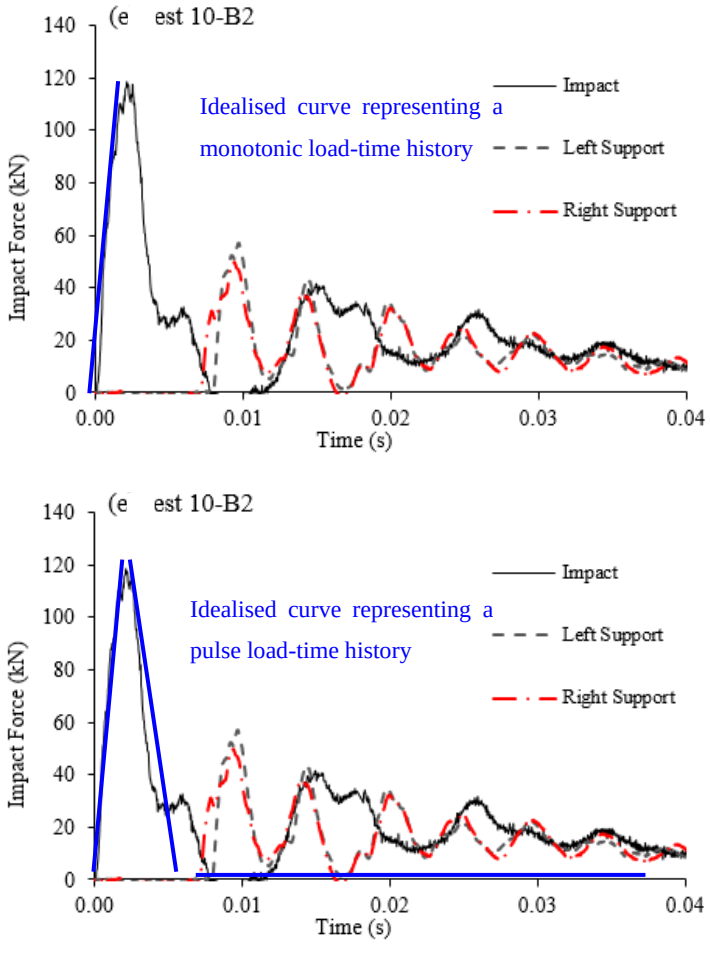

Figure 5-19 Idealised form of a typical impact force-time history extracted from the drop-weight test 10 (See chapter 3), used in ADINA to represent the impact load in the form of (a) the monotonic loading and (b) pulse loading (Bottom)

A parametric study was carried out to assess the true ultimate limit state (ULS) and associated load-carrying capacity exhibited by the specimens when subjected to different loading rates matching those applied during drop-weight tests in Chapter 3 and 4 (i.e. ranging from 10 to 1000 kN/ms). During this study, the intensity of the impact load was reduced gradually and applied in pulses to pinpoint the actual failure point (see Fig. 5.20). Therefore, during the parametric studies, each beam specimen was subjected to a series of

pulse loads characterised by different loading rates and intensities in order to identify the true load carrying capacity of the specimens.

The time function presented in Fig. 5.19 forms a simplification of the real impact force-time history (see Fig. 5.20) recorded, when conducted the drop-weight tests. The descending branch of the curve is followed by a horizontal plateau which has a value (i.e. magnitude of load), close to zero. Defining the horizontal plateau is essential for obtaining a full description of the exhibited response of the beam after the impact loading is imposed. During drop-weight testing, it was observed that the specimen continues to deflect well after the impactor hits the specimen. In the current study, initially, the impact load was applied monotonically (at loading rates ranging between 10 and 1000 kN/ms) up to the failure of the specimen. Subsequently, the intensity of the imposed load was reduced (to a percentage of the peak load recorded under monotonic loading for the same loading rate) and the load was applied in the form of a pulse load.

Emphasis is presently focused on studying certain important aspects of RC structural response such as the mode of failure as well as the deformation and cracking profiles exhibited throughout the loading process. In order to determine the actual load-bearing capacity of the RC beams for a specific value of loading rate ($\dot{P}$) a parametric study is carried out in the present section in which the intensity (peak value) of the imposed dynamic pulse load is varied as shown in Fig. 5.20. For the case of static loading, the load is applied monotonically until failure in the form of displacement increments (displacement control). In the dynamic case studies, the load is imposed at a constant rate in the form of load increments. The Peak load (shown as ‘P’ in Fig. 5.20 correspond to the numerical results obtained under monotonic impact loading).

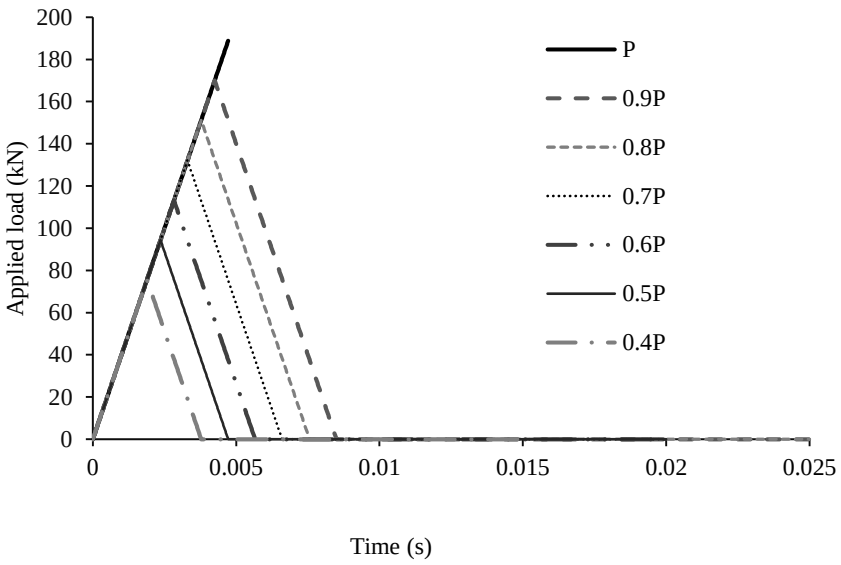

Figure 5-20 Force time-function representing the contact force generated during impact

5.6 MESH SENSITIVITY

The accuracy of the FE solution was checked through a mesh sensitivity analysis in which the impact problem was modelled using three different meshes as shown in Fig. 5.21. For all three FE models, 27-node bricks elements were used. A finer mesh was used in the impact region to capture the stress-strain distributions more accurately which are high in the contact region. A coarser mesh is used away from the contact area considering the stress-strain distributions are low.

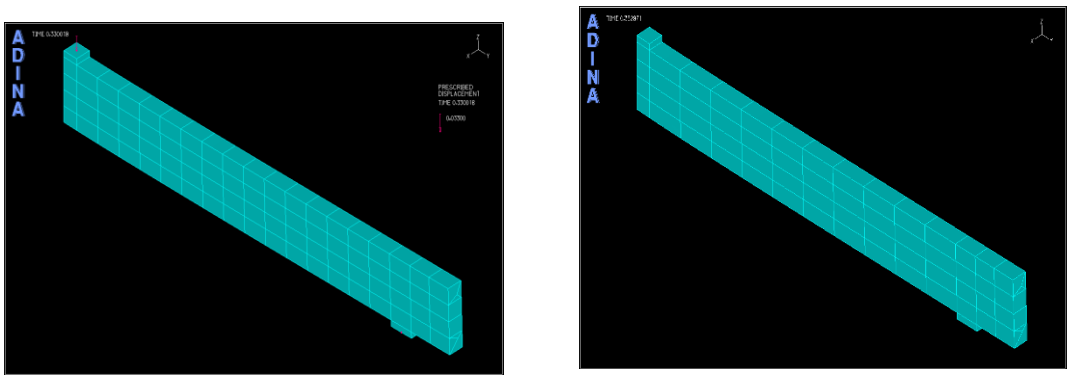

(a) (b)

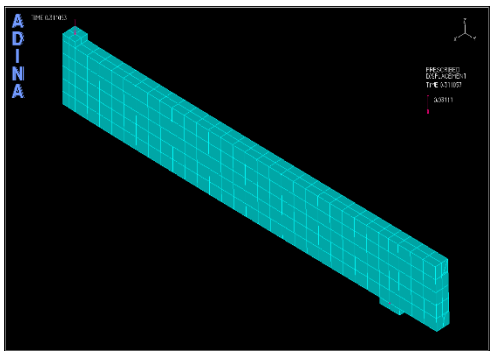

(c)

Figure 5-21 Mesh sensitivity (a) mesh 1 (b) mesh 2 and (c) mesh 3.

The static force versus the mid-span displacement obtained for all three meshes is shown in Fig. 5.22. It can be seen that despite the differences in the mesh density adopted the numerical solutions obtained are not different. As mentioned before, 27-node bricks element is the most accurate, yet it requires high computational cost, to compensate for this, a dense mesh was used.

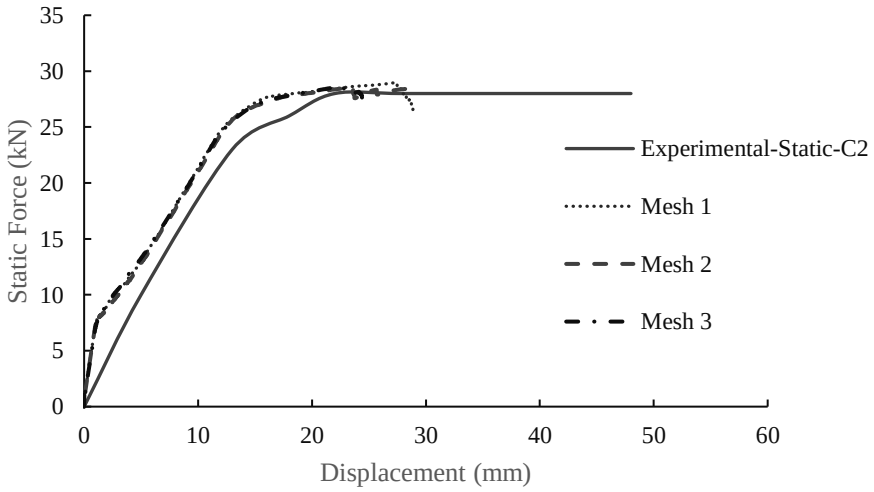

Figure 5-22 Force vs displacement with different meshes.

5.7 NUMERICAL RESULTS

5.7.1 Static Loading

The predictions obtained concerning certain aspects of the response exhibited by the specimens presented in Table 11 under static loading are provided in Figs. 5.23-5.32. The predictions are presented in the form of the load-displacement curves which represent the relation between the applied load and the mid-span deflection at the load point (i.e. mid-span).

Slender beams-The numerical response exhibited by slender beams are in good agreement with their experimentally established counterparts discussed in Chapter 3 in terms of the value of the load-carrying capacity. The amount of ductility, however, predicted by the numerical investigation is less than the experimentally established counterparts particularly in the case of A1 and B1 (see Figs. 5.24 and 5.25). It should be reminded that the concrete behaviour is modelled through the use of a brittle concrete model (Kotsovos and Pavlovic 1995) in the current investigation and this affects the maximum deflection predicted by the software. Furthermore, in the current numerical investigation, failure is associated with the failure of the concrete in the compressive region and any resistance provided by the post-failure mechanism (e.g. auxiliary actions) is not considered as the true load-carrying capacity of the concrete itself. The use of the latter model results in ADINA to often provide conservative/safe predictions concerning load-carrying capacity or/and deflection.

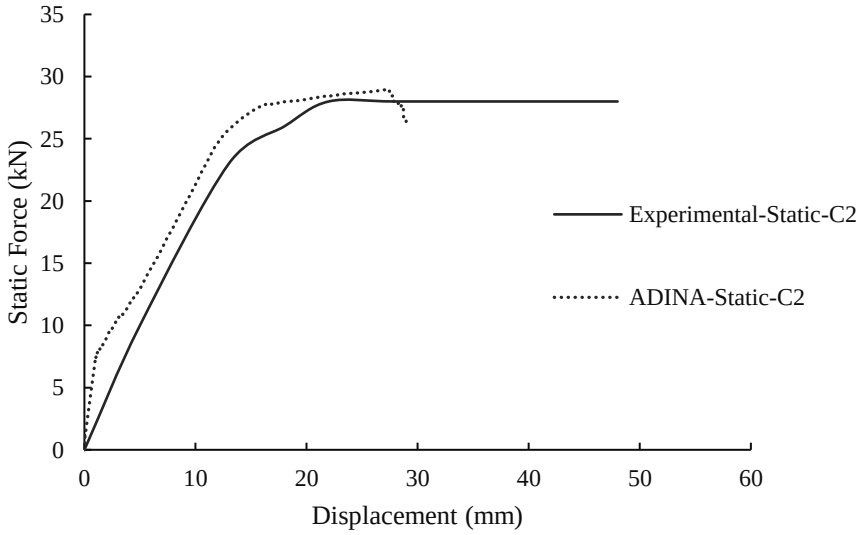

(a)

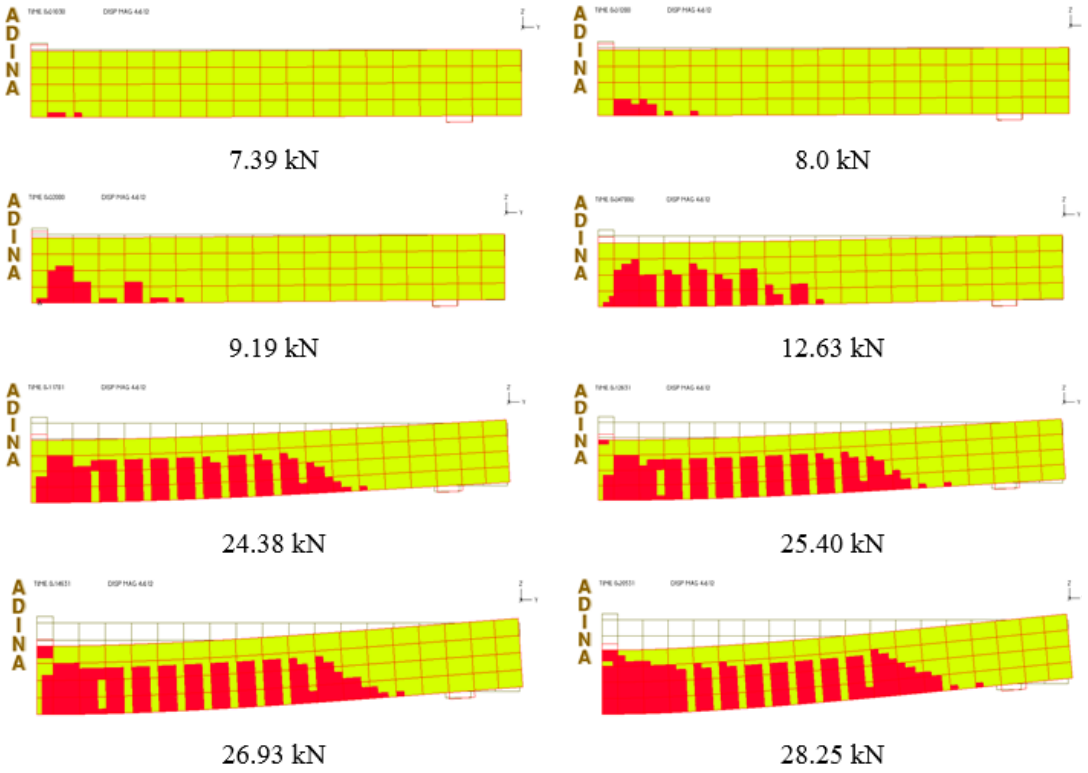

(b)

Figure 5-23 (a) comparison between experimentally and numerically established load-deflection curves accompanied by (b) the deformation and cracking profiles exhibited by beam C2 at different levels of static loading.

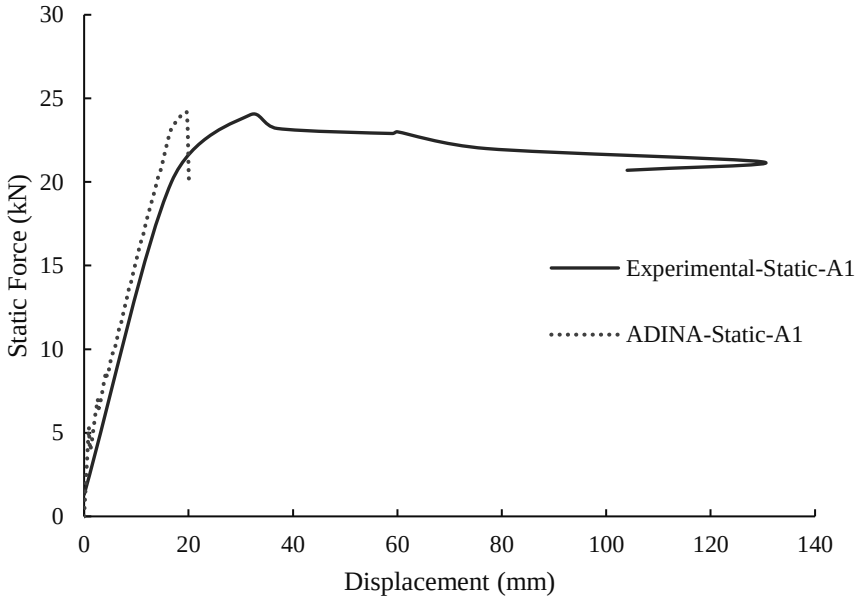

Figure 5-24 Comparison between experimentally and numerically established a load-carrying capacity of specimen A1 under static loading.

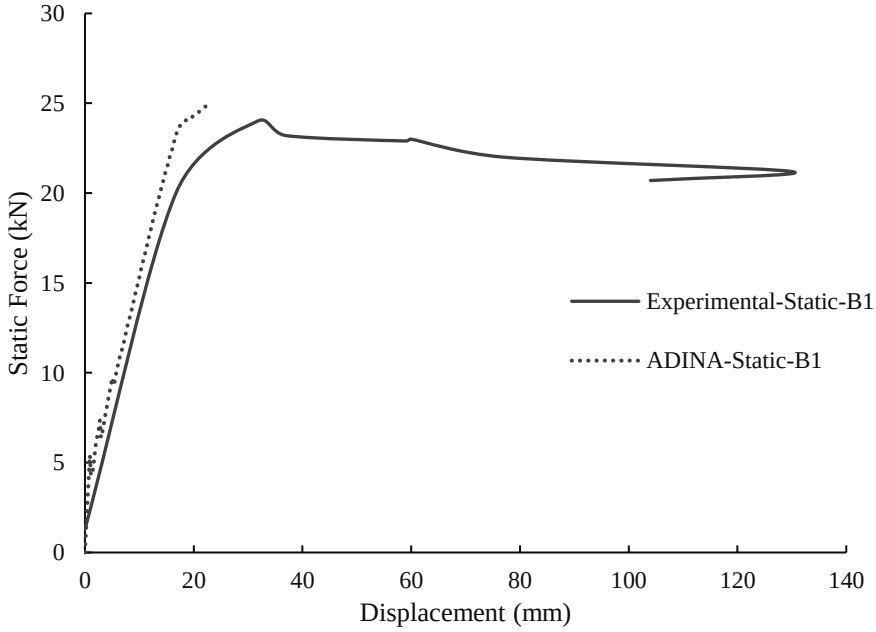

Figure 5-25 Comparison between experimentally and numerically established a load-carrying capacity of specimen B1 under static loading.

Short Beams- The behaviour of the short beams during static testing (Fig. 2.26-2.32) was mainly influenced by the number of stirrups used along the span of the beam. The divergence between the numerical predictions and the experimentally established results was more profound in the case when the specimen had smaller amounts of transverse reinforcement (e.g. SS0 and SC). In the case of the latter specimens, the maximum deflection predicted appeared to be in good agreement with their counterparts established experimentally (see Figs. 5.26- 5.29). It should be noted that for specimens SS0 to SS3 (Saatci and Vecchio 2009) the results predicted by ADINA were compared against VecTor2 predictions reported by the authors due to the lack of available test data. Furthermore, the mode of failure exhibited by the specimens during the static testing was in agreement with that predicted numerically. In the case of specimens SS2 and SS3, the predicted values of load-carrying capacity were in agreement with -what was measured during testing. However, it is noted that the predicted level of ductility was lower than what was established experimentally. This is attributed to the brittle nature of the concrete material model adopted. The use of the latter model results in ADINA to often provide conservative predictions concerning load-carrying capacity or/and deflection.

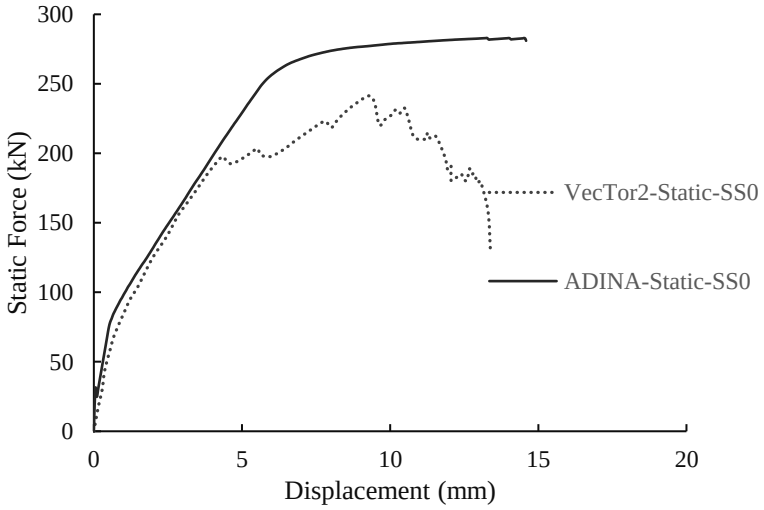

Figure 5-26 Static force vs mid-span displacement of specimen SS0 (Saatci and Vecchio 2009).

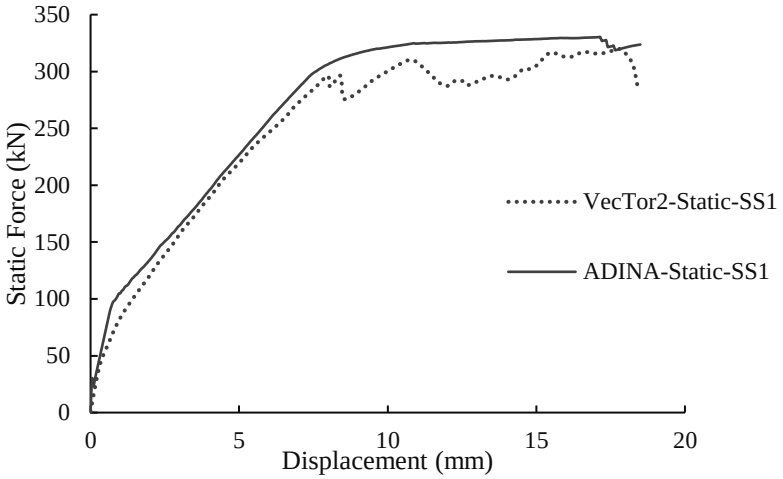

Figure 5-27 Static force vs mid-span displacement of specimen SS1 (Saatci and Vecchio 2009).

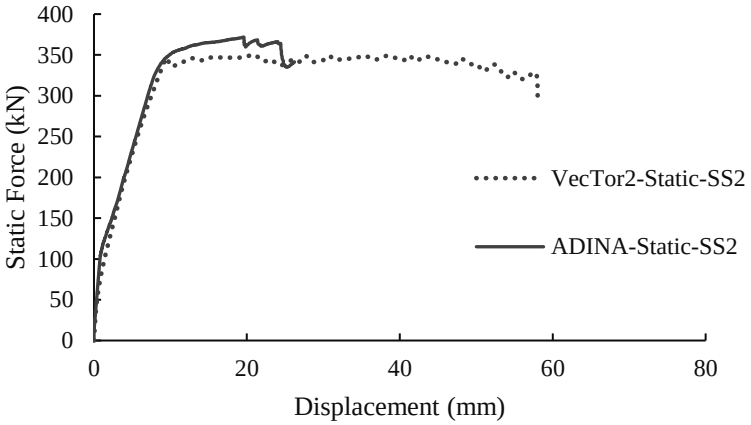

Figure 5-28 Static force vs mid-span displacement of specimen SS2(Saatci and Vecchio 2009).

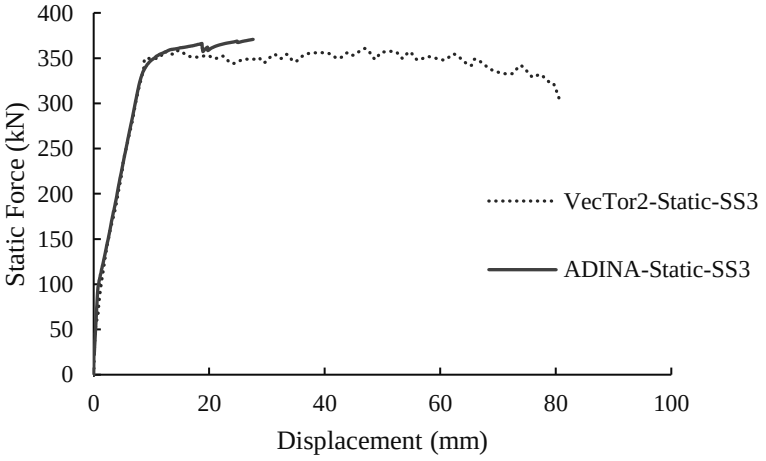

Figure 5-29 Static force vs mid-span displacement of specimen SS3(Saatci and Vecchio 2009).

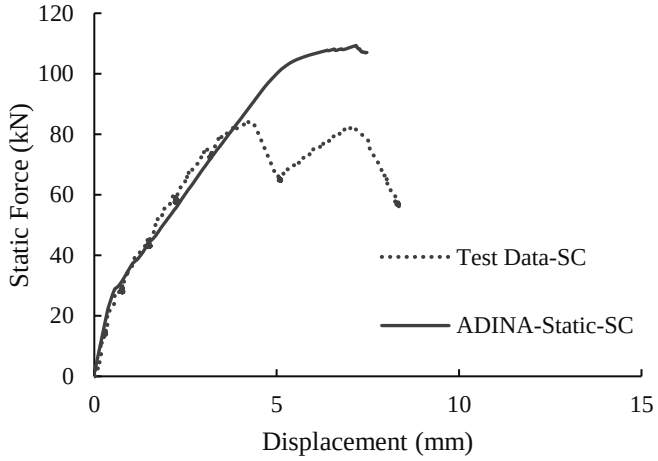

Figure 5-30 Static force vs mid-span displacement of specimen SC.

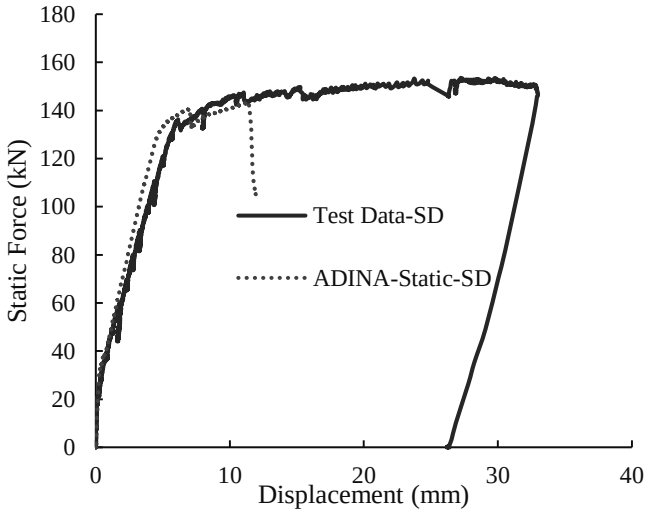

Figure 5-31 Static force vs mid-span displacement of specimen SD.

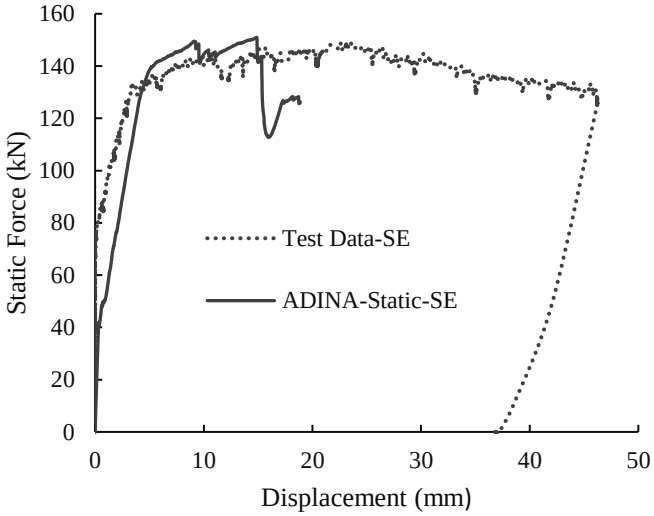

Figure 5-32 Static force vs mid-span displacement of specimen SE.

5.7.1.1 Crack pattern and deformation profile

Figs. 5.33-5.42 show the deformation and cracking profiles predicted for the case of slender (A1, B1 and C2) and short specimens (SS0, SS1, SS2, SS3, SC, SD and SE) at different stages of the loading process. Based on the experimental measurements obtained during testing, all the slender beams exhibited ductile behaviour, with failure occurring after yielding of the longitudinal reinforcement bars in the mid-span region of the specimen, resulting in the formation of extensive cracking that, ultimately, led to the loss of load-carrying capacity of the compressive zone at this location. Figs. 5.33-5.35 show the deformation and cracking profiles of specimens C2, A1 and B1 at different stages of the loading process. Concerning the short beams under static loading, both brittle (i.e. SS0, SS1, SS2, SS3 and SC) and flexural/ductile (i.e. SD and SE) type of behaviour is predicted. In the absence of relevant experimental data (i.e. SS0, SS1, SS2 and SS3 see Figs. 5.36-5.39) the numerical predictions are compared to published numerical data (Saatci and Vehicco 2009).

Overall, the numerical investigation concerning the response of the RC beam specimens is generally in good agreement with that established experimentally. From the predicted crack patterns, it can be seen that flexural cracks begin to appear in the mid-span region of the specimen and, as the imposed load increases, they gradually spread towards the supports.

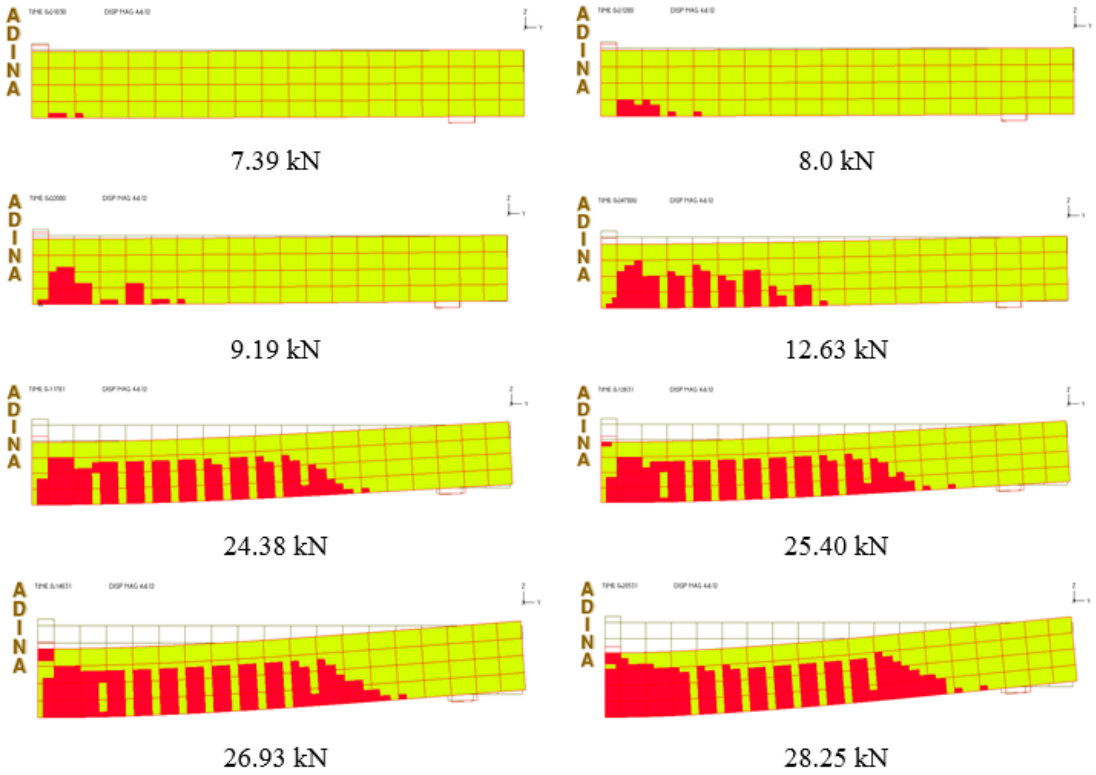

Figure 5-33 Predicted deformation and cracking profiles exhibited by beam C2 at different levels of static loading.

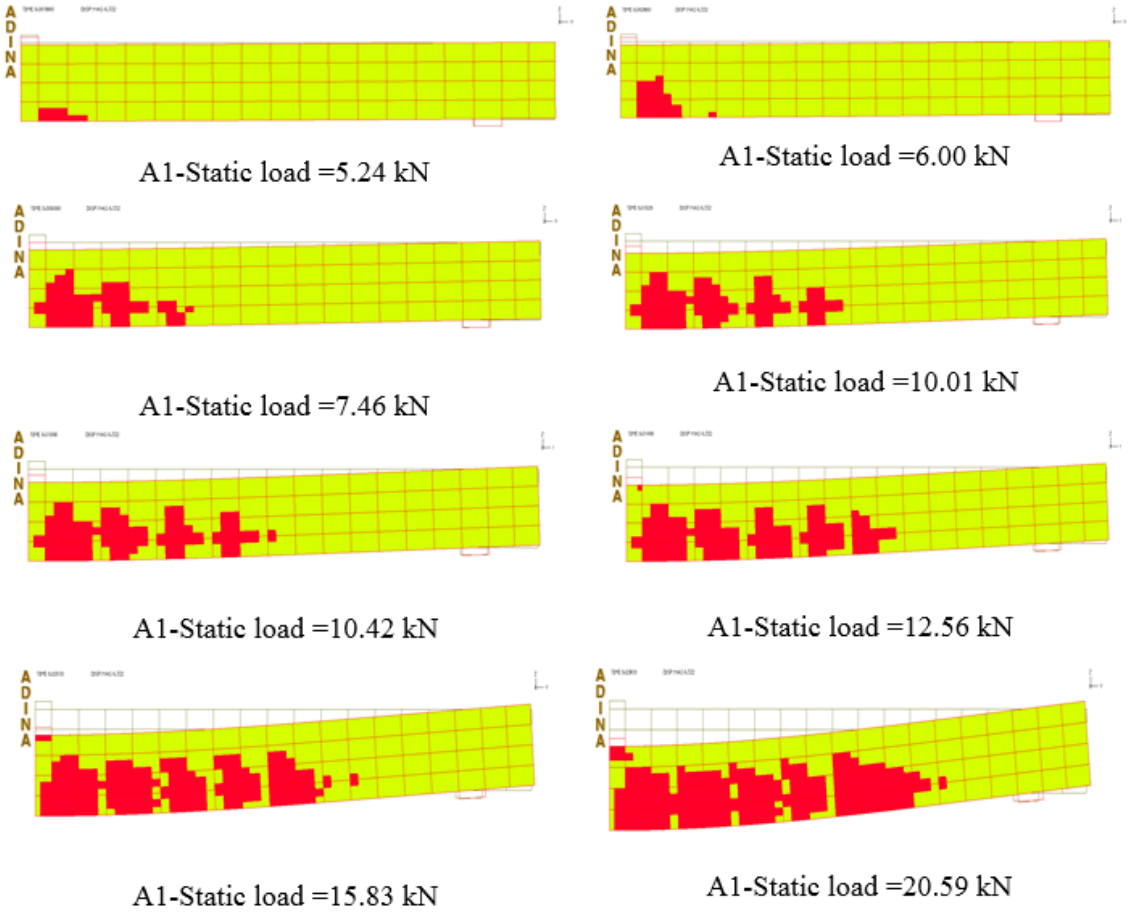

(a)

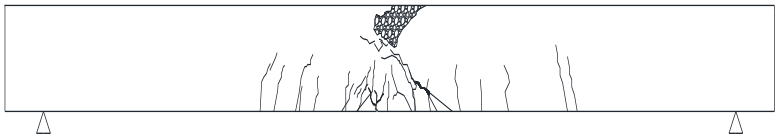

(b)

Figure 5-34 (a) Predicted deformation and cracking profiles exhibited by beam C1 at different levels of static loading (b) crack pattern obtained during experimental static testing.

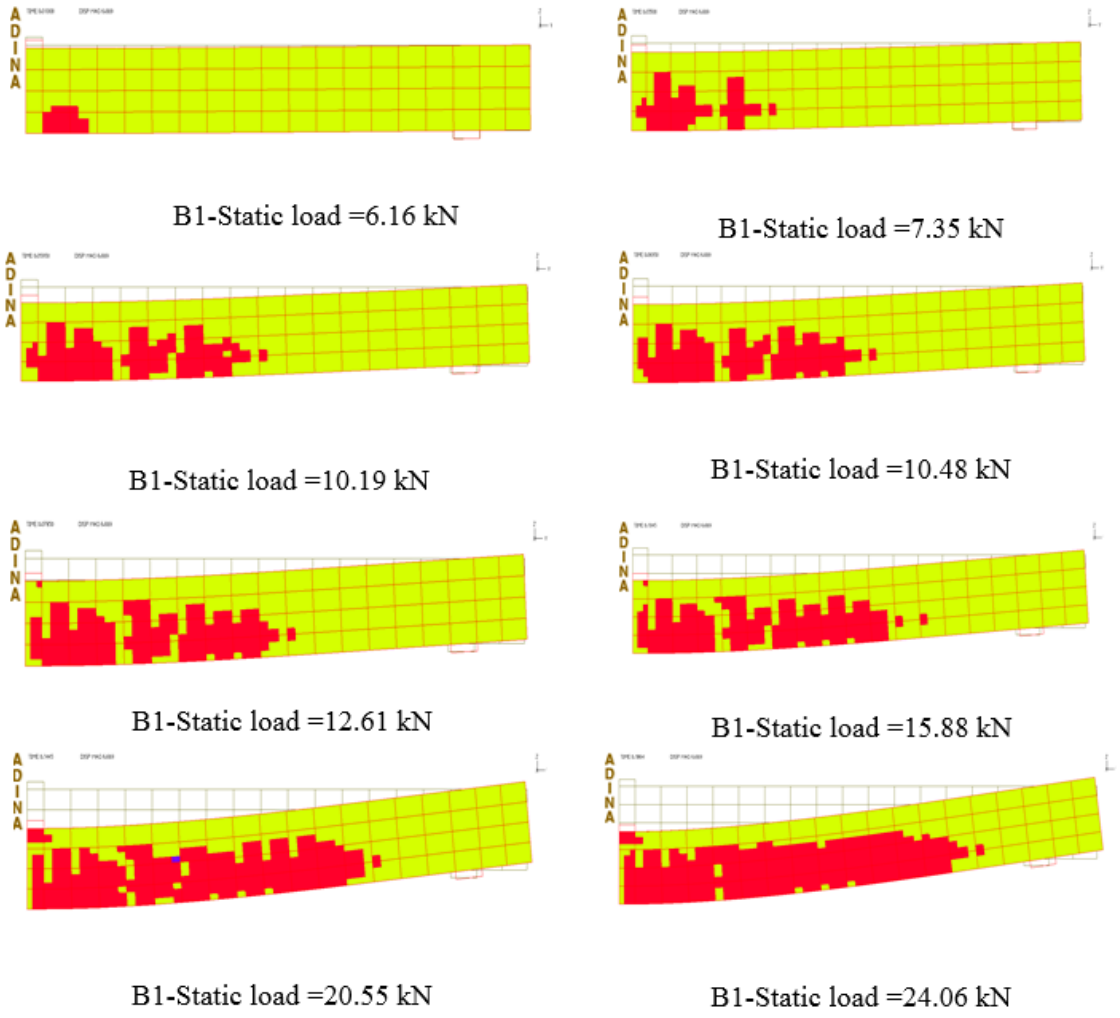

Figure 5-35 Predicted deformation and cracking profiles exhibited by beam B1 at different levels of static loading.

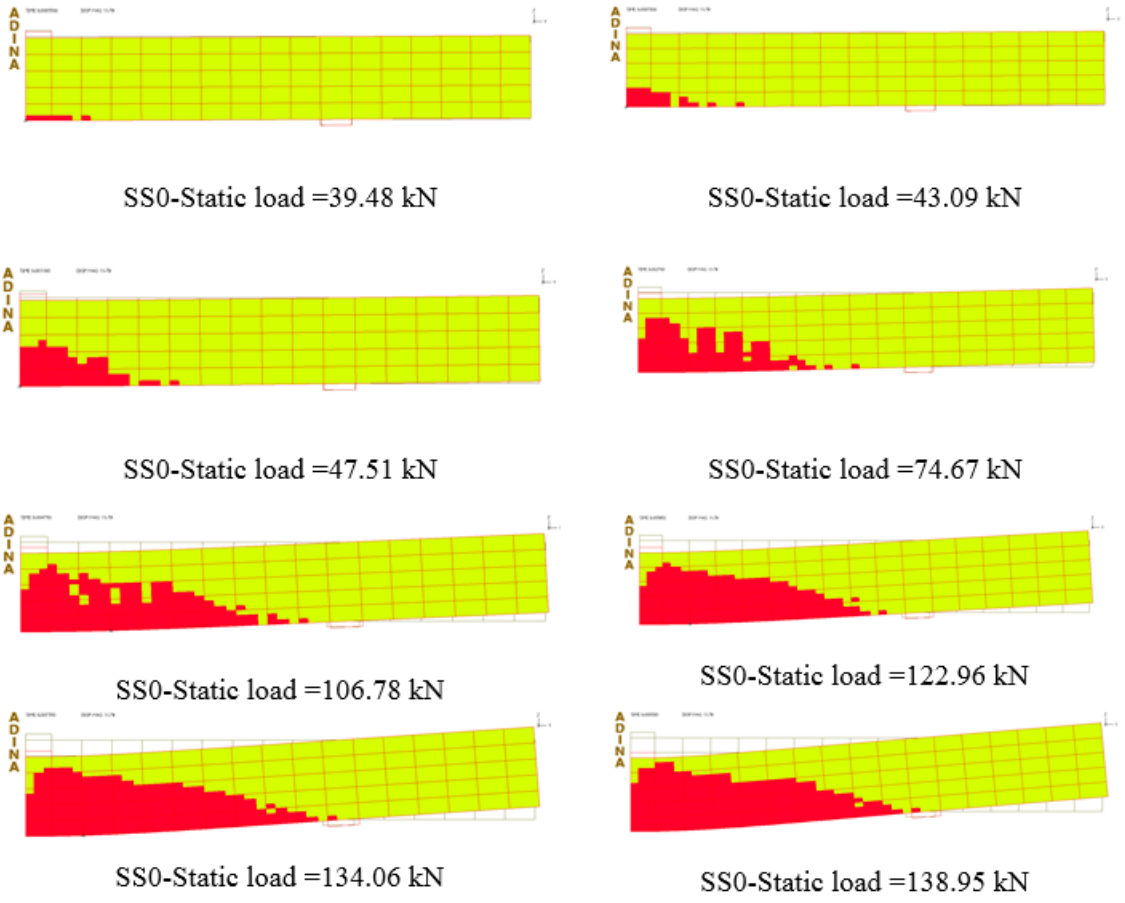

Figure 5-36 Predicted deformation and cracking profiles exhibited by beam SS0 at different levels of static loading.

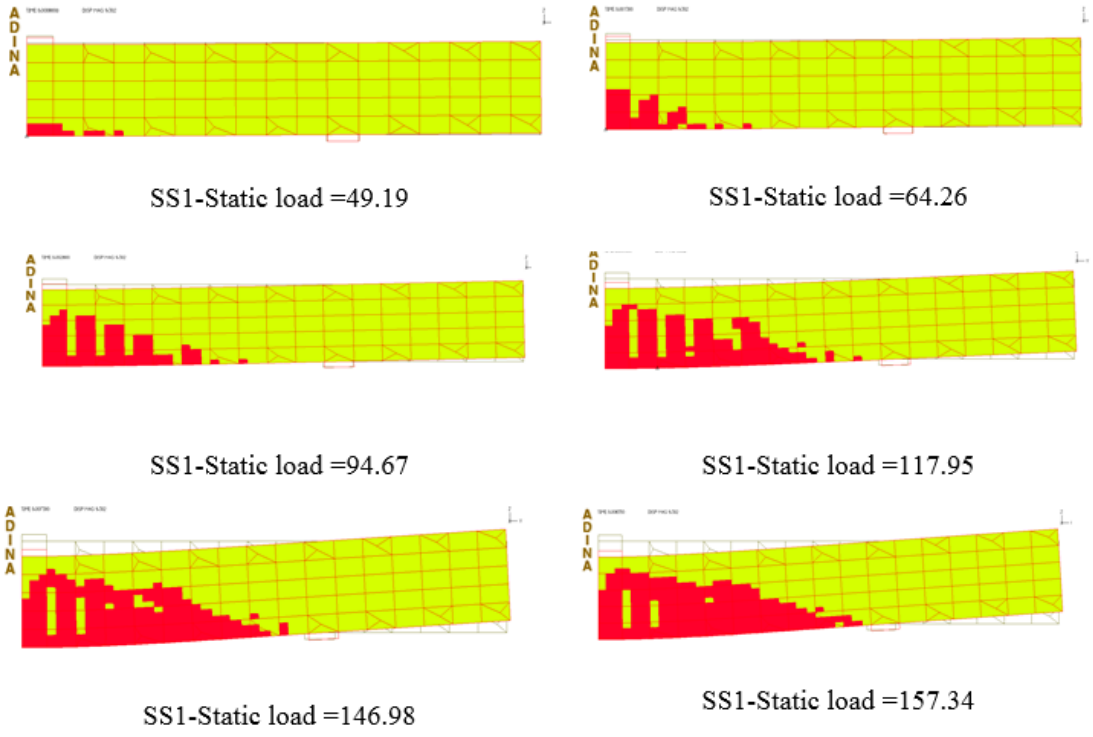

Figure 5-37 Predicted deformation and cracking profiles exhibited by beam SS1 at different levels of static loading.

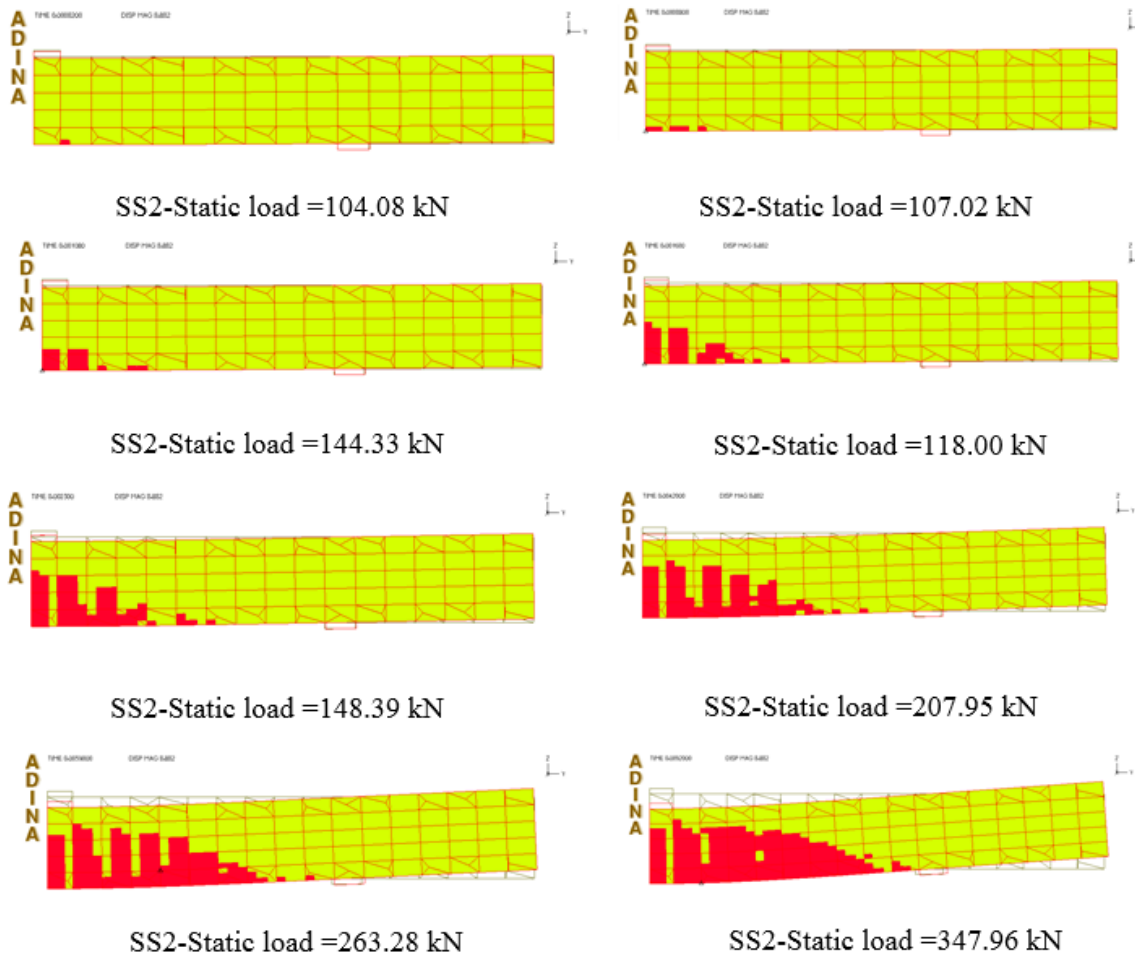

Figure 5-38 Predicted deformation and cracking profiles exhibited by beam SS2 at different levels of static loading.

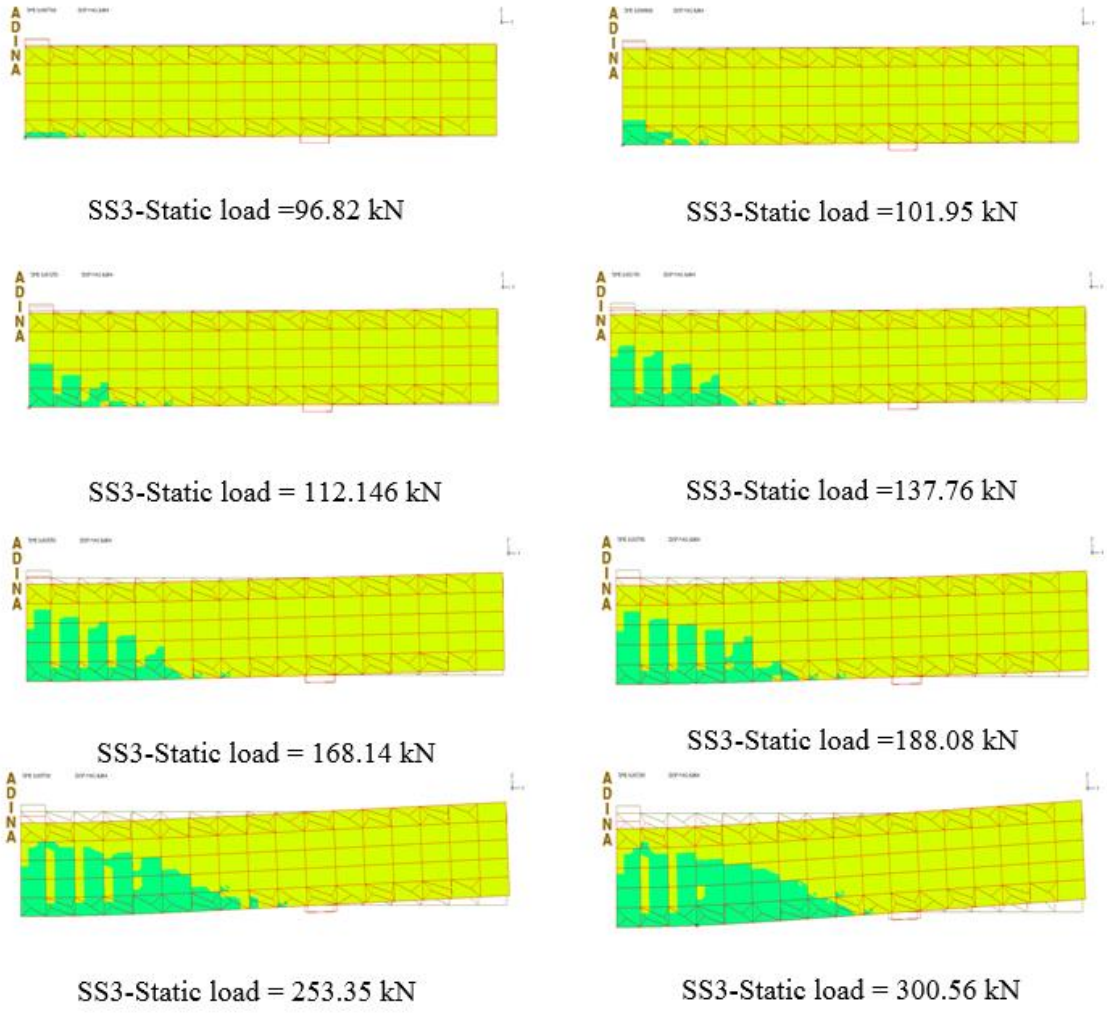

Figure 5-39 Predicted deformation and cracking profiles exhibited by beam SS3 at different levels of static loading.

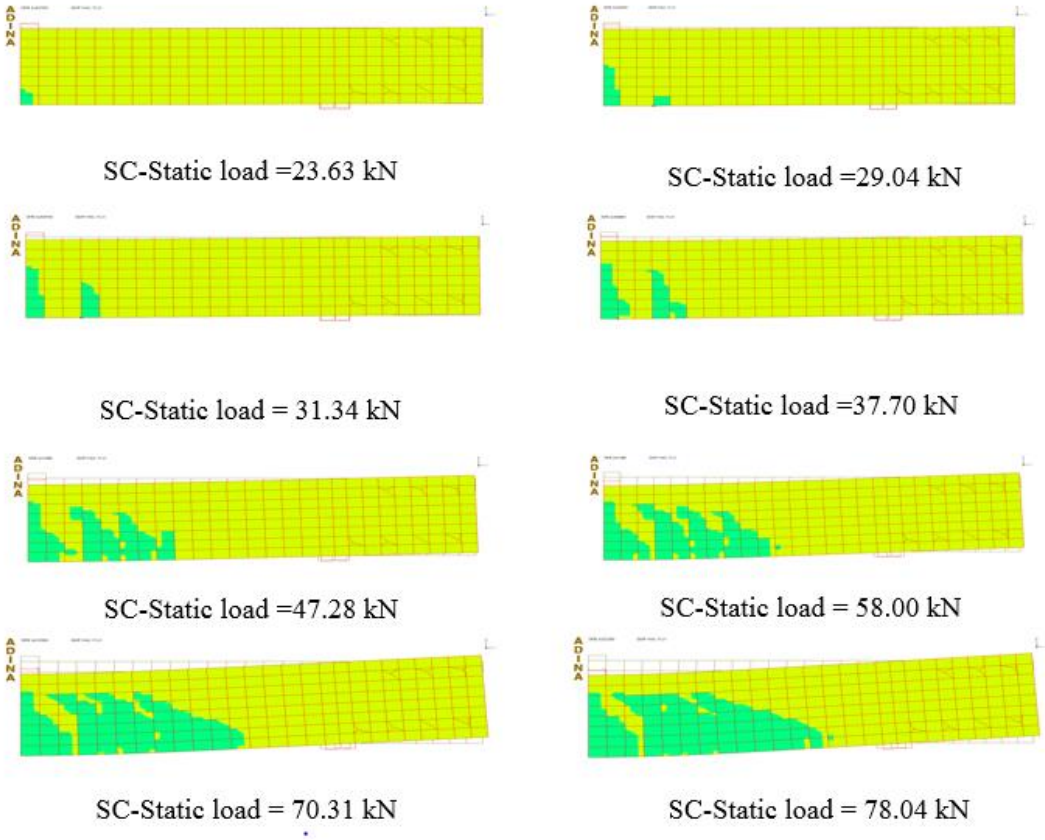

(a)

(b)

Figure 5-40 (a)Predicted deformation and cracking profiles exhibited by beam SC at different levels of static loading (b) crack pattern obtained during experimental static testing.

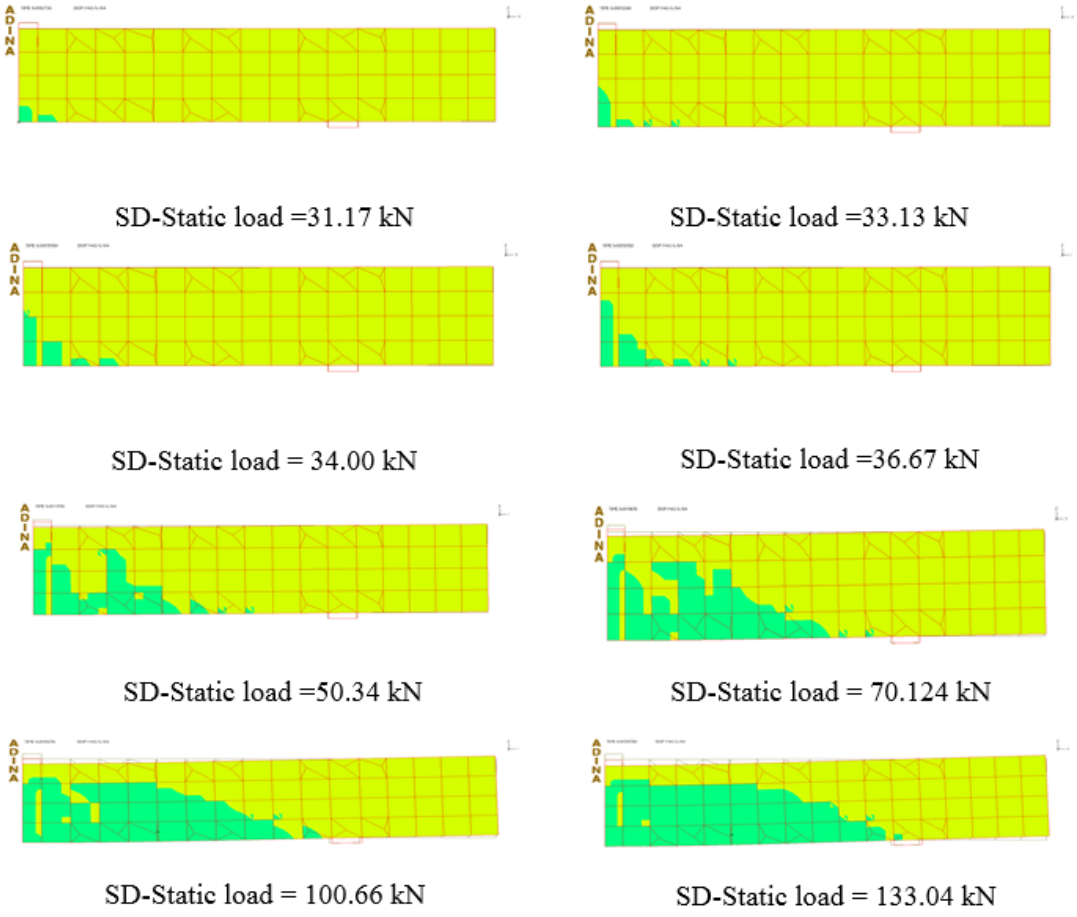

(a)

(b)

Figure 5-41 (a) Predicted deformation and cracking profiles exhibited by beam SC at different levels of static loading (b) crack pattern obtained during experimental static testing.

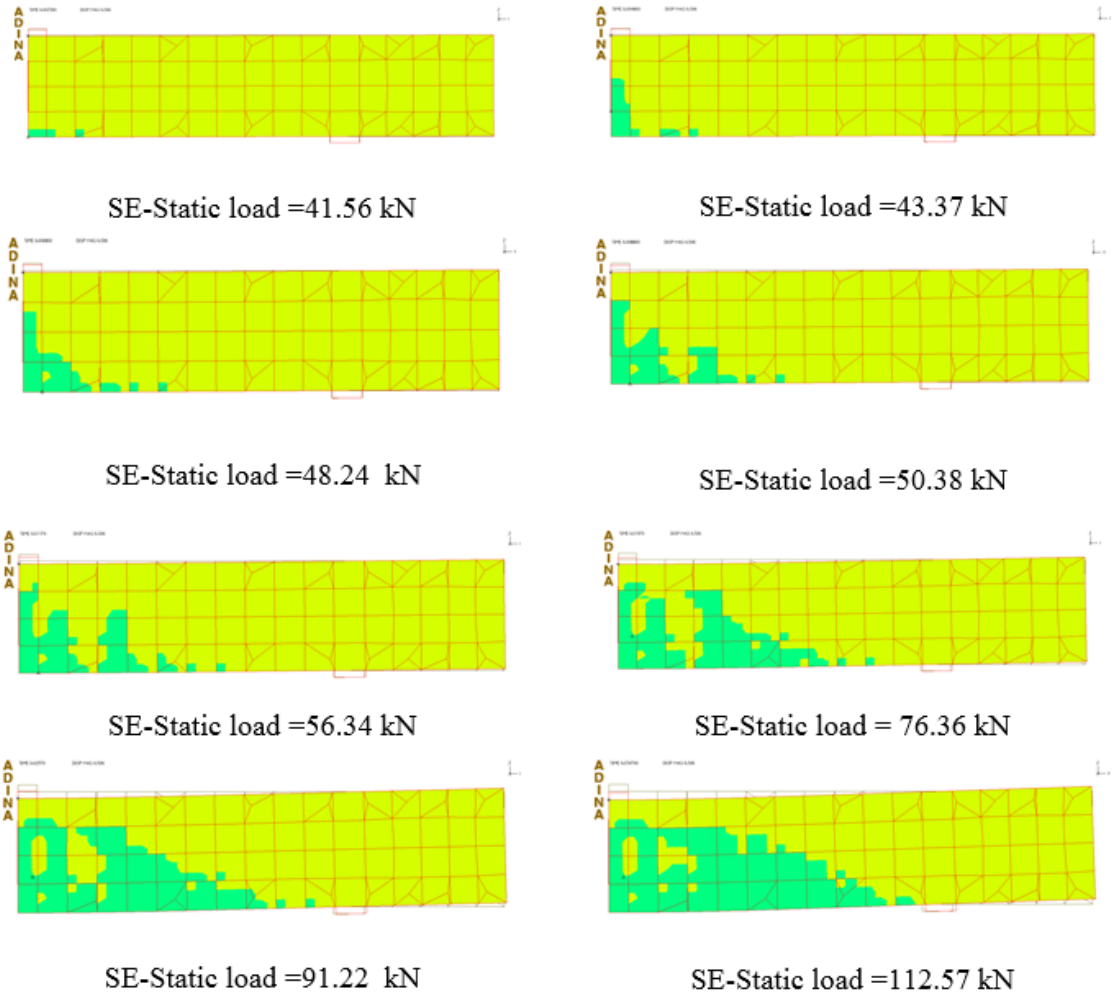

(a)

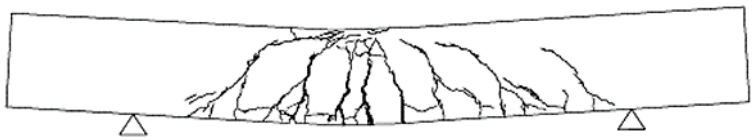

(b)

Figure 5-42 (a) Predicted deformation and cracking profiles exhibited by beam SE at different levels of static loading (b) crack pattern obtained during experimental static testing.

5.7.2 Specimens behaviour under high rate loading

5.7.2.1 Specimen behaviour under high rate loading applied monotonically to failure

Under high rate loading, the values of the applied loading rate considered in the numerical study, range from 10 to 1000 kN/ms. This range of values includes the average loading rates characterising the contact force generated during each drop-weight test (see Chapter 3). From the predicted load-deformation curves presented in Figs. 5.43 and 5.44, it appears that an increase in the loading rate leads to an increase in stiffness and maximum sustained load. Among slender beams (i.e. A1, B1 and C2), specimen A1 was characterised by a higher value of compressive reinforcement ratio sustained higher value of impact loading (see Fig. 5.43c). In the case of the short beams, the specimens sustained higher values of impact load comparing to slender beams except for Type C in which no stirrups were used (see Fig. 5.44e).

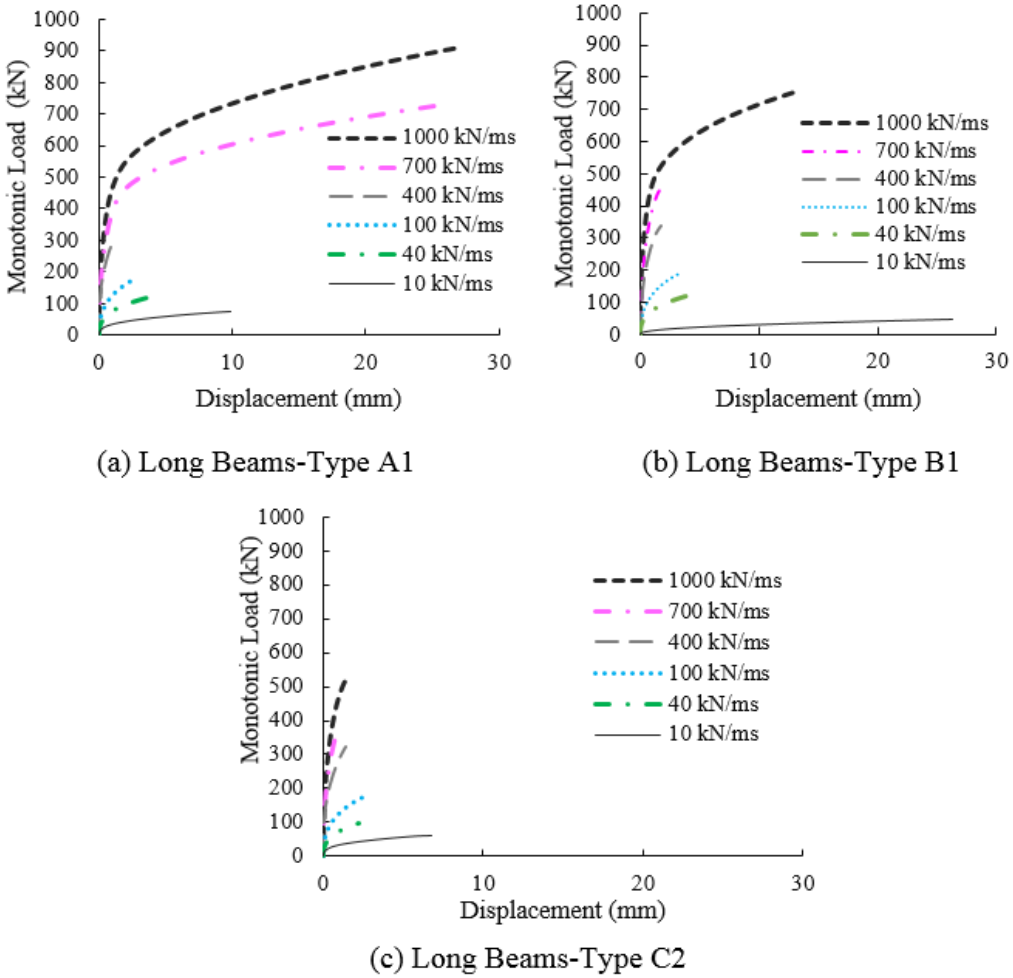

Figure 5-43 Numerical established load-deflection curves for the case of slender beams.

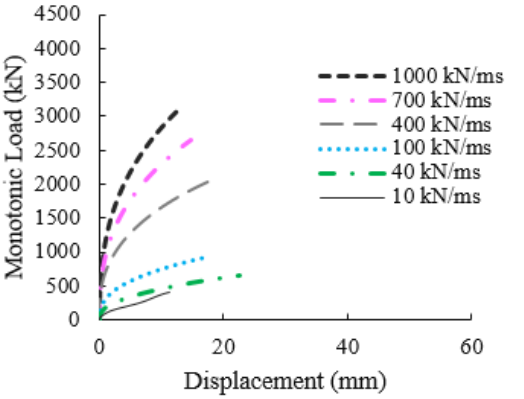

(a) Short Beams-SS0

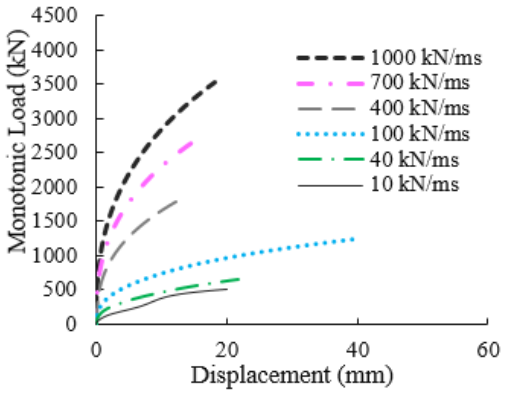

(b) Short Beams-SS1

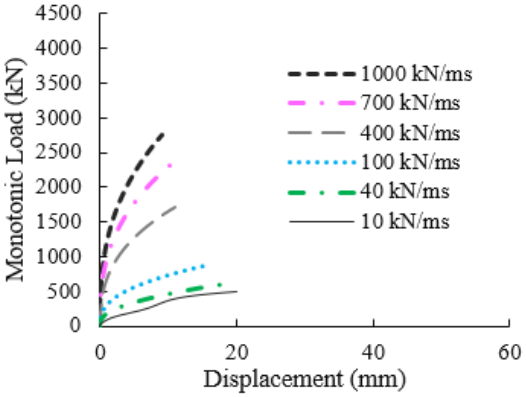

(c) Short Beams-SS2

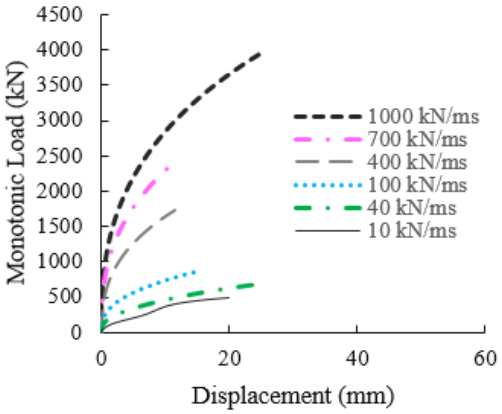

(d) Short Beams-SS3

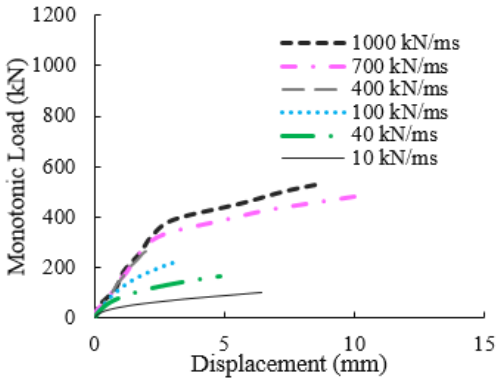

(e) Short Beams-C

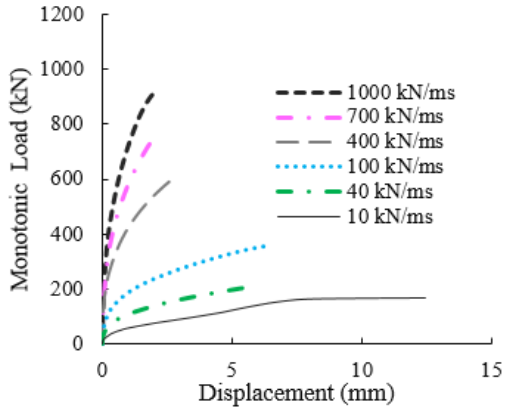

(f) Short Beams-D

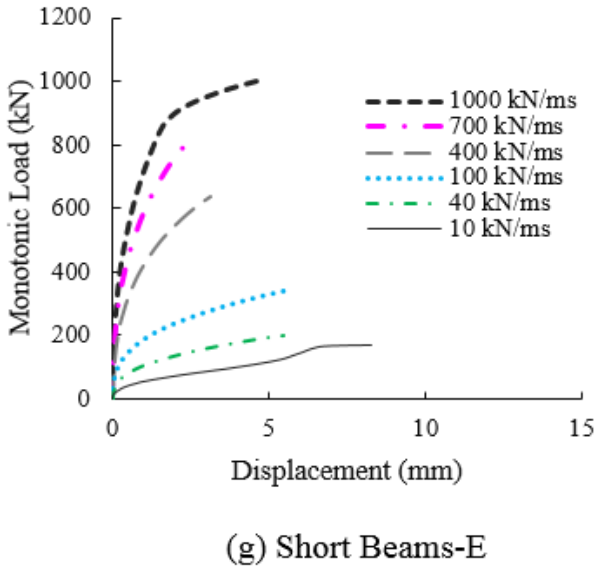

(g) Short Beams-E

Figure 5-44 Numerical established load-deflection curves for the case of short beams.

The cracking and deformation profiles presented in Figs. 5.45-5.47 indicate that, under relatively low rates of impact loading, the behaviour of the slender beam specimens is similar to that exhibited under static loading in the sense that the entire span reacts to the response. It is noted that the crack patterns shown in Figs. 5.45-5.54 correspond to the peak value of the load applied monotonically until the specimen fails (see Figs. 5.43-5.44).

It is inevitable to conclude that the level of damage (i.e. cracking) sustained during impact testing, is more severe comparing those during static loading (see Figs. 5.33-5.35). As the rate of loading increases, the portion (L_{eff}) of the beam mostly affected by the applied load reduces. For relatively high rates of loading, L_{eff} is confined to the region extending on either side of the mid-span cross-section to a distance marked by the formation of vertical (flexural) cracking initiating at the upper face and extending downwards, whereas the remainder of the beam, (i.e. the portions extending between the supports and the aforementioned cracking) practically remain unaffected by the applied load (see Figs. 5.45-5.47).

The numerically predicted deformation profiles and related crack-patterns exhibited by the short RC beam D and E shown in Figs. 5.48-5.54 indicate that the full span of these specimens reacts to the imposed impact load and that localised response is exhibited at much higher loading rates (compared to those established for the of the slender beams).

The failure of the specimen C (without stirrups) under higher rates of loading (i.e. 400 and 1000 kN/ms) was associated with the failure of concrete in compression zone near the impact region where extensive cracks develop as well as the formation of severe shear cracks. Specimen D and E developed (inclined) shear cracks which ultimately led to the failure.

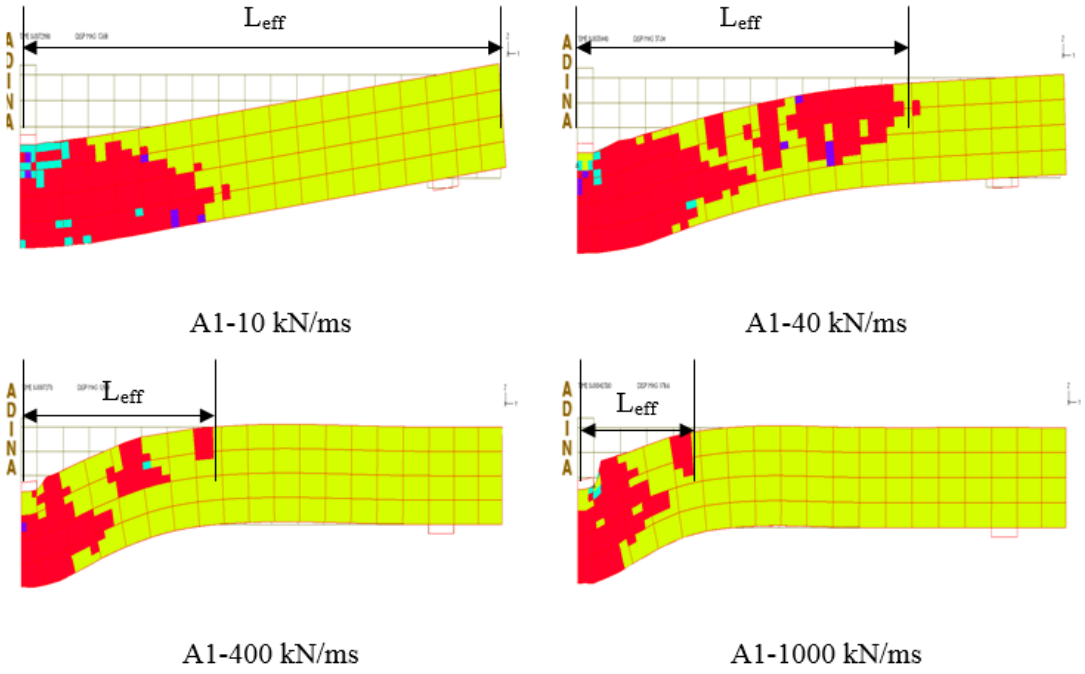

Figure 5-45 Numerically predicted deformation and cracking profiles exhibited at different rates of loading for the case of beam A1 under monotonic impact loading.

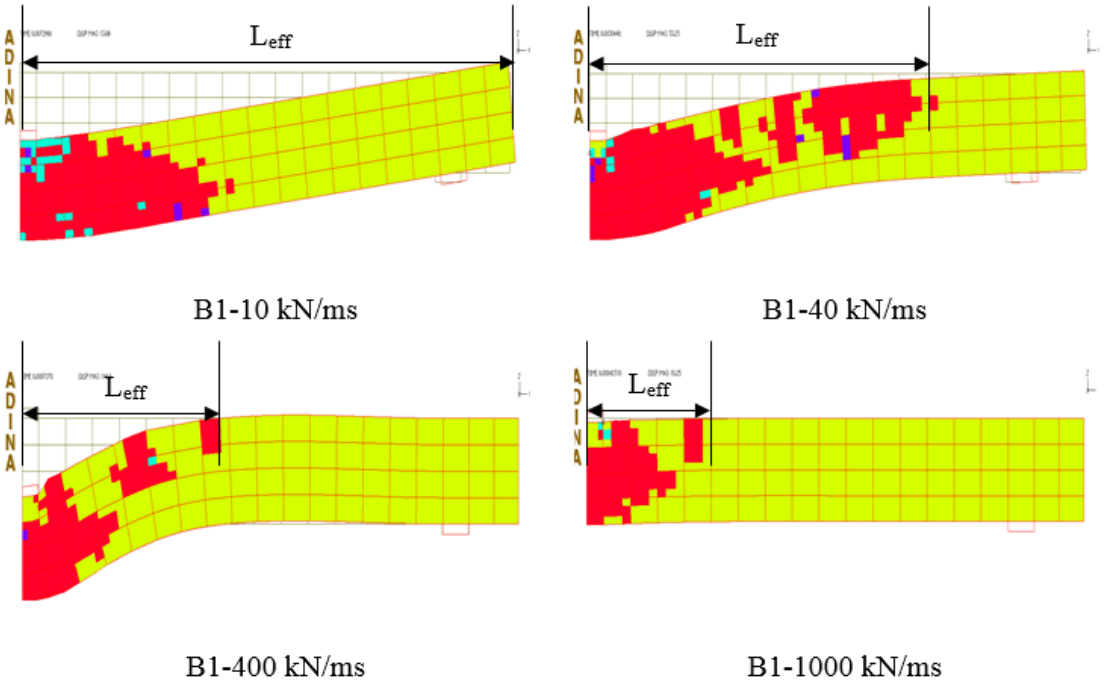

Figure 5-46 Numerically predicted deformation and cracking profiles exhibited at different levels of levels for the case of beam B1 under monotonic impact loading.

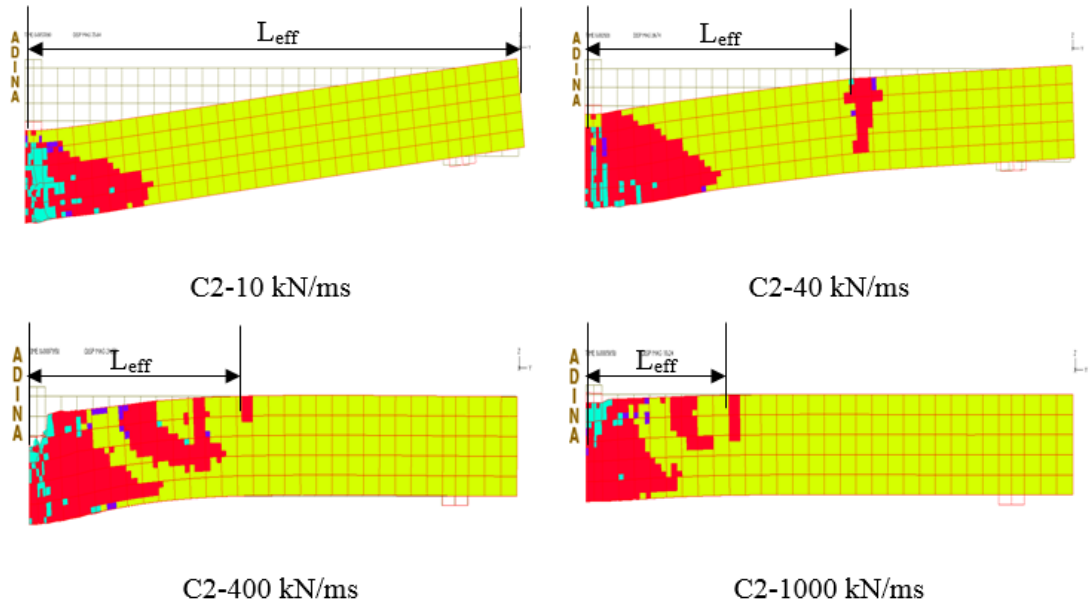

Figure 5-47 Numerically predicted deformation and cracking profiles exhibited at different levels of levels for the case of beam C2 under monotonic impact loading.

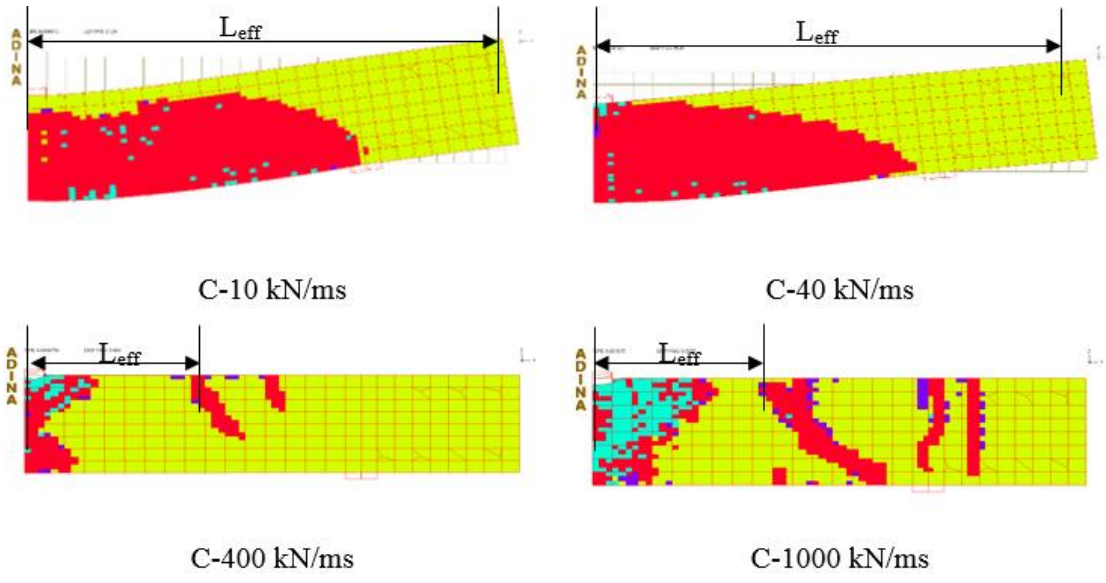

Figure 5-48 Numerically predicted deformation and cracking profiles exhibited at different levels of levels for the case of beam C under monotonic impact loading.

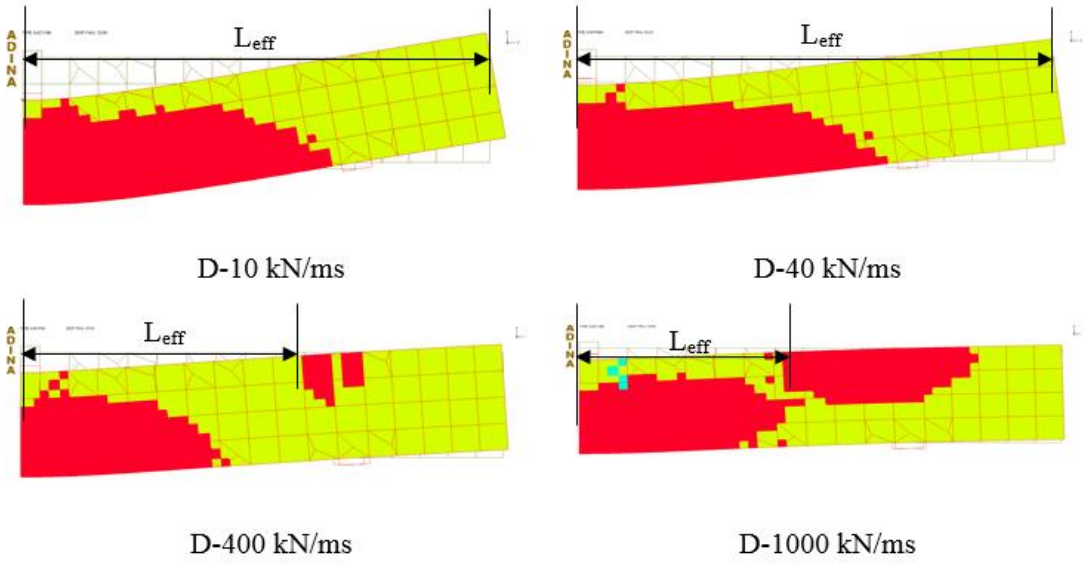

Figure 5-49 Numerically predicted deformation and cracking profiles exhibited at different levels of levels for the case of beam D under monotonic impact loading.

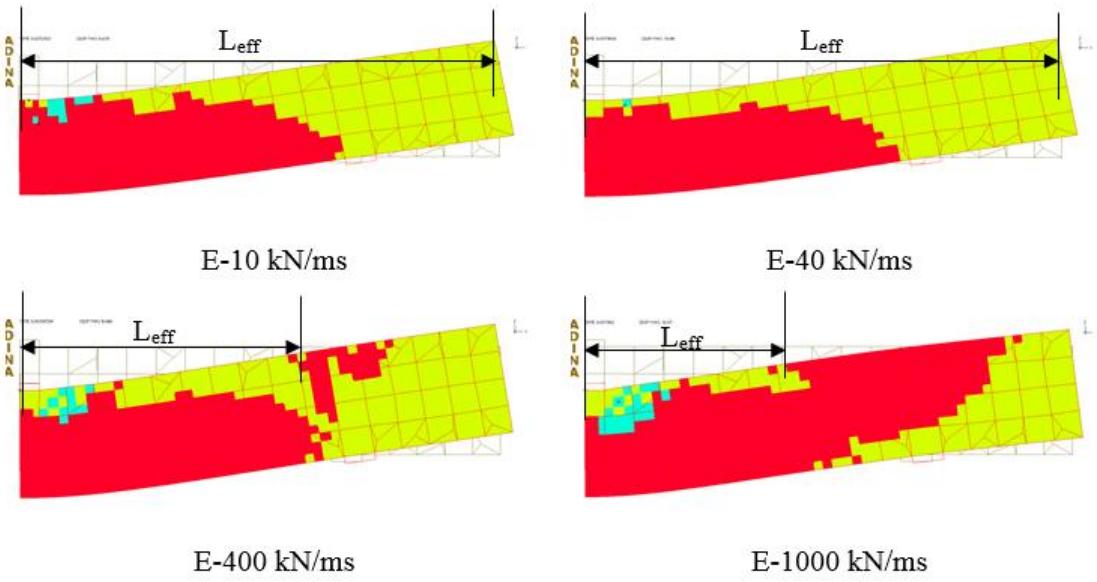

Figure 5-50 Numerically predicted deformation and cracking profiles exhibited at different levels of levels for the case of beam E under monotonic impact loading.

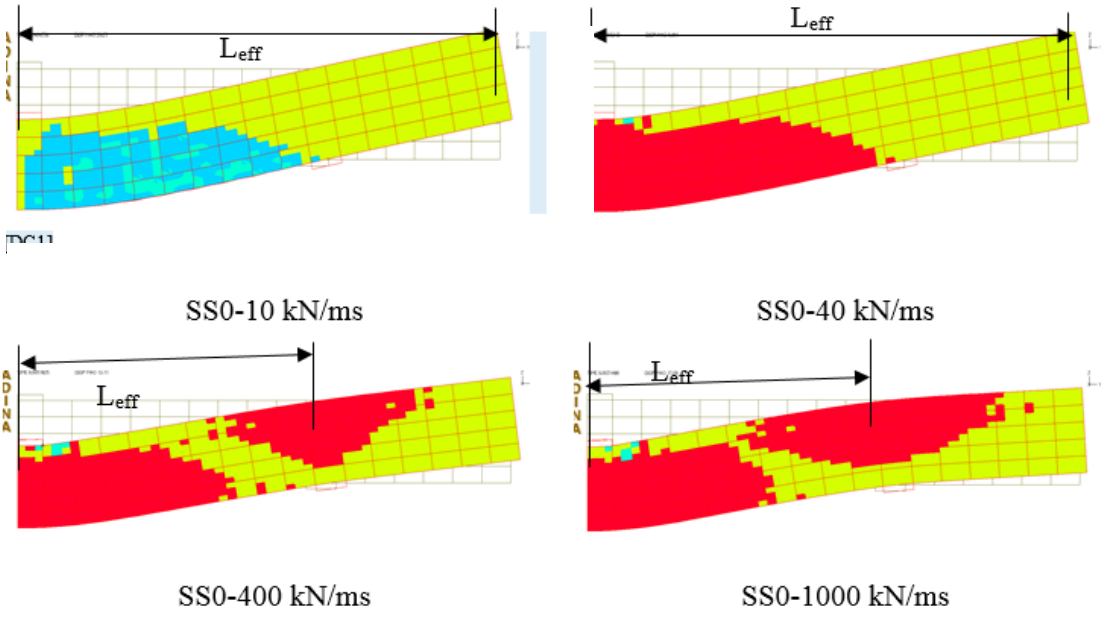

Figure 5-51 Numerically predicted deformation and cracking profiles exhibited at different levels of levels for the case of beam SS0 under monotonic impact loading.

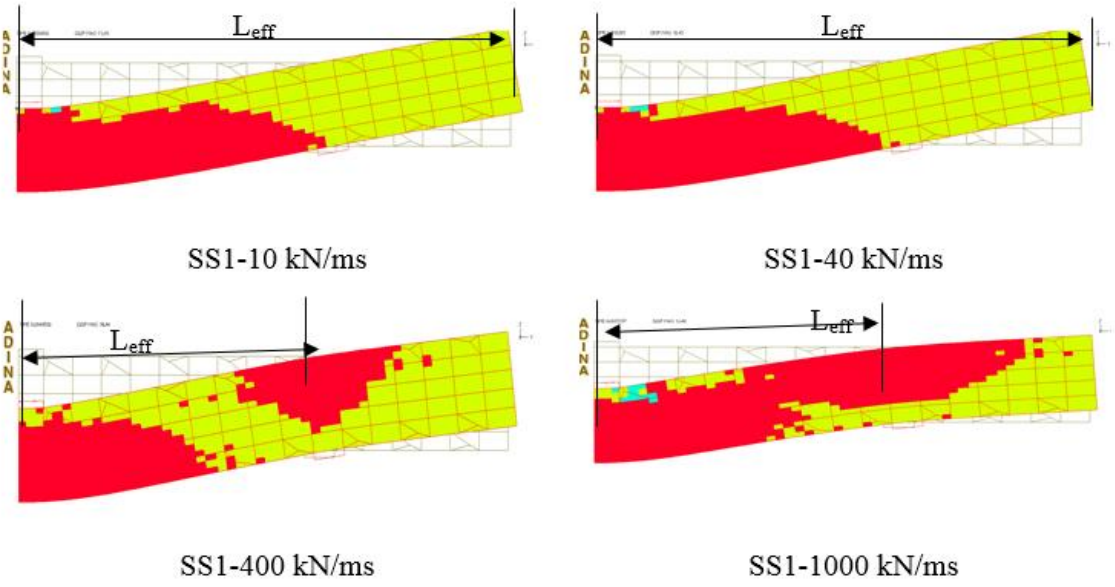

Figure 5-52 Numerically predicted deformation and cracking profiles exhibited at different levels of levels for the case of beam SS1 under monotonic impact loading.

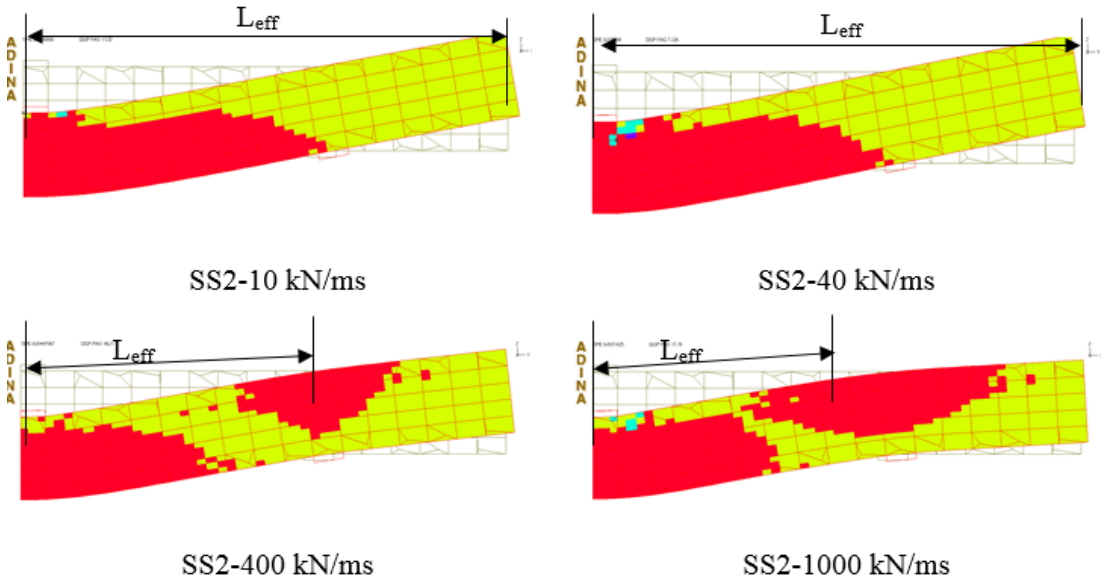

Figure 5-53 Numerically predicted deformation and cracking profiles exhibited at different levels of levels for the case of beam SS2 under monotonic impact loading.

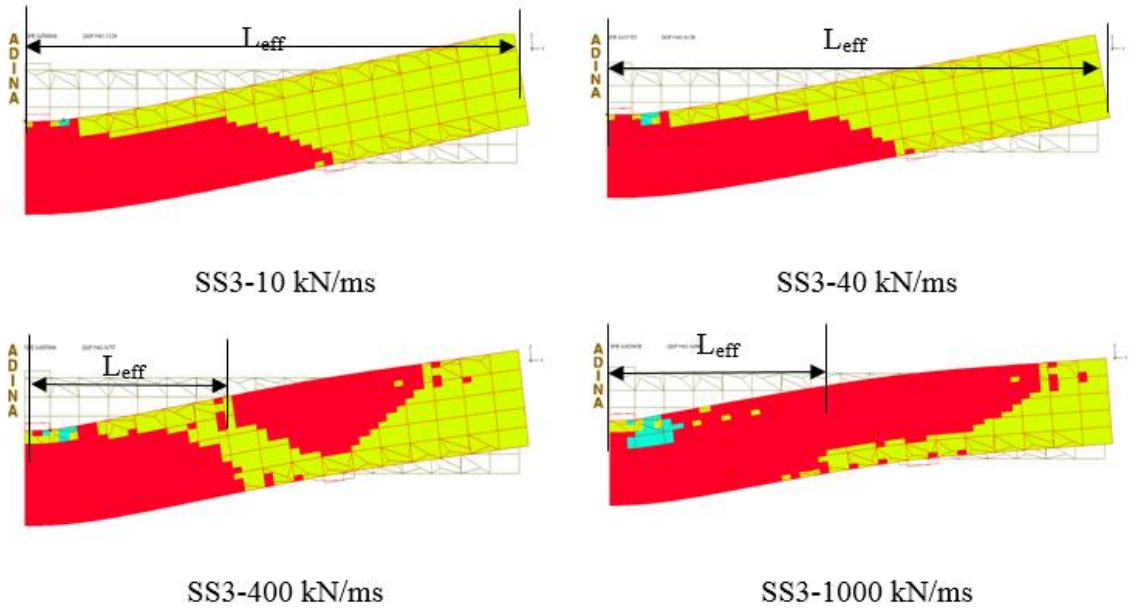

Figure 5-54 Numerically predicted deformation and cracking profiles exhibited at different levels of levels for the case of beam SS3 under monotonic impact loading.

5.7.2.2 Load applied in the form of a pulse

The predictions obtained from the pulse loading is presented in Figs. 5.55-5.57 for the case of the slender beams and in Figs. 5.58-5.64 for the case of the short beam specimens. The figures express the numerical predictions in the form of a concentrated pulse load (P_{pulse}) versus the mid-span deflection curve. The specimens were subjected to different rates of loading ($\dot{P}$) ranging from 10-1000 kN/ms but different intensities (i.e. P_{pulse} is *a percentage of* P_{max} obtained for the case of monotonic see Figs. 5.43 and 5.44). The lowest percentage of the pulse presented in the figures corresponds to the true load-bearing capacity of the RC beams for the particular loading rate. The true load-bearing capacity of an RC beam is assumed to correspond to a peak value at which the externally applied load is resisted by the RC member. Consequently, the RC members (after exhibiting its maximum deflection) do not fail as the deflection gradually start to reduce.

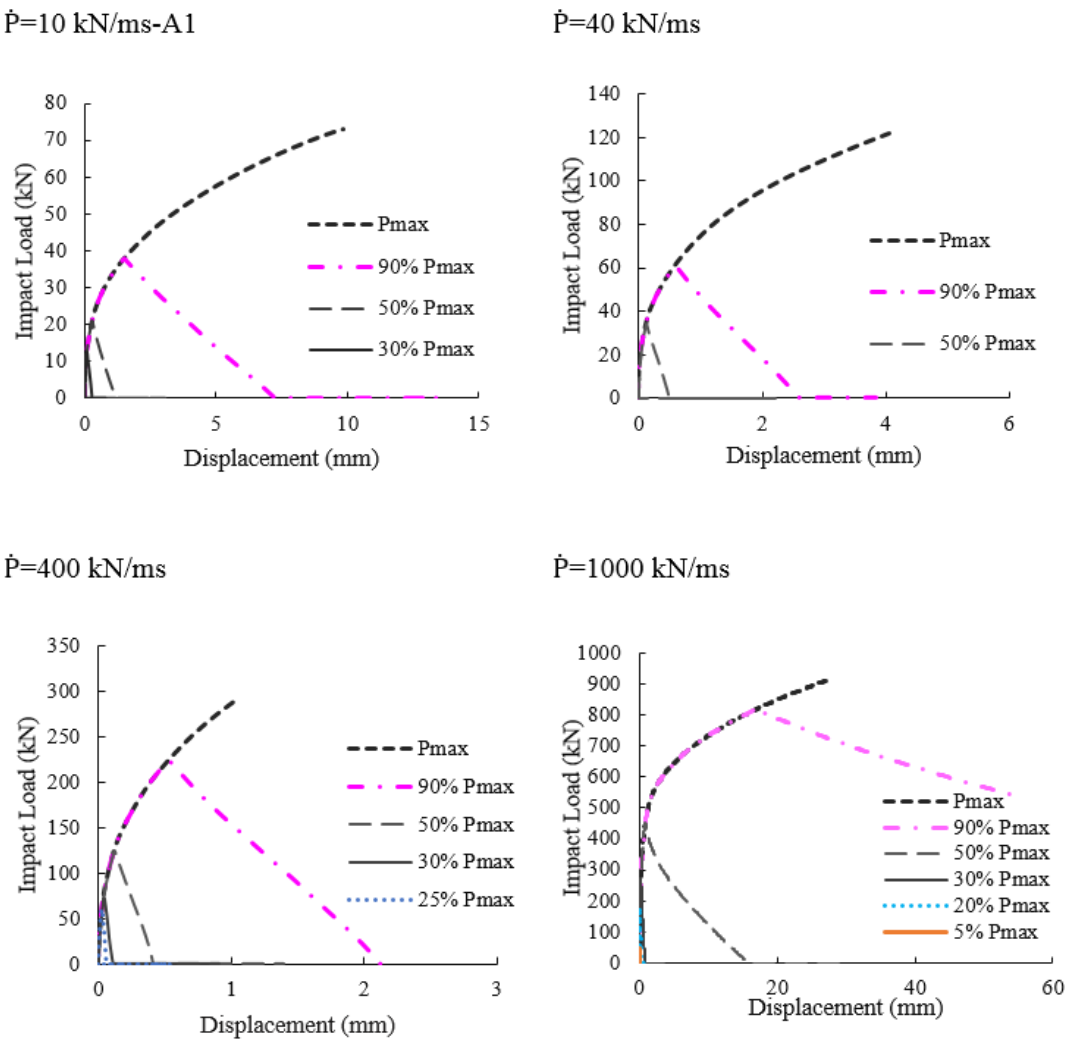

Figure 5-55 Beam A1 under the varied pulse loading with different rates and intensities.

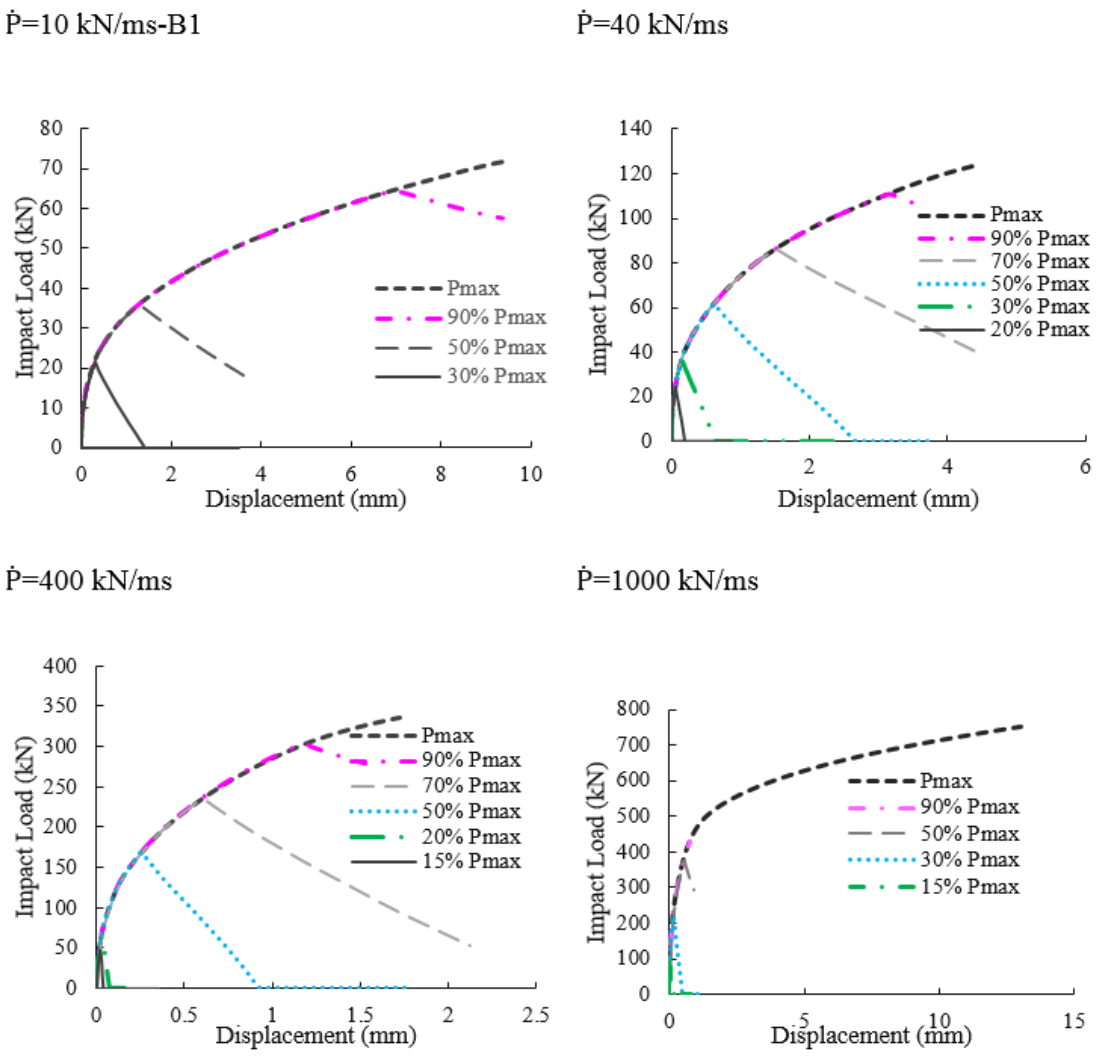

Figure 5-56 Beam B1 under the varied pulse loading with different rates and intensities.

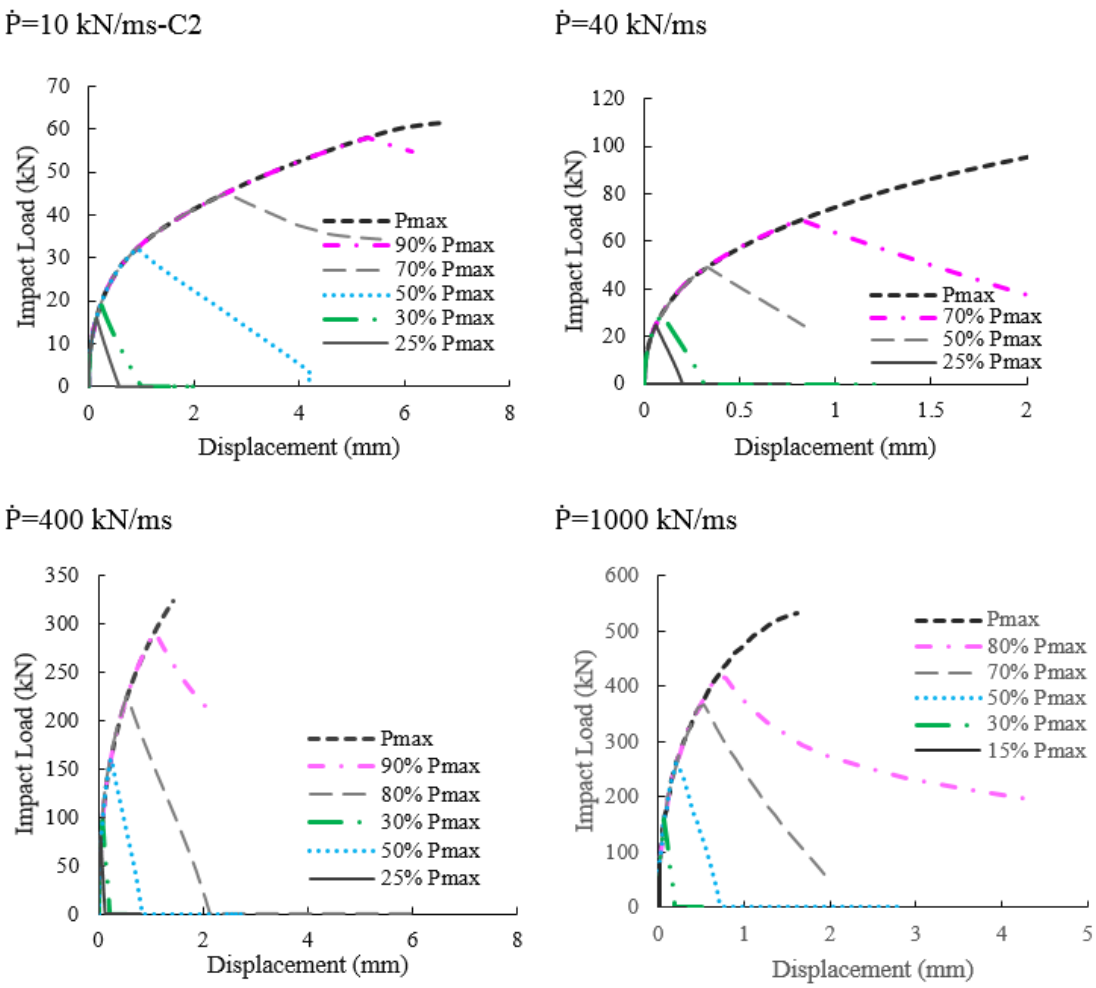

Figure 5-57 Beam C2 under the varied pulse loading with different rates and intensities.

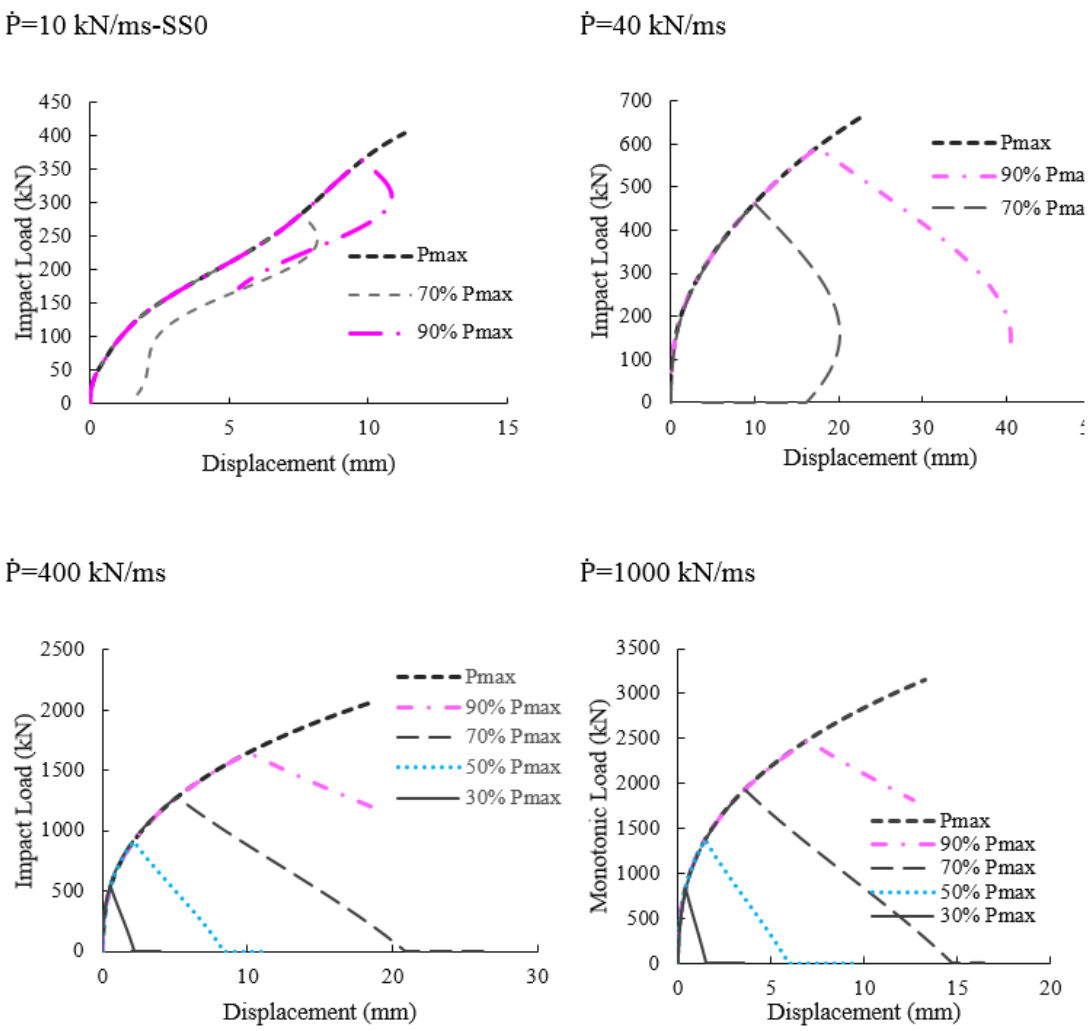

Figure 5-58 Beam SS0 under the varied pulse loading with different rates and intensities.

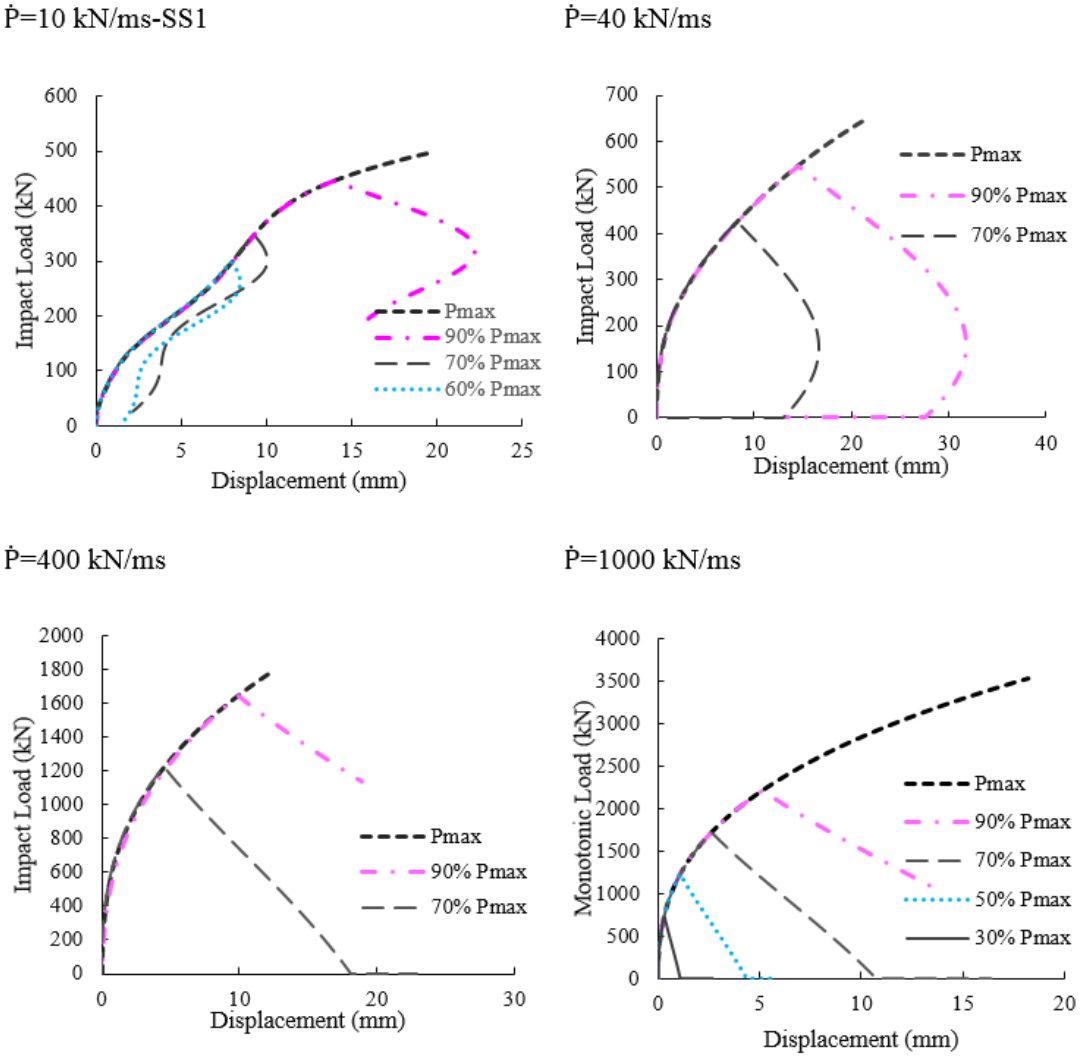

Figure 5-59 Beam SS1 under the varied pulse loading with different rates and intensities.

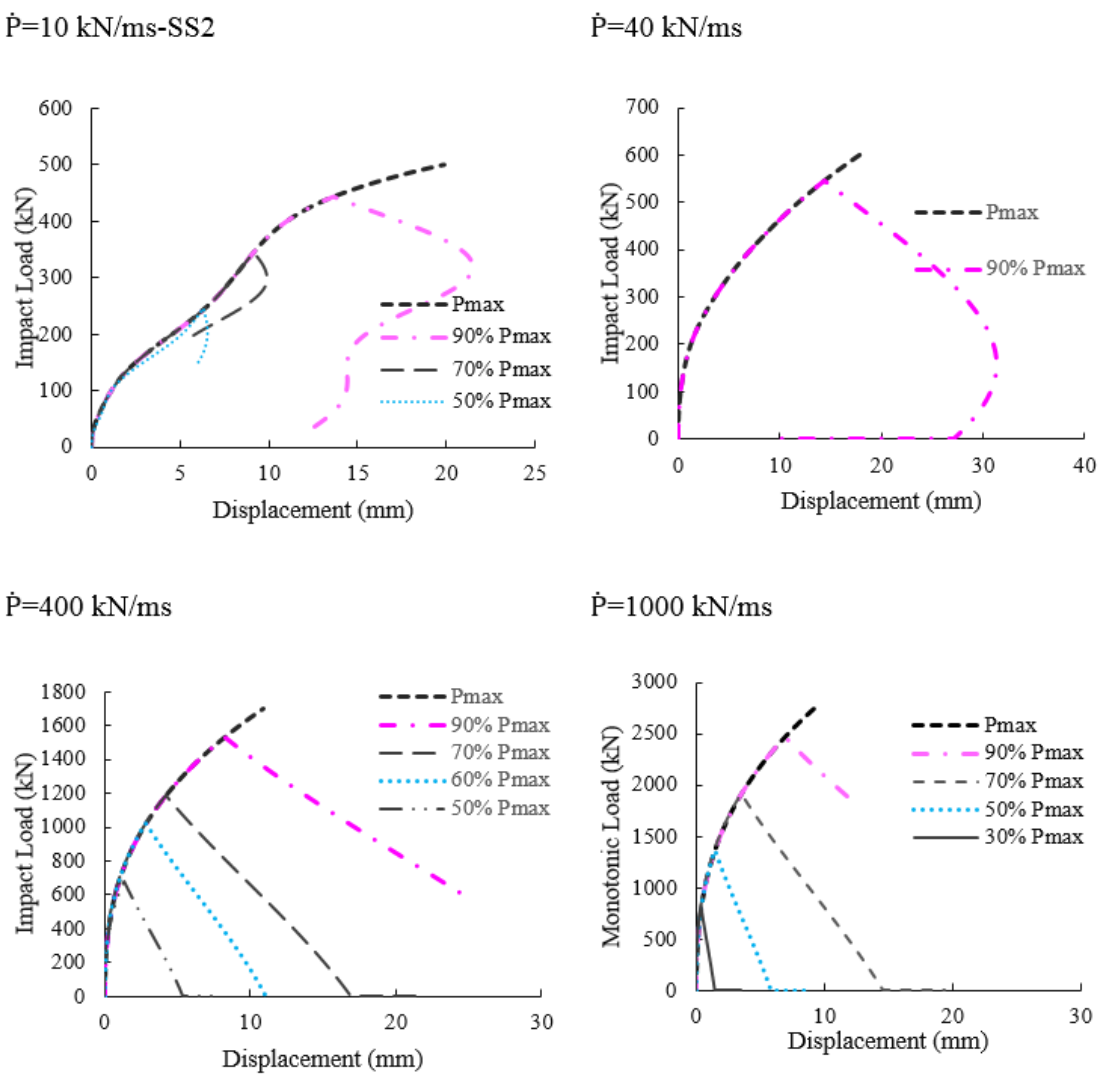

Figure 5-60 Beam SS2 under the varied pulse loading with different rates and intensities.

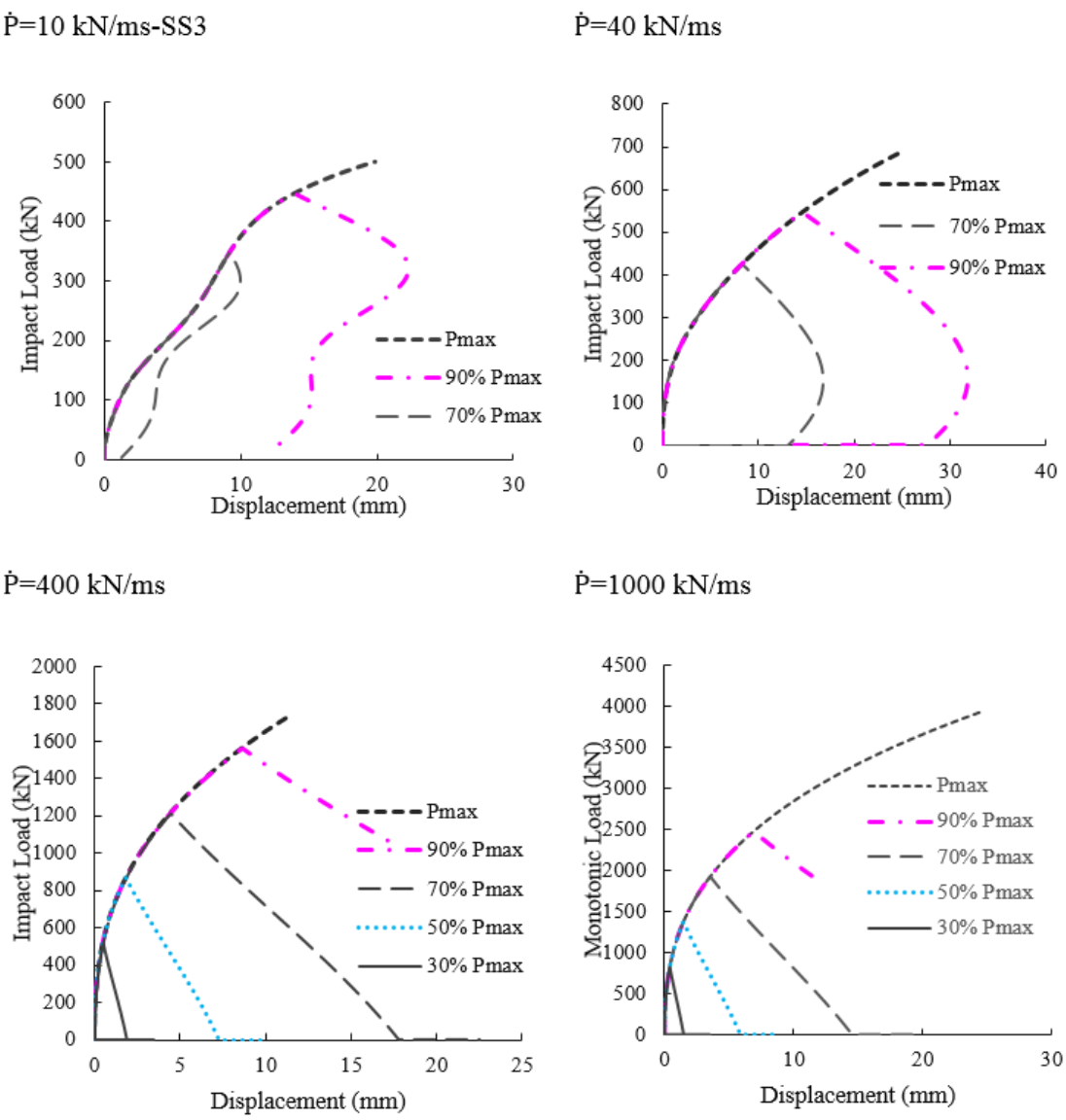

Figure 5-61 Beam SS3 under the varied pulse loading with different rates and intensities.

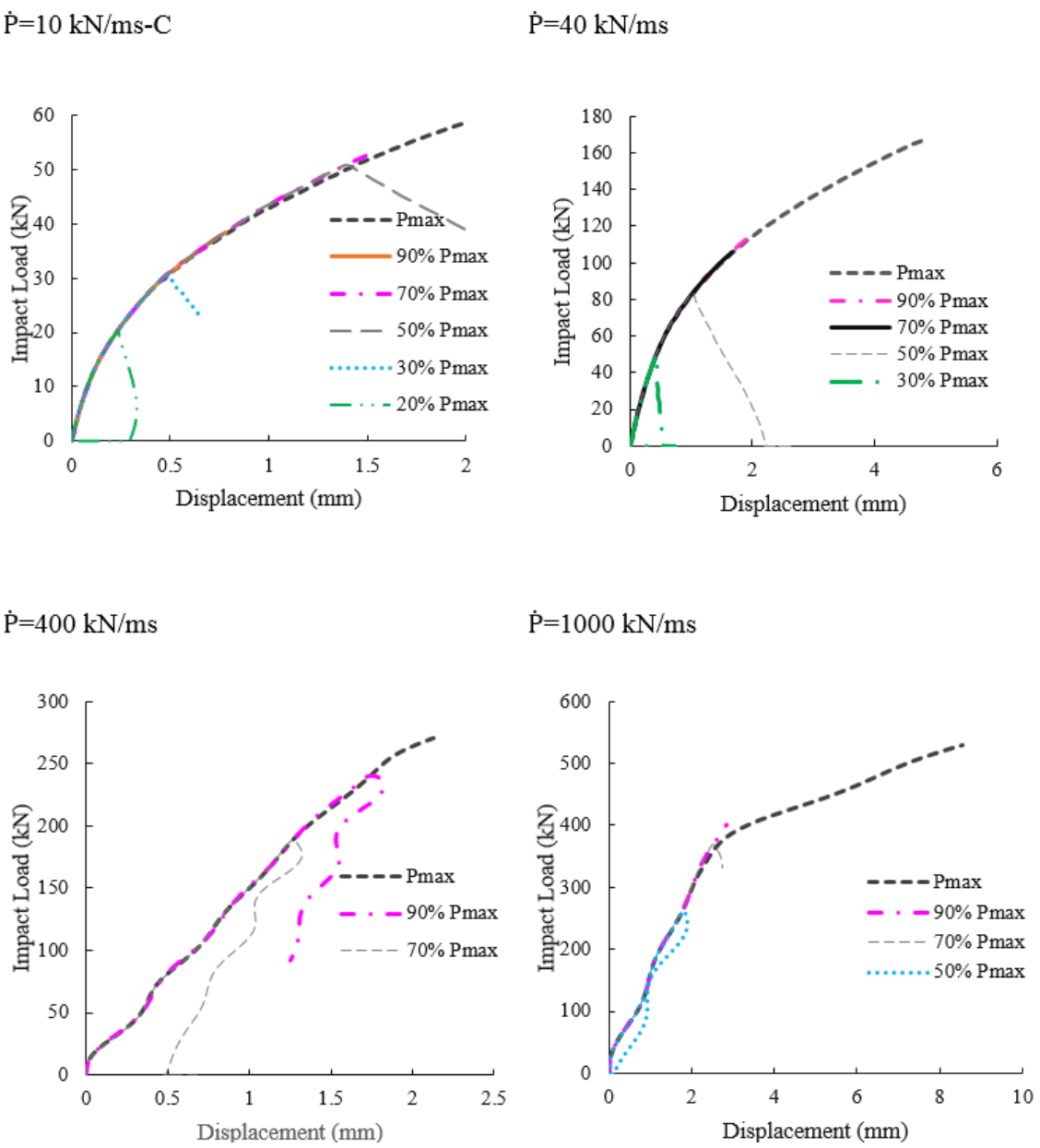

Figure 5-62 Beam C under the varied pulse loading with different rates and intensities.

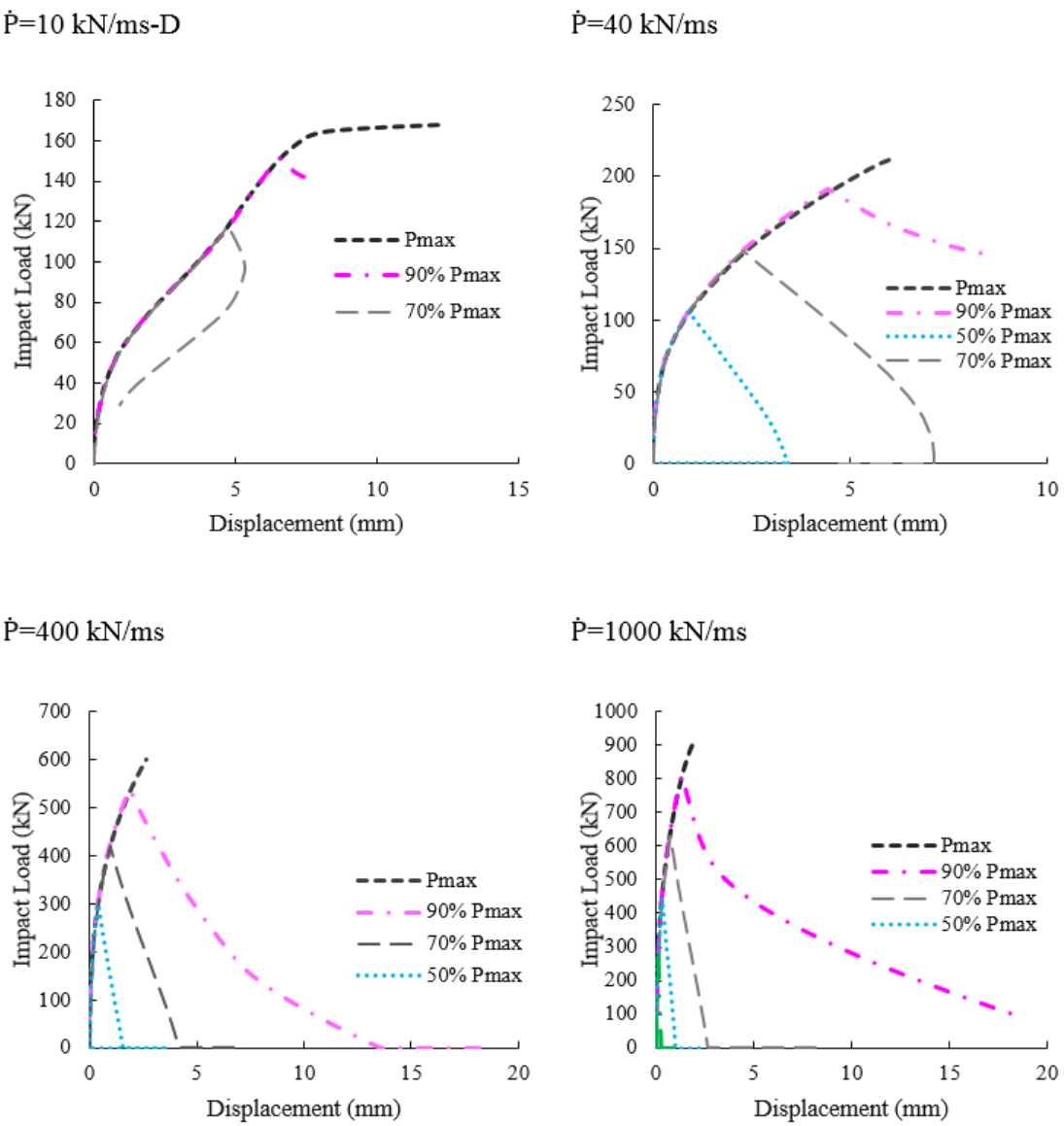

Figure 5-63 Beam D under the varied pulse loading with different rates and intensities.

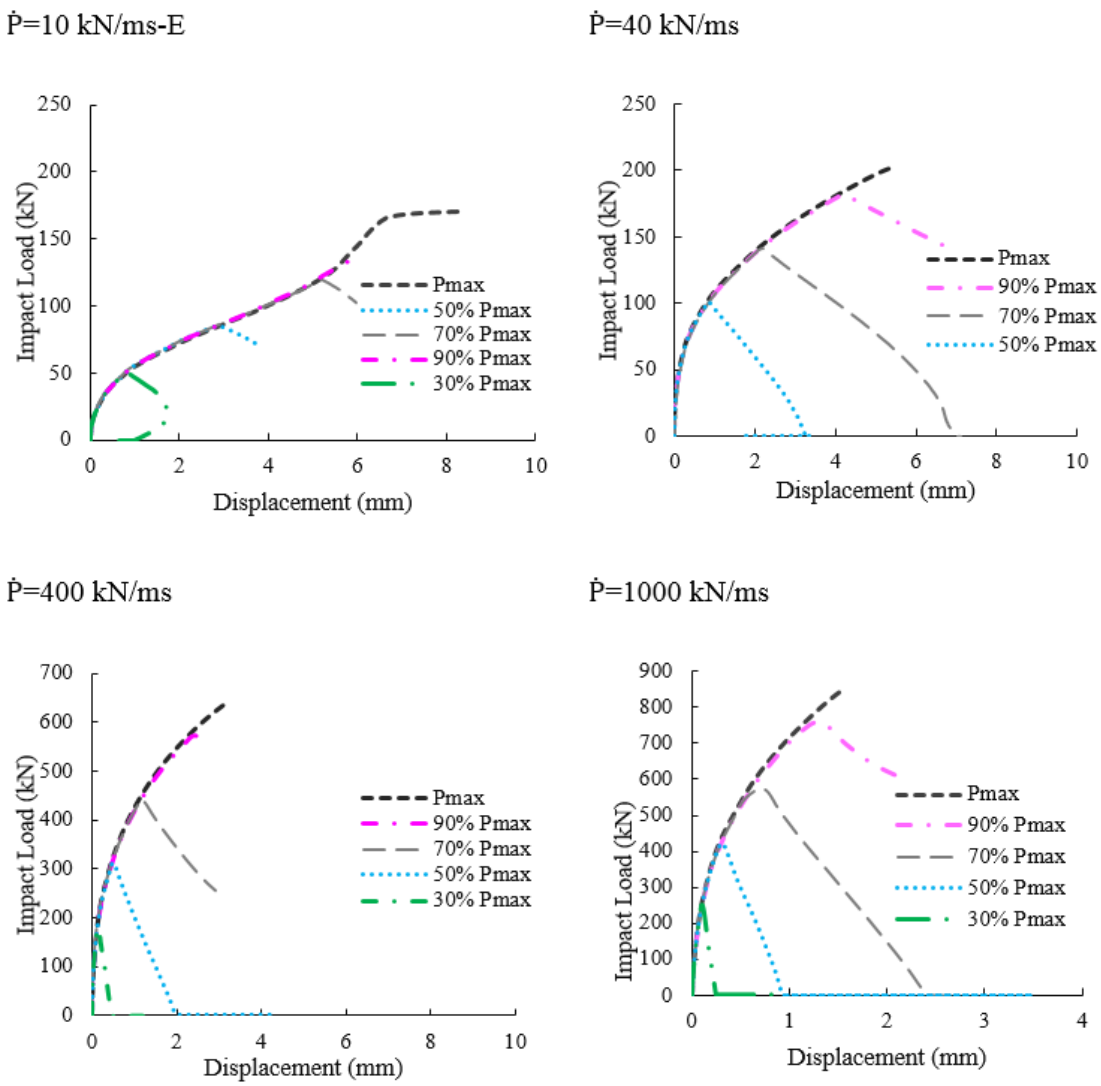

Figure 5-64 Beam E under the varied pulse loading with different rates and intensities.

The variation of Dynamic Increase Factors (DIF) associated with the peak value of the monotonically applied load (ultimately resulting in failure of the RC beam) and the pulse load that *will not* result in failure of the member is presented in Fig. 5.65 for the case of slender and short RC beams. As discussed previously in section 5.5 a pulse load herein, refers to the impact load applied in the form of a pulse (see Fig. 5.20b), exhibiting the same rate of loading (as the monotonic loading) with the magnitudes less than those adopted for the case of monotonic loading. The magnitude of the pulse load (used in ADINA) is a percentage of the monotonic load. The percentage reduces gradually ranging from 90% to 5% (with 10% interval). Reducing the magnitude of the pulse load continues right before the failure of the RC element, up to which no residual deflection occurs (i.e. the beam returns to its neutral position and residual displacement is zero).

The value of DIF is equal to the ratio of peak value or the dynamic load applied and the static load carrying capacity i.e. $P_{dynamic}/P_{static}$. When the impact load is applied monotonically (Fig. 5.20a), the latter ratio is expressed as P_{max}/P_s where P_{max} is the peak value of the monotonic load and P_s is the static load. When the impact load is applied as a pulse (Fig. 5.20b), the ratio is expressed as P_{pulse}/P_s where P_{pulse} the peak value of the pulse load. In Fig. 5.65, the DIF values predicted numerically by ADINA for the case of slender and short beams, associated with the application of pulse loads are presented in comparison to their counterparts established numerically for the case of monotonic loading and experimentally. These results suggest that the data obtained from drop-weight tests on RC beams (which is in good agreement with P_{max} predicted numerically for the case of monotonic loading) are essentially associated with the post-failure behaviour of the RC specimens. As a result, it can be concluded that the true load-bearing capacity of the RC beams under impact loading is much lower than the latter values. Furthermore, it is established that the higher the loading rate and intensity of the impact load the larger the latter difference becomes (see Fig. 5.65).

From the figure, it can be seen that the value of DIF corresponding to the slender RC beams are considerably higher than those associated with short beams. The latter is justified by looking at the impact problem as a wave propagation problem in the sense that in the case of short beams (i.e. beams with $a_v/d<5$) the impact-induced stress-wave, has more time to travel within the span of the member and reach the supports in doing so more portion of the element length (i.e. L_{eff}) react to the applied impact load and that will reduce the maximum sustained load to a great extent (in comparison with slender beams) and result in the value of DIF significantly lower than those obtained for the case of slender beams. The above assumption is obvious from the crack patterns depicted in Figs. 5.45-5.54.

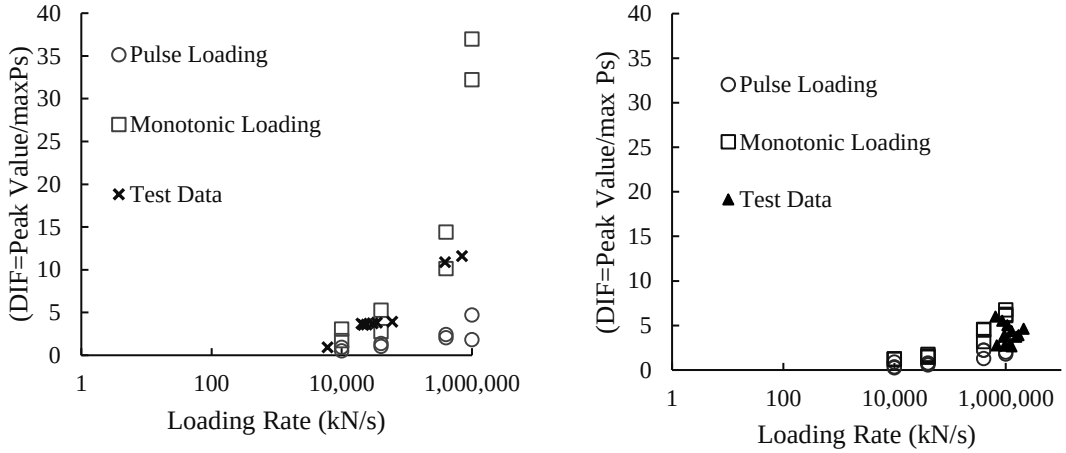

(a) (b)

Figure 5-65 Comparison of experimental and numerical predictions expressing the variation of the load-carrying capacity of the RC (a) slender (a_v/d=6.755) and (b) short (a_v/d=2.835) beams conducted at Heriot-Watt University with loading rate (for the case of monotonic and pulse loading).

5.7.2.3 Crack Pattern and deformation profile

The predicted deformation profiles of slender and short RC specimens are shown in Figs. 5.66 and 5.67 respectively when subjected to monotonic (P_{max}) and pulse loading with two different rates of $\dot{P}$ = 10 and 1000 kN/msec but different intensities. The predictions are expressed in the form of mid-span displacement-time history. The figures suggest that for the specific loading rate, as the intensity of the applied load (i.e. ranging from P_{max}-0.05 P_{max}) decreases the amount of ductility exhibited by the RC beams increases. The curves in Figs. 5.66 (a) and (b) reveal that for the case of Type A (i.e. the slender beam defined in Chapter 3, see Fig. 3.1), subjected to the rates of 10 and 1000 kN/msec, while the *peak values* of the pulse load are higher than 50% and 5% of P_{max} (obtained for the case of monotonic loading) the RC beam fails during unloading. However, when the peak value of the pulse load becomes equal or less than the minimum intensity of the peak value (e.g. 50% and 5% of P_{max} for Type A), the RC beam does not fail and continues to oscillate after unloading takes place. The latter peak values (≈ 50% and 5% P_{max}) can be considered as the true load-bearing capacity of the RC beam for $\dot{P}$ = 10 and 1000 kN/msec respectively for Type A. Such assumption, applied to other types of the subject specimens (i.e. B, C, D and E) with the minimum value of the pulse load varies for each type. The comparison between the deformation profile of slender and short RC specimens suggest that the latter exhibits less amount of ductility (see Figs. 5.66 and 5.67).

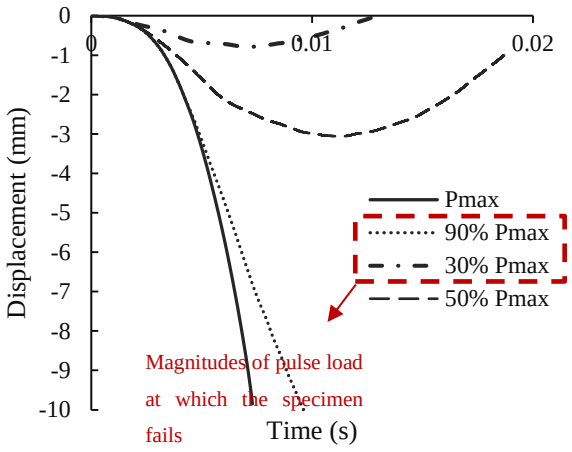

(a) Type A Ṗ=10 kN/ms

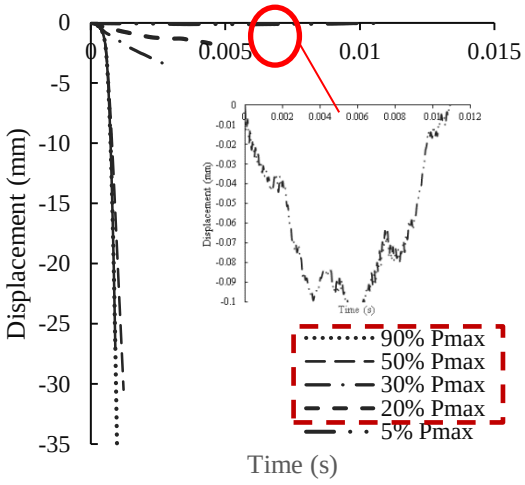

(b) Type A Ṗ=1000 kN/ms

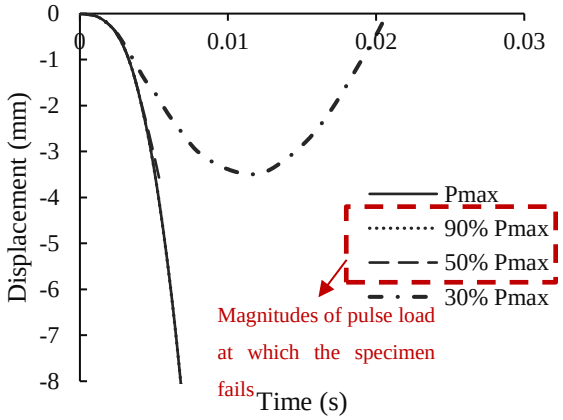

(c) Type B Ṗ=10 kN/ms

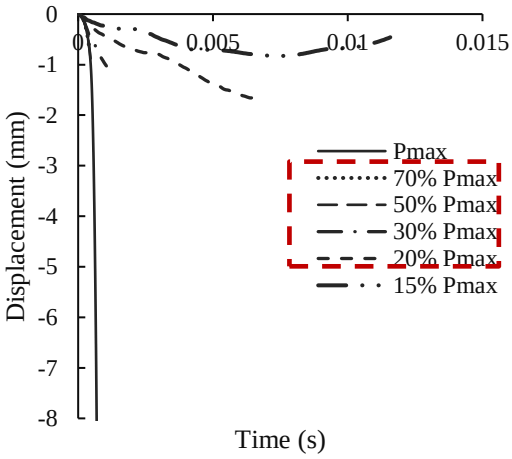

(d) Type B Ṗ=1000 kN/ms

Figure 5-66 Predicted mid-span displacement time history obtained for pulse loads with (a), (c) Ṗ=10 and (b), (d) Ṗ=1000 kN/ms but different intensities for slender specimens A and B.

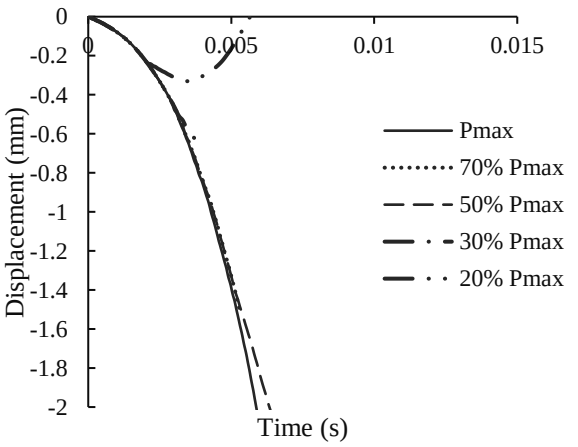

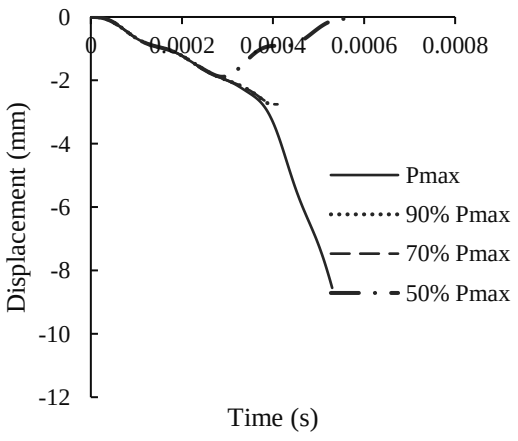

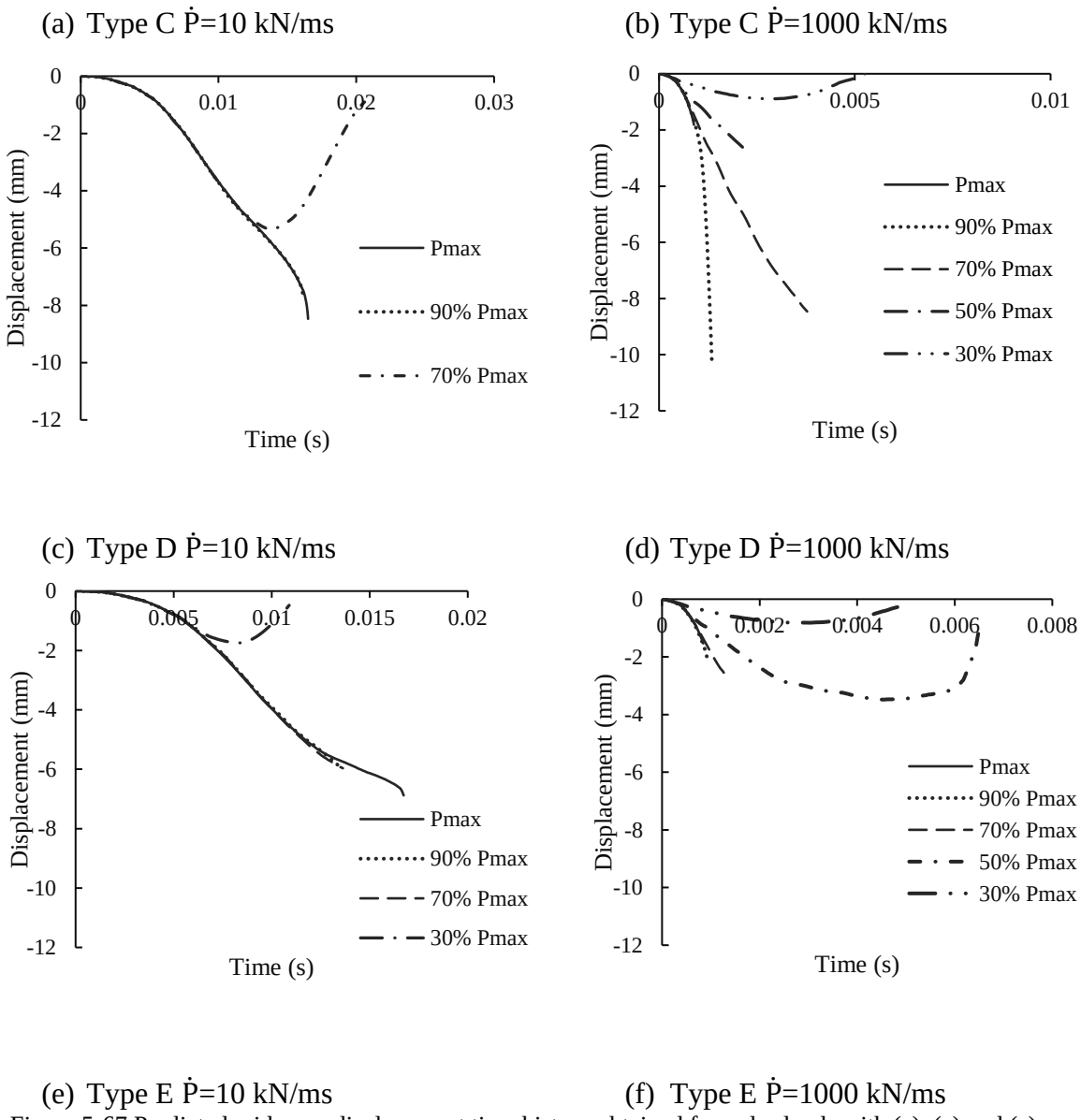

Figure 5-67 Predicted mid-span displacement time history obtained for pulse loads with (a), (c) and (e) Ṗ=10 and (b), (d) and (f) Ṗ=1000 kN/ms but different intensities for slender specimens A and B.

The associated crack patterns developing on RC specimens are depicted in Fig. 5.68 and 5.69 for slender beams and Fig. 5.70 -72 for short specimens. Concerning the deformation profile of slender RC beams (i.e. Types A and B), the ductility of Type A (see Fig. 5.66), (i.e. stronger beam in terms of the amount of compressive reinforcement) is significantly higher than those predicted for Type B (i.e. weaker specimen among slender beams), see Fig. 5.67. The latter observation can also be supported by the deformed shape exhibited by Types A and B shown in Fig. 5.68. The crack patterns are shown in Fig. 5.68-5.72 reveals that a larger portion of the span reacts to the applied load. This suggests that the L_{eff} and therefore the mechanics underlying RC structural response will be affected by both the rate of applied loading and intensity of the imposed impact load.

A-10 kN/ms

A-1000 kN/ms

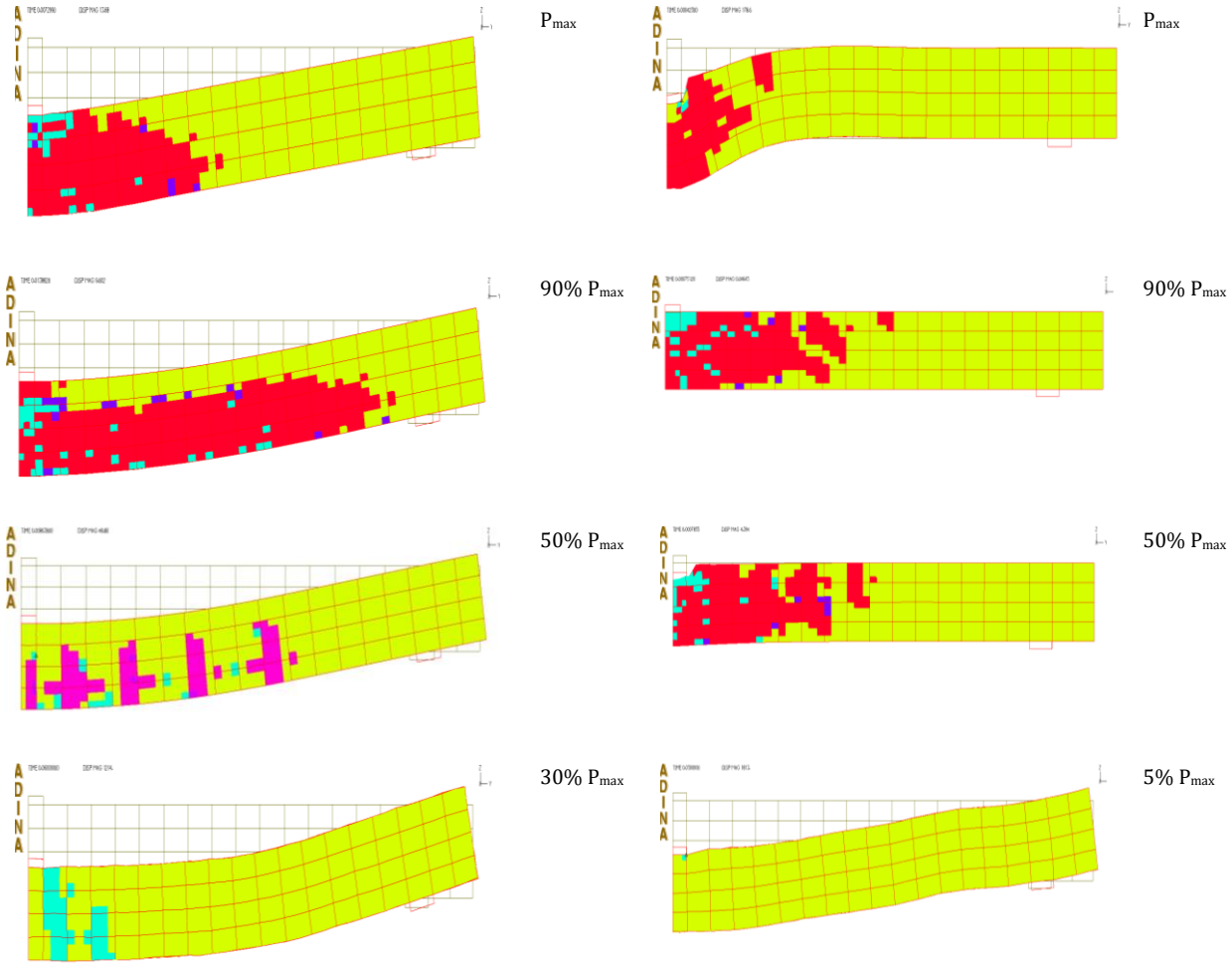

Figure 5-68 Predicted crack patterns and deformation profiles for specimen A for pulse loads with Ṗ=10 kN/ms (left) and Ṗ=1000 kN/ms (right) but different intensities.

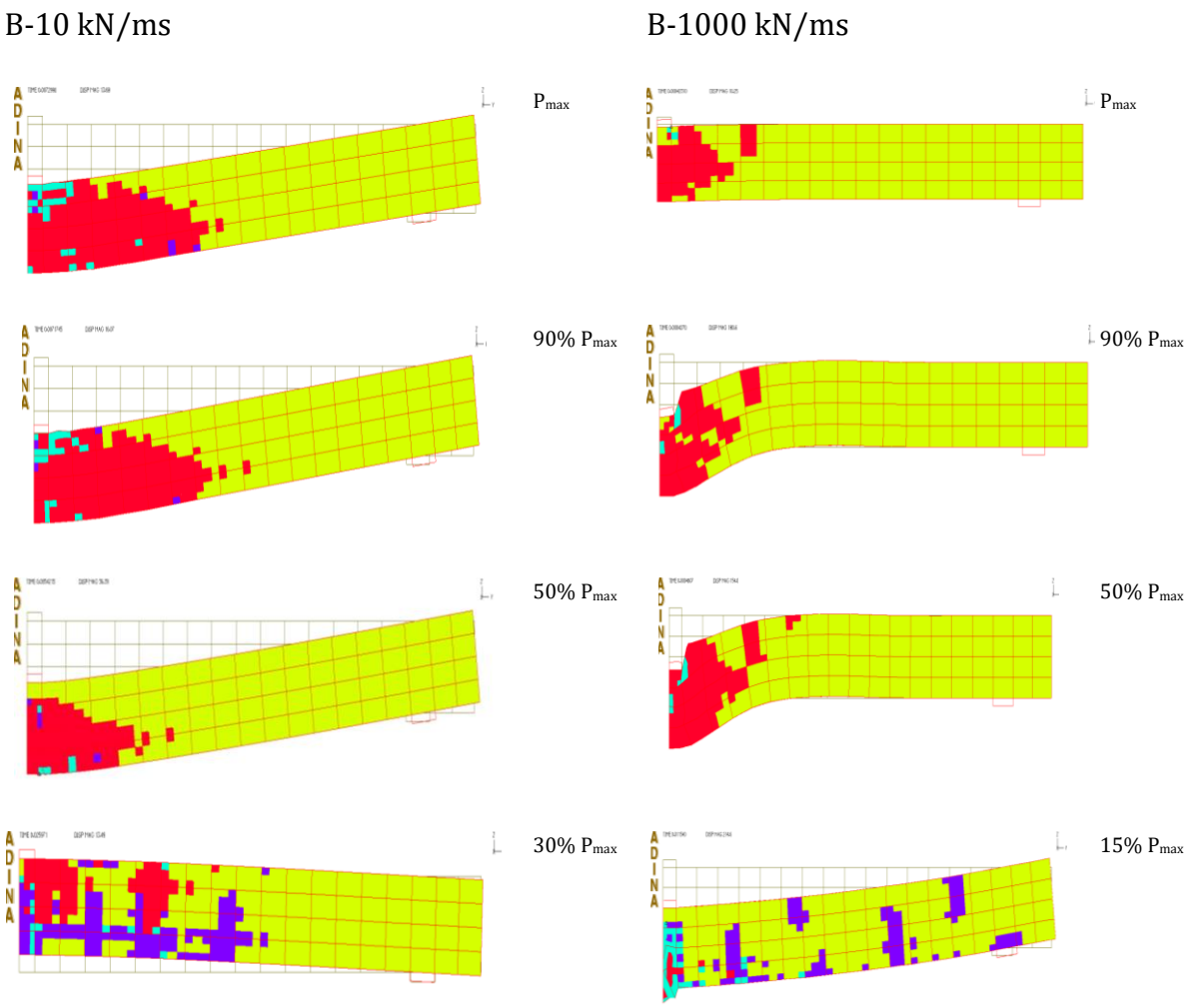

Figure 5-69 Predicted crack patterns and deformation profiles for specimen B for pulse loads with Ṗ=10 kN/ms (left) and Ṗ=1000 kN/ms (right) but different intensities.

C-10 kN/ms

C-1000 kN/ms

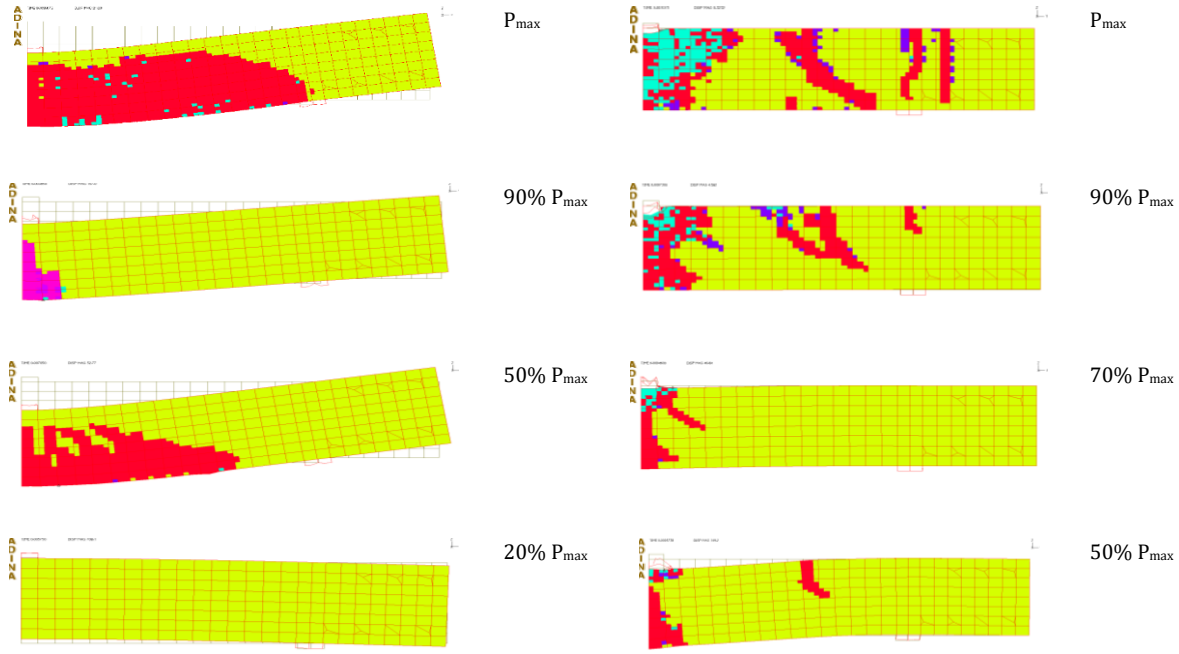

Figure 5-70 Predicted crack patterns and deformation profiles for specimen C for pulse loads with Ṗ=10 kN/ms (left) and Ṗ=1000 kN/ms (right) but different intensities.

D-10 kN/ms

D-1000 kN/ms

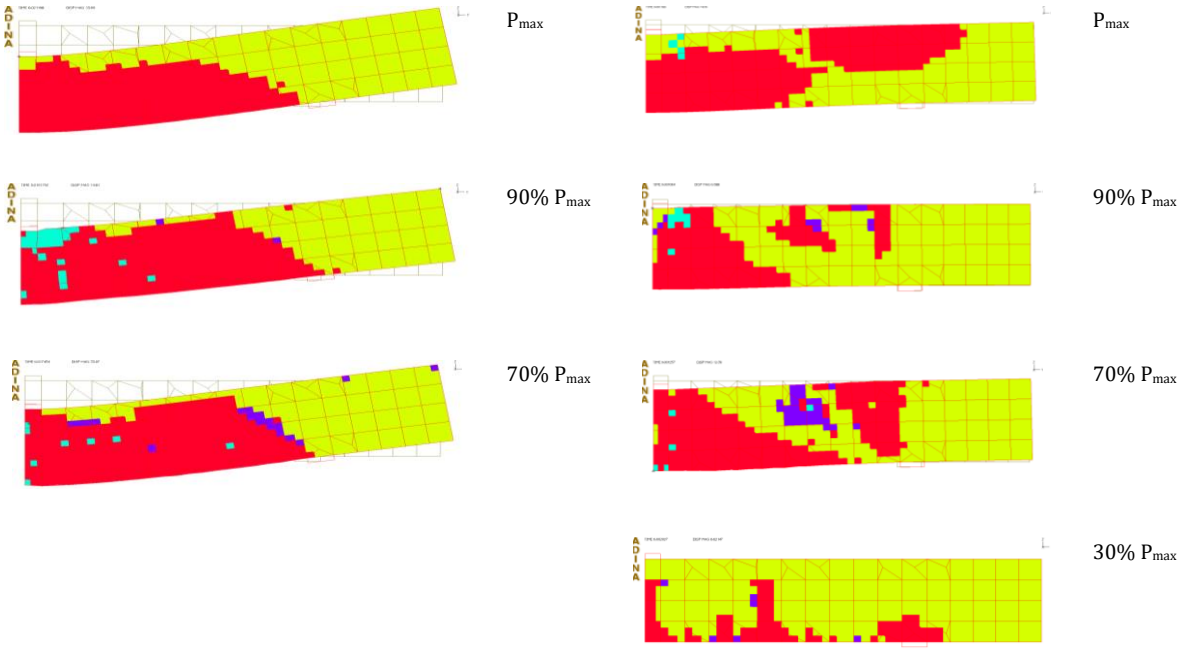

Figure 5-71 Predicted crack patterns and deformation profiles for specimen D for pulse loads with Ṗ=10 kN/ms (left) and Ṗ=1000 kN/ms (right) but different intensities.

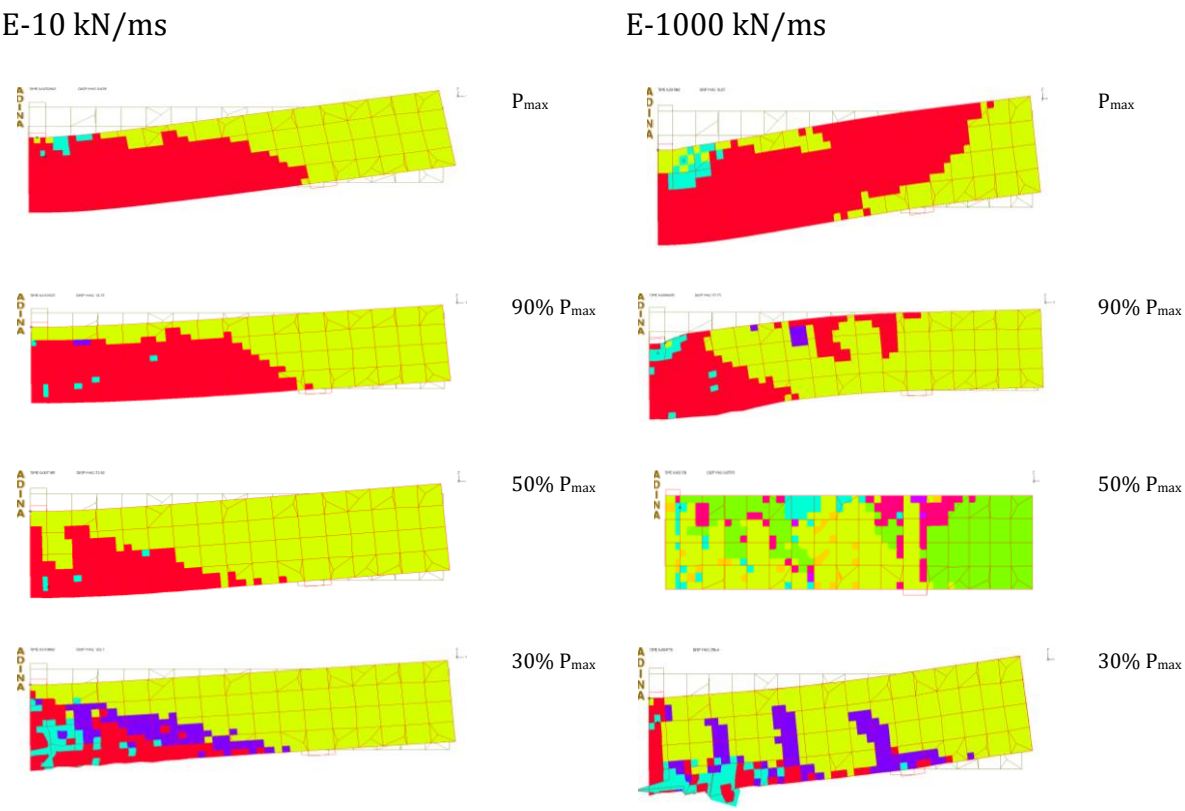

Figure 5-72 Predicted crack patterns and deformation profiles for specimen E for pulse loads with $\dot{P}$=10 kN/ms (left) and $\dot{P}$=1000 kN/ms (right) but different intensities.

5.8 CONCLUSIONS

The brittle constitutive model used by the FE program in the present study to analyse the behaviour of RC beams under impact loading applied at the mid-span is based on static material properties, and hence are strain-rate independent (for both steel and concrete). For the case of the beams considered, the comparative study between numerical and experimental data revealed that such constitutive models are capable of providing realistic and safe predictions of the experimentally established behaviour of the RC beams under increasing rates of loading. Such predictions encompass not only the member's strength but also the deformed shape and crack patterns at failure under the impact. One may, therefore, conclude that the effect of the loading rate on the specimen's behaviour reflects, on the one hand, the influence of inertia loads and, on the other, that of stress waves which reduce the length of the beam that responds to the applied load. This leads to an increase of the beam's stiffness and load-carrying capacity as well as to a reduction of its maximum vertical displacement under the load point. It should also be noted that ignoring the strain rate sensitivity widely considered to characterise steel behaviour was found to have no apparent effect on the predicted structural behaviour. Based on the analysis of the numerical

predictions it was in the manner in which the structural element responds to the applied load rather than to an increase in flexural capacity due to a postulated (temporary) strength increase of the concrete.

Furthermore, the results obtained from drop-weight testing appear to be in good agreement with their counterparts predicted numerically for the case of high rate loading applied monotonically to failure. This close correlation suggests that the relevant tests data are essentially associated with the post-failure behaviour of the RC beam specimens. As a result, it can be concluded that the true load-bearing capacity of the RC beams under impact loading is much lower than the latter values. Furthermore, it is established that the higher the loading rate and intensity of the impact load the larger the latter difference becomes. From the deformation profiles, it is observed that for a specific loading rate as the peak value of the pulse load reduces a larger portion of the span reacts to the applied load. This suggests that the Leff and therefore the mechanics underlying RC structural response will be affected by both the rate of applied loading and intensity of the imposed impact load.

Further detailed experimental and numerical studies are required in future to investigate the effect of a range of parameters on RC structural response under impact loading. The latter should also be extended in order to include other RC structural configurations such as columns and frames.

CHAPTER 6 ASSESSMENT THROUGH THE USE OF A NOVEL EQUIVALENT STATIC METHOD

6.1 INTRODUCTION

As discussed in the previous chapters, the available experimental and numerical methods employed to date for studying in detail RC structural response under impact loading are characterised by a certain degree of complexity and the predictions obtained by a certain level of uncertainty. In an attempt to predict RC structural response under impact in a practical way, Single Degree of Freedom (SDOF) models have been developed (TM5-855-1 1998) which rely on the available physical models (e.g. strut & tie models) generally adopted for describing the mechanisms underlying RC structural response when approaching the ultimate limit state (ULS). The latter simplified methods bypass the complexities associated with the available experimental and numerical assessment methods but fail to accurately account for the nature of the problem at hand (a wave propagation problem within a highly nonlinear material) and the true mechanisms underlying RC structural response (Cotsovos et al 2008, Cotsovos 2010, Cotsovos & Pavlovic 2012).

The work presented herein aims at further developing a practical method for assessing the behaviour of reinforced concrete beams under impact loading. The test data discussed in Chapters 3 and 4, revealed that, with increasing loading rates, RC structural response becomes more localised, since the portion of the structural member reacting to the applied load reduces in length as failure occurs prior to the generated stress waves reaching the supports. This phenomenon, combined with the inertia forces developing along the element span, underlie the mechanisms governing RC structural response. The equivalent static method is adopted herein that accounts for the localised response exhibited under impact loading and the ensuing shift it exhibits under increasing loading rates compared to that established under equivalent static loading. The validation of the proposed method is achieved by comparing its predictions against relevant experimental data obtained from drop-weight tests and the predictions obtained from nonlinear finite element analysis describing the behaviour of beams under impact loads characterised by different loading rates and intensities.

The simple, yet practical, method proposed herein links the shift in structural behaviour observed under increasing loading rates with the shortening of the span of the RC beam reacting to the applied load (Cotsovos and Pavlović 2012, Cotsovos 2010), see Chapters 3 and 4. The development of the subject method is based on the Compressive Force Path (CFP) method (Kotsovos 2014) which described the mechanics underlying RC structural behaviour under static loading when approaching the ultimate limit state (ULS). The localised response exhibited during impact loading justifies the observed increase in maximum sustained load and stiffness exhibited by the specimens under increasing loading rates (Cotsovos and Pavlović 2012). The validation of the proposed method is achieved by comparing its predictions to its counterparts established experimentally, via drop-weight testing, and numerically, through the use of nonlinear finite element analysis (NLFEA) for the case of slender ($a_v/d > 5$) and short ($a_v/d < 5$) RC beams. The subjected method is also to carry out a preliminary study on the effect of axial loading on the behaviour of RC beams under the impact.

6.2 LIMITATIONS OF THE AVAILABLE ASSESSMENT METHOD

Data obtained from drop-weight tests are characterised by considerable scatter partly due to a wide range of parameters (associated with the experimental setup and the design of the specimen) which differ from test to test (Cotsovos et al. 2008, Cotsovos and Pavlović 2012 and Cotsovos 2010). The observed scatter also reflects the difficulty in correlating the measured response to the actual physical state of the specimens (e.g. the measured maximum value of the imposed load often corresponds to a specimen physical state characterised by high concrete disintegration and low residual load-bearing capacity and stiffness) (Cotsovos et al. 2008, Cotsovos and Pavlović 2012 and Cotsovos 2010). In view of the above, the available test data cannot provide detailed insight into the mechanics underlying RC structural response.

NLFEA offers a safer method for investigating RC structural behaviour under impact loading. It is capable of providing more detailed insight into the mechanisms underlying RC structural response compared to drop-weight testing. However, as it usually employs dense 3D finite element meshes, combined with complex constitutive material laws implemented through the use of iterative solution strategies, the computational resources required for solving such problems are high. As a result, the use of NLFEA is generally limited to the analysis of relatively simple structural forms. Moreover, its ability for

providing realistic predictions of RC structural behaviour is usually linked to the use of case-study dependent constitutive models often incorporating empirical amplification factors to account for the effect of strain-rate sensitivity on concrete material behaviour (Kotsovos 2014).

To avoid the complications and uncertainties associated with the previous assessment methods and in order to simplify the analysis and design procedures, relevant (mainly military) design codes (TM5-855-1 1998) employ equivalent simple lumped mass-spring systems for modelling individual structural elements with distributed mass and loading. The equivalence is based upon energy approximations that rely on an assumed deflected shape (e.g. the first eigenvector or the deflected shape under equivalent static loading). The latter methodology relies on a number of simplifications concerning both material behaviour and structural response. These include the use of simple uniaxial material laws, empirical amplification factors (attributed to the strain-rate sensitivity of concrete material behaviour), assumptions concerning the deformed shape of the structural elements and elastic or elasto-plastic laws for describing structural behaviour. However, such simplifications do not allow the methodology to account for the brittle nature of concrete and its sensitivity to triaxial stress conditions, the true mechanics governing RC structural response as well as the localised response often exhibited under impact loading.

6.3 THE COMPRESSIVE FORCE PATH METHOD (CFP)

Unlike the truss analogy (TA) method, which forms the basis of current design codes for RC structures (Eurocode 2 1992, ACI 318-02 1992), the CFP method (Kotsovos 2014) assumes that an RC structural element approaching ULS behaves essentially as an arch-like structure (for the case of a simply supported beam) or a system of arch-like structures connected at the point of contra-flexure (in the case of structural configurations characterised by static indeterminacy, see Fig. 6.1(Kotsovos et al. 2005). The latter type of behaviour is enforced by the available reinforcement. The CFP method adopts a fundamentally different physical model for describing RC structural behaviour at the ULS. Failure is considered to occur due to the development of transverse tensile stresses at specific locations along the path followed by the compressive force. These locations (L1 to L4 shown in Fig. 6.1 (Kotsovos et al. 2005) are dependent on the value of a_v/d. Fig. 6.1b depicts the model considered by the CFP method as the most suitable for providing a simplified, yet realistic, description of the physical state of a two-span linear element

subjected to the maximum transverse load that is capable of sustaining at the middle of its larger span combined with a concentric axial load inducing a nominal compressive stress of the order $0.2f_c$. For comparison purposes, the figure also includes the TA for this type of structural member (i.e. continuous beam). A comparison between the physical models adopted for the CFP method for the case of an indeterminate RC beam when subjected to lateral loading only and a combination of lateral and axial loading is shown in Fig. 6.2.

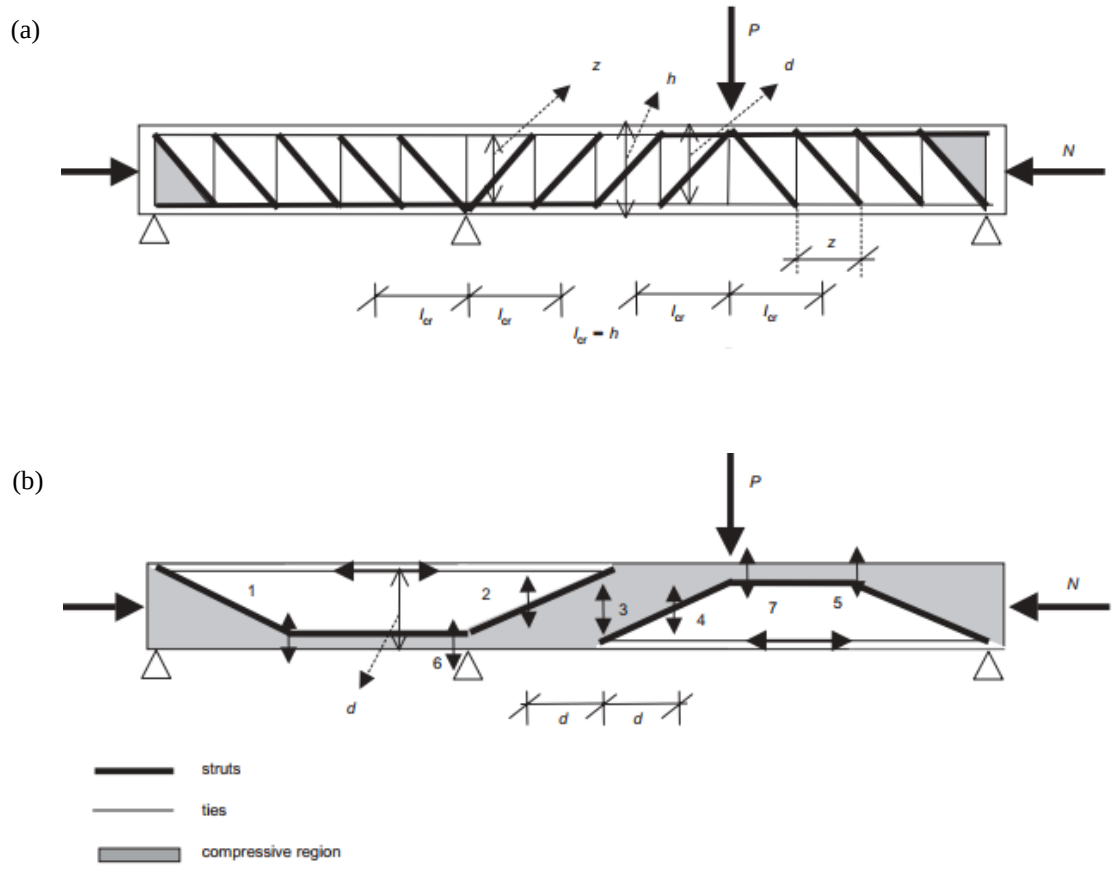

1 to 7 regions of critical transverse tensile stresses

Figure 6-1 Physical models for a two-span continuous beam based on (a) truss analogy (TA) and (b) compressive force path (CFP) (Kotsovos et al. 2005) $l_{cr,}$ critical lengths as defined in codes (Kotsovos et al. 2005)

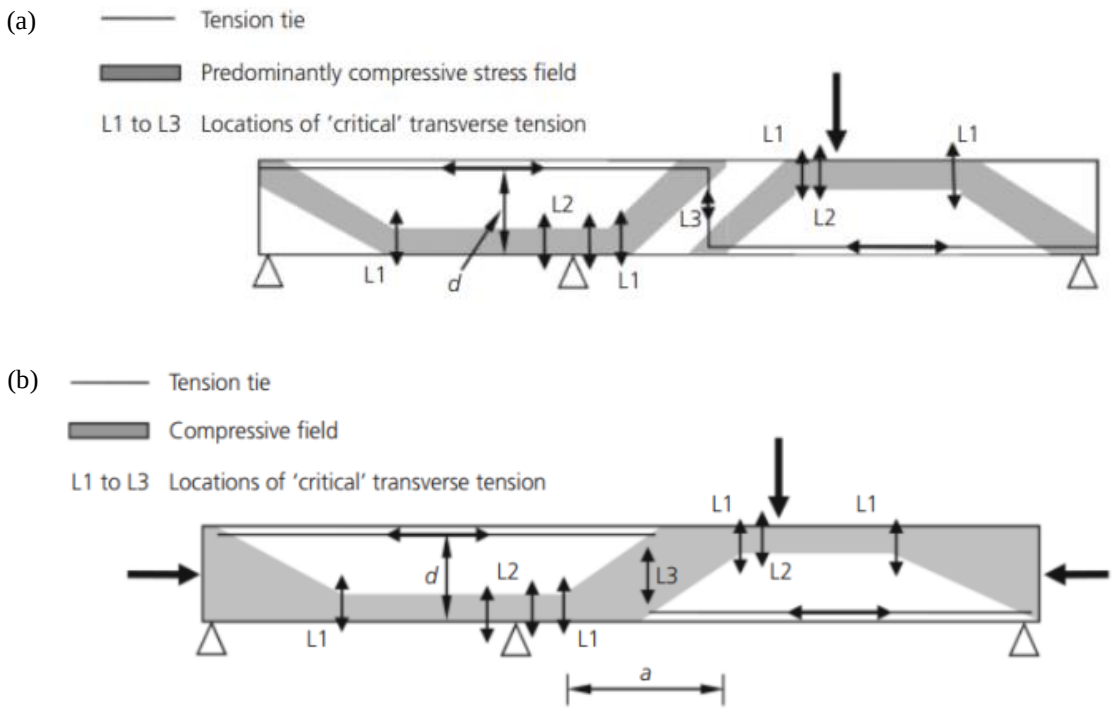

Figure 6-2 Schematic representation of the physical model adopted by the CFP method for the case of an indeterminate RC beam when subjected to (a) lateral loading only and (b) a combination of lateral and axial loading (Kotsovos 2014).

The manner in which a_v/d affects the load-carrying capacity (expressed as M_u/M_f) is indicated in Fig. 6.3 (Kotsovos 2014) in which four distinct types of structural behaviour are identified. A detailed description of the CFP method is provided elsewhere (Kotsovos 2014) and only a concise description is presented herein.

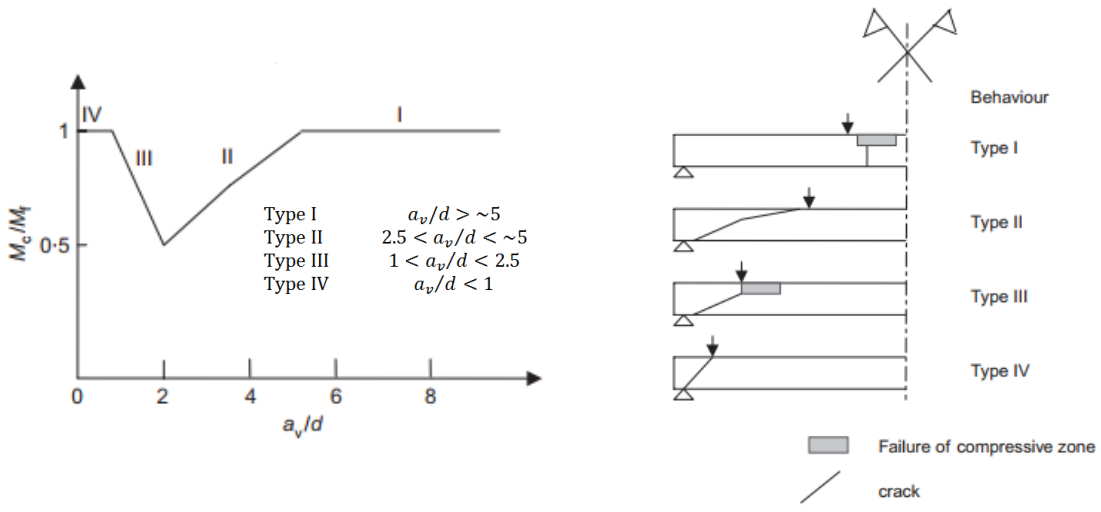

(a) (b)

Figure 6-3 Schematic representation of the physical model adopted by the CFP method for the case of an indeterminate RC beam when subjected to (a) lateral loading only and (b) a combination of lateral and axial loading (Kotsovos 2014).

Type I behaviour is characterised by a flexural mode of failure preceded by the longitudinal splitting of the concrete in the compressive zone of the beam. This occurs when concrete strength in the compressive zone is exhausted due to the development of transverse tensile stresses induced by volume dilation of concrete in the adjacent regions which include primary flexural cracks (Kotsovos 2014). This allows the maximum stresses developing within the compressive zone of the beam to attain values approximately equal to 1.5 times the uniaxial compressive strength of concrete f_c.

Type II behaviour is characterised by a brittle mode of failure usually caused by tensile stresses developing either in the region of change of the CFP direction (L1, see Fig. 6.2) or in the region of the cross-section where the maximum bending moment combines with the shear force (L2, see Fig. 6.2). The transverse stress resultant at location L1 is considered numerically equal to the acting shear force, and, its effect is considered to spread over a distance *d*, on either side of location L1 (Kotsovos 2014). The value of the tensile force sustained at this location is given by Eq. (6.1) (Kotsovos 2014).

$$T_{II,1}=0.5 \cdot b \cdot d \cdot f_t \qquad \text{Eq. (6.1)}$$

where: b : width of the beam

d : effective depth of the beam

f_t : tensile strength of concrete

If the developing shear force is higher than the value provided by Eq. (6.1), stirrups are uniformly placed over a length d on both sides of location L1 in a quantity sufficient to sustain the whole value of the shear force corresponding to flexural capacity. The spacing (s) of the stirrups should not exceed 0.5d.

$$V_f=A_{sw,\,II1} \cdot f_{yw} \cdot (2d/s+1) \qquad \text{Eq. (6.2)}$$

where: $A_{sw,II1}$: one cross-section area associated with one stirrup

s : spacing between stirrups

f_{yw} : yield stress of transverse reinforcement

In the presence of axial compression ($N\neq0$), the slope of the inclined compression at L1 reduces, see Fig. 6.4b and Eq. (6.3) (Kotsovos 2014). Based on Eq. (6.3) the presence of axial loading reduces the transverse tension at location L1 and as a result, a larger transverse load is required to increase transverse tension to its limiting value.

(a)

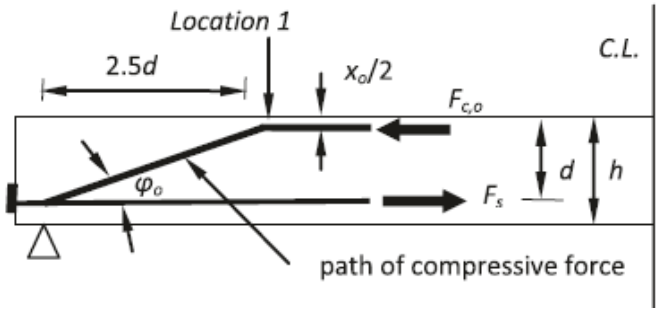

(b)

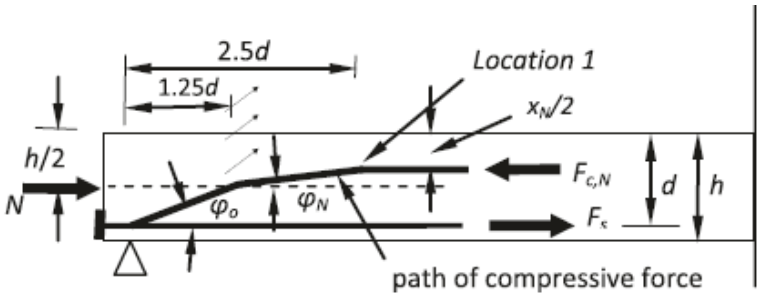

Figure 6-4 The path of the compressive force along the shear span of an RC beam for (a) N=0 and (b) N≠0 (Kotsovos 2014).

$$T_{II,1,0}/T_{II,1,N} = \tan\varphi_0/tan\varphi_N \qquad \text{Eq. (6.3)}$$

where φ_0 and φ_N are the values of the slope of the axial compression and $T_{II,1,0}$ and $T_{II,1,N}$ are the values of transverse tension developing at location 1 for N=0 and N≠0 respectively.

Transverse tensile stresses within the compressive zone may also develop at location L2 (Fig. 6.2a) due to the loss of bond between the longitudinal reinforcement and the surrounding concrete (Kotsovos 2014). Loss of bond can lead to an extension of cracking and a reduction of the depth of the compressive zone. This can result in an increase of the intensity of the compressive stress field thus leading to dilation of the volume of concrete in the compressive zone, which in turn causes the development of transverse tensile stresses (σ_t) in the adjacent regions Eq. (6.4) (Kotsovos 2014).

$$|\sigma_t| = f_c/[5(f_{yk} \cdot A_s/V_f - 1)]$$ Eq. (6.4)

where: A_s : one cross-section area associated with one longitudinal reinforcement

f_{yk} : yield stress of longitudinal reinforcement

By considering these transverse tensile stresses and the ensuing complex triaxial stress state it is possible to express the shear force ($V_{II,2}$) that can be sustained at locations 2 form Eq. (6.5) (Kotsovos 2014).

$$V_{II,2} = F_c \cdot [1 - 1/(1 + 5 \cdot f_t/f_c)]$$ Eq. (6.5)

If the developing shear force is higher than the value provided by Eq. (6.5), stirrups are needed. The number of stirrups required is assessed by calculating the vertical and horizontal stress resultants – through the use of Eqs. (6.6) and (6.7) respectively – in the region between the area where the inclined and the horizontal portion of the compressive path meet (location L1, Fig.6.4) and the point at which the load is applied.

$T_{II,2v}=\sigma_t b(\alpha_v 2d)/2$ Eq. (6.6) $T_{II,2h}=\sigma_t b(\alpha_v 2d)/2$ Eq. (6.7)

Based on Eqs (6.6) and (6.7), the number of stirrups required is obtained from Eqs (6.8) and (6.9):

$A_{sw,112v}=T_{II,2v}/f_{yw}$ Eq. (6.8) $A_{sw,112h}=T_{II,2h}/f_{yw}$ Eq. (6.9)

Type III behaviour is characterised by a brittle mode of failure caused by the deep penetration of the inclined crack into the compressive zone of the beam (see Fig.6.5a). This crack reduces the strength of the concrete in the compressive zone in the region where the inclined and the horizontal compressive force path meet. This causes a reduction of the flexural capacity of the beam. A measure of the maximum shear force that concrete alone can carry in this region is provided by Eq. (6.10).

$$V_{III} = M_{III}/a_v$$ Eq. (6.10)

Where: $$M_{III} = M_{II}^{(2.5d)} + \frac{(M_f - M_{II}^{(2.5d)})(2.5d - a_v)}{(1.5d)}$$ and

$$M_{II}^{(2.5d)} = 2.5dV_{II,1}$$

The stirrups required are provided by Eq. (6.11) and are distributed within the shear span α_v with a spacing *s* smaller than *0.5d*:

$$A_{sw,III} = 2(M_f - M_{III})/(a_v f_{yw}) \quad \text{Eq. (6.11)}$$

Type IV behaviour can be characterised either by failure of the horizontal element of the CFP model or failure of the un-cracked end portion of the beam (inclined leg of the 'frame' of the CFP model) in compression. From the moment equilibrium of the free body in Fig. 6.5b, the flexural capacity (M_f) can be easily calculated and consequently, the associated load-carrying capacity (P_f) can be determined from Eq. (6.12).

$$P_f = M_f/a_v \quad \text{Eq. (6.12)}$$

On the other hand, the load-carrying capacity (P_D) corresponding to the strength of the inclined leg of the 'frame' is equal to the vertical component of the load (F_D) that can be carried by this leg. As indicated in Fig. 6.5b, F_D is calculated by taking the depth of the leg equal to $a_v/3$ (Kotsovos 2014).

$$P_D = F_D \, z/(z+a_v) \, l/2 \quad \text{Eq. (6.13)}$$

Where: $F_D = (a_v/3) \, b \, f_c$

$$M_{II}^{(2.5d)} = 2.5 d V_{II,1}$$

Therefore, the load-carrying capacity of the beam will be: $P_u = min\,(P_F, P_D)$

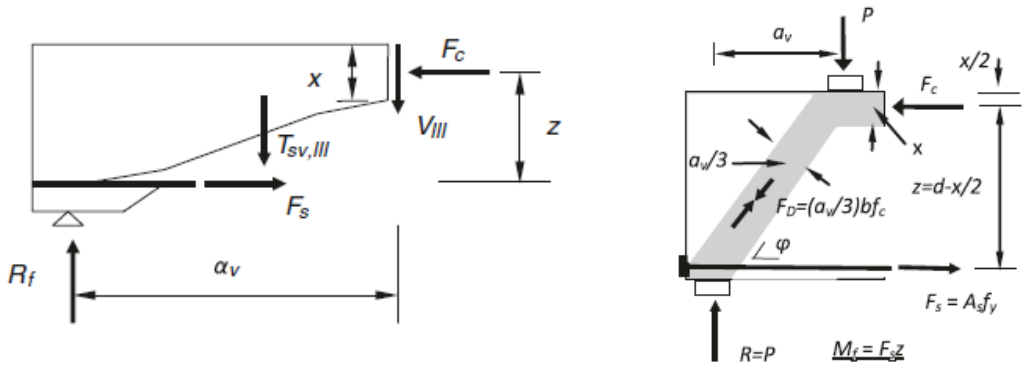

(a) (b)

Figure 6-5 Internal actions developing in an RC beam exhibiting (a) type III and (b) type IV behaviour.

Point of contra-flexure: Fig. 6.2b shows the region (location L3) through which the compressive force developing (due to the combined action of the bending moment and axial compression) is transferred from the compressive zone of the right-hand side upper portion of the beam to the compressive zone of the left-hand side lower portion of the RC beam. At location 3 (point of contra-flexure) concrete is subjected to tensile stresses acting transverse to the compressive force path. This is in contrast with the tensile stress conditions developing in location 3 when N=0 (see Fig. 6.2a). When the strength of concrete is exhausted at location L3, for either of the two cases considered (N=0, N≠0), the presence of transverse tension will lead to cracking however when N=0 the crack formation is ultimately linked with unstable crack extension leading to structural collapse, while when N≠0 crack extension will change direction so as to follow the path of the inclined compression and this in turn will delay the crack propagation process.

Since concrete at location L3 is only subjected to transverse tension, its strength may be assessed through the use of Eq. (6.1). Any load in excess of that that can be sustained by the concrete at location 3 will cause the formation of cracking which, within the transverse tensile stress field prevailing in the region of this location, will extend in an unstable manner leading to immediate loss of load-carrying capacity of the structural element.

6.4 EFFECT OF THE LOADING RATE

In the previous section, the CFP method was concisely described with reference to four distinct types of structural behaviour for the case of an indeterminate RC beams based on the value of the span to depth ratio (i.e. a_v/d). On the basis of the CFP method and through incorporating the findings of experimental (i.e. Chapters 3 and 4) and numerical methods (i.e. Chapter 5) a physical model was adopted in the current assessment. The assumed manner through which the stress waves generated in the impact region reach the supports is presented in Fig. 6.6 (a-d). Previous studies reveal that for low loading rates the beams tend to respond in a manner similar to that observed for the case of static loading as the stress waves affect the entire span of the specimen (Cotsovos et al. 2008). However, as the loading rate increases beyond a certain limit, the stress waves generated are unable to reach the supports prior to the failure of the specimen due to the damage sustained along its span. From the above, it can be assumed that only a portion of the specimen span (referred to as effective length L_{eff}) reacts to the impact load applied. A schematic representation of the inertia forces resisting the action of an impact load exerted at the mid-span section of a

simply supported RC beam is shown in Figs. 6.6a and 6.7a for N=0 and N≠0 respectively, together with the corresponding shear force (Figs. 6.6b-d and 6.7b-d) and bending moment (Figs. 6.6e-g and 6.7e-g) diagrams which help to identify the portion of the RC beam's span (L_{eff}) reacting to the imposed impact load (Figs. 6.6h and 6.7h). This span (L_{eff}) can be considered fully or partially fixed at its ends. Figs. 6.6i and 6.7i show the assumed proposed physical model (based on the CFP method) describing the mechanics underlying the structural response of the RC beam for three different rates of impact loading (low, intermediate and high) for N=0 and N≠0 respectively. The proposed physical model accounts for the inertia forces by assuming a simplified bending moment and shear force diagram under transient impact load. It should be noted that as this stage, the study was aimed to assess the extent to which L_{eff} contributes to the response. Furthermore, based on the (small) mid-small deflection of the tested RC specimen (in Chapters 3 and 4) and localised failure (i.e. cracking) *during initial stage of impact loading*, it was assumed that the acceleration was insignificant as a result the current assessment method neglects the inertia forces as F=ma where F is the applied impact force, m is the mass of subject specimen and a is the acceleration of the beam. However, when considering the equilibrium of internal and external forces in impact problem (see Figs. 6.6a and 6.7a) the development of inertia forces (acting as internal forces) can be beneficial in resisting the impact load and hence leads to an increase in the load-carrying capacity. Although neglecting such forces can lead to a more conservative approach in predicting the RC structural response (under impact loading), it might diverge the predictions from the actual response of the elements and hence as part of developing the current proposed model, the quantitative effects of inertia forces should be also taken into account assessed further.

Under static loading, the flexural capacity of the beam is $M_u = maxP_s \cdot L/4$ where $maxP_s$ is the static load-carrying capacity and L is the clear span of the beam (distance between the two supports) (Cotsovos et al. 2008, Costovos 2010). Under impact loading, only the portion of the beam reacting to the imposed load (L_{eff}) is considered with a plastic hinge forming at its mid-span. Considering different degrees of fixity applied at the ends of the L_{eff}, the bending moment at these locations at ULS (M'_u) can be considered equal to: (i) the flexural capacity M_{F_2} (assuming that the ends are fully fixed) (see Fig. 6.6a-d and 6.7a-d) or (ii) the bending moment M_{CR_2} at which cracking initiates at the upper face of the ends of L_{eff} (assuming intermediate support conditions). Based on the above, the plastic moment at mid-span is given by Eq. (6.15).

$$M_u = P_d.\frac{L_{eff}}{4} - M'_u$$ Eq. (6.14)

where P_d is the applied impact load expressed as the product of the loading rate $\dot{P}$ and the duration of loading Δt_c (i.e. $P_d = \dot{P} \cdot \Delta t_c$). Δt_c is the time period within which cracks form at the upper face of the end sections of L_{eff} (Cotsovos et al. 2008, Cotsovos. and Pavlović 2012, Cotsovos 2008). As previously mentioned, the inertia force (F=ma) was neglected in Eq. (6.14) as; (i) it was assumed the inertia forces were insignificant during the initial stage of the impact and (ii) the study was aimed to assess the extent to which L_{eff} contributes to the response.

Based on the above an estimate of L_{eff} can be provided by Eq. (6.15).

$$L_{eff} = 2 \cdot \upsilon_w \cdot \Delta t_c$$ Eq. (6.15)

with $\upsilon_w = \sqrt{(G/\rho)}$ being an estimate of the velocity with which the stress wave travels within the concrete medium, where $G=E/(2+2v)$ is the shear modulus, E the modulus of elasticity, v the Poisson's ratio and ρ the density of concrete.

The value of the imposed load at which cracking forms at the upper face of the ends of L_{eff} is $P_{d,cr} = \dot{P} \cdot \Delta t_c = 8 \cdot M_{cr2}/(\alpha \cdot L_{eff})$. The term α correspond to; (i) the level of fixity of the boundary conditions of the RC member and (ii) the region in which the plastic hinge develops (i.e. Top or bottom reinforcement). Replacing L_{eff} in the latter equation through the use of Eq. (6.15) and solving with respect to Δt_c results in Eq. (6.16).

$$\Delta t_c = [4 \cdot M_{cr2}/(\alpha \cdot \dot{P} \cdot \upsilon_w)]^{0.5}$$ Eq. (6.16)

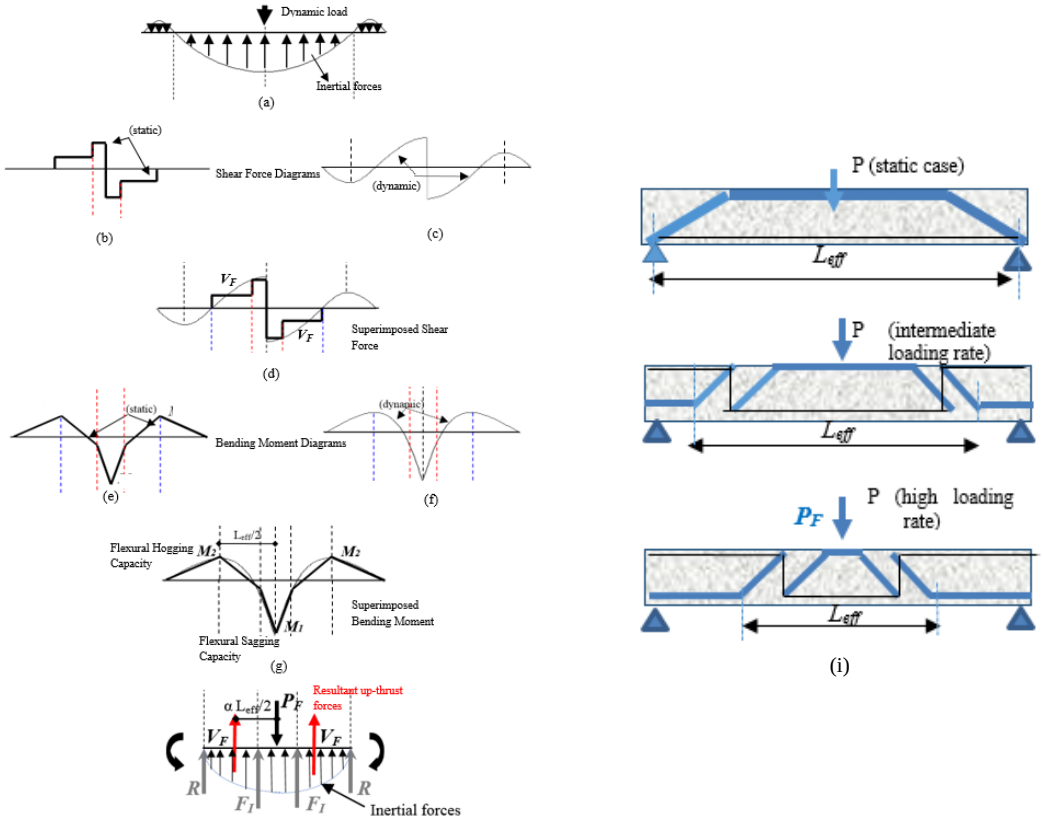

Figure 6-6 Internal actions developing under increasing loading rates (a)-(h) and the proposed physical model (i) for N=0.

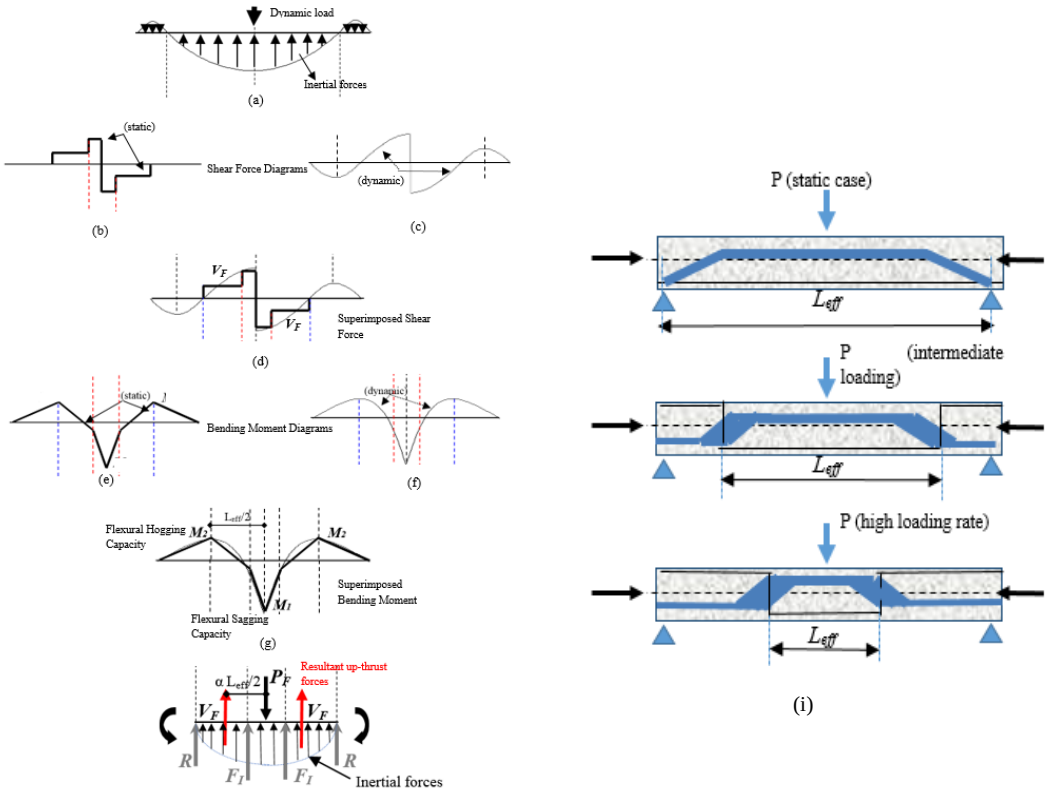

Figure 6-7 Internal actions developing under increasing loading rates (a)-(h) and the proposed physical model (i) for N≠0.

Substituting the value of Δt_c obtained from Eq. (6.16) into Eq. (6.15) provides the value of L_{eff}. Based on the above assumptions the load-carrying capacity of the beam will be:

$$P_F=2V_F \quad \text{Eq. (6.17)}$$

Where: $V_F = (2/a)(M_{F1} + M_{F2})/L_{eff}$

Or $V_F = (2/a)\ (M_{F1} + M_{CR2})/L_{eff}$

with V_F being the resultant of the up-thrust forces (i.e. the resultant of the inertial forces F_I and the reactions *R)* acting on L_{eff} and *a* parameter defining the distance of V_F from P_F as a percentage of $L_{eff}/2$ which may be assessed on the basis of the available experimental and numerical data (see Figs 6.6d and 6.7d for N=0 or N≠0 respectively). M_{F1} and M_{F2} refer to flexural sagging and hogging capacities, respectively, assuming that the ends are fully fixed.

Under low loading rates, when the whole span reacts to the impact load, it is assumed that the RC beam behaves as a *simply supported beam*. For the higher rates, the beam's behaviour gradually shifts from *simply supported* to that of a *reduced span (fully or partially) fixed-end beam*. Assuming that the RC beam is simply supported and behaves elastically Eq. (6.18) may be employed to provide an estimate of the value of the eigenvalue T_1 corresponding to the first (dominating) mode characterising the exhibited response of the beam.

$$T_1=2\pi/\omega_1 \quad \text{Eq. (6.18)}$$

Where: $\omega_1=(\pi^2/L_{eff})\ (E\cdot I / \rho\cdot A)^{0.5}$

It should be noted that when the duration of the loading is less than the value of T_1, failure is exhibited prior to the beam being able to oscillate as is the case observed for low loading rates. For durations of loading equal to or longer than T_1, the beam is assumed to exhibit a load-carrying capacity practically equal to that established under static loading. Therefore, the maximum loading rate, which allows the specimen to exhibit global behave is assumed equal to the ratio of the beam's static load-carrying capacity ($\max P_s$) and the beams eigenvalue (T_1), i.e.

$$\dot{P} = maxP_s/T_1$$ Eq. (6.19)

Having established the maximum loading rate for which the applied load is considered as static ($\dot{P}_s$ = maxP_s/T) and the rate at which the load-carrying capacity is given from Eq. (6.17) for L_{eff}=L ($\dot{P}_1 = P_F/\Delta t_c = 2 \cdot u_w \cdot P_F / L_{eff}$), the load-carrying capacity of the beam associated with values of loading rate between the latter two limits can be obtained via linear interpolation. For values of loading rate higher than $\dot{P}_1 = 2 \cdot u_w \cdot P_F / L_{eff}$ the load-carrying capacity can be directly calculated from Eq. (6.17).

6.5 IMPLEMENTATION OF CFP METHOD ON RC BEAMS

A comparative study between the predicted variation of dynamic increase factor (DIF) increasing loading rate for the slender beams types A and B (see Fig. 3.1) with and without axial loading is shown in Figs. 6.7-6.8. The DIF is the ratio of peak value or dynamic load-carrying capacity (which is calculated using the current assessment method for different rates of loading) to the static load-carrying capacity. It should be reminded that specimens A and B were previously tested under impact loading as discussed in Chapter 3. The results suggest that regardless of the number of shear links used, the presence of axial loading reduces the value of the maximum sustained load (compared to that predicted for N=0 see Fig. 6.7). As mentioned before the presence of axial loading increases the moment related to flexural capacity (M_f) and crack-initiation (M_{cr}) which in turn result in an increase of $\Delta t_{cr}=\sqrt{4M_{cr}/\dot{p}u_w}$. Since $L_{eff}=2\Delta t_{cr}\, u_w$, an increase in the time (required for the stress wave to travel), results in the development of cracking at the ends of L_{eff}. This can result in the increase in the length (L_{eff}) of the span of the beam reacting to the imposed impact load (compared to that established when *N=0)*. Based on the above when subjected to axial loading a larger portion of the beam span will react to the imposed impact load increased (compared to that observed when N=0).

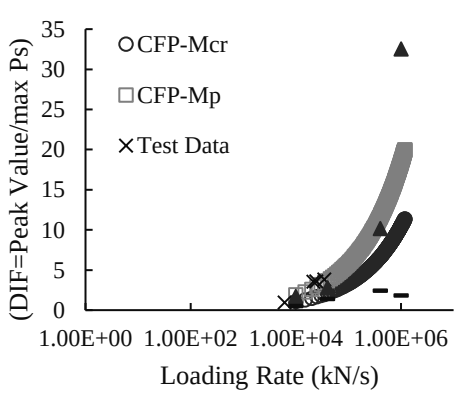

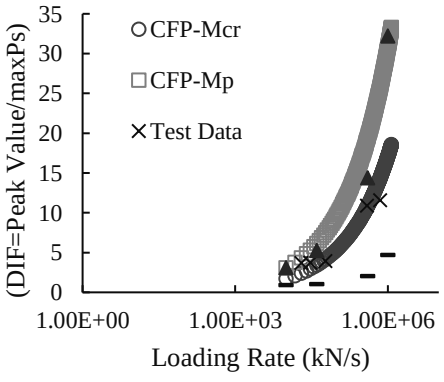

(a)Type A (b)Type B

Figure 6-8 Variation of DIF = $maxP_d/maxP_s$ with increasing loading rate for slender RC beams: (a) A and (b) B when N=0.

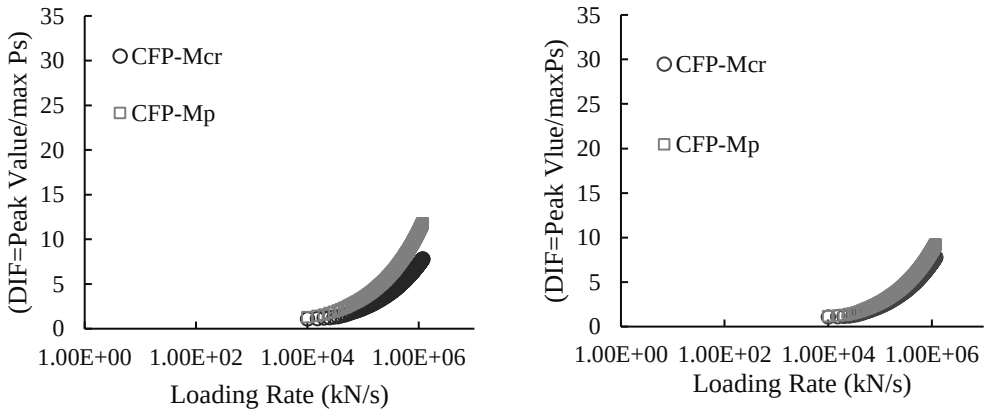

(a)Type A (b)Type B

Figure 6-9 Variation of DIF = $maxP_d/maxP_s$ with increasing loading rate for slender RC beams: (a) A and (b) B when N≠0.

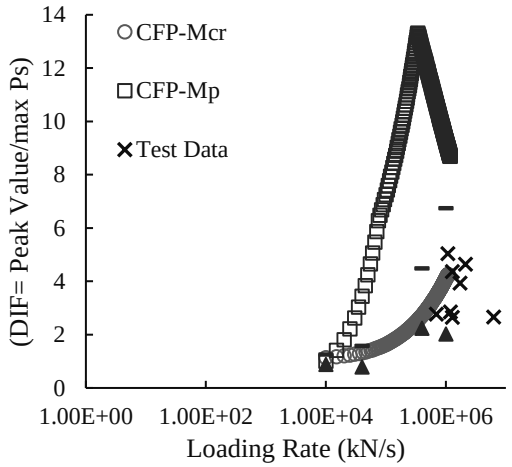

(a)Type D

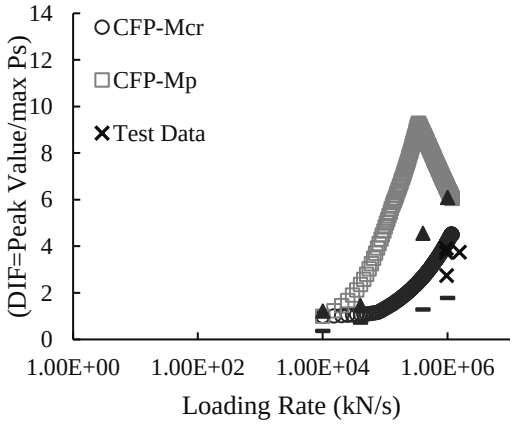

(c)Type E

Figure 6-10 Variation of DIF = maxP_d/maxP_s with increasing loading rate for short RC beams: (a) D and (b) E when N=0.

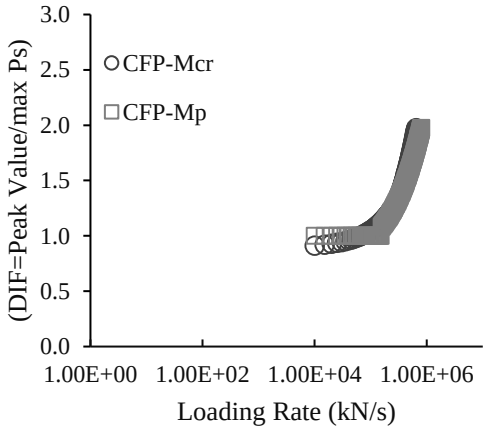

(a)Type C

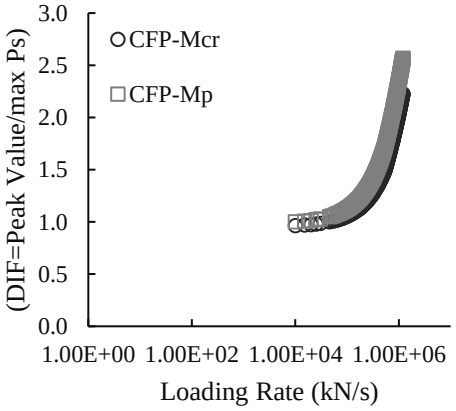

(b)Type D

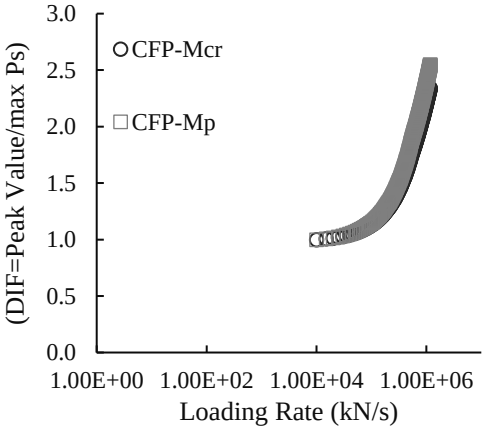

(c)Type E

Figure 6-11 Variation of DIF = maxP_d/maxP_s with increasing loading rate for short RC beams: (a) C, (b) D and (c) E when N≠0.

The predictions of the proposed assessment method exhibits good agreement with its experimentally and numerically established counterparts for the majority of the cases-studies considered (with the ends of L_{eff} being partially or fully fixed and the applied axial force being N =0 or 15% N_c) In the case of specimen SS0 (short RC beam without stirrups) with N=0 a significant difference is observed between the predictions of the subject method and those obtained from NLFEA and drop-weight testing. The main reason for this difference is associated with the brittle (abrupt) mode of failure exhibited by the specimen

during testing. As a result, the maximum impact force generated during impact cannot be associated with the true load-carrying capacity of the specimen, but it is largely linked to the inertia forces developing due to the deformation that the specimen exhibits.

Fig. 6.11a show close predictions (in the form of DIF value) for Type C (see Chapter 4) for both cases of CFP-M_p and CFP-M_{cr} (i.e. predictions using moment related to flexural capacity and crack-initiation respectively). It should be reminded that, as previously shown in Chapter 4, the short RC beam Type C (without stirrups) exhibited a shear mode of failure under static loading. This implies that the beam fails before the formation of any plastic hinges, hence Eq. (6.14) is no longer valid. This suggests, when incorporating the current assessment method, for brittle types of failure, one should consider using the moment associated with crack-initiation for predicting the DIF values.

6.6 DISCUSSION OF ASSESSMENT METHOD

The proposed assessment method is capable of describing the response of RC beam and columns when approaching the ULS under impact loads characterised by different loading rates. The proposed assessment method is found to be capable of providing predictions in agreement with the test data recorded and the predictions obtained from NLFEA particularly for slender beams where the contribution of the L_{eff} in the overall response was more apparent compared to the short beams. The results obtained suggest that the application of axial loading increases the load-capacity of the specimens under static loading as it delays the cracking process the specimens undergo. However, under impact loading, the rate with which the DIF ($maxP_d/maxP_s$) increases with higher loading rate reduces when the specimen is subjected to higher levels of axial (compressive) loading. This attributed to the fact that development of the cracking (defining the L_{eff}) is delayed and as a result occurs later in the loading process allowing the stress waves to travel more along the specimen allowing a larger portion of the element span to react to the imposed load. Larger L_{eff} results in the proposed method predicting smaller values of load-carrying capacity.

The proposed physical model incorporated the equilibrium of the internal and external forces by partially accounting for the inertia forces through the change of L_{eff} which is influenced by the change of rates of loading. It also assumes a simplified bending moment

and shear force diagram accounting for both fully or partially fixed end conditions. Furthermore, based on the test data presented in Chapters 3 and 4, during the initial stage of the impact loading, the deflection of RC beam was small and localised failure was observed (i.e. cracks developed and L_{eff} was small). It has been assumed that in order for an RC beam to exhibit a large deflection, the acceleration should be significant enough and as the inertia force is expressed as F=ma, small acceleration can yield to development of insignificant inertia.

Although neglecting the effects of inertia can result in predicting rather conservative load-carrying capacity, it may also diverge the predictions from the actual response of RC structural element. To address the latter shortcoming of the current assessment method, the proposed simplified method should be further refined to account for the effects of the inertia forces on the predicted load-carrying capacity. Nevertheless, the current method can be used towards the development of a new SDOF model capable of providing realistic predictions concerning the behaviour of individual RC structural elements under impact loading.

Furthermore, as part of further development of the current method, a wider range of specimens (i.e. case studies) concerning different cross-sections and design details should be assessed using the current method.

6.7 CONCLUSIONS

The proposed physical model is capable of describing the response of RC beams when approaching the ULS under high rates of loading. The proposed simplified method should be further refined and forms the basis for the development of a new SDOF model which will be capable of providing realistic predictions concerning the behaviour of individual RC structural elements under impact loading. The current method requires further development and as part of future studies, it is recommended to assess the effects of inertia forces in the predictions.

CHAPTER 7 CONCLUSIONS AND RECOMMENDATIONS FOR FUTURE WORK

7.1 INTRODUCTION

The key findings of the current experimental and numerical work on the dynamic response of RC structures under impact loading are summarised in the following sections. The main conclusion drawn from the literature review presented in Chapter 2, concerning the available test data and numerical analyses, are also provided herein. Furthermore, an assessment method is proposed capable of providing realistic predictions concerning certain aspects of the exhibited response under impact loading. Finally, the recommendations for future work are provided.

To date, a number of drop-weight tests and numerical studies have been conducted to investigate the dynamic response of RC members (mainly beams and columns) under impact loading. The dynamic response exhibited by reinforced concrete (RC) beams under impact loading exhibits significant departures from that recorded during equivalent static testing as certain thresholds of applied loading rate are surpassed. The analysis of the published experimental and numerical data reveals that the observed shift in structural response is owed to the combined effect of the inertia forces developing along the element span and the exhibited localised response. More specifically, it has been established that the length of the element span (effective length, L_{eff}) reacting to the applied load, reduces with increasing loading rates. This can be explained when viewing the problem at hand as a wave propagation problem within a highly nonlinear medium. In such cases, the deformation exhibited by RC beams, when subjected to impact loads is dependent on: (i) the intensity and speed of the stress waves, generated during impact, which travel away from the impact region towards the supports of the structural member considered as well as (ii) the level of damage (cracking) sustained which locally reduces the stiffness of the RC element. Under high loading rates, structural failure can be exhibited prior to the stress waves reaching the specimen supports resulting in a localised response. The higher the loading-rate the more localised the response becomes as the distance within which the stress-waves travel prior to failure gradually reduces, concentrating around the area of impact. This reduction of the element span reacting to the imposed load can be used to

explain the observed increase in stiffness and load-carrying capacity exhibited by RC beams when subjected to impact loads characterised by increasing loading rates and intensities.

A review of the available test data reveals that the maximum load sustained by RC members increases when subjected to increasing levels of high-rate loading (when compared to its counterpart established under equivalent static loading). The work presented in this thesis predominantly attributes the observed shift in structural performance attributed to the inertia forces (developing along the element span) and ensuing localised response (exhibited by the specimen considered). It should be noted that drop-weight tests are difficult to conduct as the intensity of the loads generated during impact increase rapidly (in a few milliseconds) from zero to a maximum value often leading to explosive (brittle) forms of failure which can in turn damage the instruments employed. Furthermore, data obtained from such tests are characterised by large scatter due to the effect of a wide range of parameters (associated with the different experimental techniques used, the variation of the size and shape of the impactor and the design details of the RC specimens) which differ from test to test. Furthermore, it is noted that the available experimental information does not usually provide a detailed description of the response exhibited by the specimens throughout the loading process. Instead, the available data provided, concerning crack patterns and deformation profiles, is usually measured after (and not throughout) the application of the impact load. As a result, it is difficult to correlate the measured responses obtained from drop weight tests to the actual physical state of the specimens as the measured maximum value of imposed load frequently corresponds to a specimen that is already disintegrated, exhibiting low residual load-bearing capacity and stiffness. This stage of structural response has little practical significance as it depends heavily on *post*-failure mechanisms (e.g. dowel action) for transferring the applied loads to the specimen supports. Based on the above it appears that the true load-carrying capacity is likely to be significantly lower than the maximum value of the contact force measured during testing. In addition, it can be also concluded that the available test data cannot provide detailed insight into the mechanisms underlying RC structural response; it can, however, provide a qualitative description of the effect of loading-rate on certain important aspects of specimen behaviour.

The available test data reveals that the effect of axial loading on the dynamic response of RC members under impact loading has not been studied in detail. The available test data suggest that the application of axial loading can increase the load-carrying capacity of RC members under both static and impact loading as it delays the cracking process that the specimen undergoes.In other words, the presence of axial load increases the moments associated with flexural capacity and crack-initiation. As a result, the time required for the cracks to developed at the end of L_{eff} is also increased. This means that it takes longer for the stress wave to travel through the span and reach the supports and consequently a large portion of the element span reacts to the impact load. The larger the effective length is, the more global the response tends to be (See Chapter 6). Due to the uncertainties concerning the mechanics underlying the behaviour of RC beams and columns under impact loading, further studies are required to examine the effect of the configuration of the reinforcement on the exhibited RC structural response under impact loading.

7.2 LIMITATIONS OF DETAILED NLFEA

NLFEA can be used in a safer and more cost-efficient manner for investigating a wider range of problems than those studied experimentally. It is capable of providing realistic predictions and more detailed insight into the mechanisms underlying RC structural response under high-rate loading. However, as it usually employs dense 3D finite element meshes combined with complex constitutive material laws implemented through the use of iterative solution strategies, the required computational resources are high. As a result, its use is generally limited for the analysis of relatively simple RC structural forms. Moreover, its ability for providing realistic predictions of RC structural behaviour is, in most cases, linked with the use of case-study dependent constitutive models often incorporating empirical amplification factors to account for the effect of strain-rate sensitivity on concrete material behaviour**.** This apparent lack of generality is the main drawback of NLFEA of RC structures, the results of which are often treated with suspicion as regards the validity of the predictions obtained.

7.3 LIMITATIONS OF ASSESSMENT METHODS EMPLOYED IN PRACTICE

To avoid the complexities and uncertainties associated with the existing assessment methods and in order to simplify the analysis and design procedures, many (mainly military) design codes employ equivalent simple lumped mass-spring systems for modelling individual structural elements with distributed mass and loading. The

equivalence is based on energy approximations that rely on an assumed deflected shape (the first eigenvector or the deflected shape under equivalent static loading). After predicting the behaviour of the individual structural element under high-rate loading, the response of the whole structure is assessed through the use of practical structural analysis packages. Such packages employ beam or shell elements to model individual structural members whereas the nonlinear response is accounted for through plastic hinge formation or by employing layered elements. The use of such packages requires considerably less computational resources than their counterparts employed mainly for research purposes, thus allowing the modelling of more intricate structures.

The above methodology, on the other hand, relies on a number of simplifications concerning both material behaviour and structural response. These include the use of simple uniaxial material laws, the description of post-failure behaviour, empirical amplification factors attributed to the strain-rate sensitivity of concrete behaviour, assumptions concerning the deformed shape of the structural elements and the use of elastic or elasto-plastic laws for describing structural behaviour. However, such simplifications do not allow the methodology to account for important characteristics of the problem at hand (a wave propagation problem within a highly nonlinear medium), the brittle nature of concrete and its sensitivity to triaxial stress conditions, the true mechanics governing RC structural response and the localised response often exhibited. This raises questions concerning the validity of the predicted behaviour and the effectiveness of the obtained design solutions.

7.4 BEHAVIOUR OF SLENDER RC BEAMS

The shift in structural performance exhibited by slender RC beam specimens (with $a_v/d>5$) when subjected to drop-weight testing compared to the behaviour exhibited by the same specimens under equivalent static loading confirms the findings of published experimental and numerical studies showing that with increasing loading rates the peak load sustained by the slender RC beam specimens increases compared to the load-carrying capacity established under equivalent static loading. This shift in structural response is attributed to the increasingly localised behaviour exhibited by the beams This is also confirmed by the analysing the photographic evidence collected during testing which reveals that the portion of the beam span reacting to the imposed load tends to concentrate around the impact region.

Based on the analysis of the photographic evidence recorded by the high-speed camera, it can be concluded that high values of strain rate exhibited in the mid-span area of the beam are exhibited once the concrete medium suffers considerable cracking and, as a result, these high strain rates do not correspond to a concrete material but are linked to post-failure behaviour of the cracked area of the beam. The values of strain rate in the critical early stages of the impact test were found to be considerably lower than the threshold established experimentally (over decades of testing) describing the variation of the concrete compressive and tensile strength under different strain rates. Thus, the increase in load-carrying capacity with the rate of loading observed in the present study cannot be attributed to an increase in the material strength due to strain rate sensitivity. It should also be borne in mind that the terms '*failure*' and '*load-carrying capacity*' require careful qualification as it will first be necessary to establish the post-impact performance criteria (such as the residual strength required and the level of damage that can be tolerated) in order to arrive at meaningful estimates.

7.5 BEHAVIOUR OF SHORTER BEAMS UNDER IMPACT LOADING

A total one nine short RC beams (with a_v/d) were tested on static or impact loading. The test data collected, were then compared to those obtained from the impact tests carried out on the slender RC beams. Attention was focused on the deformation profile and the associated crack patterns developing along the specimen span throughout the loading process, the mode of failure and the time history of the impact and the reaction forces generated at the impact region and at the supports respectively. The analysis of the photographic evidence collected during each test produced data that are in good agreement with the displacement measurements obtained during testing through the use of conventional instruments (e.g. strain gauges or deflection transducers).

The experimentally predicted deformation profiles and related crack-patterns exhibited by the short RC beam specimens (see Chapters 4) indicate that the full span of these specimens reacts to the imposed impact load and that localised response is exhibited at much higher loading rates (compared to those established for the of the slender beams). From the above, it can be concluded that, under high rates of loading, beam behaviour depends on the length of the span reacting to the imposed load (L_{eff}). A comparison between the experimentally and numerically established variation of DIF (expressed as the maximum load sustained by the RC beams under high rate loading normalised with respect to its counterpart under static loading) $maxP_d/maxP_s$, with increasing values of loading rate reveals that the slender RC

beams tend to exhibit higher load-carrying capacity comparing to the short beams (see Chapters 3 and 4).

Furthermore, the predictions obtained for the case of shorter beams suggest that, regardless of the amount of shear reinforcement used, the response of RC members with a shear span-to-depth ratio less than five tends to be more global. Despite this, the effect of transverse reinforcement on the exhibited failure modes of the members cannot be neglected. As shown in Chapter 4. Under impact loading, the specimens with no stirrups exhibited shear failure accompanied by inclined/shear cracks extending diagonally from the supports, deep into the compressive region. From the available photographic evidence, it is evident that cracking initiates early in the loading process. It is interesting to note that the crack patterns developing on the short RC beams under impact loading are similar to those developing under equivalent static loading. Furthermore. Under static and impact loading the short RC beams exhibited global response with the full span reacting to the imposed load.

Similar to the response observed for RC slender beams, high values of strain rate in the mid-span area of the beam are exhibited once the concrete medium suffers considerable cracking and, as a result, these high strain rates do not correspond to a concrete material but are linked to post-failure behaviour of a cracked area of the beam.

7.6 COMPARISON BETWEEN EXPERIMENTALLY AND NUMERICALLY ESTABLISHED BEHAVIOUR

The comparative study between the numerical predictions and their experimental counterparts reveals that the brittle concrete material model presently employed by ADINA is capable of providing realistic predictions concerning certain aspects of the response exhibited by RC beams under increasing rates of impact loading.

The predictions obtained from monotonic loading confirms the findings of previously published numerical studies which suggest that effect of loading rate on RC structural response reflects the influence of inertia and the nature of the problem at hand: a wave propagation problem within a highly nonlinear medium. The response was found to be associated with a specimen physical state characterised by considerable concrete disintegration and low residual stiffness and load-bearing capacity. The higher the loading rate and intensity of the impact load the larger the latter difference becomes.

The numerical results from *pulse loading, on the other hand,* reveal that the true load-bearing capacity is frequently significantly lower than the maximum sustained load recorded experimentally. As discussed in Chapter 5, the lowest percentage of the pulse corresponded to the true load-bearing capacity of the RC beams for the particular loading rate. The true load-bearing capacity of an RC beam was assumed to correspond to a peak value at which the externally applied load is resisted by the RC member (and in particular by concrete) prior to the development of any post-failure mechanism.

Concerning the deformation profile of RC beams, the ductility of the stronger (slender) beams in terms of the amount of compressive reinforcement was significantly higher than those predicted for weaker specimen among slender beams). The numerically predicted crack patterns revealed that a larger portion of the span reacts to the applied load. This suggests that the L_{eff} and therefore the mechanics underlying RC structural response will be affected by both the rate of applied loading and intensity of the imposed impact load.

7.7 PROPOSED ASSESSMENT METHOD

An equivalent static method is proposed assessing the behaviour of RC beams under impact loading which is based on the CFP method. Existing assessment methods appear to ignore the true behaviour exhibited by the RC beam specimens under impact loading as they do not account for the true nature of the problem at hand (a wave propagation problem within a highly nonlinear material) and the localised response exhibited. This raises concerns regarding the validity of the predictions provided by these codes and the effectiveness of the obtained design solutions. Unlike previous methods, the proposed assessment method links the observed shift in structural response to the localised behaviour exhibited with increasing rates of applied impact loading. The proposed assessment method, on the other hand, is found to be capable of providing predictions in agreement with the test data recorded and the predictions obtained from NLFEA.

The results obtained suggest that the application of axial loading increases the load-capacity of the specimens under static loading as it delays the cracking process the specimens undergoes. However, under impact loading, the rate with which the DIF ($maxP_d/maxP_s$) increases with higher loading rate reduces when the specimen is subjected to higher levels of axial (compressive) loading. This attributed to the fact that development of the cracking (defining the L_{eff}) is delayed and as a result occurs later in the loading process allowing the stress waves to travel more along the specimen allowing a larger portion of the element

span to react to the imposed load. Larger L_{eff} results in the proposed method predicting smaller values of load-carrying capacity.

7.8 RECOMMENDATIONS FOR FUTURE WORK

The drop-weight test currently adopted for the impact response of RC slender and short beams can be improved by accounting for different types of support conditions and expanded to other structural configurations such as slab and columns. Other forms of sophisticated instrumentations such as Laser Displacement Sensors can be adopted to improve the accuracy of the measured (displacement) data. The use of a High-speed camera with the ability to capture higher numbers of frames per second (in comparison with the one currently adopted) can significantly improve the accuracy of the experimental predictions in the form of photographic evidence.

The numerical analysis carried out can be conducted for assessing more complex form of structures such as frames, it can also be implemented in railway studies for simulation of multi-impacts (induced by trains) on concrete sleepers or concrete bridge decks/slabs. Furthermore, the currently adopted NLFEA package can be used to study the effects of a wide range of parameters such as support conditions, reinforcement configurations and axial loads. It can also be used for assessing and designing the strengthening members (e.g. FRP coated beams and columns). Finally, the current numerical analysis can be incorporated in assessing the full structural response through methods such as progressive collapse method.

The proposed assessment method requires further refinement for a wider range of RC structural forms (e.g. columns and slabs) in terms of their configuration details and design specifications (e.g. boundary conditions, reinforcement details, shear span-to-depth ratio and rate of loading and etc.) Finally, the predictions obtained using the method should be validated against a wider range of test data to form the basis of a new single degree of freedom system (SDOF) model which will be capable of addressing the drawbacks of the existing (military) codes in which the localised response of the members is essentially neglected.

REFERENCES

Abbas. H, and et al., “Nonlinear response of concrete beams and plates under impact loading.” International Journal of Impact Engineering 30, pp. 1039-1053, 2004.

Abbas. A.et. al, “Structural response of RC wide beams under low-rate and impact loading.’’ Magazine of Concrete Research 62(10), PP. 723-740, 2010.

Adhikary. S. D. et al., “Dynamic behaviour of reinforced concrete beams under varying rates of concentrated loading.” International Journal of Impact Engineering 47, PP. 24-38, 2012.

Adhikary, Satadru, Bing Li, and Kazunori Fujikake. "Low Velocity Impact Response of Reinforced Concrete Beams: Experimental and Numerical Investigation." International Journal of Protective Structures 6.1 (2015): 81-112.

Adhikary, Satadru Das, Bing Li, and Kazunori Fujikake. "State-of-the-art review on low-velocity impact response of reinforced concrete beams."Magazine of Concrete Research (2015): 1-23.

ADINA R & D, Inc: “Theory and Modelling Guide” Volume 1, Report ARD 13-8, December 2013.

American Concrete Institute, “Building Code Requirements for Structural Concrete (ACI 318-02) and Commentary (ACI 318R-02)”, 2002.

Bathe. K.-J, “Finite element procedures.” Prentice-Hall, New Jersey, 1996.

Bhatti, Abdul Qadir, et al. "Elasto-plastic impact response analysis of shear-failure-type RC beams with shear rebars." Materials & Design 30.3 (2009): 502-510.

Brara. A, Klepaczko. J. R, “Experimental characterization of concrete in dynamic tension.” Mech Mater. 38, pp. 253–67, 2006.

Barnard. P. R, “Researchers into the complete stress-strain curve for concert.” Mag. Res, 16, pp. 203-210, 1964.

Bischoff. P. H, and Perry. S. H, “Compressive behaviour of concrete at high strain rates”, Materials & Structures., RILEM, 24, PP. 425-450, 1991.

Bischoff. P. H, Perry. S. H, “Impact behaviour of plain concrete loaded in uniaxial compression.” J Eng Mech 24, pp. 425–50, 1995.

Corbett, G.G., Reid, S.R. and Johnson, W., “Impact loading of plates and shells by free-flying projectiles: a review”. International Journal of Impact Engineering, 18(2), pp.141-230, 1996.

Cotsovos. D. M. and Pavlović. M. N, “Numerical investigation of concrete subjected to compressive impact loading. Part 1: A fundamental explanation for the apparent strength gain at high loading rates”, Computers & Structures, Vol. 86, No. 1-2, pp. 145-163, January 2008.

Cotsovos. D. M. and Pavlović. M. N, “Numerical investigation of concrete subjected to compressive impact loading. Part 2: Parametric investigation of factors affecting behaviour at high loading rates”, Computers & Structures, Vol. 86, No. 1-2, pp. 164-180, January 2008.

Cotsovos. D. M. and Pavlović. M. N, “Numerical investigation of concrete subjected to high rates of uniaxial tensile loading”. International Journal of Impact Engineering, Vol. 35, No. 5, pp. 319-335, May 2008.

Cotsovos. D. M, Stathopoulos. N. D, and Zeris. Ch, “Behaviour of RC beams subjected to high rates of concentrated loading.” Journal of Structural Engineering ASCE 134(12), pp. 1839-1851, 2008.

Cotsovos. D. M. and Pavlović. M. N, “Modelling of RC beams under impact loading.” Proceeding of the ICE-Structures and buildings 165 (2), pp. 11-94, 2012.

Cotsovos. D. M. “Numerical Investigation of Structural Concrete under Dynamic (Earthquake and Impact) Loading.” PhD thesis, University of London, UK, 2004.

Cotsovos. D. M, “A simplified approach for assessing the load-carrying capacity of reinforced concrete beams under concentrated load applied at high rates.” International Journal of Impact Engineering 37, pp. 907-917, 2010.

Cook R.D., Malkus,D.S., Plesha, M.E. and Witt, R.J, “Concepts and applications of Finite Element analysis 4th Edition”. United States, John Wiley and Sons,Inc. 1989.

Eurocode 2, “Design of concrete structures”, 1992.

Eurocode 8, “Design of structures for earthquake resistance”, 1998.

Fujikake K, Li B and Soeun S (2009). Impact response of reinforced concrete beam and its analytical evaluation. ASCE, Journal of Structural Engineering, 135(8), pp.938-950.

Fujikake. K, Li. B, Soeun. S, “Impact response of reinforced concrete beam and its analytical evaluation.” ASCE Journal of Structural Engineering; 135(8), PP. 938-50. August 2009.

Gary. G, Bailly. P, “Behaviour of quasi-brittle material at high strain rate.” Eur J Mech. 17, pp. 403–20, 1998.

Grote. D. L, Park. S. W. and Zhou. M, “Dynamic behaviour of concrete at high strain rates and pressures” I. Experimental characterization, Int. J. Impact Eng. 25, pp. 869-886, 2001.

Griffith. A. A, “The phenomenon of rupture and flow in solids.” Phil. Trans. Roy. Soc., London, Series A, 221, pp.163-198, 1921.

Gerstle. K. H, et al., “Strength of concrete under multiaxial stress states.” Proc. Douglos McHenry International Symposium on Concrete and Concrete structures, SP-55, American Concrete Institute, Detroit, pp. 103-131, 1978.

Guo J-L, Cai J., and Zuo Z-L Simplified dynamic analysis of reinforced-concrete beams under impact actions. Proceedings of the Institution of Civil Engineers - Structures and Buildings 170:3, 211-224;2017.

H. M. I. Thilakarathna*, D. P. Thambiratnam, M. Dhanasekar, N. Perera , “Numerical simulation of axially loaded concrete columns under transverse impact and vulnerability assessment.” International Journal of Impact Engineering, 37, 1100e1112, 2010.

Hughes. G. and Spiers. D. M, “An investigation on the beam impact problem.” Cement and Concrete Association, Technical Report 546, 1982. Izatt. C. et al., “Perforation owing to impacts on reinforced concrete slabs.” Proceedings of the ICE-Structures and Buildings 162(1), PP. 37-44, 2009.

Izatt. C. et al., “Perforation owing to impacts on reinforced concrete slabs.” Proceedings of the ICE-Structures and Buildings 162(1), PP. 37-44, 2009.

N.Jones, “Structural Impact”. Cambridge, Cambridge University Press, 1990.

Kani. G. N. J, “The Riddle of Shear Failure and Its Solution.” ACI Journal Vol. 61, No. 4, pp. 441-462, April 1964.

Kaewunruen. S. and A. M. Remennikov, “Progressive failure of the prestressed concrete sleepers under multiple high-intensity impact loads.” Engineering Structures 31(10), PP. 2460-2473, 2009.

Kishi. N. et al., “Numerical Simulation of Reinforced Concrete Beams under Consecutive Impact Loading.” ACI structural Journal 108 (4), PP. 444-452, 2011.

Kishi. N, Mikami. H, and Ando. T, “An applicability of the FE impact analysis on shear-failure-type RC beams with shear rebars.” 4th Asia-Pacific Conference on Shock and Impact Loads on Structures, pp. 309-315, 2001.

Kishi N, Mikami H, Matsuoka KG, Ando T."Impact behaviour of shear-failure-type RC beams without shear rebar." International Journal of Impact Engineering 27.9: 955-968,2002.

Kishi, N., and Mikami, H. “Empirical Formulas for Designing Reinforced Concrete Beams under Impact Loading.” ACI Structural Journal, 109(4), 509-519, 2012.

Kishi, N., Nakano, O., Matsouka, K.G., and Ando, T. “Experimental Study on Ultimate Strength of Flexural-Failure-Type RC Beams under Impact Loading.” Transactions, SMIRT 16, Washington DC, August 2001.

Kotsovos. M. D. and Pavlović. M. N, “Structural Concrete: Finite-element analysis and design “. London, Thomas Telford, 1995.

Kulkarni, S.M. and Shah, S.P., “Response of reinforced concrete beams at high strain rates”. Structural Journal, 95(6), pp.705-715, 1998.

Kotsovos. M. D, “Consideration of Triaxial Stress Conditions in Design: A Necessity.” ACI Structural Journal 84 (1), pp. 266-273, 1987.

Kotsovos. M. D. “Compressive force path concept: basis for reinforced concrete ultimate limit state design.” ACI Structural Journal, 86 (1), PP. 68-75, 1988.

Kotsovos. M. D, and Bobrowski. J. A, “A design model based on the concept of the compressive force path.” ACI Structural Journal, 90 (1), PP. 12-20, 1993.

Kotsovos. M. D, and Michelis. P, “Behaviour of structural concrete elements designed to the concept of the compressive force path.” ACI Structural Journal, 93 (4), PP. 428-437, 1996.

Kotsovos. M. D. “Effect of testing techniques on the post-ultimate behaviour of concrete in compression.” Materials & Struct. RILEM 16, No. 1, pp. 3-12, 1983.

Kotsovos. M. D. and Newman. J. B, “Fracture mechanics and concrete behaviour’, Magazine of Concrete Research.” 31, pp. 103-112, 1981.

Kotsovos. M. D. and Newman. J. B, “A mathematical description of the deformational behaviour of concrete under complex loading.” Mag. Concrete Res., 31, pp. 77-90, 1979.

Kotsovos. G. M and et al., “Improving RC seismic design through the CFP method.” Structures and buildings, 158:291302, 2005.

Kulkarni. S. M, and Shah. S. P, “Response on reinforced concrete beams at high strain rates.” ACI Structural Journal 95, No. 6, pp. 705–715, 1998.

Kotsovos, M. D. and Spiliopoulos, K. V., “Modelling of crack closure for finite-element analysis of structural concrete”, Comput. Struct., 69, 383-398, 1998a.

Kotsovos, M. D. and Spiliopoulos, K. V., “Evaluation of structural-concrete design-concepts based on finite-element analysis”, Comput. Mech., 21, 330-338,1998b.

May. I. M, Chen. Y, Roger. D, Owen. J, Feng. Y. T, and Thiele. P. J, “Reinforced concrete beams under drop-weight impact loads.” Computers and Concrete 3, No 2-3, pp. 79-90, 2006.

Miyamoto. A, King. M. W, and Fujii. M, “Non-linear dynamic analysis and design concepts for RC beams under impulsive loads.” Bulletin of the New Zealand National Society for Earthquake Engineering, vol. 22, pp. 98-111, 1989.

Ožbolt, J., Sharma, A., İrhan, B. and Sola, E., 2014. Tensile behaviour of concrete under high loading rates. International Journal of Impact Engineering, 69, pp.55-68, 2014.

Pham, T.M. and Hao, H., “Effect of the plastic hinge and boundary conditions on the impact behaviour of reinforced concrete beams”. International Journal of Impact Engineering, 102, pp.74-85, 2017.

Rayleigh J.W., “On the production of vibrations by forces of relatively long duration with application to the theory of collisions”, Phil. Mag., 11,1906.

Reinhardt. H. W, Rossi. P, van. Mier. J. G. M, “Joint investigation of concrete at high rates of loading.” Mater Struct 23, pp. 213–6, 1990.

Ross. C. A, Tedesco. J. W, Kuennen. S. T, “Effects of strain rate on concrete strength.” ACI Mater J, 92, pp. 475–81, 1995.

Ross. C. A, Jerome. D. M, Tedesco. J. W, Hughes. L. M, "Moisture and strain effects on concrete strength." ACI Mater J 93, pp. 293–300, 1996.

Robert. D. Cook "Finite Element Modelling for stress analysis" John Wiley and Sons, Inc. United States, 1995.

Saatci. S, and F. J. Vecchio, "Nonlinear Finite Element Modelling of Reinforced Concrete Structures under Impact Loads." ACI structural Journal 106 (5), PP. 717-725, 2009.

Saatci. S. and F. J. Vecchio, "Effects of shear mechanisms on impact behaviour of reinforced concrete beams." ACI structural Journal 106 (1), PP. 78-86, 2009.

W.Goldsmith, "Impact: The Theory and Physical Behaviour of Colliding Solids". London, Edward Arnold, 1960.

Sukontasukkul. P. and et al., "Effect of loading rate on damage of concrete." Cement and Concrete Research (34), pp 2127-2134, 2004.

Saatci. S, "Behaviour and modelling of reinforced concrete structures subjected to impact loads." PhD thesis, University of Toronto, Canada, 2007.

Shaha. W, "Experimental and numerical studied on plain and fibre-reinforced high-strength subjected to high strain rate loadings." PhD thesis, National University of Singapore, 2011.

Schuler. H, Mayrhofer. C, Thoma. K, "Spall experiments for the measurement of the tensile strength and fracture energy of concrete at high strain rates." Int J Impact Eng. 32, pp. 1635-1650, 2006.

TM5-855-1, "Design and Analysis of Hardened Structures to Conventional Weapons Effects." The Departments of Army, Air Force and Navy and the Defence Special Weapons Agency, USA, 1998.

Thabet. A, and Haldaen. D, "Three-Dimensional Simulation of Nonlinear Response of Reinforced Concrete Members Subjected to Impact Loading." ACI Structural Journal 97(5), PP. 689-702, 2000.

Tejchman. J, and Bobinski. J, "Continuous and discontinuous modelling of fracture in concrete using FEM." Springer, Berlin, 2013.

Takeda. J.-I, Tachikawa. H, and Fujimoto. K, "Basic concept on the responses of structural members and structures under impact or impulsive loading. Concrete Structures under Impact and Impulsive Loading." Proceedings of RILEM, CEB, IABSE, IASS-Interassociation Symposium. BAM, Berlin (West), pp. 13–18, 1982.

Takeda. J.-I, Tachikawa. H, and Fujimoto. K, "Fracture of reinforced concrete structural members and structures subjected to impact or explosion. Concrete Structures under Impact and Impulsive Loading." Proceedings of RILEM, CEB, IABSE, IASS-Interassociation Symposium. BAM, Berlin (West), pp. 289–295, 1982.

Van. Mier. J. G. M. "Strain-softening of concrete under multiaxial loading conditions." PhD thesis, Eindhoven University of Technology, 1984.

Van. Mier. J. G. M, Shah. S. P, Armand. M, Balayssac. J. P, Bascoul. A, Choi. S, Dasenbrock. D, Ferrara. G, French. C, Gobbi M. E, Karihaloo. B. L, Konig. G, Kotsovos. M. D, Labuz. J, Lange-Korbar. D, Markeset. G, Pavlović. M. N, Simsch. G, Thienel. K-C, Turatsinze. A, Ulmer. M, van. Geel. H. J. G. M, van. Vliet. M. R. A. and Zissopoulos. D, "Strain softening of concrete in uniaxial compression." Materials and Structures RILEM 30, No.3, pp. 195-209, 1997.

Wu. H, Zhang. Q, Huang. F, Jin. Q, "Experimental and numerical investigation on the dynamic tensile strength of concrete." Int J Impact Eng. 32, pp. 605–17, 2005.

Wu, Mingxin, Zhenfu Chen, and Chuhan Zhang. "Determining the impact behaviour of concrete beams through experimental testing and meso-scale simulation: I. Drop-weight tests." Engineering Fracture Mechanics 135 (2015): 94-112.

Wu, Mingxin, Zhenfu Chen, and Chuhan Zhang. "Determining the impact behaviour of concrete beams through experimental testing and meso-scale simulation: I. Drop-weight tests." Engineering Fracture Mechanics 135 (2015a): 94-112.

Wu, Mingxin, Chuhan Zhang, and Zhenfu Chen. "Determining the impact behaviour of concrete beams through experimental testing and meso-scale simulation: II. Particle element simulation and comparison." Engineering Fracture Mechanics 135 (2015): 113-125.

Zhang, X. X., G. Ruiz, and Rena C. Yu. "A New Drop-Weight Impact Machine for Studying Fracture Processes in Structural Concrete." Strain46.3 (2010): 252-257.

Zhang, X. X., et al. "Fracture behaviour of high-strength concrete at a wide range of loading rates." International Journal of Impact Engineering 36.10 (2009): 1204-1209.

Zhang. X. X. and et al., "Fracture behaviour of high-strength concrete at a wide range of loading rates." International Journal of Impact Engineering 36, pp. 1204-1209, 2008.

Zielinski. A. J, "Concrete Structures under Impact Loading, Rate Effects", Department of Civil Engineering, TH Delft, Delft, Report 5-84-14, 1984.

Zissopoulos. P. M, Kotsovos. M. D, and Pavlović. M. N, "Deformational behaviour of concrete specimens in uniaxial compression under different boundary conditions." Cement and Concrete Res. 30, Issue 1, pp. 153-159, 2000.